AFRL-AFOSR-VA-TR-2024-0261

Hypersonic Boundary Layer Turbulence (BOLT-II) Flight Test Experiment

Bowersox, Rodney
TEXAS ENGINEERING EXPERIMENT STATION COLLEGE STATION
1470 WILLIAM D FITCH PKY
COLLEGE STATION, TX,
US

06/28/2024
Final Technical Report

DISTRIBUTION A: Distribution approved for public release.

Air Force Research Laboratory
Air Force Office of Scientific Research
Arlington, Virginia 22203
Air Force Materiel Command

REPORT DOCUMENTATION PAGE

PLEASE DO NOT RETURN YOUR FORM TO THE ABOVE ORGANIZATION.

1. REPORT DATE	2. REPORT TYPE	3. DATES COVERED	
20240628	Final	START DATE 20190501	END DATE 20230930

4. TITLE AND SUBTITLE
Hypersonic Boundary Layer Turbulence (BOLT-II) Flight Test Experiment

5a. CONTRACT NUMBER	5b. GRANT NUMBER	5c. PROGRAM ELEMENT NUMBER
	FA9550-19-1-0154	61102F
5d. PROJECT NUMBER	**5e. TASK NUMBER**	**5f. WORK UNIT NUMBER**

6. AUTHOR(S)
Rodney Bowersox

7. PERFORMING ORGANIZATION NAME(S) AND ADDRESS(ES)
TEXAS ENGINEERING EXPERIMENT STATION COLLEGE STATION
1470 WILLIAM D FITCH PKY
COLLEGE STATION, TX
US

8. PERFORMING ORGANIZATION REPORT NUMBER

9. SPONSORING/MONITORING AGENCY NAME(S) AND ADDRESS(ES)	10. SPONSOR/MONITOR'S ACRONYM(S)	11. SPONSOR/MONITOR'S REPORT NUMBER(S)
Air Force Office of Scientific Research 875 N. Randolph St. Room 3112 Arlington, VA 22203	AFRL/AFOSR RTA1	AFRL-AFOSR-VA-TR-2024-0261

12. DISTRIBUTION/AVAILABILITY STATEMENT
A Distribution Unlimited: PB Public Release

13. SUPPLEMENTARY NOTES

14. ABSTRACT
A basic research hypersonic flight experiment was executed. The objective was to improve the understanding and prediction of heat flux and skin friction associated with hypersonic boundary layer turbulence during flight on a geometry that created a complex flow path with pressure gradients, stationary vortex streaks, and competing transition mechanisms. The accomplishments included design and fabrication of flight hardware, supporting numerical simulations, ground test, flight stability, preliminary/critical design reviews, ground test of the flight hardware, integration into payload, flight experiment (March 21, 2022), and post-flight data analyses. The database was delivered to AFOSR.

15. SUBJECT TERMS

16. SECURITY CLASSIFICATION OF:			17. LIMITATION OF ABSTRACT	18. NUMBER OF PAGES
a. REPORT U	b. ABSTRACT U	c. THIS PAGE U	UU	143

19a. NAME OF RESPONSIBLE PERSON	19b. PHONE NUMBER *(Include area code)*
AMANDA CHOU	00000000

Standard Form 298 (Rev.5/2020)
Prescribed by ANSI Std. Z39.18

DISTRIBUTION A: Distribution approved for public release.

REPORT DOCUMENTATION PAGE

1. REPORT DATE	2. REPORT TYPE	3. DATES COVERED	
		START DATE	END DATE
20240129	FINAL REPORT	20190501	20230930

4. TITLE AND SUBTITLE
HYPERSONIC BOUNDARY LAYER TURBULENCE (BOLT-II) FLIGHT TEST EXPERIMENT

5a. CONTRACT NUMBER	5b. GRANT NUMBER	5c. PROGRAM ELEMENT NUMBER
	FA9550-19-1-0154	

5d. PROJECT NUMBER	5e. TASK NUMBER	5f. WORK UNIT NUMBER

6. AUTHOR(S)
RODNEY BOWERSOX, AARON DUFRENE, HELEN REED, TIM WADHAMS, ED WHITE

7. PERFORMING ORGANIZATION NAME(S) AND ADDRESS(ES)
TEXAS A&M ENGINEERING EXPERIMENT STATION
3124 TAMU
COLLEGE STATION TX 77843-3124

8. PERFORMING ORGANIZATION REPORT NUMBER

9. SPONSORING/MONITORING AGENCY NAME(S) AND ADDRESS(ES)	10. SPONSOR/MONITOR'S ACRONYM(S)	11. SPONSOR/MONITOR'S REPORT NUMBER(S)
USAF, AFRL DUNS 143574726 AF OFFICE OF SCIENTIFIC RESEARCH 875 NORTH RANDOLPH STREET, RM 3112, ARLINGTON VA 22203-1954	AFOSR	

12. DISTRIBUTION/AVAILABILITY STATEMENT
UNLIMITED

13. SUPPLEMENTARY NOTES
PREPARATION WITH COLLABORATION WITH
CUBRC AERONAUTICS
455 GENESEE ST. SUITE 106
BUFFALO NY 14225

14. ABSTRACT
A basic research hypersonic flight experiment was executed. The objective was to improve the understanding and prediction of heat flux and skin friction associated with hypersonic boundary layer turbulence during flight on a geometry that created a complex flow path with pressure gradients, stationary vortex streaks, and competing transition mechanisms. The accomplishments included design and fabrication of flight hardware, supporting numerical simulations, ground test, flight stability, preliminary/critical design reviews, ground test of the flight hardware, integration into pay-load, flight experiment (March 21, 2022), and post-flight data analyses. The database was delivered to AFOSR.

15. SUBJECT TERMS
HYPERSONIC FLIGHT TEST, BOUNDARY LAYER TRANSITION, TURBULENCE

16. SECURITY CLASSIFICATION OF:			17. LIMITATION OF ABSTRACT	18. NUMBER OF PAGES
a. REPORT	b. ABSTRACT	C. THIS PAGE		
U	U	U	UU	141

19a. NAME OF RESPONSIBLE PERSON	19b. PHONE NUMBER *(Include area code)*
RODNEY D. W. BOWERSOX	(979) 845-0139

PREVIOUS EDITION IS OBSOLETE.

STANDARD FORM 298 (REV. 5/2020)
Prescribed by ANSI Std. Z39.18

DISTRIBUTION A: Distribution approved for public release.

INSTRUCTIONS FOR COMPLETING SF 298

1. REPORT DATE.
Full publication date, including day, month, if available. Must cite at least the year and be Year 2000 compliant, e.g. 30-06-1998; xx-06-1998; xx-xx-1998.

2. REPORT TYPE.
State the type of report, such as final, technical, interim, memorandum, master's thesis, progress, quarterly, research, special, group study, etc.

3. DATES COVERED.
Indicate the time during which the work was performed and the report was written.

4. TITLE.
Enter title and subtitle with volume number and part number, if applicable. On classified documents, enter the title classification in parentheses.

5a. CONTRACT NUMBER.
Enter all contract numbers as they appear in the report, e.g. F33615-86-C-5169.

5b. GRANT NUMBER.
Enter all grant numbers as they appear in the report, e.g. AFOSR-82-1234.

5c. PROGRAM ELEMENT NUMBER.
Enter all program element numbers as they appear in the report, e.g. 61101A.

5d. PROJECT NUMBER.
Enter all project numbers as they appear in the report, e.g. 1F665702D1257; ILIR.

5e. TASK NUMBER. Enter all task numbers as they appear in the report, e.g. 05; RF0330201; T4112.

5f. WORK UNIT NUMBER.
Enter all work unit numbers as they appear in the report, e.g. 001; AFAPL30480105.

6. AUTHOR(S). Enter name(s) of person(s) responsible for writing the report, performing the research, or credited with the content of the report. The form of entry is the last name, first name, middle initial, and additional qualifiers separated by commas, e.g. Smith, Richard, J, Jr.

7. PERFORMING ORGANIZATION NAME(S) AND ADDRESS(ES). Self-explanatory.

8. PERFORMING ORGANIZATION REPORT NUMBER.
Enter all unique alphanumeric report numbers assigned by the performing organization, e.g. BRL-1234; AFWL-TR-85-4017-Vol-21-PT-2.

9. SPONSORING/MONITORING AGENCY NAME(S) AND ADDRESS(ES). Enter the name and address of the organization(s) financially responsible for and monitoring the work.

10. SPONSOR/MONITOR'S ACRONYM(S). Enter, if available, e.g. BRL, ARDEC, NADC.

11. SPONSOR/MONITOR'S REPORT NUMBER(S). Enter report number as assigned by the sponsoring/monitoring agency, if available, e.g. BRL-TR-829; -215.

12. DISTRIBUTION/AVAILABILITY STATEMENT. Use agency-mandated availability statements to indicate the public availability or distribution limitations of the report. If additional limitations/ restrictions or special markings are indicated, follow agency authorization procedures, e.g. RD/ FRD, PROPIN, ITAR, etc. Include copyright information.

13. SUPPLEMENTARY NOTES. Enter information not included elsewhere such as: prepared in cooperation with; translation of; report supersedes; old edition number, etc.

14. ABSTRACT. A brief (approximately 200 words) factual summary of the most significant information.

15. SUBJECT TERMS. Key words or phrases identifying major concepts in the report.

16. SECURITY CLASSIFICATION. Enter security classification in accordance with security classification regulations, e.g. U, C, S, etc. If this form contains classified information, stamp classification level on the top and bottom of this page.

17. LIMITATION OF ABSTRACT. This block must be completed to assign a distribution limitation to the abstract. Enter UU (Unclassified Unlimited) or SAR (Same as Report). An entry in this block is necessary if the abstract is to be limited.

PREVIOUS EDITION IS OBSOLETE.

STANDARD FORM 298 (REV. 5/2020)
Prescribed by ANSI Std. Z39.18

DISTRIBUTION A: Distribution approved for public release.

FINAL REPORT

AFOSR PROJECT FA9550-19-1-0154

HYPERSONIC BOUNDARY LAYER TURBULENCE (BOLT II) FLIGHT TEST EXPERIMENT

01/29/2024

BY

DR. RODNEY BOWERSOX (PI),[1] DR. AARON DUFRENE (CO-PI),[2]
DR. HELEN REED (CO-PI),[1] MR. TIM WADHAMS (CO-PI),[2] DR. ED WHITE (CO-PI)[1]

TAMU STUDENTS:[1] ETHAN BEYAK (PHD), HEATHER KOSTAK-TEPLICEK (PHD),
BRYAN MORREALE (PHD), ERIC SWINNY (MS), DANIEL MULLEN (PHD),
AF 2LT JOHN WIRTH (PHD),

[1]AEROSPACE ENGINEERING
TEXAS A&M UNIVERSITY
COLLEGE STATION, TX 77845

[2]AERONAUTICS
CUBRC
BUFFALO, NY 14225

TO

DR. BRETT POKINES
AIR FORCE OFFICE OF SCIENTIFIC RESEARCH
875 NORTH RANDOLPH STREET
ARLINGTON VA 22203-1954

DISTRIBUTION A: Distribution approved for public release.

EXTENDED ABSTRACT

A basic research **bo**undary **l**ayer **t**urbulence (BOLT II) hypersonic flight experiment was executed. The research objective was to provide new data to close existing knowledge gaps to improve understanding and prediction of heat flux and skin friction associated with hypersonic flight. The flight geometry introduced a complex flow with pressure gradients, stationary vortex streaks, competing transition mechanisms, and a complex turbulent flow. The flight experiment was sponsored by the Air Force Office of Scientific Research (AFOSR). The name was changed by AFOSR to the "BOLT II Flight Experiment in Memory of Mike Holden." The flight system design included determining the flight geometry, laminar and Reynolds averaged Navier-Stokes simulations, boundary layer stability analyses, subscale surface heating and off body measurements, flight system aerodynamic database generation, preliminary design review, flight vehicle design review, critical design review, thermal and structural loading analyses, instrumentation layout design, and design/procurement flight computers/data acquisition boards. The computations and stability analyses took place at Texas A&M University (TAMU), and the subscale tests took place in the TAMU Mach 6 Quiet tunnel (M6QT) and Actively Controlled Expansion tunnel. The fabrication included manufacture of the research geometry at CUBRC, installation of the instruments/flight computers/data acquisition boards, and ground tests on the instrumented flight hardware in the CUBRC LENSII tunnel. The flight experiment accomplishments included integration of the flight test article into the NASA flight payload, preflight tests, flight experiment (March 21, 2022), and postflight analyses. The full database was delivered to AFOSR. The following key observations are noted. Transition was first observed in a mixed second and cross flow mode region on the -z side of the vehicle at Re_x = 4.0–6.0x10^6. This result is consistent with the TAMU Mach 6 ground tests, where transition was first observed in this region at Re_x = ~3.5x10^6. In the +z mixed-mode region, transition took place at higher Reynolds numbers, Re_x = 7.0–10.0x10^6. Pressure spectra in mixed-mode region showed a peak around 300-500 kHz. Stability calculations indicated that both second mode and crossflow were present. Off-body hot-film results on a 25% subscale model in the M6QT indicated that Type-I and -II secondary instabilities associated with stationary mixed 2nd and crossflow mode vortex streak were the likely transition mechanism. Centerline transition was initiated in roll-up vortices just off the center line at Re_x = 5.5−7.5x10^6. High-frequency pressure sensors indicated that all pressure fluctuations remained below 300 kHz. Leading-edge transition was observed in row 4 at Re_x = 12.0–16.0 x 10^6. The analyses also showed that the spatial evolution to turbulence varied with respect to location of the vortex heating streaks. Prominent overshoots were observed in the turbulence within the streak. In addition to transition, turbulenc data was collected for Reynolds numbers Re_L up to 45x10^6. Conjugate heat transfer simulations, both laminar and turbulent, agreed well with the experimental data, including the laminar leading edge. The Reynolds analogy ratios based on the curve-fits to the data, including compressibility, were generally between 0.9 and 1.0, which was slightly higher than the theoretical value of $Pr^{2/3}$. The observed differences were likely the result of spatial separation of the sensors and slightly different definitions of Stanton number normalization between flight and theory.

DISTRIBUTION A: Distribution approved for public release.

TABLE OF CONTENTS

EXTENDED ABSTRACT ii
TABLE OF CONTENTS iii
PROJECT NARRATIVE 1

1. Introduction 1
1.1. Motivating Challenges 1
1.2 Basic Research Objective, Goals, and Nature of Expected Results 3
2. Background Review 5
2.1 Hypersonic Boundary Layer Stability and Transition 5
2.2 Hypersonic Boundary Layer Turbulence 6
2.3 CUBRC HIFiRE 5 Ground Test 9
2.4 BOLT Thermal Loading 10
2.5 BOLT II Transition and Turbulence Simulations 10
3. Research Approach 13
3.1 Scientific Approach and Contributions 13
3.2 Project Timeline and Task Milestones 13
4. Research Results – Task 1 Determine the Flight Geometry 15
4.1 Flight System Stability 15
4.2 Boundary Layer Stability Analyses 18
4.3 Subscale Ground Tests 20
4.3.1 Test Articles 20
4.3.2 Infrared Thermography in the M6QT and ACE 24
4.3.3 Surface Pressure Fluctuation Spectra in the M6QT and ACE 28
4.2.4 Off Body Hot-Film Measurements in the M6QT 33
4.4 Flight Geometry Materials Selection and Thermal Protection 38
4.5 Flight Geometry Instrumentation Selection 44
4.6 PDR and CDR 49
4.7 *Risks and Risk Mitigation* 50
4.7.1 Flight System Risks 50
4.7.2 Research Geometry Risks 50
4.7.3 Science Mission Risks 50
5. Research Results – Task 2 Develop the Flight Research Hardware 52
5.1 Manufacture the Flight Research Vehicle 52
5.2 Instrument the Flight Research Vehicle 55
5.3 Ground Test of Flight Geometry in LENS II 56
5.4 Integration of the Flight Geometry with NASA Payload System 59
6. Research Results – Task 3 Flight Experiment and Data Analysis 60
6.1 Flight Experiment Summary 60
6.2 BOLT II Flight Data 62
6.2.1 Database Summary 62
6.2.2 Data Reduction Methods 64
6.2.3 Numerical Simulations 66
6.2.4 Post Flight Results - Boundary Transition and Turbulence 69
6.2.5 Post Flight Results – Reynolds Analogy 81
7. Conclusions 90

DISTRIBUTION A: Distribution approved for public release.

7.1 Summary 90
7.2 Key Findings 91
7.2 Publications to Date 92
8. Facilities and Instrumentation **94**
8.1 TAMU National Aerothermochemistry and Hypersonic Flight Laboratory 94
8.2 CUBRC LENS Shock Tunnel Facilities 97
8.3 Computational Resources 98
8.4 Design and Analysis Software at TAMU and CUBRC 99
8.5 Machining Capabilities 99
8.5.1 CUBRC 99
8.5.2 TAMU 100
9. Acknowledgement and Disclaimer **101**
10. References **102**
APPENDIX A – PDR REQUEST FOR ACTION (RFA) RESPONSES **109**
A.1 RFA #1: Flight Objective 109
A.2. RFA GROUP #2: BOLT II Instrumentation Design 114
APPENDIX B – CDR RFA RESPONSES **128**
B.1 Configuration Control 128
B.2 PCB Data 130
B.3 Side B Experiment 131
B.4 Flight System RFA Group 136

DISTRIBUTION A: Distribution approved for public release.

PROJECT NARRATIVE

1. INTRODUCTION

A key challenge encountered by hypersonic vehicle designers is accurate prediction of viscous thermal loading. This challenge is relevant to many vehicle classes, including gliding reentry, long-range cruise systems, and interceptors. Summarized in this Section are motivating challenges and project objectives.

1.1. MOTIVATING CHALLENGES

Precise knowledge of high-speed, high Reynolds number turbulent gaseous flow is essential for the design of efficient hypersonic flight systems. Thermal management is a key technological challenge. Hence, accurate prediction of aerodynamic heating is a critical capability. The impact of turbulence on surface thermal loading is depicted on the space shuttle reentry infrared image shown in Fig. 1a (Horvath *et al.* 2010). Referring to Fig. 1a, the large higher heating region (yellow) that originates near the leading edge was the result of an unexpected protuberance tripping the flow to turbulence, which impacted the wing heating (red). On the opposite wing, the small wedge heating is the result of an intentional boundary layer trip.

Direct simulation of the turbulent flow leading to the increased heating is challenged by the wide range of fluctuating turbulent scales, as shown in the Mach 5 boundary layer image in Fig. 1b. This problem is exasperated by the presence of hypersonic flow effects, such as strong pressure gradients, high-temperature effects, strong shock waves, and viscous-inviscid interactions. Thus, for the foreseeable future, simulation of hypersonic high Reynolds number complex flight vehicle systems is limited to either the Reynolds Averaged Navier-Stokes (RANS) or Large-Eddy Simulation (LES) methods. These methods introduce second-order moments between fluctuating flow properties. The prevalent terms include the Reynolds stress tensor and the heat flux vector.

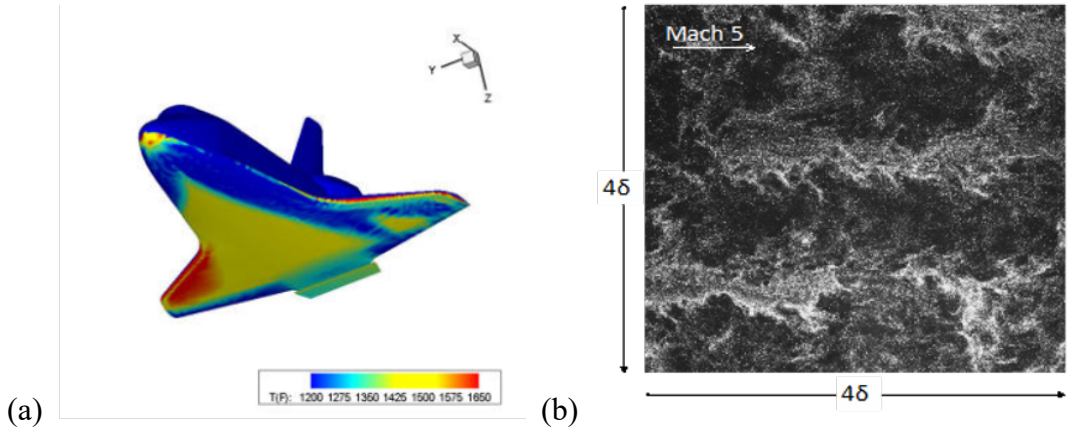

(a) (b)

Figure 1. Motivating images. (a) Shuttle heating during reentry (Horvath *et al.* 2010), where the increased heating wedges on the lower surface are the result of boundary layer tripping from laminar to turbulent flow. (b) Laser Mie scattering image of a Mach 5 (Re_θ = 30,000) turbulent boundary layer (top view) from the PI's laboratory.

DISTRIBUTION A: Distribution approved for public release.

Th Reynolds stress and the resulting transport equation are the basis for a spectrum of models, with many near-wall and compressibility treatments; a summary of which is given in Section 2. The turbulent heat flux is ubiquitously modeled in terms of a mean enthalpy gradient, with a constant turbulent Prandtl number. This approach has proven tunable for low speeds and simple geometries. However, the disadvantages of this approach include: (i) pressure gradient effects are not explicit in the formulation, (ii) an inability to predict realistic values of all three components as the model aligns the heat flux with the mean scalar gradient (Wikstrom *et al.* 2000), (iii) the asymptotic near-wall behavior does not agree with DNS data (Bowersox 2009), and (iv) inaccurate simulation of the heat flux under hypersonic cold-wall conditions (Gnoffo *et al.* 2013).

In 2017, the Air Force Office of Scientific Research (AFOSR) established a basic research flight experiment program to advance understanding and prediction of boundary layer transition (BOLT) physics on low-curvature concave surfaces with swept leading-edges at high Mach number. The BOLT Flight Geometry is shown in Fig. 2a. This configuration created a complex flow path with pressure gradients and wall temperature effects, which led to competing transition mechanisms and ultimately a complex turbulent flow. High fidelity numerical simulation results showing the three dimensional and vortex streak characterized flow are presented in Figs. 2b and 2c. A key goal of BOLT project was to critically assess modern ground test and numerical simulation tools in the prediction of transition (Wheaton *et al.* 2021).

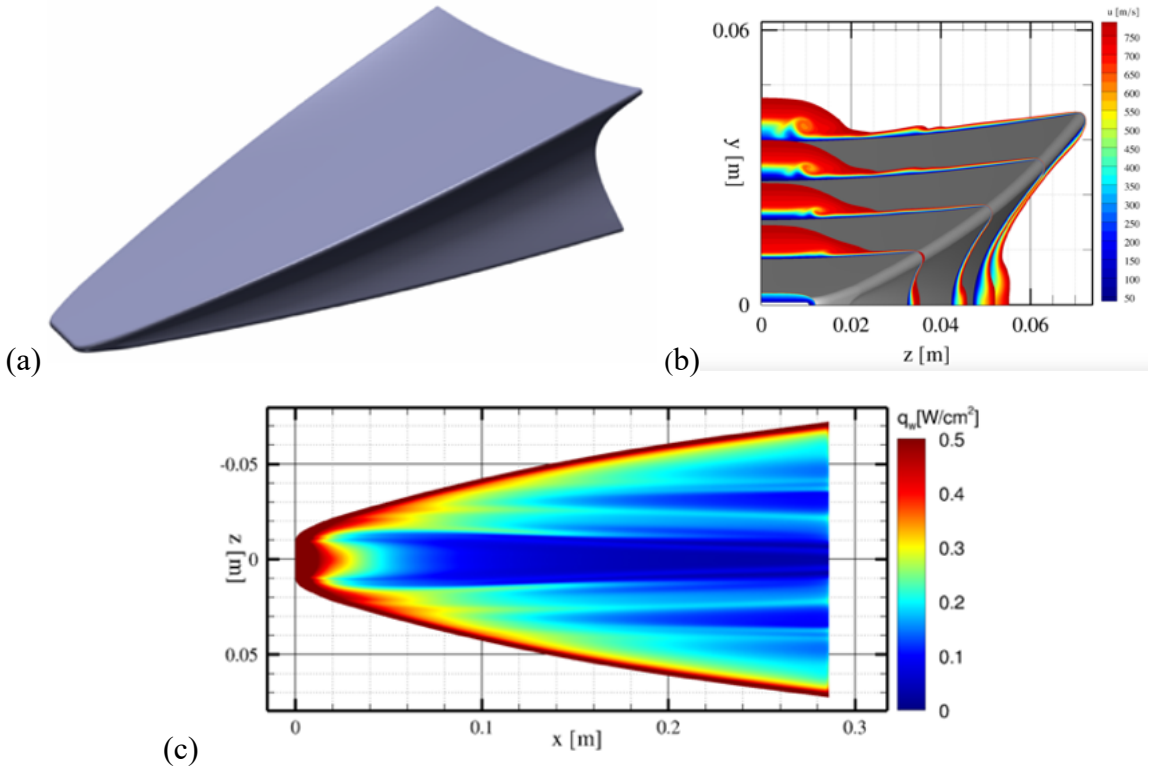

Figure 2. BOLT Laminar CFD results (Thome *et al.* 2018). (a) Sketch of Geometry, (b) Complex mean flow, and (c) Surface Heat Flux.

DISTRIBUTION A: Distribution approved for public release.

An important observation from the BOLT program was that achieving natural transition within current quiet facilities (Purdue University and Texas A&M University) was difficult due to the upper limits on the quiet flow Reynolds number (e.g., Kostak *et al.* 2019). This finding is significant for hypersonic turbulence simulation validation. For example, this limitation adds uncertainty in (1) knowing the range of applicability of the local similarity hypothesis for hypersonic flow under quiet conditions and (2) predicting the role of transition mechanism and secondary flow on the underlying structure of turbulence before similarity is achieved.

The estimated maximum Reynolds number for the BOLT flight tests exceeded that available in contemporary quiet tunnels by a factor of approximately 5, as indicated by the map presented in Fig. 3. Hence, flight test offers the possibility to provide validation data under quiescent conditions for transition and turbulence processes that cannot be achieved in ground test, such as the two listed above. This requirement, coupled with the TAMU-CUBRC team experience in turbulence modeling, transition modeling, ground test, and the BOLT flight test, formed the basis for this project.

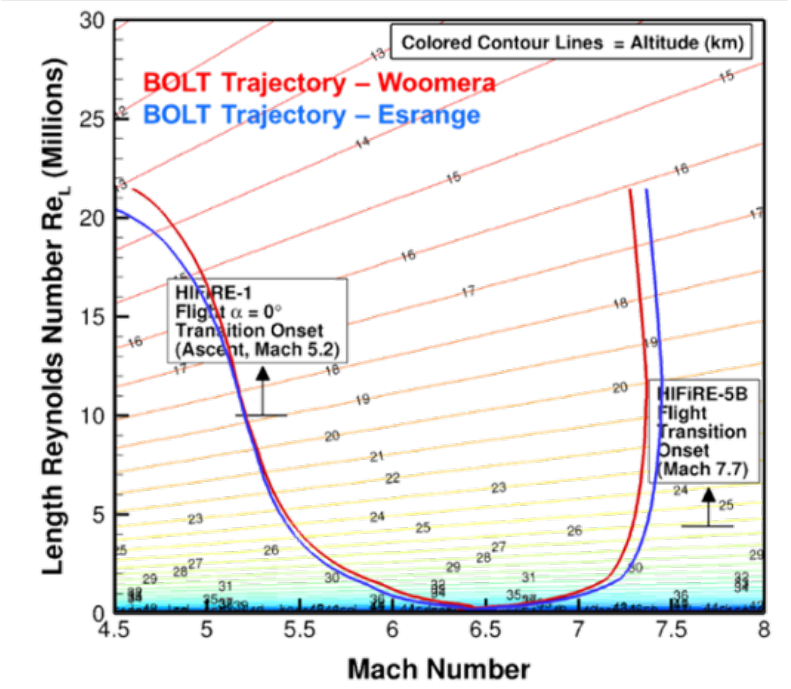

Figure 3. Estimated BOLT Trajectory (Wheaton *et al.* 2021)

1.2 Basic Research Objective, Goals, and Nature of Expected Results

A basic research objective of the **bo**undary **l**ayer **t**urbulence (BOLT II) hypersonic flight experiment was to provide new data to close existing knowledge gaps to improve understanding and prediction of heat flux and skin friction associated with hypersonic flight on a geometry. The geometry introduced a complex flow path with pressure gradients, stationary vortex streaks, competing transition mechanisms, and a complex turbulent flow. The flight experiment was sponsored by the Air Force Office of Scientific Research (AFOSR). The name was changed by AFOSR to the "BOLT II Flight Experiment in Memory of Mike Holden." The flight involved two experiments

DISTRIBUTION A: Distribution approved for public release.

(i) naturally occurring transition on Side A and (ii) forced on Side B. The Side A experiment was the focus of this project. Side B was led by S. Berry at NASA Langley Research Center, which was described in a companion NASA report. The BOLT II testbed was derived from the AFOSR **bo**undary **l**ayer **tr**ansition (BOLT) configuration.

The project had four goals, which were accomplished through a systematic research plan described in Section 3.

- **Goal 1 –** *Add to the national database by quantifying the heat flux and skin friction on the BOLT II configuration during hypersonic flight with natural transition*. Flight test was preferred as natural transition within quiet tunnels has proven difficult to achieve and the wall temperature ratios are mismatched. Filling this void in the hypersonic database reduces uncertainty in (1) understanding the initial structure of turbulence in the presence of secondary flow and stationary instability vortices and (2) knowing when local similarity begins under flight conditions.
- **Goal 2 -** *Characterize the turbulent flow structure using state-of-the-art ground test and numerical simulation methods, while assessing the ability of these tools to predict thermal loading during flight.* The comparison of full-scale flight test at CUBRC with the actual flight represented a unique opportunity to advance both our understanding of the turbulent flow structure during flight and our ability to extend ground test to flight. Supporting laminar, RANS, boundary layer stability analyses, and 25% subscale tests were performed.
- **Goal 3 -** *Advance turbulent heat flux treatments for strained, non-adiabatic flow on the BOLT II configuration.* The focus was the manner that secondary flow, strain rates, and vortex flow patterns alter the near wall dynamical structure and thermal transport. Critical assessment of model performance provided a new basis to guide research into new theories.
- **Goal 4 –** *Promote external interaction*. Continuing the collaboration with the BOLT team Johns Hopkins Applied Physics Laboratory (JHUAPL) on BOLT II and inviting industrial volunteers to participate on the project expanded the impact and promoted dissemination of data and research tools.

The first three goals listed above are scientific. The fourth goal was performed to help mitigate project risk and facilitate dissemination of state-of-the-art methods to industry.

A three-year milestone driven program was accomplished. The plan, as explained in Section 3, utilized the experience of the Research Team in turbulence, stability and transition, quiet tunnel testing, full-scale flight duplication testing, and flight test article fabrication and instrumentation. The Research Team also gained experience as active participants in the original BOLT program. The expected result is a benchmark database for hypersonic heating during flight, with supporting numerical, ground test analyses. These databases represent new contributions to the hypersonic knowledgebase to aid in improving thermal management and vehicle efficiency.

DISTRIBUTION A: Distribution approved for public release.

2. BACKGROUND REVIEW

A brief review of relevant literature and progress on hypersonic transition and turbulence is presented in this section. This review is not exhaustive, but instead is provided to place this project into the context of improved prediction of transition and turbulent during flight.

2.1 HYPERSONIC BOUNDARY LAYER STABILITY AND TRANSITION

The stability and transition of high-speed boundary layer flow remains a scientifically challenging problem with many important applications. Hence, many reviews are available (e.g., see Reshotko 1976, 1991, 2007, 2008; Mack 1984; Stetson 1987; Morkovin & Reshotko 1990; Stetson & Kimmel 1992; Kimmel *et al.* 1999; Schneider 1999, 2001, 2004, 2006, 2008, 2010; Horvath *et al.* 2002; Lau 2008; Lin 2008; Fedorov 2011; Zhong & Wang 2012; Reed *et al.* 1996, 1997, 2015). As the Mach number exceeds 5.0, the flow undergoes changes that challenge many of the approximations and theories that have guided modeling and simulation.

Hypersonic flight introduces viscous and inviscid interactions, which lead to multiple gradients in velocity, temperature, pressure, and entropy. Boundary layer transition from laminar to turbulence evolves in many ways depending on the conditions of the mean flow and disturbances. The available pathways from laminar to turbulent flow represent a complex and often coupled mapping of mechanisms; see Fig. 4 for a schematic of known pathways. Once transitioned, turbulent boundary layers result in increased heat transfer. However, turbulence is often preferred near control surfaces and inlets to help prevent large-scale separated flow. Hence, accurate simulation (ground test and computation) of both transition and turbulence is a key enabling technology that can significantly improve vehicle survivability and efficiency.

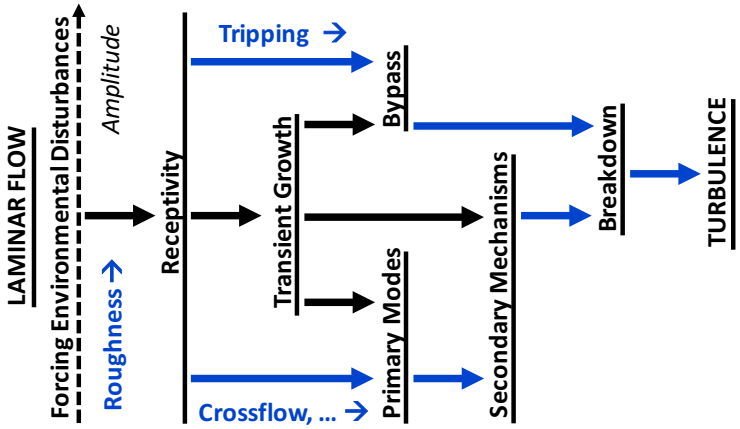

Figure 4. Transition pathways from laminar to turbulent flow (left-to-right), with passages relevant to the present study highlighted in blue. Adapted from Morkovin and Reshotko (1990).

Much of the early work on hypersonic boundary-layer stability has focused on planar bodies or axisymmetric shapes, with associated first- and second-mode instability mechanisms; these are now reasonably well understood. See, for example, Mack (1984), Fedorov (2011) and Reed *et al.* (2015). The crossflow instability mechanism becomes significant in regions of spanwise curved streamlines. Stationary crossflow instability is an instability with early nonlinear effects and a

DISTRIBUTION A: Distribution approved for public release.

strong dependence on surface roughness/receptivity (Reed & Saric 1989; Saric *et al.* 2003; Balakumar & Owens 2010; Schuele *et al.* 2013; Dinzl & Candler 2016). Near the leeward, windward, and symmetry planes, other instabilities dominate (e.g., Paredes & Theofilis 2014; Paredes *et al.* 2014). Many experiments have been completed and indicate that the basic stability mechanisms in 3-D boundary layers consist of multiple modes with some occurring simultaneously, e.g., first mode, second mode, stationary and traveling crossflow, secondary instabilities, and so forth (e.g., Borg *et al.* 2011, 2012*,* 2015; Craig & Saric 2016; Borg & Kimmel 2016, 2017; Sweeney et al 2016; Neel *et al.* 2017). Recent direct numerical simulations, parabolized stability equations (PSE, both linear and nonlinear), and global methods have provided mechanism identification (e.g., Balakumar & Reed 1991; Kimmel et al 1999; Choudhari et al 2009; Balakumar & Owens 2010; Li *et al.* 2010, 2011, 2012; Paredes *et al*. 2014; Kuehl *et al.* 2012; Gronvall *et al*. 2012; Paredes & Theofilis 2014; Oliviero *et al.* 2015; Reed *et al.* 2015; Dinzl & Candler 2016; Kocian *et al.* 2016, 2017).

Relevant to the BOLT II geometry, Kocian *et al.* (2016, 2017) used the TAMU NPSE/LPSE code to investigate the crossflow and 2-D instabilities on the HIFiRE-5 elliptic cone and compare with the steady DNS of Dinzl & Candler (2016) and the experiments of Borg & Kimmel (2016, 2017). EPIC LPSE N-factors suggest that transition would occur farther downstream on the paths closer to the symmetry planes than those on the shoulder of the cone due to crossflow. There is qualitative and quantitative agreement with the experiments of Borg & Kimmel.

The TAMU group also performed an experimental study examining the role of freestream disturbances on the transition process on a 38.1% scale HIFiRE-5 2:1 elliptic cone (Neel *et al.* 2017, 2018; Corke *et al.* 2018). Neel *et al.* showed that the surface heat flux and surface pressure spectra agreed qualitatively and quantitatively to within the measurement uncertainty between the tunnels at Purdue and TAMU. For this project, the important results from these studies are the significant differences in the transitional fronts and surface spectra under quiet and conventional flows. Presented in Fig. 5 are example transition front results from numerical simulation and experiments within the TAMU Mach 6 quiet tunnel. A key feature is the persistence of the stationary crossflow structure into the turbulent high heating regions (red). Modeling the impact of the crossflow vortices on boundary layer turbulence and heat transfer is uncertain.

2.2 Hypersonic Boundary Layer Turbulence

The structure underlying the turbulence within boundary layers in low-speed flows is well characterized (e.g., see Adrian *et al.* 2000). Our group (Peltier *et al.* 2016) provided experimental characterization of this canonical structure at hypersonic conditions. An example convective velocity plot is shown in Fig. 6. The dashed line depicts the outer boundary of a very-large-structure, and the circled structures indicate the signatures of hairpin vortices. Structure data, such as this, have proven useful in helping to provide new understandings with implications in Reynolds averaged Navier-Stokes (RANS) and large-eddy simulation (LES) modeling.

Wall temperature, pressure gradient, and roughness all fundamentally alter the canonical flow structure shown in Fig. 6 (Duan *et al.* 2010; Tichenor *et al.* 2013; Peltier *et al.* 2016). For cold

DISTRIBUTION A: Distribution approved for public release.

walls, the structures are elongated, with what appears to be less dynamical content, as compared to the adiabatic and heated wall cases, which has profound impact on the wall heat transfer. Similarly, pressure gradients alter this structure (Ekoto *et al.* 2009; Tichenor *et al.* 2013, 2017; Peltier *et al.* 2012, 2016; Neel *et al.* 2017) and the corresponding Reynolds stresses. The Reynolds stresses τ_{ij}^{T} have been observed to change by order ±100% for modest mechanical non-equilibrium curvatures. Hypersonic and supersonic flows are often treated in ad hoc manner, where low-speed models are extended via compressibility corrections. Compounding the inaccuracies is a clear lack of experimental data; this is especially true for studies within a low disturbance environment.

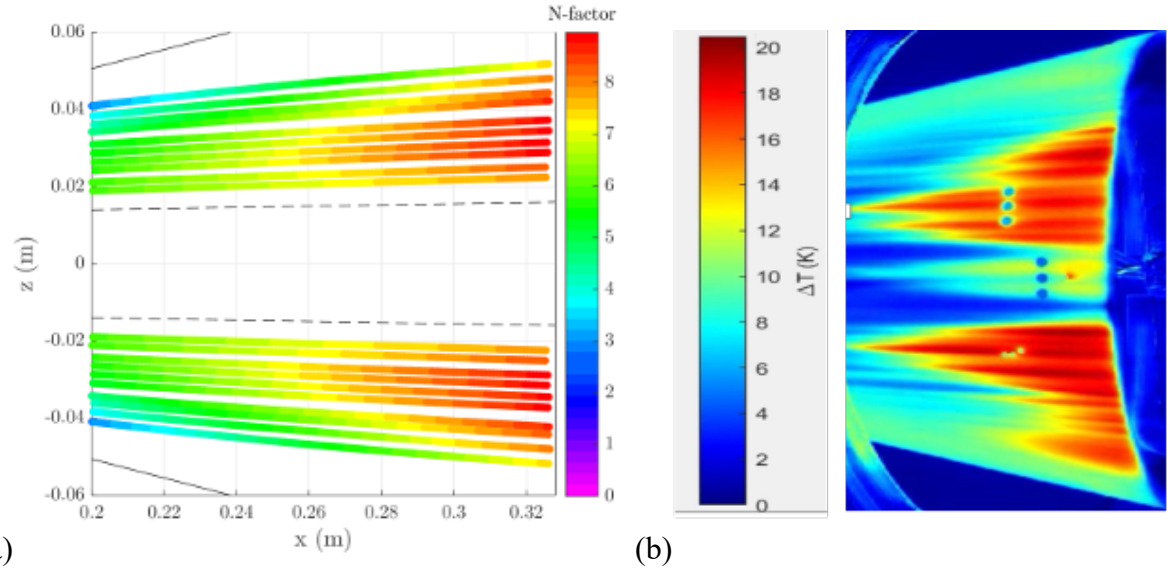

Figure 5. Comparison of transition front on 2:1 Elliptic Cone at Mach 6. (a) TAMU EPIC LPSE N-factor results. (b) Quiet flow IR thermometry TAMU M6QT.

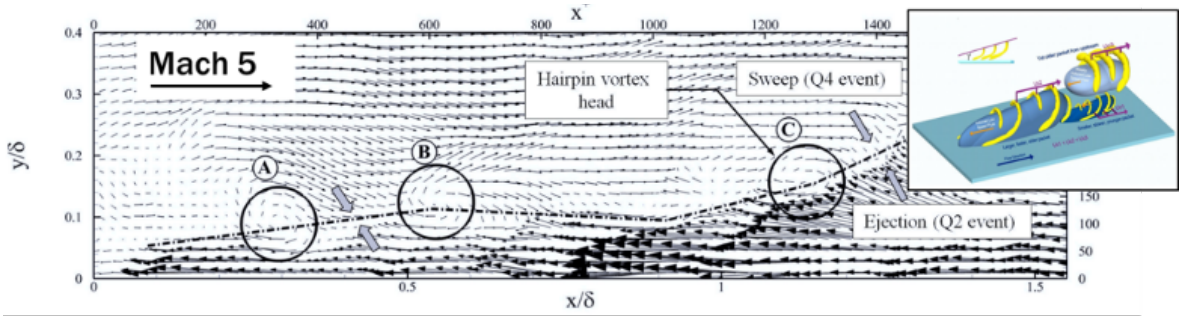

Figure 6. Mach 5 boundary layer convective velocity measurement showing the underlying coherent structure (PIs' Lab, Peltier *et al.* 2016). The insert is from Adrian *et al.* (2000).

Turbulence modeling of compressible wall bounded flows has received considerable attention, where references are available (e.g., Cebeci & Smith 1974, Speziale 1996, Pope 2000, Wilcox 2003, Lesieur *et al.* 2005, Roy and Blottner 2006, Schetz and Bowersox 2011, Gatski & Bonnet 2013). In summary, a wide range of models have been developed to account for the enhanced

DISTRIBUTION A: Distribution approved for public release.

transport due to turbulence. The current models for the Reynolds stress include algebraic (e.g., Cebeci & Smith 1974), one-equation (e.g., Spalart & Allmaras 1992), two-equation (e.g., k-ε/ω, Wilcox 2003), and second order transport (e.g., Launder *et al.* 1975). There are also many variations of these models, primarily focused on near wall and compressibility effects. Compressible flow models are based largely on extensions of incompressible models founded primarily on (i) Morkovin's hypothesis (1961), which states that the essential dynamics of supersonic shear flows follow the incompressible pattern, and (ii) the similarity of the compressible mean flow equations to the incompressible equations when mass-weighted time-averaging (Favre 1969) is applied. However, Morkovin's arguments were validated with flat plate turbulence data, and the realm of applicability has been questioned (Smits and Dussuage 1996).

The turbulent heat flux q_i^T is most often modeled in terms of the eddy-viscosity μ_T, from the Reynolds stress model, and the mean enthalpy gradient, with a constant turbulent Prandtl number Pr_T. The advantages of this approach are simplicity and acceptable accuracy for 2-D flows at low speeds (Kays and Crawford 1993). The disadvantages include: (i) an inability to predict realistic values for all three components of the heat flux since this model aligns the scalar flux with the mean scalar gradient (Wikstrom *et al.* 2000), (ii) pressure gradient effects are not included in the formulation, and (iii), the asymptotic heat flux behavior as the wall is approached does not agree with DNS data (Bowersox 2009).

To overcome these problems, algebraic truncation models based on the turbulent heat flux transport equation have been proposed (Daly & Harlow 1970, Wikstrom *et al.* 2000). Building on this concept, an energy flux modeling treatment was developed by the PI to provide improved heat flux closure for hypersonic flows (Bowersox 2009). This approach begins with physics-based transport equations for the energy flux vectors, which are defined as the density-weighted moment (averaged product) between the fluctuations (double prime) in internal energy (e) and velocity (u_k).

The key advantages of the transport equation framework are that resulting expressions naturally introduce: (i) explicit pressure gradient effects, (ii) realistic 3-D treatment of the energy (and heat) flux vector, (iii) correct asymptotic behavior of the turbulent heat flux as the wall is approached, (iv) an explicit model for the turbulent energy fluctuation variance levels, and (v) a mechanism to introduce of freestream temperature disturbance effects.

The AFRL assessed the algebraic energy flux model for Mach numbers between 2.3 – 4.9 and wall temperature ratios T_W/T_{AW} between 0.5 – 2.0 through comparison with DNS/LES data (Poggie 2015). The conclusion from the study was that an "impressive match" was obtained between the model and simulations over a wide range of Mach number and wall temperature. Example results are plotted in Figs. 7a-c. Grid convergence and boundary layer and Navier-Stokes solver code-to-code verification results are also presented.

DISTRIBUTION A: Distribution approved for public release.

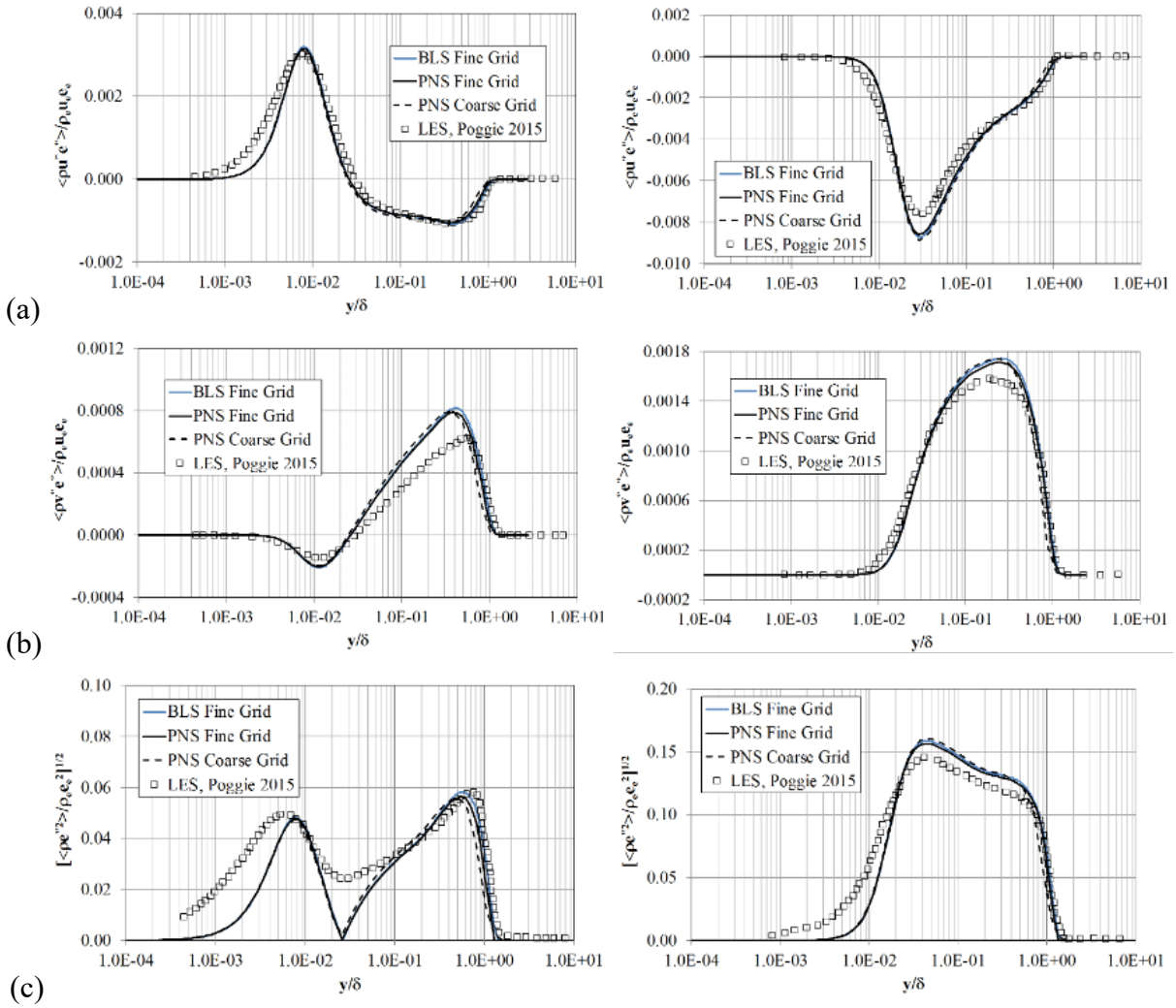

Figure 7. Example energy flux model comparisons. (a)-(c) DNS/LES data of Poggie (2015) for M = 2.3 (Left figures: Tw/Taw = 0.52, right figures: Tw/Taw = 1.0). (a) Axial energy flux. (b) Transverse energy flux. (c) Energy variance. Simulations performed by R. Bowersox (PI).

2.3 CUBRC HIFiRE 5 Ground Test

As mentioned earlier, the BOLT II geometry introduced boundary layer flow features similar to those seen on the HIFiRE 5 2:1 elliptic cone. CUBRC examined the flow for a full-scale replica of the HIFiRE-5 vehicle in support of an AFRL flight test. In these studies, temperature sensitive paint (TSP) was used to obtain heat transfer measurements on both the elliptical surface of the cone and leading edge over a range of simulated altitudes. Example results are shown in Fig. 8, where three distinct transition regions were observed. Centerline transition appeared to be originating from streaks running down the body on either side of the centerline, which were most likely due to the nose/lending edge interaction. The two off-centerline regions were the result of crossflow instabilities, evidence of which can be seen in standing crossflow streaks upstream of the transition region. In this case, the leading-edge attachment line remained laminar. But, at higher Reynolds numbers, attachment line transitioned.

DISTRIBUTION A: Distribution approved for public release.

(a) 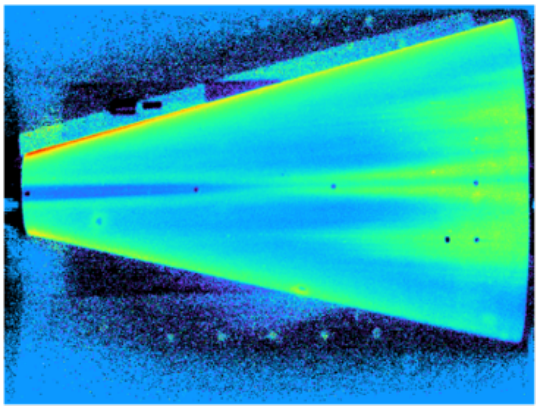 (b) 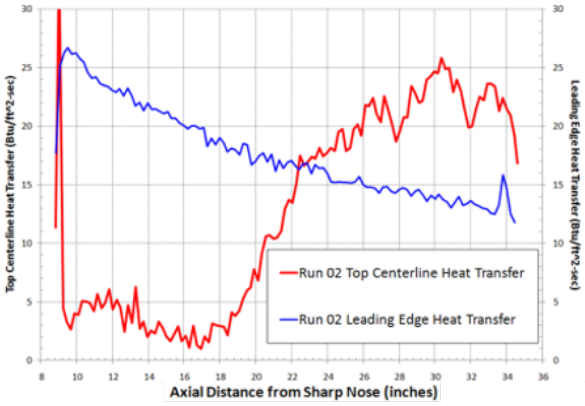

Figure 8. Example transition on HIFiRE-5 configuration at High Altitude Test Point 1. (a) Temperature sensitive paint results. (b) Heating distributions on frustum centerline and leading edge.

2.4 BOLT Thermal Loading

The JHUAPL BOLT flight geometry and thermal loading are summarized in Fig. 9. A sketch of the Flight Geometry is shown in Fig. 9a, with the test surfaces labeled, and the size indicated. The BOLT experiment contained two surfaces. One surface was focused on natural transition and the other examined roughness effects. The JHUAPL heating predictions are shown in Fig. 9b for aluminum and titanium aft sections. This comparison led to the materials selection in Fig. 9d. The JHUAPL vehicle and instrumentation design were served to help guide design of the BOLT II flight experiment.

2.5 BOLT II Transition and Turbulence Simulations

Computational work accompanying the sub-scale wind tunnel testing at TAMU described in Section 3 was conducted at the University of Minnesota (Johnston *et al.* 2021, 2022, 2023) under the direction of G. Candler. The flow simulations revealed large, roll-up vortices on the centerline and heat streaks associated with stationary crossflow vortices that aligned with the experimental transition location. The effects of forcing amplitude on the surface heating, surface pressure fluctuations, and off-body fluctuations were examined. Surface pressure measurements and off-body fluctuations agreed well with experimental data. The studies included modal analysis using total dynamic mode decomposition that provided clear identification of the mechanisms of transition. Grounding the computations with ground and flight experimental data provided a new understanding of the underlying physics of transition and turbulence. DNS and Spectral Proper Orthogonal Decomposition at $Re_L = 8.6 \times 10^6$ were performed in the (a) the mixed-mode region (2^{nd} and crossflow modes), which was halfway between the centerline and the leading edge on the back of the model and (b) the vortex region around the centerline roll-up. In the mixed-mode region, transition was not observed, but a 2nd mode instability was identified at 304 kHz along with traveling crossflow at 32 kHz (Johnston *et al.*2023). The flow field is shown in Fig. 10. For the near centerline vortical region, several instabilities were identified between 160-192 kHz which led breakdown.

DISTRIBUTION A: Distribution approved for public release.

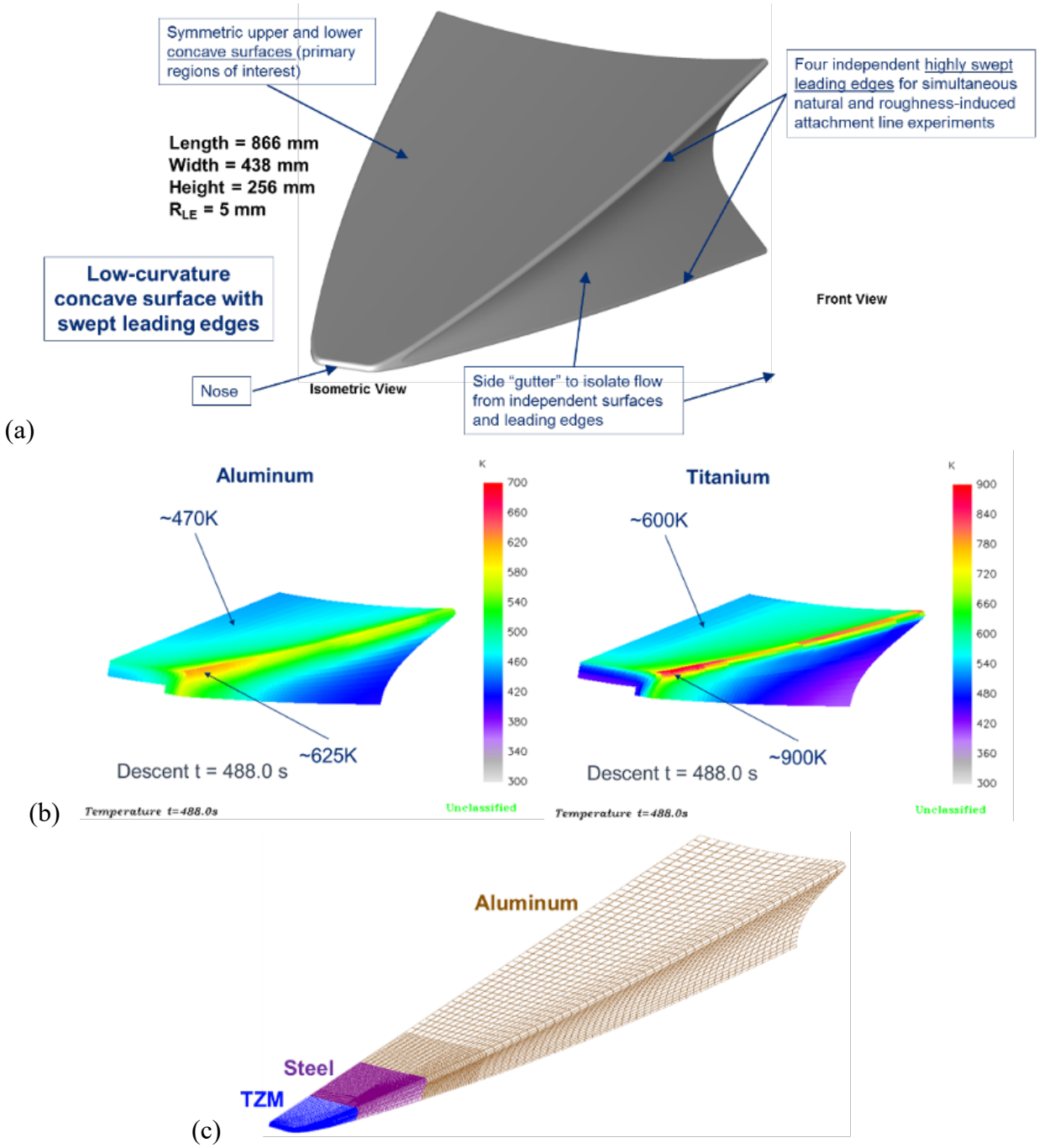

Figure 9. BOLT Flight definitions and aerodynamic heating (Wheaton *et al.* 2021). (a) Overview of Flight Geometry test surfaces. (b) Comparison of peak heating during descent (at t = 488 sec) for aluminum and titanium aft surfaces. (c) Preliminary materials selection by JHUAPL.

DISTRIBUTION A: Distribution approved for public release.

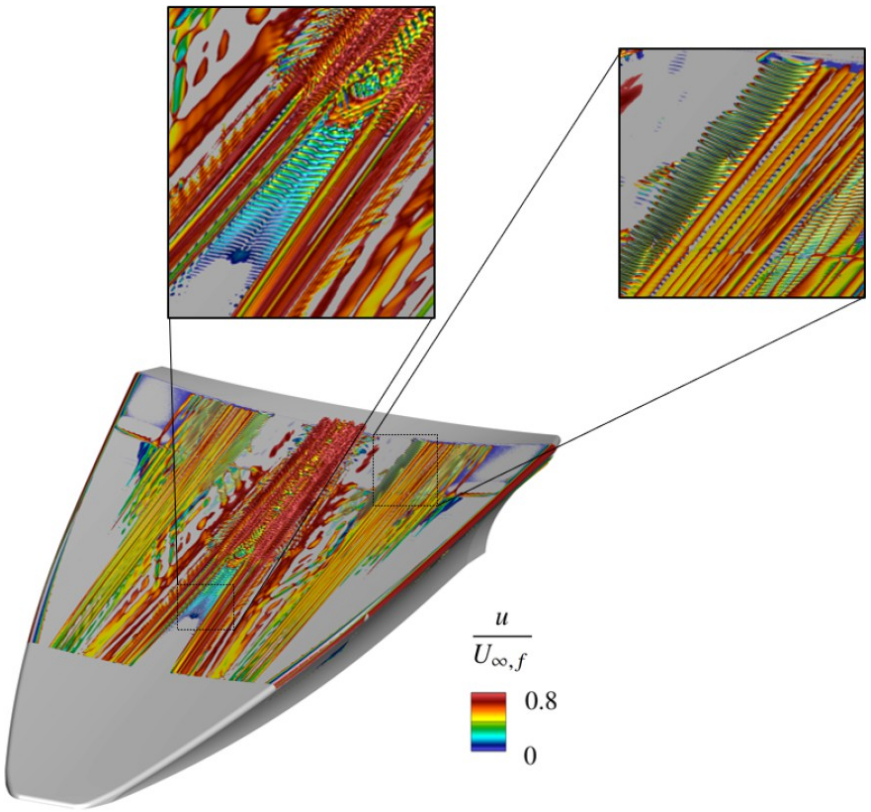

Figure 10. Vortex and velocity visualization of boundary layer instabilities across the BOLT II geometry for Re_L = 8.6 million, zoomed in to the near-centerline vortex region and the mixed-mode region is outboard (reprinted from Johnston and Candler 2023).

DISTRIBUTION A: Distribution approved for public release.

3. RESEARCH APPROACH

The scientific approach, project timeline, and milestones toward meeting the objective in Section 1.2 involved are described in this section.

3.1 SCIENTIFIC APPROACH AND CONTRIBUTIONS

The following three tasks were defined to meet the research objective described in Section 1.2.

- **Task 1** – *Define the Flight Geometry*. State-of-the-art numerical simulation and ground test methods were employed at TAMU and CUBRC to assess and modify the flight geometry as needed to achieve turbulent flow on the flight test vehicle during the test portions of the flight trajectory. This task included use of the TAMU EPIC LPSE and NPSE toolkit, ground test in the TAMU Mach 6 Quiet Tunnel, and flight matched full-scale ground test of the flight hardware at CUBRC. Additional simulations were performed by the JHUAPL team in support of BOLT II. The results from these studies guided the materials selection and determined the instrumentation and layout.
- **Task 2** – *Develop the Flight Research Vehicle*. The Flight Research Vehicle was manufactured and instrumented by the technical staffs at CUBRC and AFRL. Full-scale flight duplication experiments were performed at CUBRC on the Flight Research Vehicle. The vehicle was shipped to NASA Wallops for preparation for the flight test. This task leveraged extensive model design, fabrication, instrumentation, and testing experience at CUBRC, TAMU, and AFRL. The JHUAPL team provided additional analysis support.
- **Task 3** – *Perform the Flight Test and Post Flight Analysis*. TAMU and CUBRC supported the flight operations and performed post flight data analyses. The team also post processed the data, which included collaborations with research teams from Lockheed Martin Company, NASA, Johns Hopkins Applied Physics Laboratory, University of Minnesota, University of Maryland, University of Queensland, and Ahmic Aerospace LLC.

Generating the flight test database, including the surface thermal loading, skin friction, and pressure fluctuations during hypersonic flight, represents a new addition to the national knowledge-base. The creation of experimental databases allowed for advancement and assessment of state-of-the-art ground-based methods, which added additional databases to improve confidence and identify weaknesses to guide future research. Performing ground tests under duplicated conditions with the flight hardware allowed for the direct comparison of ground and flight test on the same hardware. To our knowledge, such a comparison has never been accomplished.

3.2 PROJECT TIMELINE AND TASK MILESTONES

The timeline for the three tasks is listed Table 1. The items denoted with an asterisk (*) represent milestones of the project. The project started on 5/1/19. However, the project experienced COVID-19, which also added significant delays to the preliminary and critical design reviews, with a subsequent funding gap between AFOSR and NASA Wallops, which was resolved. The

DISTRIBUTION A: Distribution approved for public release.

flight test was completed on 03/21/22. The final step was post-processing of the flight data, which took place under an extension of the project. The flight test model fabrication and instrumentation are supported by a separate AFOSR grant. The descriptions presented here for completeness.

Table 1 Project Timeline Summary

Task	**Date**
1 – Define the Flight Geometry	**05/01/19 – 10/28/20**
Flight Experiment Design with Supporting Ground Test and Simulations	05/01/19 – 10/28/20
* NASA Mission Initiation Conference (MIC)	05/01/19
* Air Fore Conceptual Design Review (CoDR)	10/28/19
* NASA Requirements Definition Meeting (RDM)	10/29/19
* Air Force Preliminary Design Review (PDR)	06/17/20
* NASA Flight Vehicle Design Review (DR)	10/13/20
* Air Force Critical Design Review (CDR)	10/28/20
2 – Develop the Flight Research Vehicle	**10/29/20 – 01/04/22**
Flight Experiment Design with Supporting Ground Test and Simulations	10/29/20 – 01/04/22
Design/Purchase Flight Computers, Data Acquisition, and Instruments	10/29/20 – 11/23/21
Fabricate and Instrument of Flight Geometry	10/29/20 – 12/31/21
* NASA Pre-Integration Review (PIR)	12/15/21
* Ground Test BOLT II Flight Hardware in CUBRC LENSII	01/05/22 – 01/13/22
* Ship Flight Geometry to NASA Wallops	01/18/22
3 – Perform the Flight Test and Data Analyses	**01/05/22 – 09/30/23**
Preflight Integration and Testing	
* NASA Mission Readiness Review (MRR)	03/01/22
* Air Force Technical Readiness Board (TRB)	02/02/22
* Flight Dress Rehearsal	03/18/22
* Flight Experiment	03/21/22
Flight Experiment Data Analyses	03/22/22 – 09/30/23
* Final Report	01/20/2024

DISTRIBUTION A: Distribution approved for public release.

4. RESEARCH RESULTS – TASK 1 DETERMINE THE FLIGHT GEOMETRY

The primary goal of Task 1 was to design the flight geometry and instrumentation layout to meet the research objective in Section 1.2. The requirement from AFOSR was to maximize the length of the research geometry, while maintaining the original BOLT flight 1 shape for the first 0.866 m. The plan involved assessment and modification of the BOLT geometry as needed to achieve turbulent flow during the test portions of the flight and ensure flight system stability over the entire trajectory. This task concluded with the successful completion of the CDR. This section summarizes the results from Task 1.

4.1 FLIGHT SYSTEM STABILITY

The flight system stability analyses were led by T. Gass and D. Kilcoyne with the NASA Sounding Rocket Operations Contractor (NSROC). The large surface area of the BOLT II flight test article resulted in a significant challenge to the flight system engineering, where at angles-of-attack, the payload became a lifting surface. The lift moved the center of pressure for the whole flight system forward, which resulted in a reduced static stability margin. Shown in Fig. 11a is the entire experimental flight test system. Ensuring static aerodynamic stability with a minimum margin of 2.0 calibers was necessary to meet the NASA flight requirements.

To demonstrate stability, aerodynamic databases were created for a variety of Mach numbers and incidence angles. The databases were then used in a 6 Degree-Of-Freedom code by NSROC to analyze the dynamic performance.

The necessary aerodynamic databases were computed at TAMU by B. Morealle (TAMU graduate student under the direction of R. Bowersox) using the NASA inviscid high-speed computational fluid dynamics package CART3D v1.5 (Aftosmis *et al.* 2010). Additional tools employed by NSROC in the flight stability analyses included:

- TAOS: Trajectory Optimization Software, Sandia Labs
- DRG: Automated Method of Computing Total Drag Coefficients for Sounding Rocket Vehicles, NASA GSFC/WFF
- TAD7: Theoretical Aerodynamics Derivatives Program Version 7, NASA GSFC/WFF
- FLMD II: Flight Loads, Moments, and Deflections, NASA GSFC/WFF

The CART3D adaptive mesh refinement (AMR) capability allowed for the use of a single unstructured surface mesh for a single flight system configuration. See Fig. 11b for example sections of the mesh used for the ascent flight configuration. This capability drastically reduced the turnaround time needed to generate aerodynamic databases. At the beginning of a single simulation, a coarse Cartesian volume mesh was generated around the vehicle based on the user generated surface mesh. Multiple adaptive mesh refinement cycles were performed from this initial mesh, where adjoint error estimation, based on user defined parameters, was used to add refinement in areas of large error. For all aerodynamic databases, the authors targeted the reduction of discretization error in the body forces. After all simulations were converged to the minimum residual criteria, a NASA based force and moment integration utility known as CLiC was used to generate static aerodynamic force and moment coefficients.

DISTRIBUTION A: Distribution approved for public release.

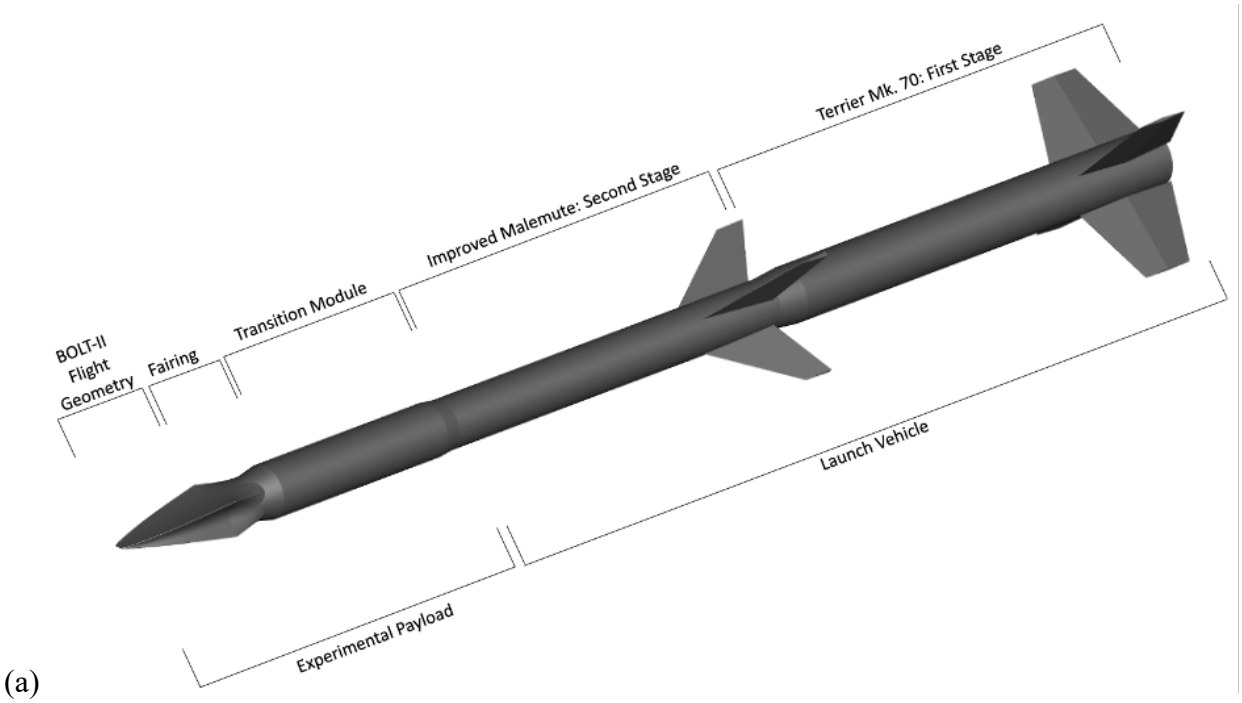

(a)

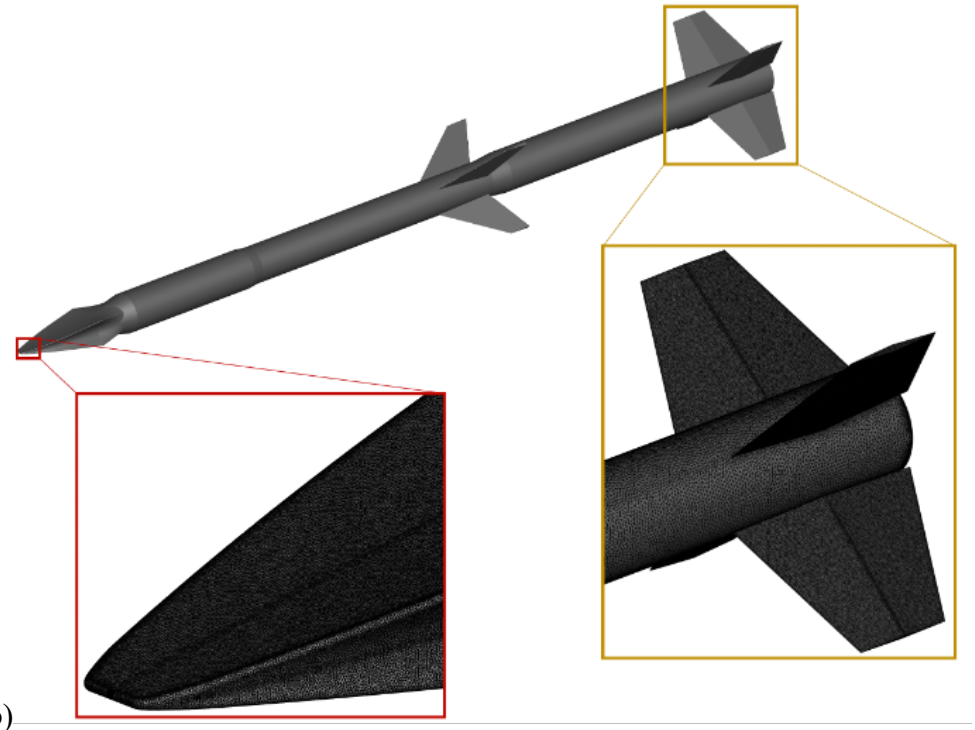

(b)

Figure 11. BOLT II Schematic. (a) Payload and launch vehicle. (b) Zoomed view of key sections of surface mesh used for aerodynamic stability analysis.

DISTRIBUTION A: Distribution approved for public release.

Shown in Figure 12 is the flow field for an example steady inviscid aerodynamic calculation. The overall static margin of the flight was assessed by determining the minimum margin throughout the trajectory. The center of pressure was computed in both the pitch and yaw planes via the aerodynamic coefficients calculated in the CART3D databases. Monte-Carlo dispersion analyses was also performed by NSROC and the JHUAPL. The redundant dispersion analyses confirmed the nominal confidence in the flight stability. The JHUAPL team recommended additional Monte-Carlo contributors for aero coefficients and decreasing 2nd stage drag based on their CFD models, which were implemented in the Design Review analysis.

After iterating over 20+ geometries, with Monte Carlo simulations of 1000 trajectories, AFOSR and NASA approved the configuration. The stability parameters are summarized in Table 2. The minimum static stability was 1.8, which is below the NASA requirement of 2.0. However, the flexible stability results were within NASA guidelines. The resulting configuration and trajectory are shown in Figs. 13a and 13b, respectively. This configuration satisfied the project scientific mission requirements for high Reynolds number ($Re > 30x10^6$) hypersonic ($M > 5$) flow. Significant ballast (186 kg of Tungsten) was required to satisfy NASA minimum margin criteria (Kilcoyne 2021).

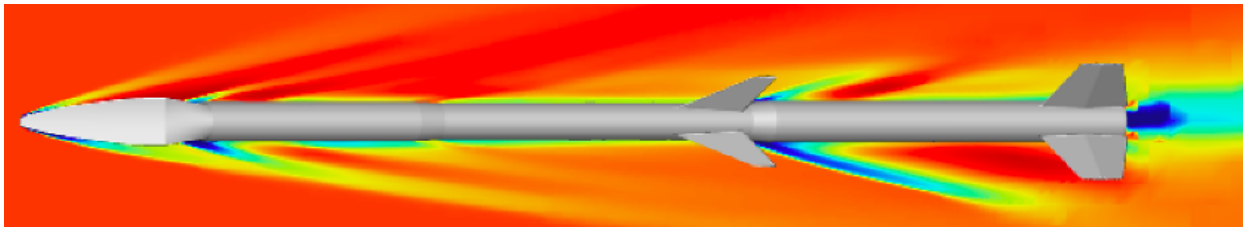

Fig. 12. Example simulation of flight system flow field at an off-nominal incidence angle

Table 2 NSROC BOLT II Flight Stability (from D. Kilcoyne, NSROC)

Parameter	**Analyzed**		**Guidelines**
	1st Stage	2nd Stage	
Min. Rigid Static Margin (RSM)	2.5	1.8	> 2.0 calibers
Min. Flexible Static Margin (FSM)	3.6	1.6	> 1.5 calibers
Min. FSM/RSM	0.67	0.70	> 0.6
Max. $Q_{nominal}/Q_{critical}$	0.24	0.27	< 0.5
Max. Bending Moment	112,000	60,000	< 207,000 in-lbs
Booster Sep. Δ Acceleration	10.4		> 2g
Spin Motor Ign. From Rail Exit	116.8		> 50 ft

DISTRIBUTION A: Distribution approved for public release.

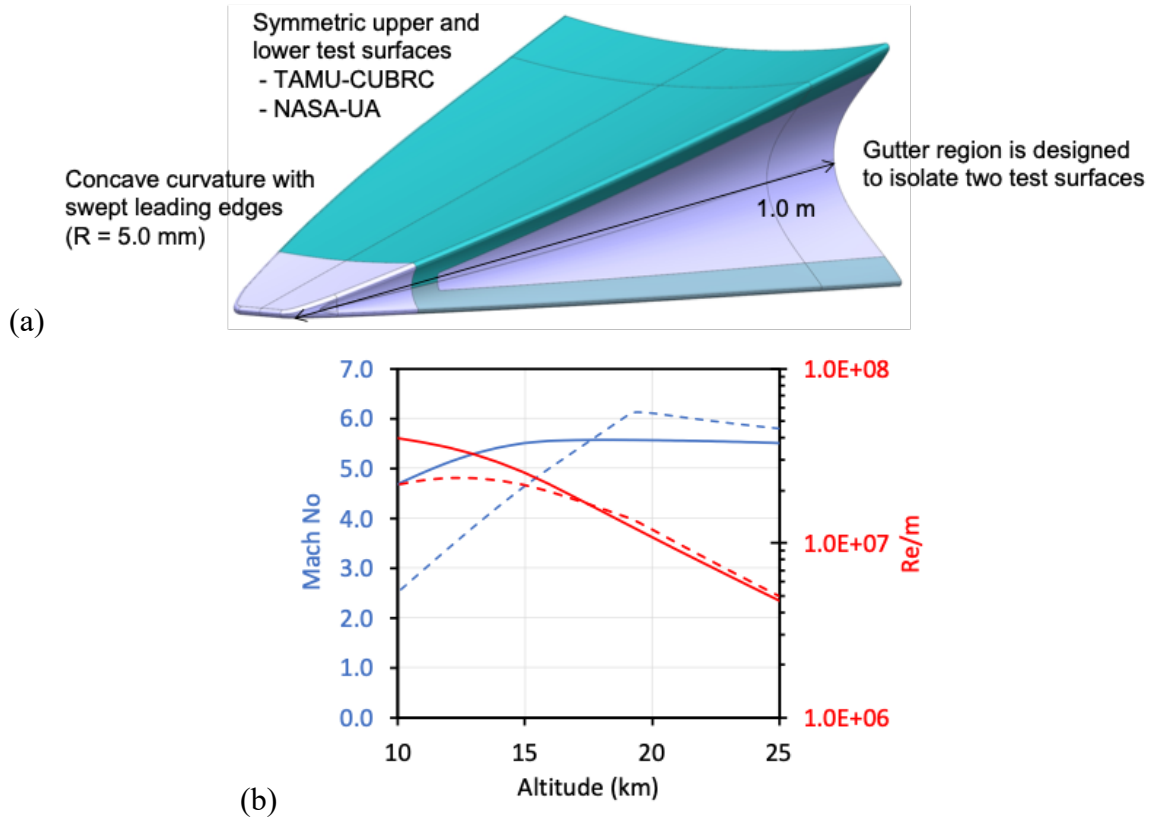

Figure 13 BOLT II Flight Experiment. (a) Flight Geometry; Side A surface for natural transition and turbulence (TAMU-CUBRC) and Side B surface for forced transition and turbulence (NASA Langley-University of Arizona), (b) Predicted Test Windows (dashed: ascent, solid: descent).

4.2 Boundary Layer Stability Analyses

Boundary layer stability predictions were performed with the 3-D Nonlinear Parabolized Stability Equation toolkit EPIC was developed in-house at TAMU (Oliviero *et al.* 2015). These simulations were the basis for the dissertation studies of D. Mullen (TAMU graduate student under the direction of H. Reed). Laminar and turbulent flow simulations were performed by B. Morealle (TAMU graduate student under the direction of R. Bowersox).

The EPIC code offers 3-D Linear and nonlinear Parabolized Stability Equation predictions. NASA DPLR and UMN US3D CFD codes, with Pointwise meshing, were used to generate laminar basic states. EPIC and its features have all been verified and validated for the range of instabilities and interactions (stationary and traveling crossflow, second mode, Görtler, oblique modes, interactions, etc.) with various 2-D and 3-D hypersonic experiments at TAMU, see, for example, Reed *at al.* (2015), Moyes *et al.* (2017a/b), Kocian et al (2016, 2017), Mullen and Reed (2021).

The basic state for BOLT II was characterized by a complex 3-D boundary layer. The surface heating due to vortices within the boundary layer is provided in Fig. 14a. The boundary layers were very thin outboard toward the edges. However, as the flow swept toward the center, a thick boundary layer roll-up region was observed. Example LPSE results showing stability simulation for BOLT II are shown in Figs. 14b and 14c. It was expected that the features shown in Fig. 14

DISTRIBUTION A: Distribution approved for public release.

would impact the transition and early turbulence processes. Hence, these data were used to guide the instrument location and selection to quantify transition and the initial conditions for the downstream turbulent flow. A key goal was to place sensors to quantify the instability growth and initial conditions flowing into the downstream turbulent region.

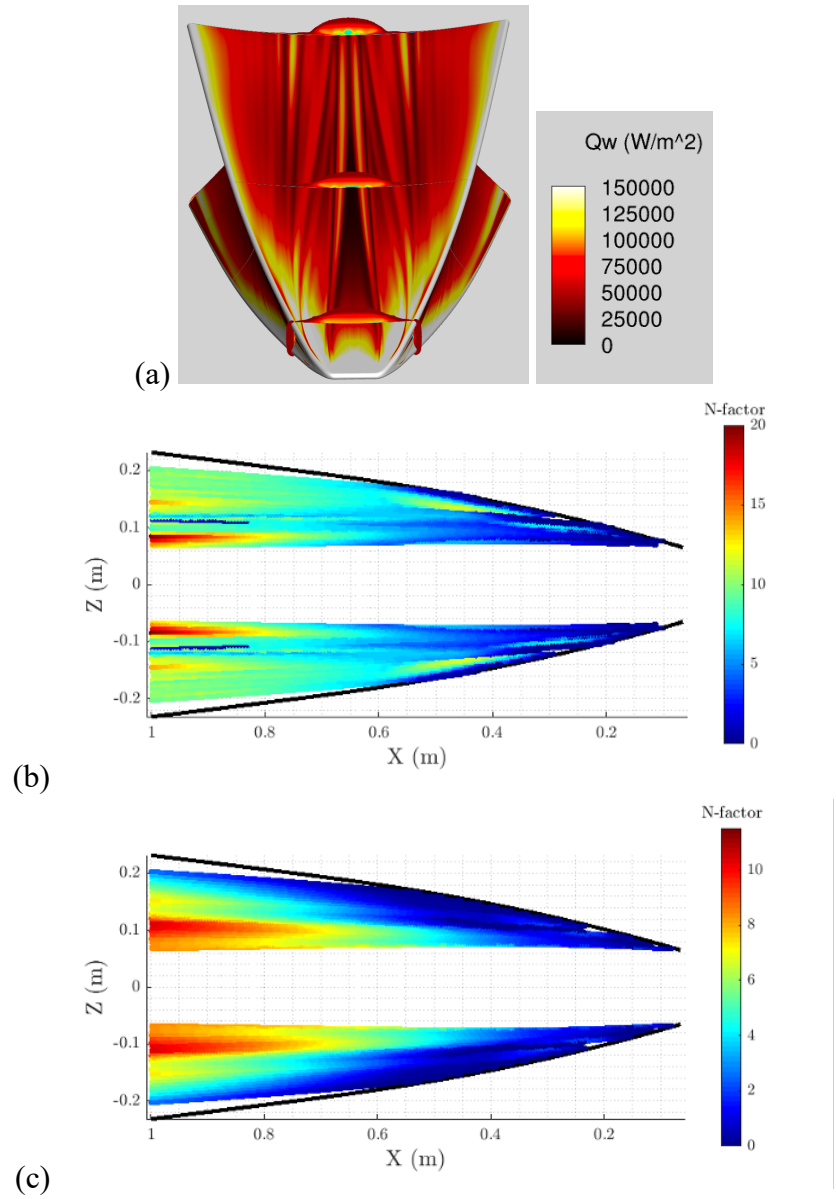

Figure 14. TAMU LPSE results for BOLT II. (a) Laminar flow structure. (b) 2nd-mode N-factors. (c) Crossflow N-factors.

The team also performed RANS simulations for these geometries using the US3D CFD code from the University of Minnesota. Example laminar, RANS, and tripped RANS results are shown in Fig. 15. The turbulence was modeled with Menter's SST (1994) formulation. Additional simulations accounting for yaw and pitch effects were performed, which are shown later. These data

DISTRIBUTION A: Distribution approved for public release.

were used to guide the instrument selection and layout on the surface to quantify the downstream turbulent flow. A key goal was to quantify the persistence of transition into the turbulence evolution from late transitional to equilibrium across the span. Also, it was deemed important to place sensors to quantify the upstream flows as an inflow condition for the downstream turbulent flow.

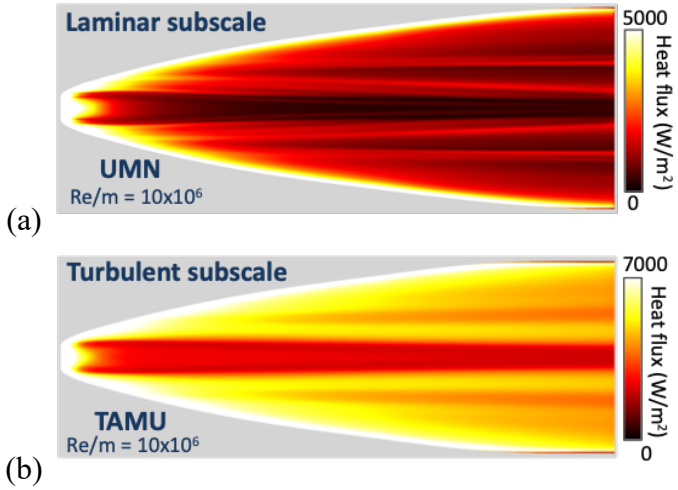

Figure 15. Simulations of BOLT II (1.5 m long version) at subscale wind tunnel conditions for (a) Laminar (Candler group at UMN). (b) Fully turbulent (Bowersox group at TAMU).

4.3 Subscale Ground Tests

The subscale ground test results described in this section were the subject of the PhD dissertation of H. Kostak-Teplicek (TAMU graduate student under the direction of R. Bowersox). For more details, see Kostak-Teplicek (2022). The experiments took place in the TAMU Mach 6 Quiet Tunnel (M6QT) and Actively Controlled Expansion (ACE) tunnel; see the Facilities and Instrumentation section for a description of the facilities and instrumentation.

4.3.1 Test Articles

The test article definitions for the BOLT II subscale tests took place early in the flight test program. The models were developed under the direction of E. White. The initial concept was an elongated model to help promote transition to fully turbulent flow during flight. The front 0.87-m of the model was chosen to be identical to the BOLT flight test article to provide redundancy in the flight results. The originally planned test article was defined to be 1.5-m long, termed the 1.5-m long BOLT II. The flight stability analysis resulted in a maximum length of 1.0-m. Natural transition was observed during the preliminary tests of the 25% scale1.5-m long BOLT II geometry in the Mach 6 Quiet Tunnel. This was not observed for the original BOLT geometry. Subscale tests (25%) were also performed on a 25% 1.35-m long BOLT II model.

The 25% scale 1.5 m long BOLT II geometry is shown in Fig. 16a. The extension was developed using 2nd order backward finite difference method to ensure continuity of slope and curvature. The blockage model was additively manufactured from polycarbonate plastic, as shown in Fig. 16b. Preliminary IR and surface pressure (Kulite and PCB results) were accomplished on the

DISTRIBUTION A: Distribution approved for public release.

1.5 long BOLT II blockage model, as shown in Fig. 16c. Sketches and photographs showing the model alignment in both the M6QT and ACE 0.23-m x 0.36-m test section are provided in Figs. 17a and b, respectively.

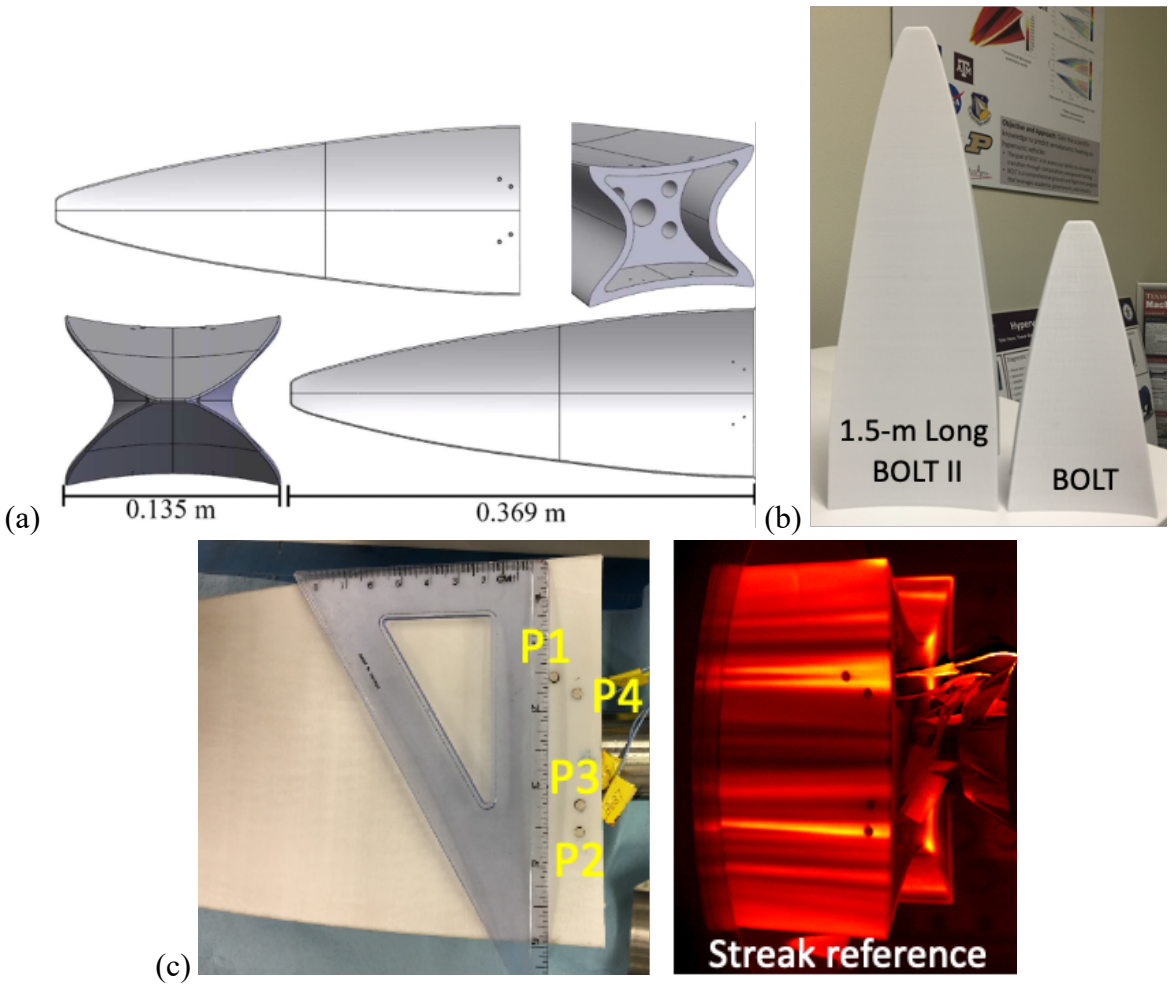

Figure 16. Scale (25%) 1.5-m Long BOLT II. (a) CAD sketches. (b) Photographs of 25% scale model of 1.5-m BOLT II, with a similarly and scaled BOLT geometry to show the planned increase in axial length. (c) PCP pressure transducers selected to quantify flow beneath the instability growth with the surface streaks.

The scaled 1.5-m long BOLT II was instrumented with four Piezotronics 132B38 model PCB high-frequency pressure transducers. The locations of the sensors were selected to quantify the fluctuations beneath the streaks observed in the IR thermography (discussed below) as shown in Fig. 16c. The locations are summarized in Table 3. The coordinate system is shown in Fig. 16a. The sensors have a manufacturer quoted resonant frequency greater than 1.0 MHz, allowing measurements in the hundreds of kilohertz, which was the expected frequency range of the second mode and potential secondary instabilities of the stationary crossflow vortices. The pressure data were acquired by an in-house developed LabVIEW VI and a pair of synchronized National Instruments

DISTRIBUTION A: Distribution approved for public release.

USB-6366 DAQ systems. All channels were acquired at 2 MS/s per channel for 100 ms per sample. PCB signals were passed through an 8-pole, Bessel, 1 MHz low-pass filter with unity gain for anti-aliasing. The manufacturer of the PCB 132B38 transducers reports a sensitivity uncertainty of ±30% over a 345 kPa range. The PSD functions were generated from 781 averages, which is a random error uncertainty of 3.6% per PSD value.

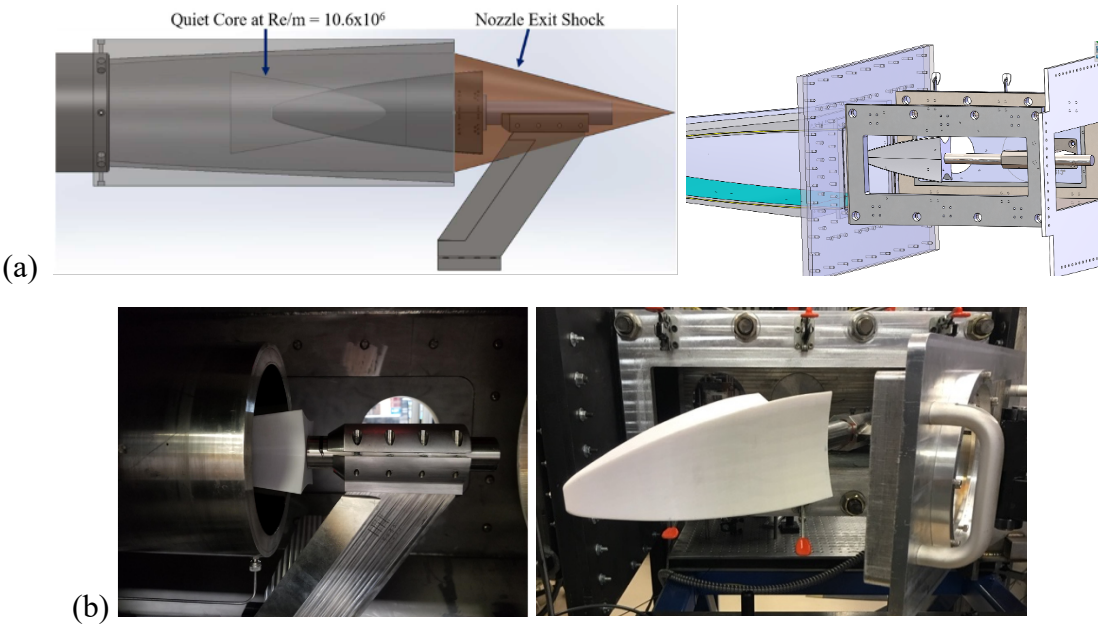

Figure 17 BOLT II Tests. (a) CAD sketched for M6QT (left) and ACE (right). (b) Photographs of blockage models in M6QT (left) and ACE (right). Flow is from left to right for both images.

Table 3 PCB Sensor Location in 1.5-m Long BOLT II

Sensor	x (m)	z (m)	Sensor	x (m)	z (m)
P1	0.352	0.026	**P3**	0.361	-0.018
P2	0.361	-0.028	**P4**	0.361	0.019

Detailed ground tests were performed on a carefully machined 25% scale version of a 1.35 m flight model. This length was longer than the allowable flight test, but it was deemed appropriate to examine breakdown on the subscale model in the M6QT. The extended length was based on the 1.5-m long BOLT II design. A schematic and photographs of the model are shown in Figs. 18a and b. The experiments included IR thermography, surface pressure fluctuations, and off-body hot-film mean flow and fluctuations. The off-body measurements were acquired in the downstream region where breakdown to turbulence was occurring. These data were acquired to help interpret flight test surface data and validate companion direct numerical simulation data at the University of Minnesota (Candler group).

DISTRIBUTION A: Distribution approved for public release.

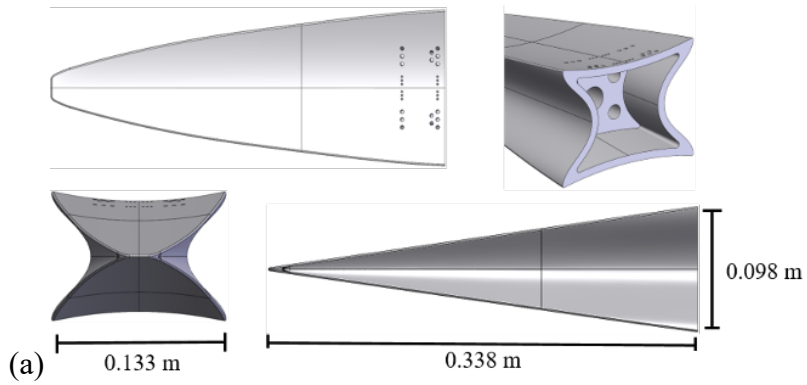

Figure 18 Scale (25%) Model of a 1.35-m long BOLT II. (a) CAD drawing of the model. (b) Photograph of BOLT II ground test model for off-body measurements.

The 1.35-m long BOLT II subscale model was instrumented with Piezotronics 132B38 model PCB and Kulite XCE-062-15A surface pressure transducers. The layout is shown in Fig. 19 with the corresponding locations listed in Table 4. The PCB high-frequency transducers have a manufacturer quoted resonant frequency greater than 1.0 MHz, allowing measurements in the hundreds of kilohertz, which was the expected frequency range of the second mode and potential secondary instabilities of the stationary crossflow vortices. The Kulite transducers have a linear frequency response up to 30% to 40% of their resonant frequency (Beresh *et al*. 2011). The pressure data were acquired by an in-house developed LabVIEW VI and a pair of synchronized National Instruments USB-6366 DAQ systems. All channels were acquired at 2 MS/s per channel for 100 ms per sample. PCB signals were passed through an 8-pole, Bessel, 1 MHz low-pass filter with unity gain for anti-aliasing. Similarly, Kulite signals were passed through an 8-pole, Bessel, 200 kHz low-pass filter with unity gain. The manufacturer of the Kulite XCE-062-15A transducer reports a factory uncertainty of ±0.1% within the sensor 103.5 kPa range. These sensors were calibrated at room temperature under a vacuum. A thermal shift of 50 K during a wind tunnel run results in a ±1% thermal zero and sensitivity shift. The manufacturer of the PCB 132B38 transducers reports a sensitivity uncertainty of ±30% over a 345 kPa range. All PSD plots for both sensors were generated from 781 averages, which is a random error uncertainty of 3.6% per PSD value.

DISTRIBUTION A: Distribution approved for public release.

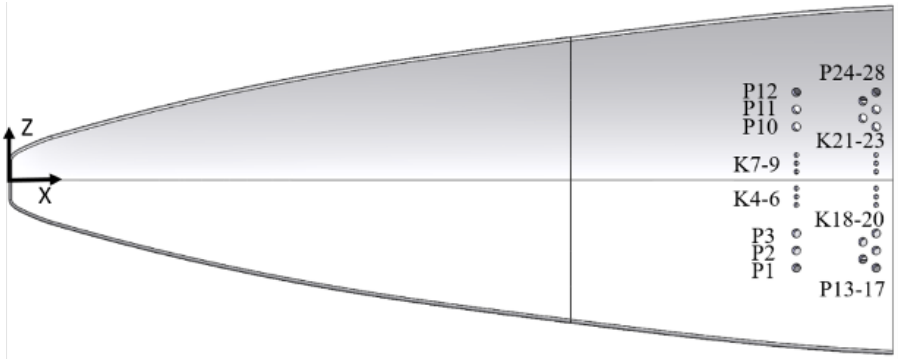

Figure 19. Location of surface pressure transducers for the 25% scale BOLT II 1.35 m model.

Table 4 Pressure transducer locations

Sensor	x (m)	z (m)	Sensor	x (m)	z (m)
P1	0.300	-0.033	**P15**	0.331	-0.033
P2	0.300	-0.027	**P16**	0.331	-0.027
P3	0.300	-0.020	**P17**	0.331	-0.020
K4	0.300	-0.010	**K18**	0.331	-0.010
K5	0.300	-0.006	**K19**	0.331	-0.006
K6	0.300	-0.003	**K20**	0.331	-0.003
K7	0.300	0.003	**K21**	0.331	0.003
K8	0.300	0.006	**K22**	0.331	0.006
K9	0.300	0.010	**K23**	0.331	0.010
P10	0.300	0.020	**P24**	0.326	0.024
P11	0.300	0.027	**P25**	0.326	0.030
P12	0.300	0.033	**P26**	0.331	0.020
P13	0.326	-0.030	**P27**	0.331	0.027
P14	0.326	-0.024	**P28**	0.331	0.033

The surface pressure experiments were performed simultaneously with IR thermography. Instabilities at various frequencies can be identified on a subscale model to further identify transition mechanisms that may occur on the BOLT II flight test vehicle.

4.3.2 Infrared Thermography in the M6QT and ACE

Infrared thermography images were acquired with a FLIR SC8100 IR camera. The camera had a resolution of 1024x1024 pixels and is sensitive to wavelengths from 3-5 μm. The camera outputs raw 14-bit data in counts which is then converted to temperature. The camera was calibrated with a thermocouple embedded in an anodized aluminum calibration plate (Leidy *et al.* 2020, 2021). A one-dimensional heat transfer correlation algorithm was employed for converting the temperature maps of the IR images into heat flux. The code was developed by Neel *et al.* (2018) and was modified for the current analyses. All experimental IR data presented in this paper was processed using this code. The code involves a forward time central difference scheme shown in Eq. (1) for solving the heat conduction equation.

DISTRIBUTION A: Distribution approved for public release.

$$(T_i^{n+1} - T_i^n) / \Delta t = \alpha(T_{i+1}^n - 2T_i^n + T_{i-1}^n) / \Delta x^2 \quad (1)$$

The heat flux is then calculated using a second order approximation of the first spatial derivative using Eq. (2).

$$q(n) = -k\left(-\frac{3}{2}T_0^n + 2T_1^n - \frac{1}{2}T_2^n\right)/\Delta x \quad (2)$$

Here, *n* and *i* are the time and spatial indices, respectively.

Uncertainty in the computations of heat flux from IR thermography involve the properties of the material, camera angle, and calibration of the camera. Of these parameters, the material properties are the main sources of uncertainty. The properties used in this study are listed in Table 5 and are based on nominal manufacturer documentation. The resulting uncertainty in the heat flux given these variations was estimated at 9.5%. Previous comparisons between the IR thermography and Schmidt Boelter heat flux gauges tested at NASA Langley results agreed to within 6.0% (Kostak and Bowersox 2021).

Table 5 Peek Property Materials with Uncertainty

Thermal Conductivity (W/mK)	Specific Heat Capacity (J/kgK)	Density (kg/m^3)
0.29 ± 6.9%	1026 ± 6.5%	1300 ± 0.4%

IR data for the 1.5-m Long BOLT II are shown in Figs. 20a and b from tests in the M6QT and ACE tunnel, respectively. Breakdown to turbulence was observed in the M6QT, as indicated by the elevated heating in the regions midway between the edges and the center. This region was termed the mixed-mode region by Knutson *et al.* 2021. In this region, both second mode and crossflow instabilities were present. The ACE tunnel is a conventional noise facility (see the Facilities and Instrumentation section), and hence transition occurred at lower Reynolds numbers as indicated in Fig. 20b. Also, the streak structure was obscured by movement of traveling crossflow waves. Also shown in Fig. 20b are overlays from the corresponding subscale BOLT geometry in the ACE at matched Reynolds numbers. The consistency between the two models was considered excellent.

Line plots of the heat flux are provided in Fig. 21. These data show the growth and breakdown toward turbulence in the M6QT (*Re*/m = 7.6 – 11.0 x10^6) and turbulent heat in ACE (*Re*/m = 5.7 x10^6). These data provided both validation for numerical simulations and helped define sensor location for flight and additional ground experiments. The BOLT II flight test provides an opportunity to provide low disturbance data to close the gap between the M6QT transitional and ACE tunnel turbulence traces, thus significantly extending the current knowledgebase.

DISTRIBUTION A: Distribution approved for public release.

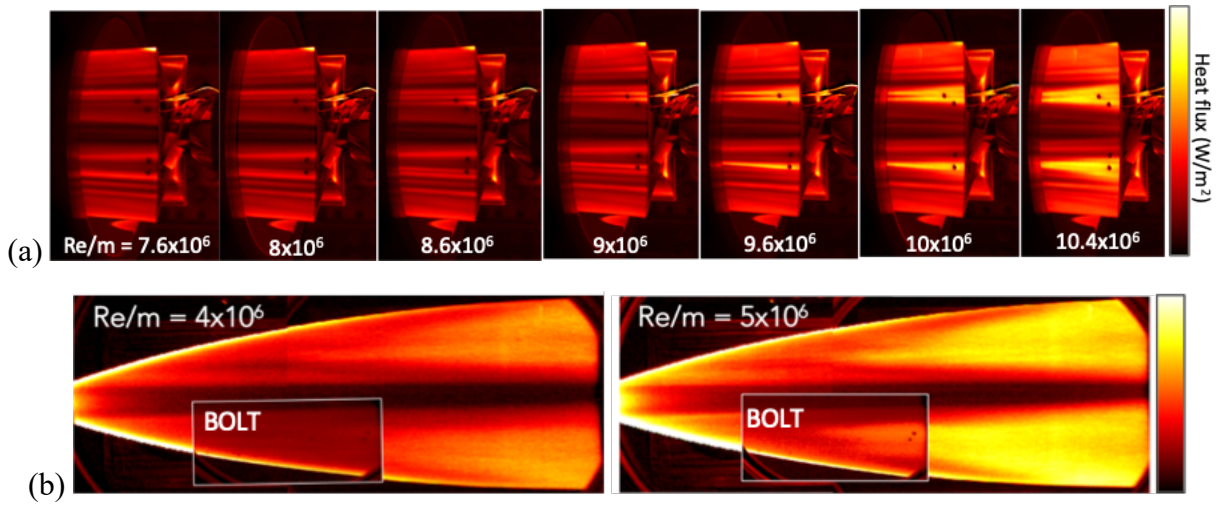

Figure 20. TAMU ground test preliminary results in the 0.25% scale 1.5-m long BOLT II model. (a) TAMU M6QT data showing the laminar streaks at low Reynolds numbers, and breakdown to turbulence at High Reynolds number. (b) Conventional tunnel results in the ACE Tunnel with overlays from the BOLT experiment.

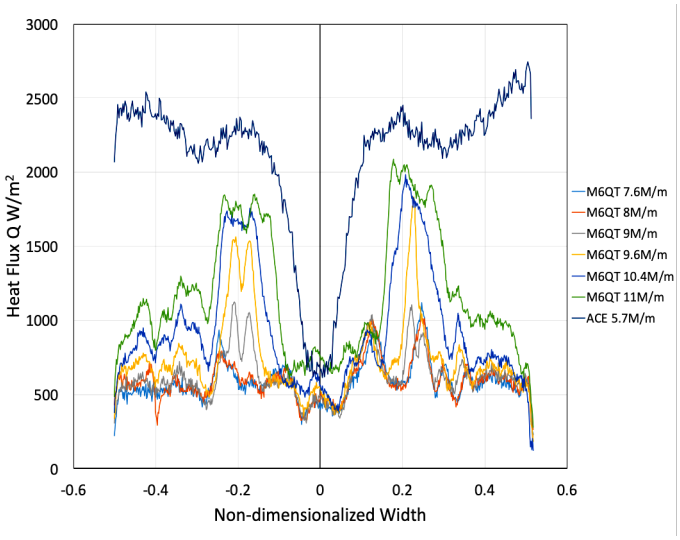

Figure 21. Heat flux slices at x = 0.355 m showing the growth of instabilities within the M6QT as the Reynolds number was increase from *Re*/m = 7.6 x10^6 to 11.0 x10^6, with the turbulent heating from ACE at *Re*/m = 5.7 x10^6.

Heat flux results for the subscale 1.35-m long BOLT II model tested in the M6QT is shown in Figs. 22a, with the flow from left to right. The yellow ellipses indicate the earliest indications of transition in the mixed-mode region. These images provide surface streak flow details needed to evaluate low dissipation numerical simulation algorithms. Quantification of these structures was the goal of the off-body measurements discussed below. Around *Re*/m = 10.0 x 10^6, transition was observed at the back of the model symmetrically and traveled upstream as the Reynolds number

DISTRIBUTION A: Distribution approved for public release.

was increased. The elevated heating along this streak region is representative of the onset of turbulence occurring. These features not only travel upstream on the model, but diffuses into the surrounding streaks around it, a feature also seen on the HIFiRE-5 model tested in this facility (Neel *et al.* 2018). The was also observed in the flight data discussed later in Section 6.

The IR thermography for the ACE tunnel is provided in Fig. 22b. As the Reynolds number was increased in the facility, wedge-like structures formed at the back and traveled upstream on the model, a similar effect was observed on the BOLT geometry tested in conventional flow (Berridge *et al.* 2018, Kostak and Bowersox 2021).

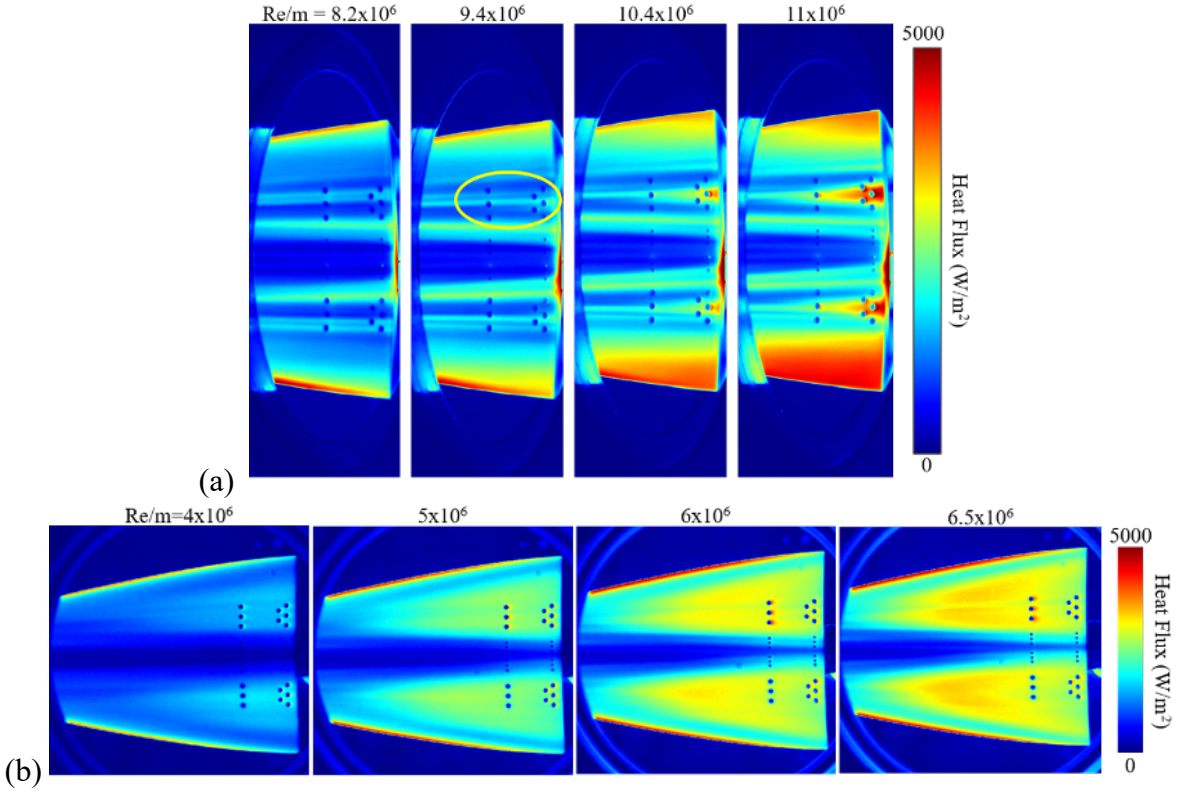

Figure 22. Heat flux results for the 25% scale 1.35 m long BOLT II model. (a) TAMU M6QT showing the laminar streaks at low Reynolds numbers, and breakdown to turbulence at high Reynolds number. (b) ACE Tunnel showing the expected wedge structure.

Line plots of the M6QT heat flux are provided in Fig. 23. These data confirmed the growth and breakdown toward turbulence in the M6QT (Re/m = 8.2 – 11.0 x10^6). The source of the heating on the wings of the model were not fully understood. This region of the model may have experienced elevated heating due to the exposure to elevated tunnel noise in this region of the flow triggering traveling crossflow instabilities (e.g., see Knutson *et al.* 2021) or it may have resulted from conduction from the leading edge. These data provided both validation for numerical simulations and helped define sensor locations for flight and additional ground experiments.

DISTRIBUTION A: Distribution approved for public release.

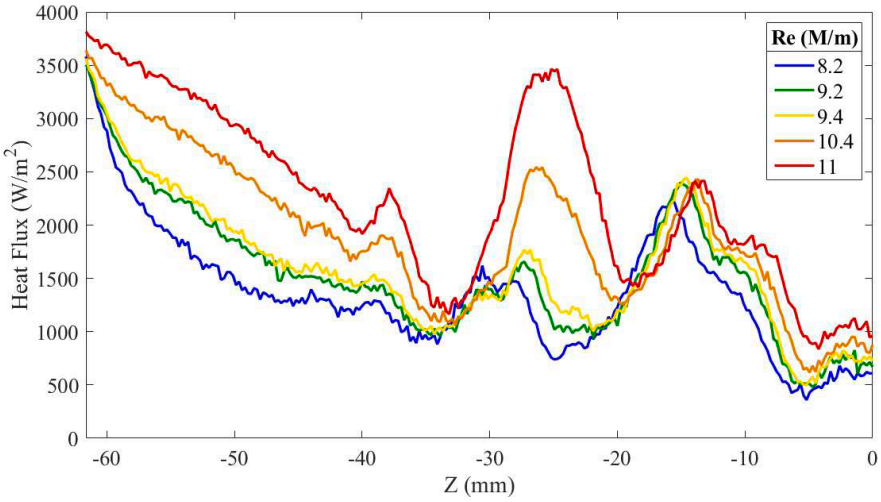

Figure 23. Heat flux slice extraction at x = 0.318 m for the M6QT data on the 25% scale 1.35-m long BOLT II model shown in Fig. 22a.

4.3.3 Surface Pressure Fluctuation Spectra in the M6QT and ACE

The power spectra density (PSD) functions from the four PCB pressure transducers for the scaled 1.5-m long BOLT II model tested in the M6QT are given in Fig. 24. These power spectra show modal instabilities that grew with Reynolds number. The most definitive was the peak centered near 200 kHz for the P1 and P4 sensors. Referring to surface heating in Fig. 20a, the P1 sensor was located under the edge of the vortex streak in the mixed-mode structure, and this frequency was considered consistent with Type-I and Type-II secondary instabilities associated with the vortex shear layers (Kocian *et al.* 2017). Type-I instabilities, as defined in Kocian *et al.* 2017, are produced by spanwise or azimuthal gradients of the streamwise mean flow and the frequency scales as approximately $f = u_e/2\delta$. Type-II instabilities are associated with wall normal velocity gradients. Similarly, the P4 sensors was near the edge of second streak. A lower frequency centered near 100 kHz, with broad modal growth, was observed for the P2 sensor at higher Reynolds numbers. This sensor was situated in a growing wedge. The P3 sensor was spectrally quiet, which is consistent with the IR image in Fig. 20a, where it was noted that the sensor was not situated within the growing instabilities. The observed low frequency near 50 kHz was considered consistent with traveling crossflow and/or Type-I secondary instabilities (Kocian *et al.* 2017). Finally, the structure near 300 kHz for all PCB sensors was the result of a sensor harmonic.

The PSD functions for the Kulite surface pressure transducers tested in the M6QT are shown in Figs. 25 and 26. An instability centered near 40 kHz was present in all Kulite transducer spectra in the M6QT. This likely the same crossflow and/or Type-I instability described above with respect to the 50 kHz peak observed in the PCB transducers for the 1.5-m Long BOLT II model. These results resemble those for the 25% scale 1.35-m long BOLT II model in the ACE tunnel (described below), as well for the BOLT geometry results in Berridge *et al.* 2021 and Kostak and Bowersox 2021. A weaker growing instability around 130 kHz was also observed in the Kulite surface pressure spectra, which was also seen on the BOLT geometry in the BAM6QT under quiet flow (Knutsen *et al.* 2021, Mckiernan *et al.* 2021).

DISTRIBUTION A: Distribution approved for public release.

The present PCB surface data for P28 in the M6QT show a mode around 180-250 kHz in Fig. 27 that grew in amplitude and in frequency as the Reynolds number was increased. This is likely the early stages of the 200 kHz peak for the 1.5-m long BOLT II model described in the previous section. Because this is associated with a secondary instability, which typically show nonlinear growth, the weak signal at the upstream location is expected. These data are available to help identify transition mechanisms and validate numerical simulations.

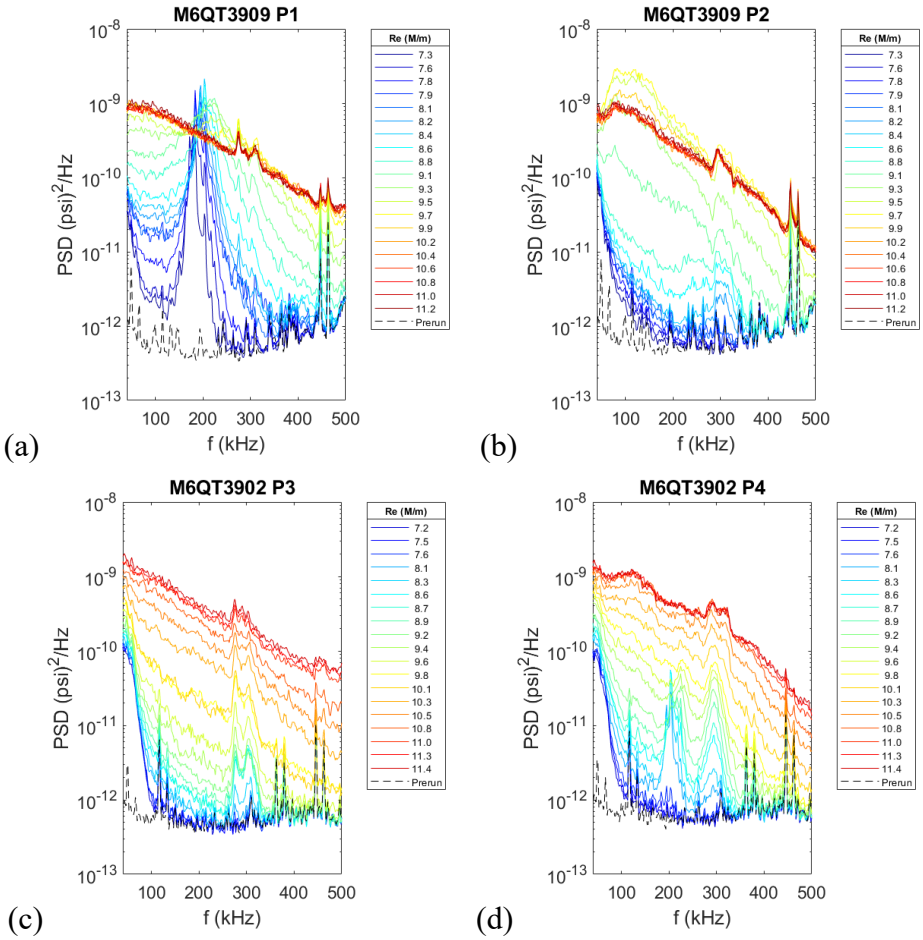

Figure 24. PCB PSD plots on the scaled 1.5-m model in the M6QT. (a) P1. (b) P2. (c) P3. (d) P4.

PSD data were also acquired in the ACE tunnel for the 1.35-m Long BOLT II model. Representative plots are given in Fig. 28. A very mild disturbance appeared in the PCB spectra in Fig. 28a between 100 – 200 kHz that grew in amplitude and frequency as the Reynolds number was increases. This structure was apparently triggered by the tunnel freestream noise associated with transition of the tunnel boundary layers near $Re/\text{m} = 3 \times 10^6$. The tunnel noise is described in the Facilities and Instrumentation Section. The spectra transited to broad band turbulence near $Re/\text{m} = 5.0 \times 10^6$. This was consistent across all PCB sensors. A 20-40 kHz instability was also observed for all Kulite sensors in ACE, which is consistent to the results for the M6QT. Representative plots are provided in Fig. 28b. A notable difference to the M6QT data was that the outboard Kulites in

DISTRIBUTION A: Distribution approved for public release.

ACE showed broad band breakdown. This is apparent in the K18 sensor shown in Fig. 28b. A jump in the amplitude of this wave for the K20 sensor in Fig. 28b occurred at *Re*/m = 3 x 10^6. Collectively, these data reveal effects of tunnel disturbances on the sensitive response of the boundary layer instabilities. Understanding these effects has the potential to enable a broader range of ground test facilities for validating prediction of boundary layer instabilities and turbulence.

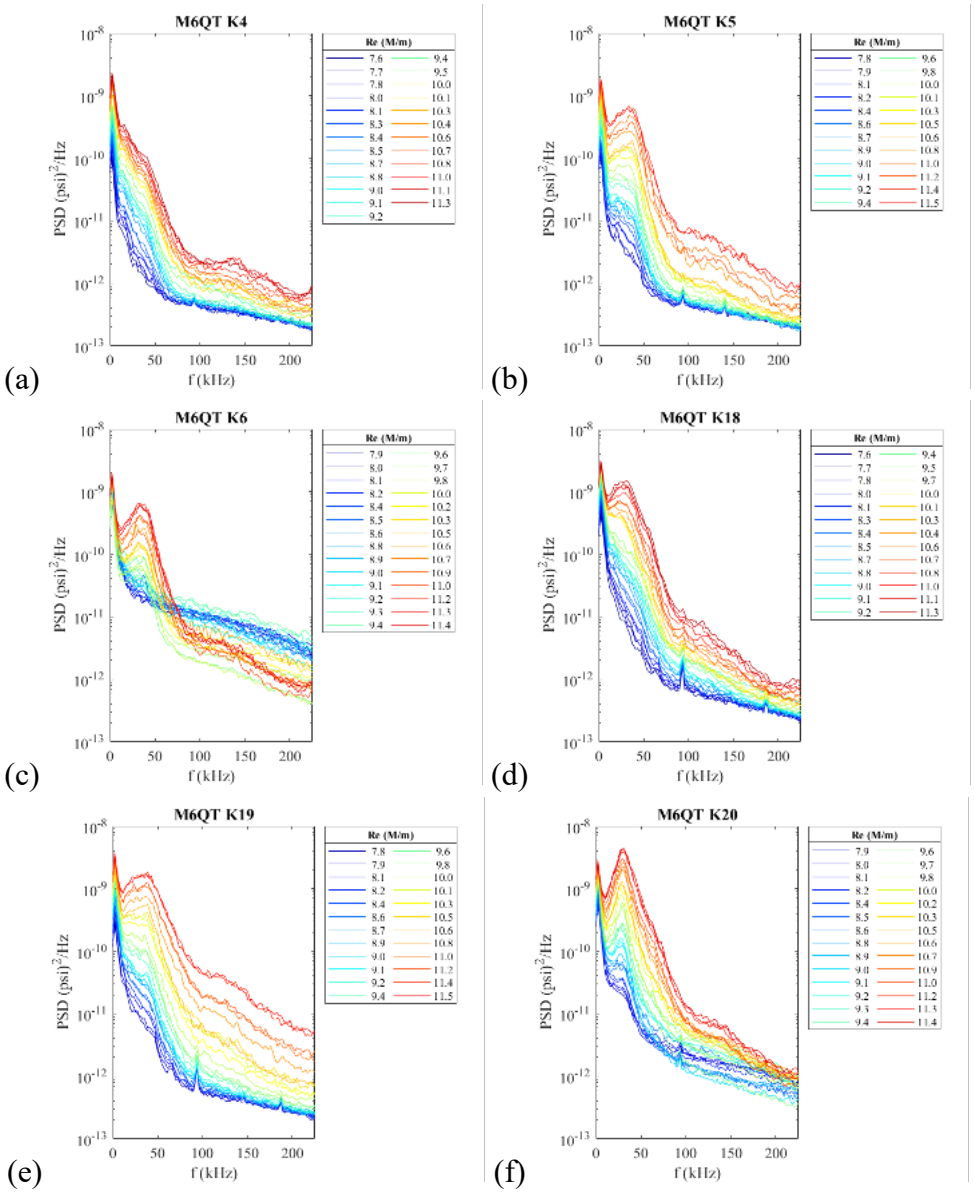

Figure 25. Kulite PSD plots on the scaled 1.35-m model in the M6QT. (a) K4., (b) K5. (c) K6. (d) K18. (e) K19. (f) K20.

DISTRIBUTION A: Distribution approved for public release.

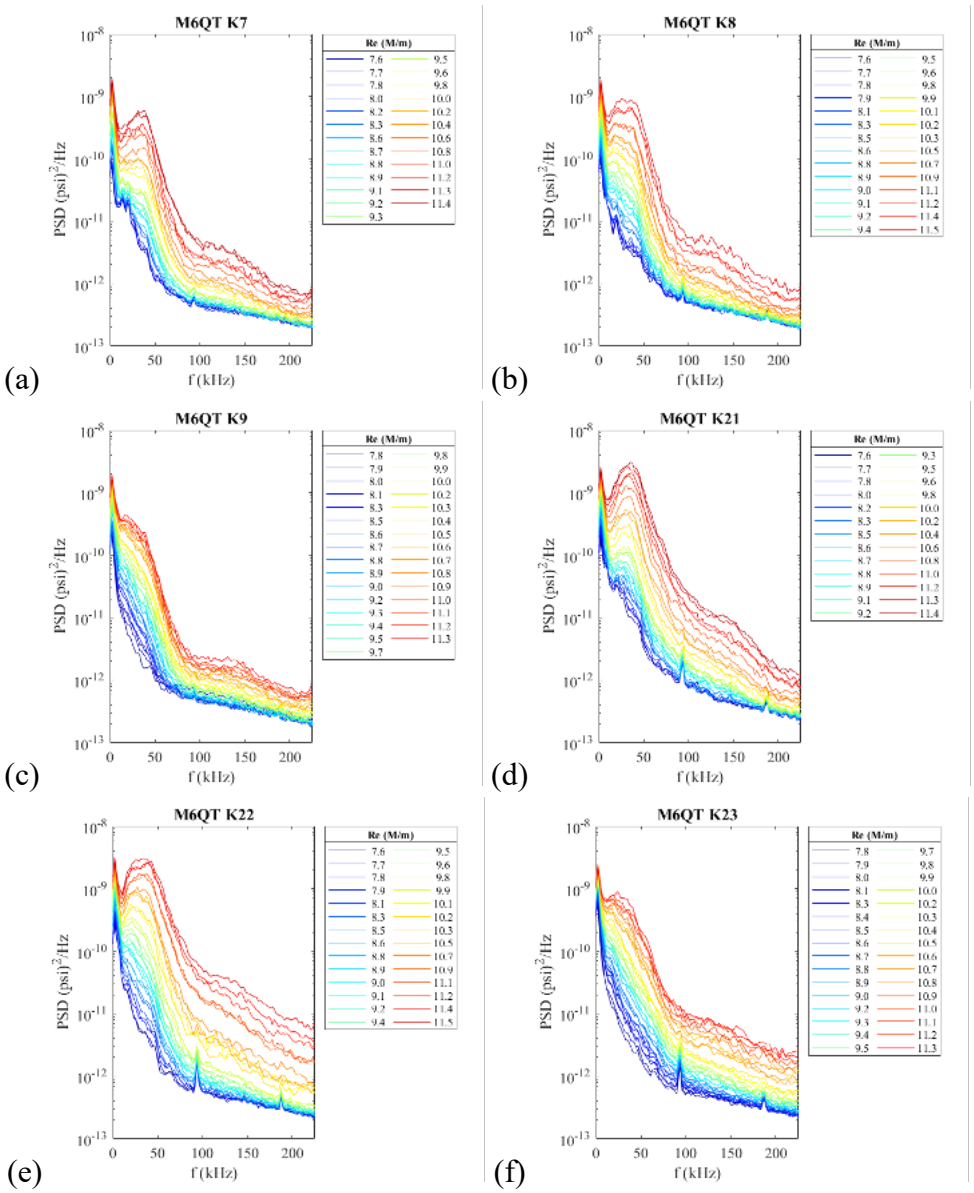

Figure 26. Kulite PSD on the scaled 1.35-m model in the M6QT. (a) K7. (b) K8. (c) K9. (d) K21. (e) K22. (f) K23.

Collectively, the surface pressure spectra highlight the importance of the flow structure in the boundary layer on the surface heat and boundary layer transition and turbulence. This motivates the quantification of these vortex structure in the off-body flow field, which is the subject of the next section. The measurements were focused on the mixed-mode region identified by the yellow ellipses on Fig. 22a.

DISTRIBUTION A: Distribution approved for public release.

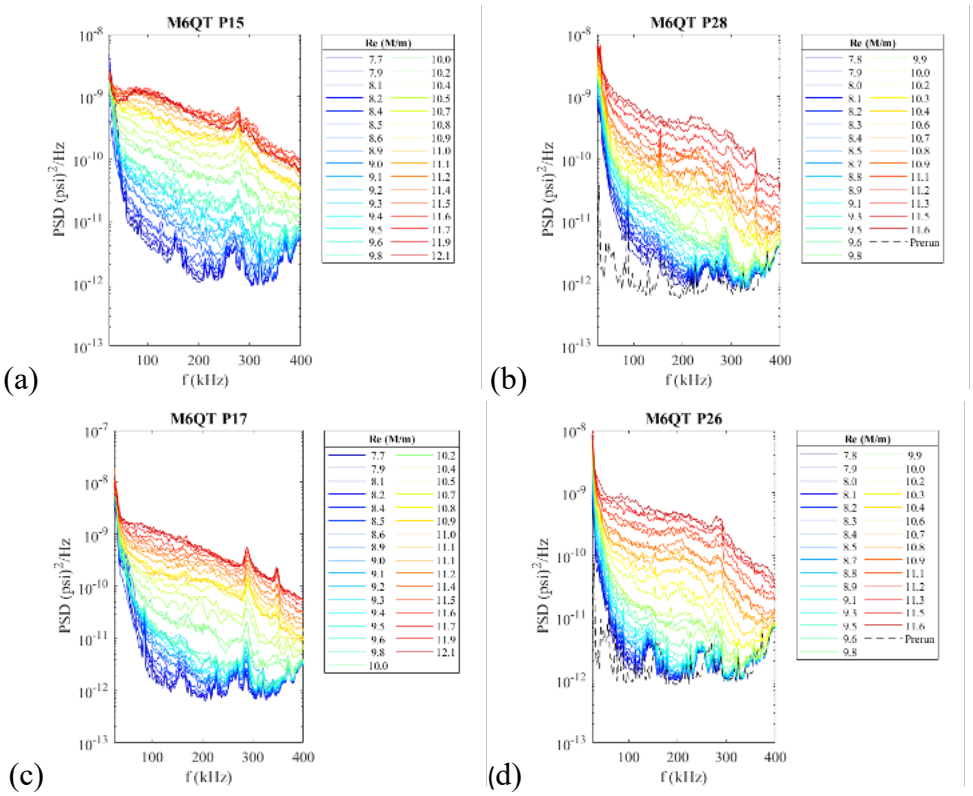

Figure 27. PCB PSD on the scaled 1.35-m model in the M6QT. (1) P15. (b) P28. (c) P17. (d) P26.

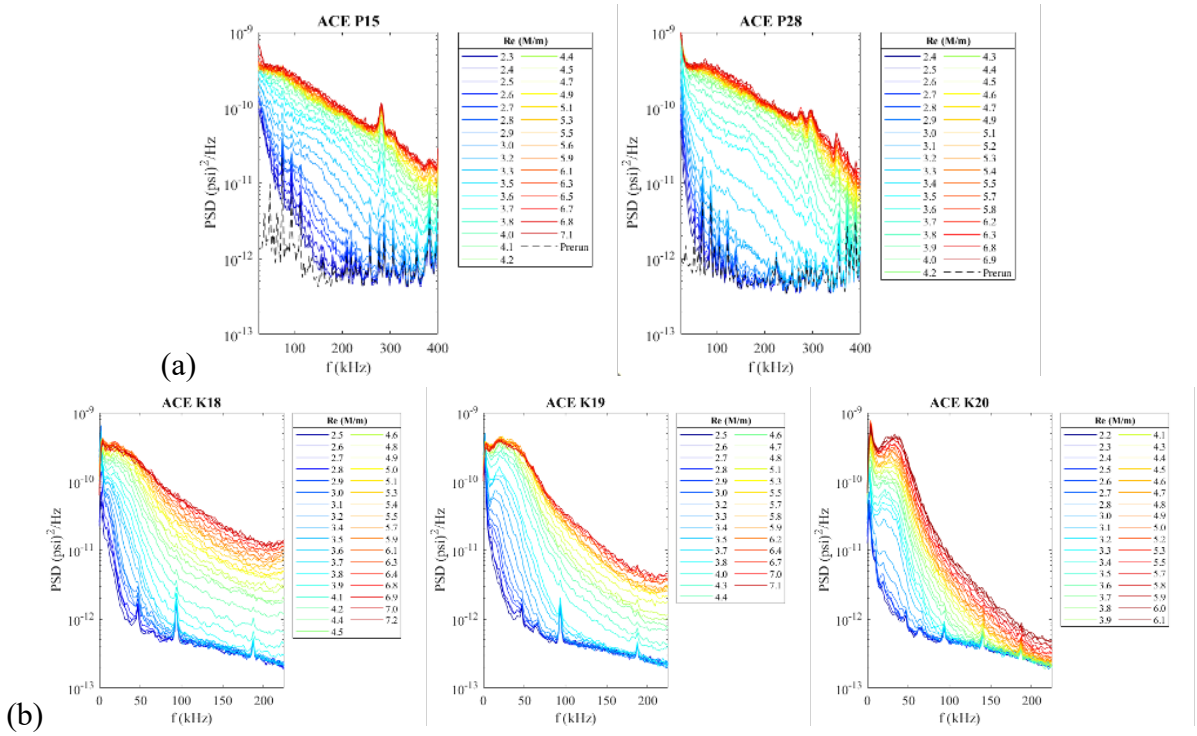

Figure 28. Selected PSD plots for scaled 1.35-m model in ACE. (a) PCB Sensors 15 and 28. (b) Kulite Sensors 18 - 20.

DISTRIBUTION A: Distribution approved for public release.

4.2.4 Off Body Hot-Film Measurements in the M6QT

Constant temperature hot-film anemometry data were acquired in the region of breakdown on the BOLT II geometry at several Reynolds numbers in the M6QT to investigate off-body structures. Hot-wires/films respond to changes in mass flux and total temperature (Bowersox 1996). Due to their robustness, TSI 1220-20 hot-films were utilized for these measurements, however, the frequency response was sacrificed; at the 3-dB roll-off, the maximum frequency response of the hot-film achieved in the M6QT was 100 kHz. The film was sampled at a rate of 500 kHz for 50,000 samples at 100 ms each. A three-axis traverse previously developed by Craig and Saric (2016). The traverse with the BOLT II model installed is shown in Fig. 29a.

To acquire a complete dataset of turbulent breakdown, multiple wind tunnel runs were required. For each wind tunnel run, the hot-film was traversed in the y and z directions. For example, the grid utilized for hot-film measurements at the downstream location on the BOLT II geometry is shown in Fig. 29b. The y-coordinate represents the location, in meters, from the center of the BOLT II geometry and the z-location, represents the location from the centerline. Each line-intersection represents the traverse measurement location. The solid black line located under the grid is the BOLT II surface; all hot-film measurements were taken 1.0 mm off the surface. The total spanwise measurement range was 14 mm with an upper measurement width of 2.8 mm at each z-location.

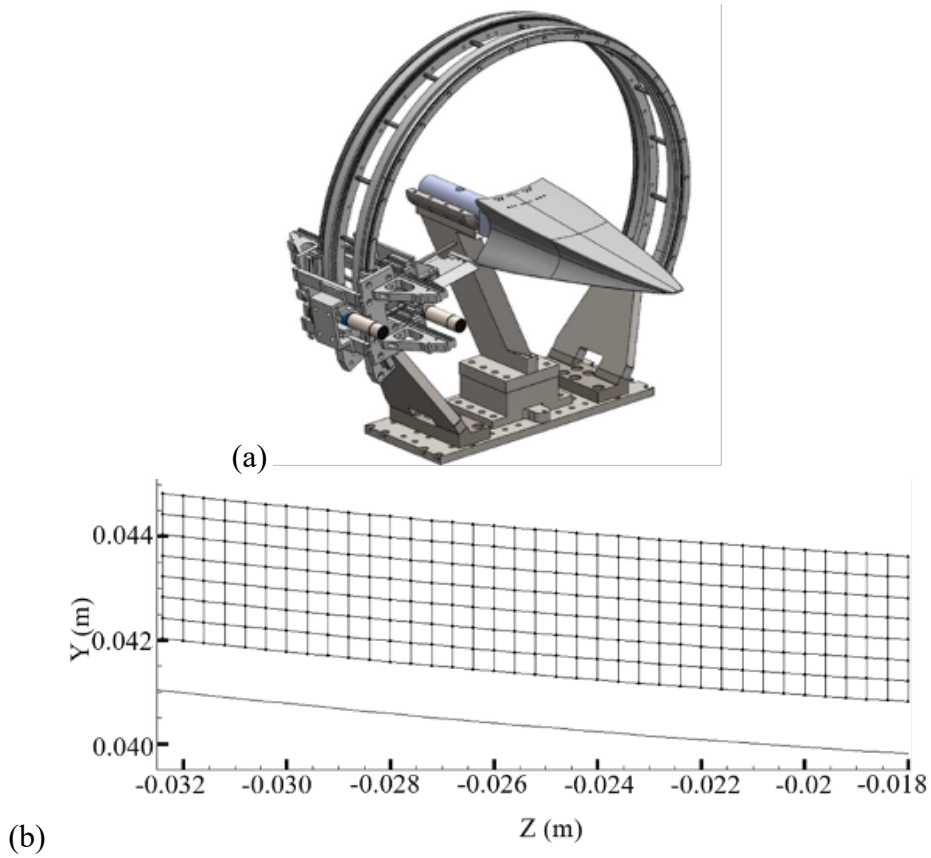

Figure 29 Hot-wire traverse. (a) Traverse mechanism. (b) Downstream location measurement grid (lower line is the BOLT II geometry).

DISTRIBUTION A: Distribution approved for public release.

Off-body measurements were acquired in the mixed-mode region of the BOLT II geometry at three Reynolds numbers: Re/m = 8.2x10^6, 9.2x10^6, and 10.4x10^6. Two streamwise locations were utilized for Re/m = 10.4x10^6 (x = 0.3175 m and x = 0.2925 m) and one streamwise location for the other tested Reynolds numbers (x = 0.3175 m). As indicated earlier in Fig. 22, the selected Reynolds numbers allow for characterization of the off-body flow for laminar flow, transitional, and breakdown due to secondary instabilities on the surface of BOLT II. Laminar flow was present on the model at Re/m = 8.2x10^6, transition appeared begins within the laminar streaks around Re/m = 9.4x10^6, and elevated heating in a turbulent wedge was seen at Re/m = 10.4x10^6 and higher.

The hot-film bridge voltage is correlated to the mass flux by $V_b^2 = A + B(\rho U)^n$, where V_b^2 represents the bridge voltage, ρU is the mass flux, and A, B, and n are calibration constants (Bowersox 1996). It has been shown that nearly linear fits ($n \sim 1.0$) were suitable at the lower densities within the facilities at TAMU (Semper and Bowersox 2017). The bridge voltage from the experiments at Re/m = 10.4x10^6 is compared to DNS mass flux data at Re/m = 10.8x10^6 provided by the University of Minnesota (Johnston and Candler 2021) in Fig. 30. The solid black line located in below the contour in the experimental plot indicates the surface of the model. Overall, the fluctuating structures were qualitatively similar between the experiment and DNS, as was their locations.

The hot-film bridge voltage 2-D contours maps at x = 31.75 mm are shown in Figs. 31a and 31b for Re/m = 8.2x10^6 and 9.2x10^6, respectively. The roll-up structures within the boundary layer in the mixed-mode region are well-captured and are indicative of the mean flow. As the Reynolds number increased, the structures became more developed and the boundary layer thinned. Measurements for Re/m = 8.2x10^6 were not extended closer to the centerline due to weak or unobservable structures in the IR thermography in Fig. 22a. The structures near z = -29 mm were more defined with increased Reynolds number.

The 2-D contours of the RMS voltage fluctuations normalized by the mean voltage for each measurement point at the downstream location are shown in Fig. 32. Regions of amplification are present at each Reynolds number. However, as transition and breakdown occurred, these regions of amplification become more apparent, grow, and merged. This amplified region is the source of the turbulent wedge within the mixed-mode region located in Fig. 22a. In Figs. 32b and 32c, the content observed in the 4.0. mm between z = -22 and -26 mm appeared to be collocated with elevated heat streak traveling within the laminar-to-turbulent transition region in Fig. 22a, which appeared around Re/m = 9.2x10^6. The two white squares located in Fig. 32b were discarded points that were apparently due to nonphysical noise.

The upstream RMS fluctuating voltage from the hot-film experiments are compared to the DNS results for x = 0.2925 m in Fig. 33. Additional fluctuation content is seen in the contour plot. A qualitative comparison of the streamwise velocity fluctuations from the DNS at x = 0.3065 m with the RMS normalized by the mean voltage at x = 0.2925 m are shown in Figure 34. The surface height difference at these two locations is 1.62 mm. Within the roll-up of the boundary layer, the voltage fluctuations in Fig. 34 are slightly more amplified than at the downstream location in Fig. 32. Between z = -22 to -26 mm, the total energy content within the region is also more amplified.

DISTRIBUTION A: Distribution approved for public release.

The shape and location of the amplified structures in the experiment are qualitatively similar to the computations in Fig. 34. The amplified content before z = -26 mm in the experiment appeared transitional, a feature not obvious in the DNS.

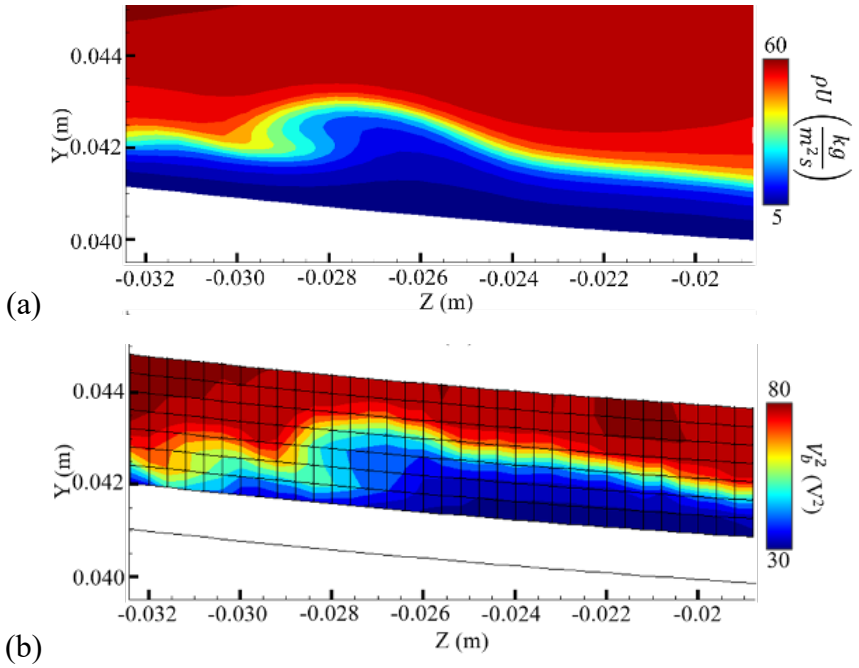

Figure 30. Visualization of the structures in the mixed-mode region at x = 0.3175 m. (a) University of Minnesota DNS mass flux at Re/m = 10.8x10^6 (modified from Johnston and Candler 2021). (b) Bridge voltage from the experiment at Re/m = 10.4x10^6.

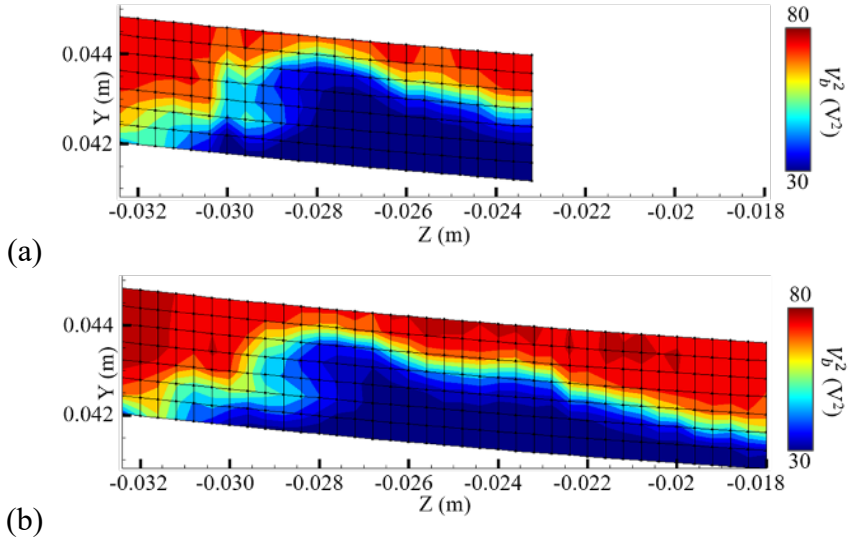

Figure 31. Hot-film bridge voltage at x = 0.3175 m for Re/m = (a) 8.2x10^6 and (b) 9.2x10^6.

DISTRIBUTION A: Distribution approved for public release.

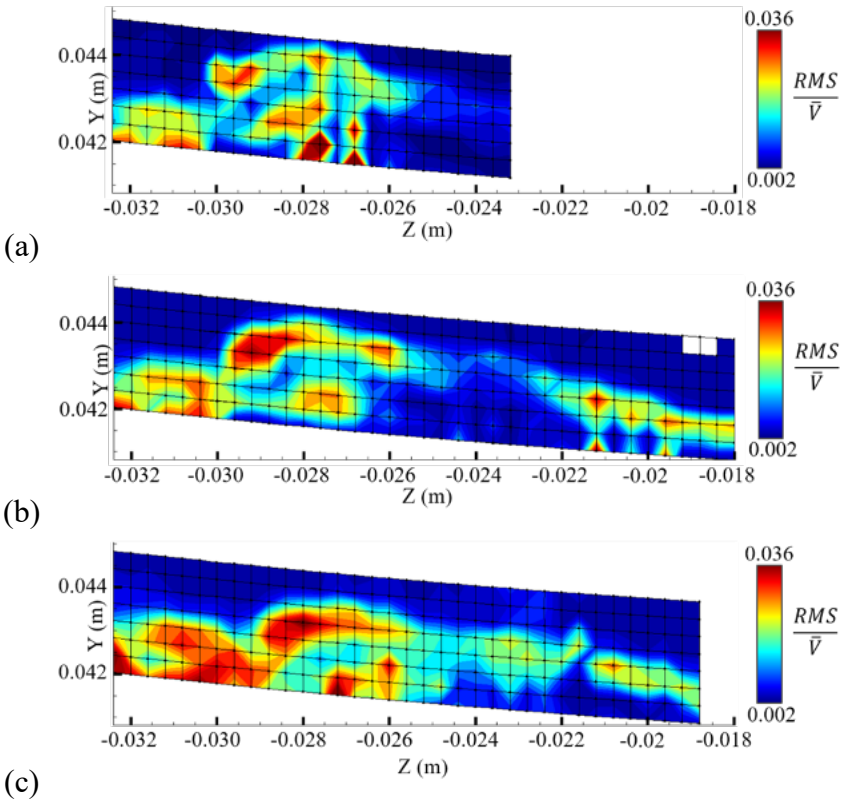

Figure 32. Contour maps of the RMS normalized by the mean voltage for *Re*/m = (a) 8.2x10^6, (b) 9.2x10^6, and (c) 10.4x10^6 at the downstream measurement location.

Power spectral density plots at the streamwise location of x = 0.3175 m shown in Fig. 35 were extracted within the intense structures located in the contour plot of Fig. 32c. The legend represents the y-location in mm from the center of the model for a specific z-location listed at the top of each plot. The pre-run data is also present in the plot (shown as a black dashed line). Modal growth in the spectra is seen within the frequency range of 50-75 kHz. As the traverse steps in and out of the structure, the overall PSD energy increases then decreases. Within this frequency range, modal growth was not apparent in the PSD at the upstream measurement location as well as the other tested Reynolds numbers.

To avoid misinterpretation due to the noise-sikes observed around 50-52 kHz (seen in Fig. 35), the PSD spectra were spectrally integrated to provide the RMS content in the 53-75 kHz band. The resulting contours are shown in Fig. 36 for x = 0.2975 m (bottom) and x = 0.3175 m (top). At the upstream location, little content is seen within this frequency band. However, at the downstream location, fluctuations in this frequency band were amplified in a region localized to the boundary-layer edge across the span of z = -22 to -28 mm. The corresponding mode shapes (transverse line plots of the normalized RMS values) are plotting in Fig. 37. Plotted along the abscissa is the fluctuation energy for five z-locations in the range of z = -25.2 to -26.8 mm. These plots provide new insight into the growth and interaction of instabilities as they move downstream within the boundary layer of the BOLT II model.

DISTRIBUTION A: Distribution approved for public release.

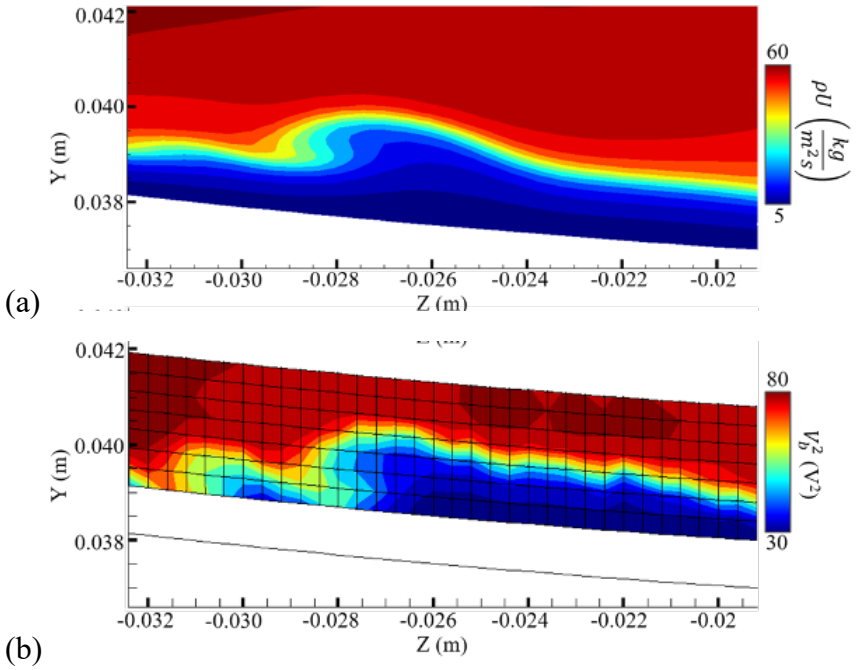

Figure 33. Visualization of the structures in the mixed-mode region at x = 0.2925 m. (a) University of Minnesota DNS in mass flux at *Re*/m = 10.8x10^6 (modified from Johnston and Candler 2021). (b) Bridge voltage from the experiment at *Re*/m = 10.4x10^6.

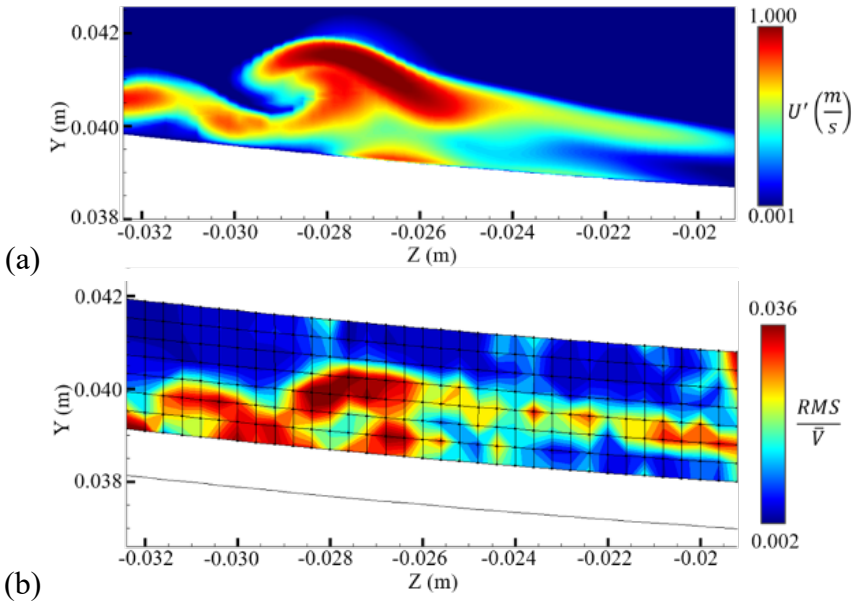

Figure 34. Streamwise velocity fluctuations at x = 0.3065 m. (University of Minnesota DNS at *Re*/m = 10.8x10^6 (modified from Johnston and Candler 2021). (b) RMS fluctuating voltage normalized by the mean at x = 0.2925 m from the experiments at *Re*/m = 10.4x10^6.

DISTRIBUTION A: Distribution approved for public release.

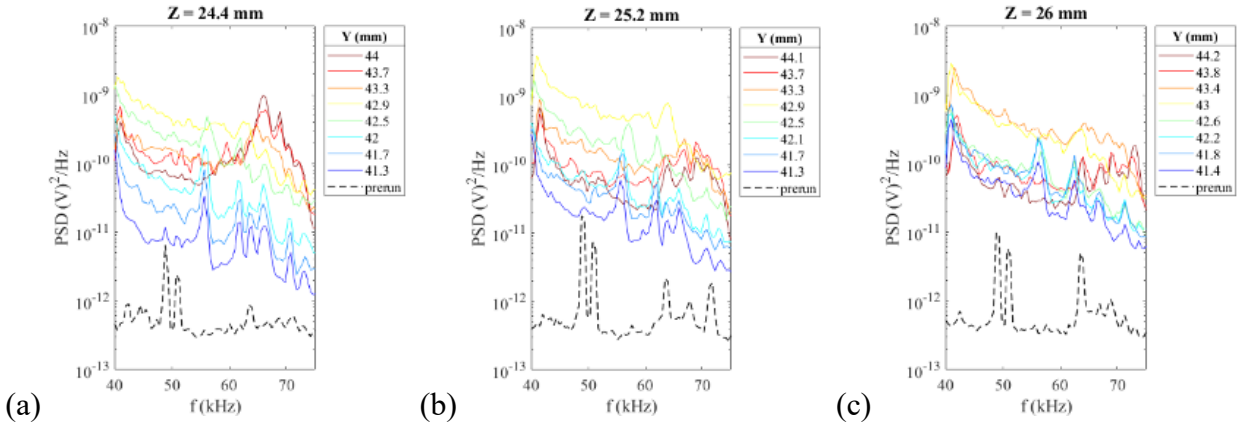

Figure 35. Hot-film anemometry power spectral density plots at the downstream location of x = 0.3175 m for several spanwise locations within the transition/breakdown region.

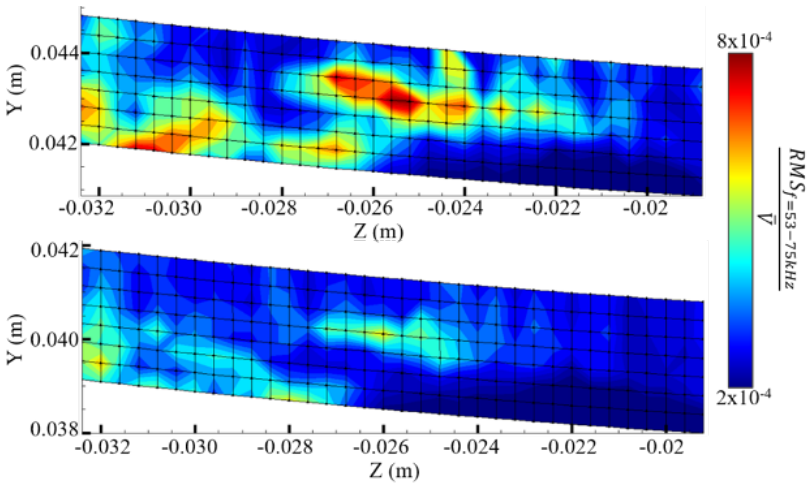

Figure 36. RMS integrated within the frequency band of 53-75 kHz normalized by the mean voltage at the downstream (top) and upstream (bottom) locations.

Collectively, the data generated by the subscale tests impacted the flight experiment by offering new insights to boundary layer transition process, which provided guidance for sensor location and helped in the interpretation of the flight experiment data.

4.4 Flight Geometry Materials Selection and Thermal Protection

The TAMU-CUBRC Team, with JHUAPL, performed the materials selection, where Nickel 201 (Ni201) was chosen for the nose and 410 stainless-steel (SS410) for the frustrum. The material configuration is shown in Fig. 38. Benefits of this materials configuration include added ballast for flight stability and reduced uncertainty in the Medtherm (MT) heat flux measurements, where the thermal diffusivity of the MT Type E sensor matches that of SS410 (see Appendix A). Also, switching from aluminum to stainless steel for the frustrum reduced the ballast requirement from 186 kg to 118 kg, while maintaining the CG location for flight stability.

DISTRIBUTION A: Distribution approved for public release.

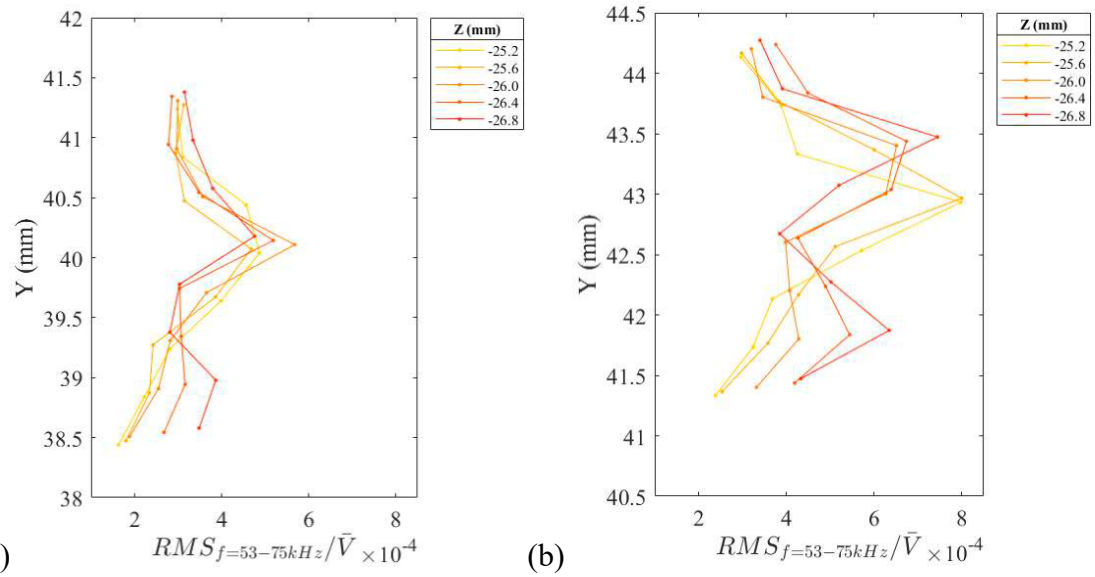

Figure 37. Mode shape plots for the most amplified regions of Fig. 36. (a) upstream. (b) downstream.

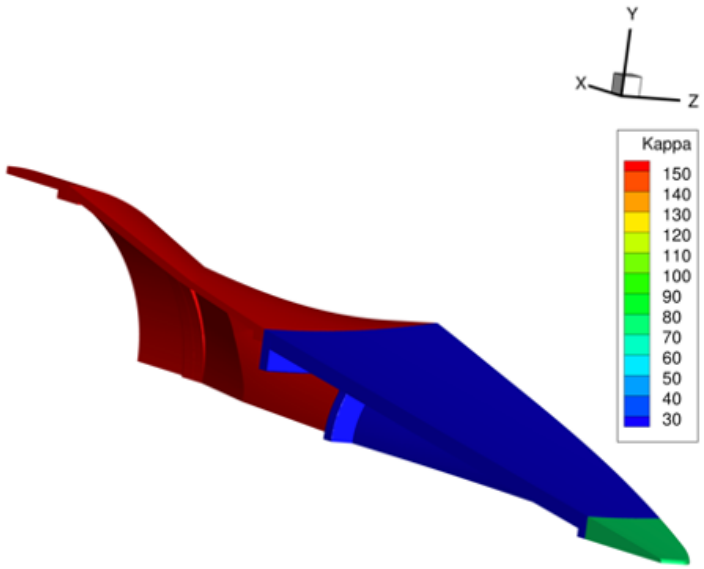

Figure 38. Thermal conductivity for BOLT II geometry. Green: Ni201 Nose, Blue: SS410 frustrum, Red: Aluminum 6061 Transition (Wheaton, JHUAPL).

Ni201 has a maximum operating temperature of 950K (ASME Boiler and Pressure Vessel Code, Section VIII, Division 1), and a thermal conductivity that is ~70-80% of TZM (Molybdenum BOLT I nose material). Also, the coefficients of thermal expansion (CTE) are similar for Ni201 and SS410, where the values for Nickel are 20-25% larger over the temperature range. With this difference, the surfaces were machined flush prior to flight as this yielded a small aft facing step

DISTRIBUTION A: Distribution approved for public release.

due to the Ni201 expanding slightly more; details are provided below with respect to the structural analysis.

As mentioned earlier, the front 86.6% of the BOLT II geometry followed that of BOLT. The BOLT results and tools were available as a guide for BOLT II. JHU/APL performed several rounds of thermal analysis for the BOLT flight supporting design work for the conceptual, preliminary, and critical design reviews via viscous-based CFD with full transitional flow modeling used for refined thermal model to close material choices, which was anchored with CUBRC wind tunnel data. Wheaton also developed multiple thermal modeling processes using different codes for the transient analysis (MSLRAD/ATLAS and CFD++). Wheaton was able to leverage existing grids, tools, knowledge base from BOLT to apply to quick turnaround analyses for the BOLT II configuration shown in Fig. 38. The analysis was performed on the payload section annotated in Fig. 10. A blow-up of this section is shown in Fig. 39, where the BOLT II research geometry (left most medium gray section), fairing to the cylindrical payload (center light gray and dark gray conical section), and initial portion of the transition module (dark gray) was simulated. These regions correspond to the green and blue research geometry and red fairing/cone/payload shown in Fig. 38, respectively. Finite element analyses of loading were performed by CUBRC.

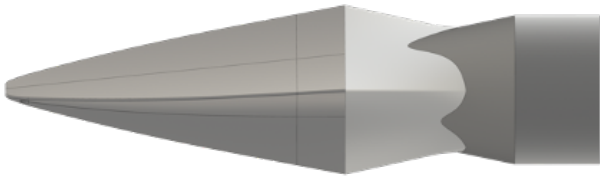

Figure 39 Blow-up view of Schematic of the payload section (see Fig. 10) simulated for the material selection analyses.

Representative results from the JHUAPL analysis are provided in Fig. 40. The simulations were run assuming fully turbulent with an additional 20% factor of safety included in heat transfer coefficient to account for off-nominal conditions. Based on the preliminary analyses, the Ni201 nose temperature peaks at ~850K during ascent and ~980K at end of flight. The SS410 frustum experiment surface reaches high temperatures ~800K on leading edge at end of flight, but bulk temperatures remain low throughout flight. The AL6061 transition and booster sections, without TPS, reach temperatures at which aluminum retains little strength (~540K bulk temperature at end of flight for transition section). TPS was deemed necessary to protect the aft aluminum sections. Preliminary 1-D estimates indicated that 3.175 mm Amorim P50 cork reduced the peak temperature to ~350K.

In addition, CFD simulations were performed on the transition section based on critical points identified along the simulated BOLT II trajectory and a previously identified condition of intense heat flux. These simulations were the subject of the MS thesis of E. Swinny (TAMU graduate student under the direction of R. Bowersox).

These simulations revealed that a significant amount of heat flux occurs on the conical transition of the payload bay downstream from the low radius edge of the fairing and that very little heat

DISTRIBUTION A: Distribution approved for public release.

flux occurs on the cylindrical section of the payload bay behind the conical transition. Further investigation of the flow field revealed that as flow moves along the low radius edge of the fairing the boundary layer experiences significant deformation and that wingtip vorticity from the BOLT II flight vehicle directly interacts with, and causes, the spots of intense heat flux on the payload bay. Angles of attack in both and increase heat flux at these spots by creating increased amounts leading edge vorticity. Heat flux observed on the fairing was highest behind the BOLT II test surface and followed patterns that were a direct continuation of heat flux on BOLT II. Angles-of-attack in created the most significant increases in heat flux at this spot due to the component of flow made incident to the test surface and the fairing behind it. For each simulation the maximum heat flux observed on the payload bay and fairing were recorded. Comparisons of solutions using two different turbulence models (Spalart-Allmaras 1992 and Menter 1994) showed good agreement, with a maximum of 0.1% difference between the two simulations. Further comparisons to wind tunnel tests which were conducted using a 25% scale model of the geometry of interest on the flight vehicle. Heat flux data was calculated for wind tunnel tests using IR imaging techniques discussed in the next Section. Comparing the wind results to the simulations at trajectory conditions, it was observed that the heat flux features observed in the simulation could be identified in wind tunnel tests. To allow for direct comparison, simulations were performed at the wind tunnel conditions. The comparison of the results presented in Fig. 40 showed that simulations correctly predicted the heat flux patterns observed in wind tunnel tests, but at elevated values. The agreement provided qualitative evidence supporting the results obtained from CFD simulations.

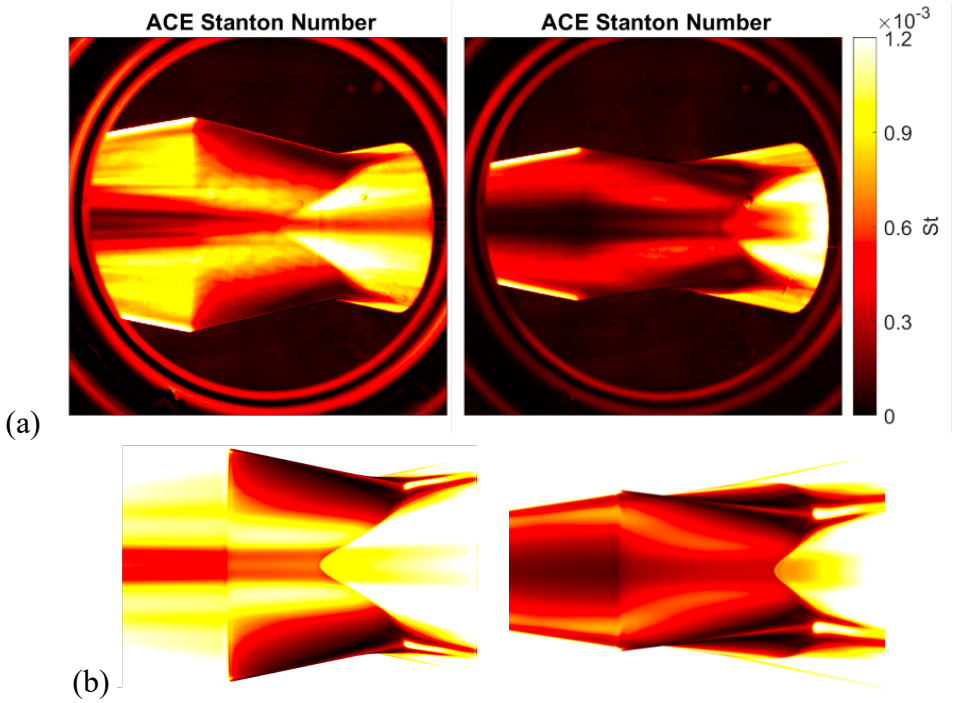

Figure 40 Fairing thermal loading. (a) ACE tunnel (left: top, right: side). (b) CFD simulations; same scale as (a) (left: top, right: side).

DISTRIBUTION A: Distribution approved for public release.

The results from the CFD and thermal analyses were then used in a finite element structural analysis to quantify loads and steps. Specifically, the CFD++ conjugate heat transfer body temperatures were imported into ANSYS Structural Analysis software. The maximum expected step between the Ni201 nose and SS410 frustrum is 0.15 mm in the corner at the end of the flight (see Fig. 41). Inertial and pressure loading were deemed negligible, and five time slices were analyzed in detail: 23.6 s (ascent max. gradient), 26.0 s (ascent max. q), 28.0 s (ascent peak temperatures), 394.0 s (descent 18 km), and 400 s (descent 8.9 km). Example results are shown in Fig. 42. These data show that the loading was well below ultimate loads at temperature for the Ni20 and SS410 components. Finally, the analyses indicated that the nose/frustrum joint followed from BOLT, and the fastener and pin equivalent stresses were well within allowable stresses. The gutter sidewall/experimental surface joints were also identical to BOLT.

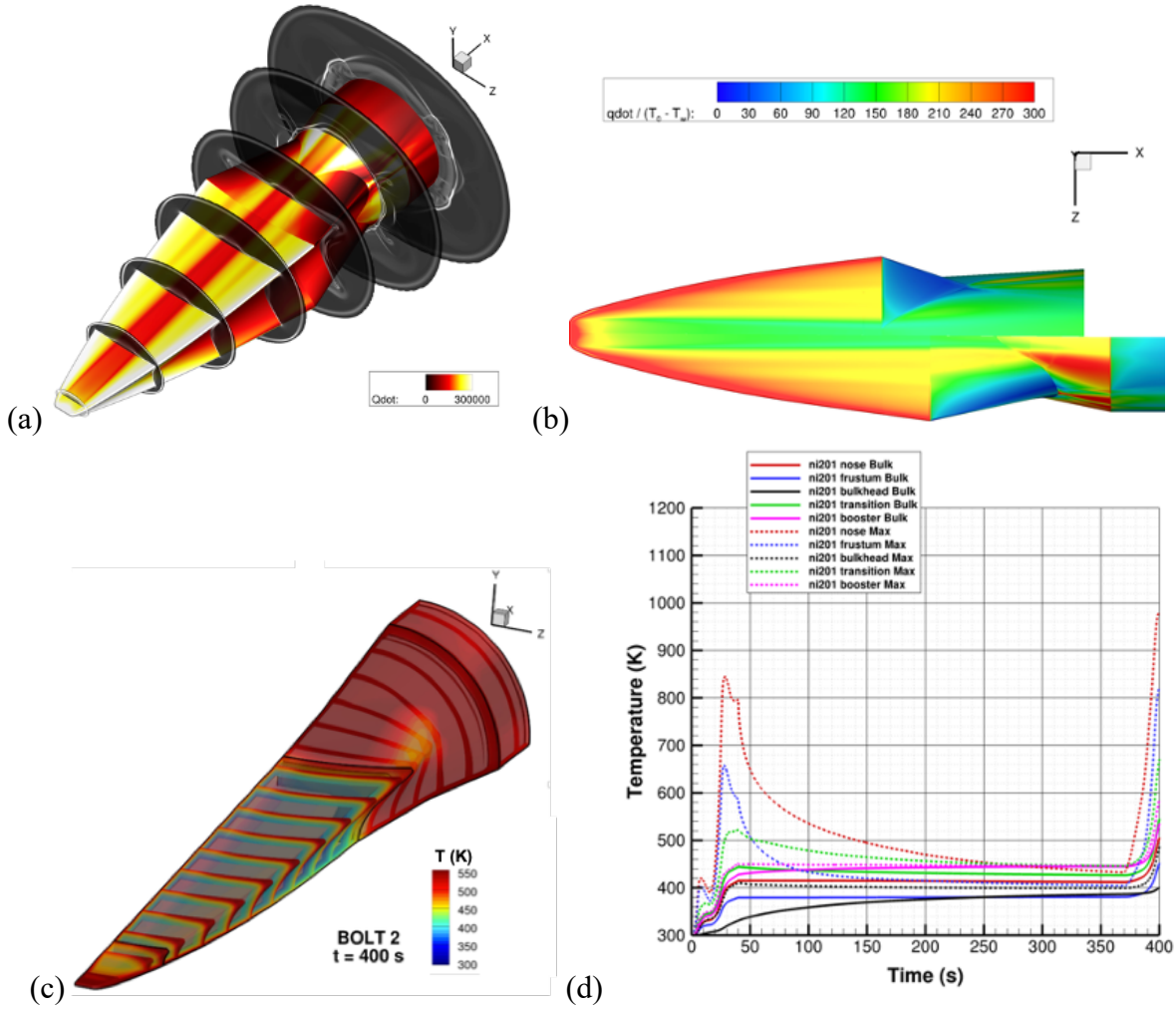

Figure 41 JHUAPL CFD-Thermal analyses. (a) Flow structure (density in grayscale) and surface heat flux. (b) Comparison of BOLTII and BOLT heat flux. (c) Maximum wall temperature for BOLT II at the end of descent. (d) Line plots of bulk and maximum temperatures for the Ni201 nose, SS410 frustrum, and AL6061 transition.

DISTRIBUTION A: Distribution approved for public release.

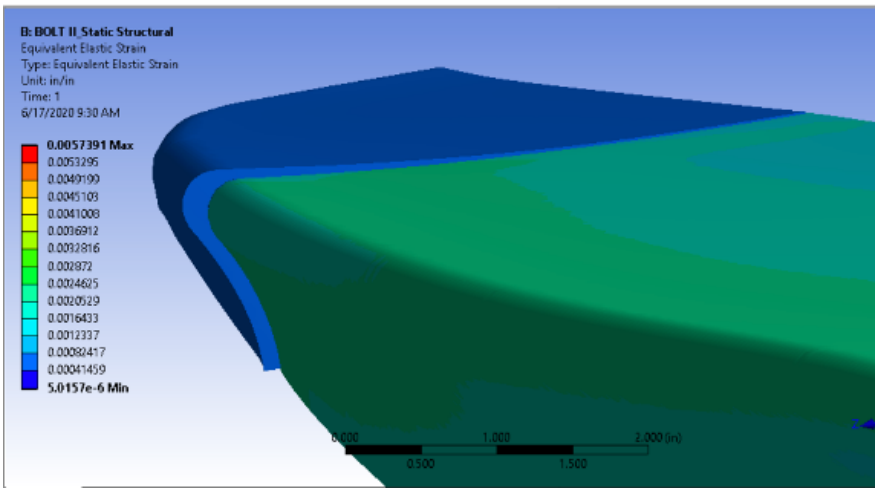

Fig. 42 Maximum step between the Ni201 nose and the SS410 frustrum (exaggerated scale).

(a)

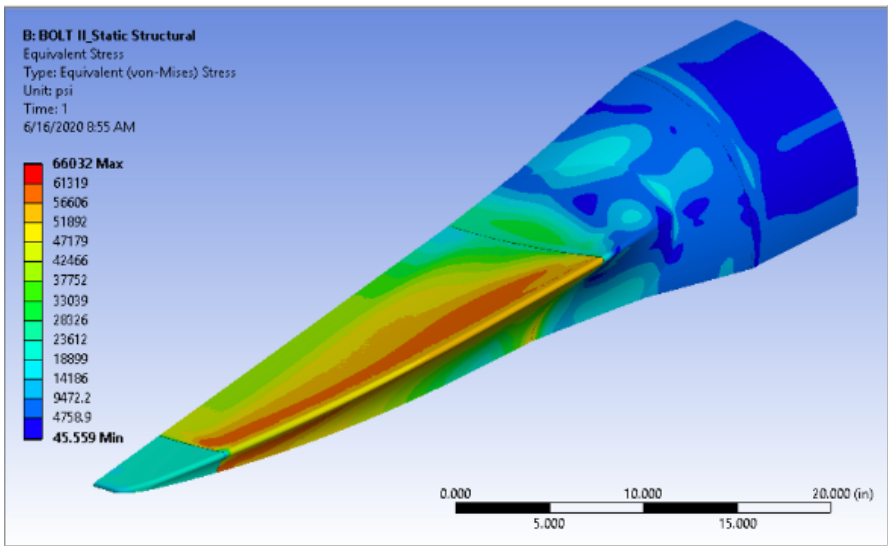

(b)

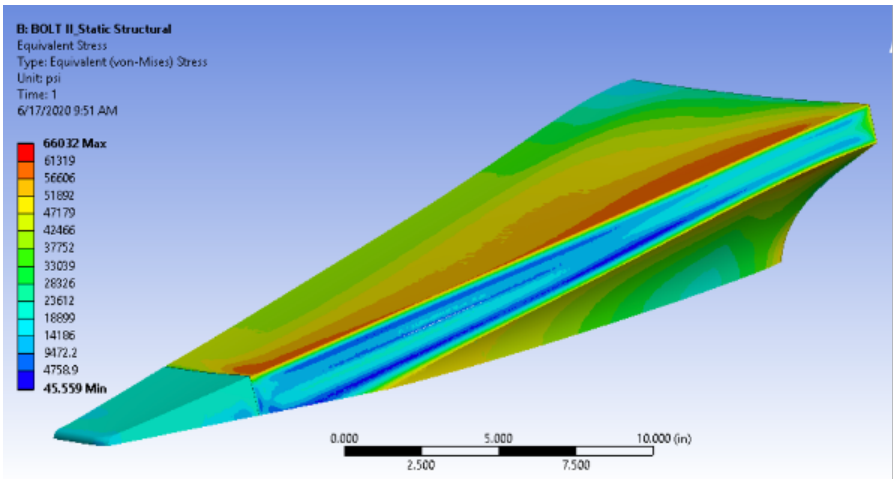

Fig. 43 CUBRC Von-Mises Stress (psi). (a) Surface. (b) Cut through leading-edge.

DISTRIBUTION A: Distribution approved for public release.

4.5 FLIGHT GEOMETRY INSTRUMENTATION SELECTION

The flight instruments were selected based on the analyses described earlier in Section 4. The instruments and layout are summarized in Table 6 and Fig. 44. The laminar, stability and turbulent flow simulations (e.g., Mullen and Reed 2021), along with the experimental data at TAMU were used to guide the instrumentation layout. Additional off nominal simulations and experiments were performed. The BOLT design and ground test results (Wheaton *et al*. 2021, Kostak and Bowersox 2021) were also used to guide the instrumentation selection. Briefly, the Medtherm thermocouples (type E) provide surface temperatures on the front and back face of the frustrum, which allowed for both surface temperature and heat flux measurements. The matched thermal diffusivity enabled high sensitivity and minimal uncertainties (see the RFA responses in Appendix A). The Vatell thermogauge sensors provided direct measurement of the heat flux. RMS surface pressure were quantified with PCB 112B05 sensors. The vehicle attitude was determined via fourteen Honeywell pressure sensors (four on each test surface and three on each gutter). The remaining mean flow Honeywell sensors were used to quantify pressure gradients near the skin friction and heat flux surface array (supported by a separate DURIP grant).

The sensor arrays are outlined by the dashed green boxes on Fig. 44. Fourteen Ahmic skin friction sensors (and RTD sensors) were used with the Medtherm thermocouple and Vatell thermogauge sensors to quantify the Reynolds analogy. High frequency PCB 132B38 sensors were located to quantify traveling crossflow, second mode, and mixed-mode instabilities leading to transition and turbulence. AFRL and GoHypersonics, Inc., under the direction of D. Adamczak, developed the PCB methods. The CUBRC thin film sensors were used to quantify turbulent bursts. Finally, accelerometers were employed to quantify dynamic loads and provide an opportunity to improve the data interpretation for the skin friction sensors.

Table 6 Flight Instrumentation

Sensor	Brand	Model	Sensitivity	Unc.[a]	Freq Resp (kHz)	Sensors per Side[d]	Samp. Freq (kHz)
Heat Flux	Medtherm	TCS-061-EE	68 μV/(deg C)	3-5%	1000	58/38	0.4
Heat Flux	Vatell	TG-2000	33 μV/(W/cm^2)	3%	1.0	48/12	2.0
RMS Press.	PCB	112B05	0.016mV/Pa	18%	200[c]	12/12	57
Pressure	Honeywell	19 C	20 mV/psia	1%[b]	1.0[c]	35/4[e]	0.4
Skin Friction	Ahmic	Custom	Custom	10%	0.5	14/0	1.0
Skin Fric. Temp	Ahmic	RTD	Custom	2K	***	14/0	400
Spectra	PCB	132B38	140 mV/psi	***	1000	4/0	2500
Thin Film	CUBRC	Custom	Custom	***	1000	36/12	10
Accelerometer	Endevco	7270AM4	100 μV/g	3%	150	5	5.0

[a] Manufacturer provided values, team experience, and the analyses, [b] Resolvable attitude angles, [c] Resonance frequency, [d] Side A / Side B, [e] Six attitude sensors are in the gutters.

DISTRIBUTION A: Distribution approved for public release.

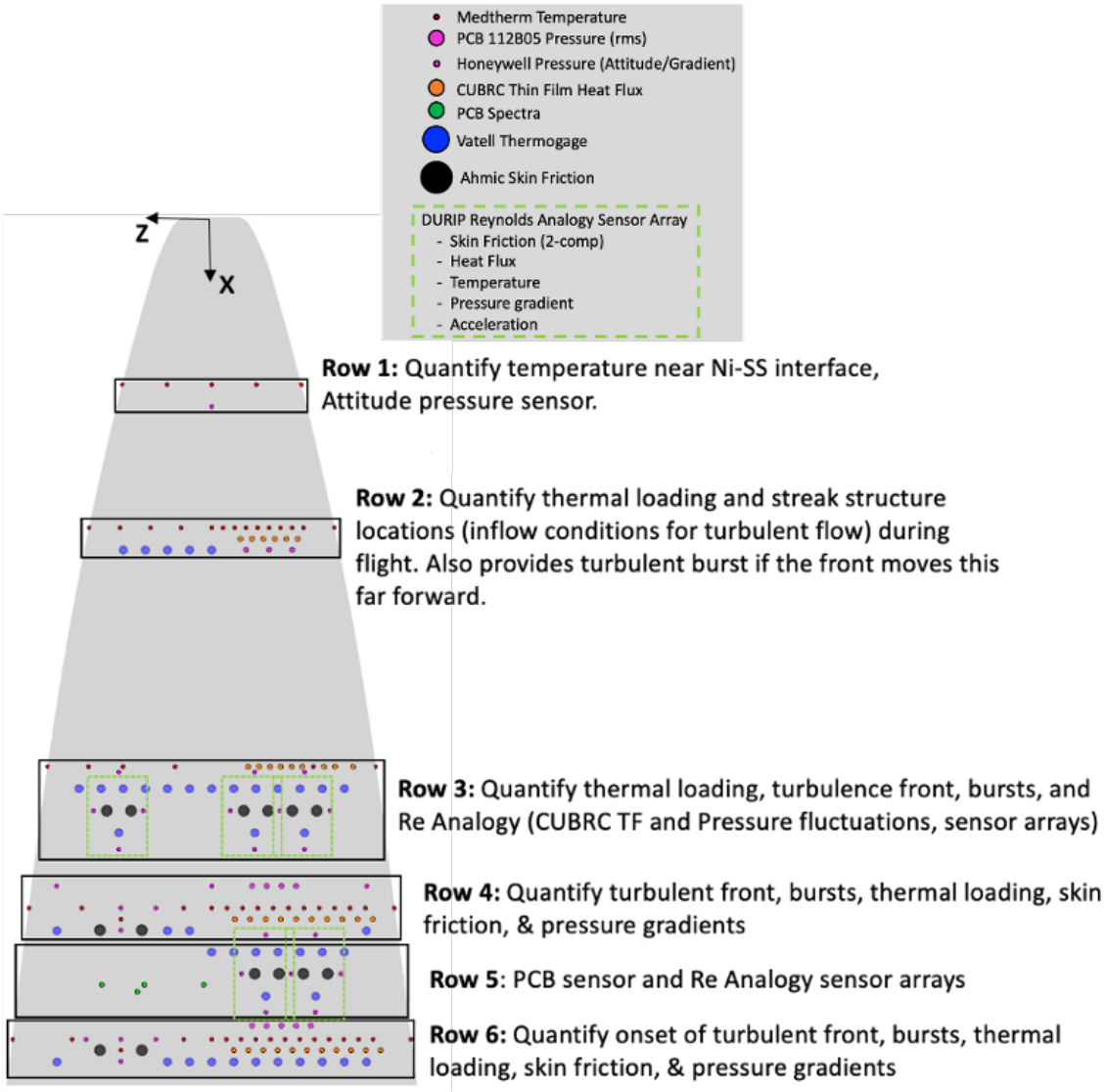

Fig. 44 Instrumentation layout and roles.

The roles of the instruments are summarized in Fig. 44, with alignment to the flow structure shown in Fig. 45, including transition, turbulence, angle-of-attack, and yaw angle effects. In Fig. 44, six basic groups (or rows) were defined with specific purposes as listed. The Medtherms in Row 1 provided thermal data to estimate the temperature and step associated with the Ni201 and SS410 interface. Also, one of the four attitude sensors was in this group. The purpose of row 2 was to quantify the streak structure leading into the downstream transition and turbulence, which provided the initial conditions. The gap between row 1 and row 2 was necessary due to the large ballast in this region of the model. The instruments in rows 3 – 6 were strategically positioned (see Fig. 45) to quantify both the transition process and the turbulence properties as function of Reynolds number during flight. The gutters were instrumented with Honeywell pressure transduces to assist with attitude determination.

DISTRIBUTION A: Distribution approved for public release.

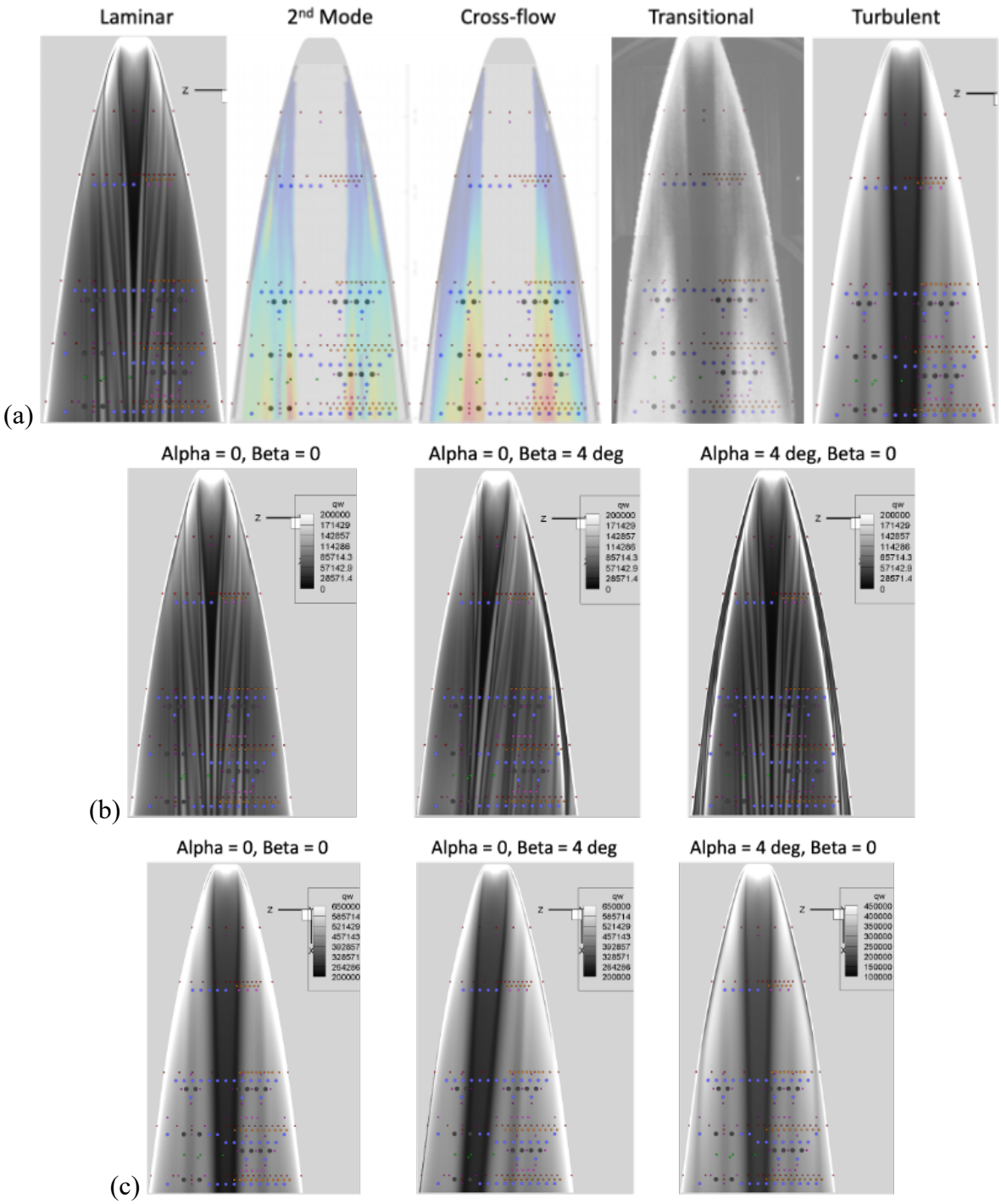

Fig. 45 Alignment of instruments with expected flow features. (a) Laminar, transitional, and turbulent) with comparison to BOLT I. (b) Angle-of-attack and yaw angle effects.

The Side A surface sensor locations are summarized in Tables 7a – 7g. The numbering methodology is based on sensor type, model side A or B, row (1 – 6), and z-location (column) counting from left-to-right as shown in Fig. 44a.

DISTRIBUTION A: Distribution approved for public release.

Table 7a Medtherm (MT) Thermocouples

Name	x (m)	y (m)	z (m)	Name	x (m)	y (m)	z (m)
MT-A-1-1	0.1930	0.0288	0.1026	**MT-A-4-2**	0.7960	0.1097	0.1494
MT-A-1-2	0.1930	0.0290	0.0513	**MT-A-4-3**	0.7960	0.1009	0.0321
MT-A-1-3	0.1930	0.0277	0.0000	**MT-A-4-4**	0.7960	0.1004	0.0000
MT-A-1-4	0.1930	0.0290	-0.0513	**MT-A-4-5**	0.7960	0.1005	-0.0177
MT-A-1-5	0.1930	0.0288	-0.1026	**MT-A-4-6**	0.7960	0.1009	-0.0353
MT-A-2-1	0.3579	0.0526	0.1407	**MT-A-4-7**	0.7960	0.1016	-0.0530
MT-A-2-2	0.3579	0.0525	0.1055	**MT-A-4-8**	0.7960	0.1025	-0.0707
MT-A-2-3	0.3579	0.0499	0.0703	**MT-A-4-9**	0.7960	0.1037	-0.0883
MT-A-2-4	0.3579	0.0482	0.0352	**MT-A-4-10**	0.7960	0.1051	-0.1056
MT-A-2-5	0.3579	0.0476	0.0000	**MT-A-4-11**	0.7960	0.1068	-0.1236
MT-A-2-6	0.3579	0.0477	-0.0132	**MT-A-4-12**	0.7960	0.1088	-0.1413
MT-A-2-7	0.3579	0.0480	-0.0264	**MT-A-4-13**	0.7960	0.1110	-0.1590
MT-A-2-8	0.3579	0.0484	-0.0396	**MT-A-4-14**	0.7960	0.1134	-0.1766
MT-A-2-9	0.3579	0.0489	-0.0528	**MT-A-4-15**	0.7960	0.1155	-0.2099
MT-A-2-10	0.3579	0.0497	-0.0660	**MT-A-4-16**	0.8087	0.1065	0.1044
MT-A-2-11	0.3579	0.0505	-0.0791	**MT-A-6-1**	0.9470	0.1376	0.2288
MT-A-2-12	0.3579	0.0514	-0.0923	**MT-A-6-2**	0.9470	0.1295	0.1606
MT-A-2-13	0.3579	0.0525	-0.1055	**MT-A-6-3**	0.9597	0.1247	0.1044
MT-A-2-14	0.3579	0.0526	-0.1407	**MT-A-6-4**	0.9470	0.1190	0.0321
MT-A-3-1	0.6330	0.0914	0.1882	**MT-A-6-5**	0.9470	0.1186	0.0000
MT-A-3-2	0.6330	0.0891	0.1417	**MT-A-6-6**	0.9470	0.1187	-0.0169
MT-A-3-3	0.6330	0.0852	0.1019	**MT-A-6-7**	0.9470	0.1191	-0.0338
MT-A-3-4	0.6330	0.0816	0.0419	**MT-A-6-8**	0.9470	0.1197	-0.0506
MT-A-3-5	0.6330	0.0865	-0.1167	**MT-A-6-9**	0.9470	0.1205	-0.0675
MT-A-3-6	0.6330	0.0914	-0.1882	**MT-A-6-10**	0.9470	0.1216	-0.0844
MT-A-4-1	0.7960	0.1155	0.2099	**MT-A-6-11**	0.9470	0.1229	-0.1012
MT-A-1-1	0.1930	0.0288	0.1026	**MT-A-6-12**	0.9470	0.1245	-0.1181
MT-A-1-2	0.1930	0.0290	0.0513	**MT-A-6-13**	0.9470	0.1263	-0.1350
MT-A-1-3	0.1930	0.0277	0.0000	**MT-A-6-14**	0.9470	0.1283	-0.1519

Table 7b Honeywell Pressure (HWP) Transducers

Name	x (m)	y (m)	z (m)	Name	x (m)	y (m)	z (m)
HWP-A-1-1	0.2184	0.0308	0.0000	**HWP-A-4-6**	0.8214	0.1081	0.1044
HWP-A-3-1	0.6394	0.0864	0.1067	**HWP-A-4-7**	0.8270	0.1058	-0.0622
HWP-A-3-2	0.6394	0.0826	-0.0495	**HWP-A-4-8**	0.8270	0.1101	-0.1194
HWP-A-3-3	0.6394	0.0864	-0.1067	**HWP-A-5-1**	0.8715	0.1100	-0.0343
HWP-A-3-4	0.6838	0.0946	0.1359	**HWP-A-5-2**	0.8715	0.1130	-0.0914
HWP-A-3-5	0.6838	0.0896	0.0787	**HWP-A-5-3**	0.8715	0.1188	-0.1486
HWP-A-3-6	0.6838	0.0871	-0.0216	**HWP-A-5-4**	0.9159	0.1165	-0.0622
HWP-A-3-7	0.6838	0.0896	-0.0787	**HWP-A-5-5**	0.9159	0.1208	-0.1194
HWP-A-3-8	0.6838	0.0946	-0.1359	**HWP-A-6-1**	0.9470	0.1274	0.1445
HWP-A-3-9	0.7283	0.0971	0.1067	**HWP-A-6-2**	0.9470	0.1232	0.1044
HWP-A-3-10	0.7283	0.0933	-0.0495	**HWP-A-6-3**	0.9470	0.1203	0.0642
HWP-A-3-11	0.7283	0.0971	-0.1067	**HWP-A-6-4**	0.9724	0.1262	0.1044

DISTRIBUTION A: Distribution approved for public release.

HWP-A-4-1	0.7706	0.1106	0.1783	**HWP-G-P-1**	0.2921	0.0000	0.1113
HWP-A-4-2	0.7706	0.0973	0.0000	**HWP-G-P-2**	0.4253	-0.0250	0.1338
HWP-A-4-3	0.7706	0.1106	-0.1783	**HWP-G-S-1**	0.2921	0.0000	-0.1113
HWP-A-4-4	0.7960	0.1050	0.1044	**HWP-G-S-2**	0.4253	-0.0250	-0.1338
HWP-A-4-5	0.7960	0.1023	0.0642	**HWP-G-S-3**	0.4253	0.0250	-0.1338

Table 7c Vatell Thermogauge (TG) Heat Flux

Name	x (m)	y (m)	z (m)	Name	x (m)	y (m)	z (m)
TG-A-2-1	0.3836	0.0552	0.1017	**TG-A-4-4**	0.8271	0.1044	0.0254
TG-A-2-2	0.3836	0.0534	0.0763	**TG-A-5-1**	0.8466	0.1065	0.0000
TG-A-2-3	0.3835	0.0520	0.0508	**TG-A-5-2**	0.8466	0.1068	-0.0254
TG-A-2-4	0.3836	0.0510	0.0254	**TG-A-5-3**	0.8466	0.1076	-0.0509
TG-A-2-5	0.3836	0.0507	0.0000	**TG-A-5-4**	0.8466	0.1090	-0.0763
TG-A-3-1	0.6584	0.0935	0.1526	**TG-A-5-5**	0.8466	0.1109	-0.1017
TG-A-3-2	0.6584	0.0906	0.1271	**TG-A-5-6**	0.8466	0.1133	-0.1271
TG-A-3-3	0.6584	0.0882	0.1017	**TG-A-5-7**	0.8466	0.1163	-0.1526
TG-A-3-4	0.6584	0.0864	0.0763	**TG-A-5-8**	0.8975	0.1143	-0.0622
TG-A-3-5	0.6584	0.0850	0.0509	**TG-A-5-9**	0.8975	0.1186	-0.1195
TG-A-3-6	0.6584	0.0841	0.0254	**TG-A-6-1**	0.9731	0.1353	0.1779
TG-A-3-7	0.6584	0.0838	0.0000	**TG-A-6-2**	0.9731	0.1228	0.0508
TG-A-3-8	0.6584	0.0841	-0.0254	**TG-A-6-3**	0.9731	0.1220	0.0254
TG-A-3-9	0.6584	0.0850	-0.0509	**TG-A-6-4**	0.9731	0.1218	0.0000
TG-A-3-10	0.6584	0.0864	-0.0763	**TG-A-6-5**	0.9731	0.1220	-0.0254
TG-A-3-11	0.6584	0.0882	-0.1017	**TG-A-6-6**	0.9731	0.1228	-0.0508
TG-A-3-12	0.6584	0.0906	-0.1271	**TG-A-6-7**	0.9731	0.1242	-0.0763
TG-A-3-13	0.6584	0.0935	-0.1526	**TG-A-6-8**	0.9731	0.1261	-0.1017
TG-A-3-14	0.7092	0.0948	0.1068	**TG-A-6-9**	0.9731	0.1285	-0.1271
TG-A-3-15	0.7092	0.0910	-0.0496	**TG-A-6-10**	0.9731	0.1316	-0.1525
TG-A-3-16	0.7092	0.0948	-0.1068	**TG-A-6-11**	0.9731	0.1352	-0.1779
TG-A-4-1	0.8220	0.1168	0.1779	**TG-A-4-4**	0.8271	0.1044	0.0254
TG-A-4-2	0.8220	0.1046	0.0508				

Table 7d CUBRC Thin Film (TF) Sensors

Name	x (m)	y (m)	z (m)	Name	x (m)	y (m)	z (m)
TF-A-2-1	0.3706	0.0497	-0.0330	**TF-A-4-4**	0.8087	0.1046	-0.0795
TF-A-2-2	0.3706	0.0502	-0.0461	**TF-A-4-5**	0.8087	0.1059	-0.0971
TF-A-2-3	0.3706	0.0508	-0.0594	**TF-A-4-6**	0.8087	0.1075	-0.1148
TF-A-2-4	0.3706	0.0516	-0.0725	**TF-A-4-7**	0.8087	0.1093	-0.1325
TF-A-2-5	0.3706	0.0524	-0.0857	**TF-A-4-8**	0.8087	0.1114	-0.1501
TF-A-2-6	0.3706	0.0534	-0.0989	**TF-A-4-9**	0.8087	0.1137	-0.1678
TF-A-3-1	0.6330	0.0816	-0.0419	**TF-A-4-10**	0.8087	0.1163	-0.1855
TF-A-3-2	0.6330	0.0821	-0.0544	**TF-A-6-1**	0.9597	0.1204	-0.0253
TF-A-3-3	0.6330	0.0828	-0.0669	**TF-A-6-2**	0.9597	0.1209	-0.0423
TF-A-3-4	0.6330	0.0835	-0.0793	**TF-A-6-3**	0.9597	0.1216	-0.0591
TF-A-3-5	0.6330	0.0844	-0.0918	**TF-A-6-4**	0.9597	0.1225	-0.0759
TF-A-3-6	0.6330	0.0854	-0.1042	**TF-A-6-5**	0.9597	0.1237	-0.0928

DISTRIBUTION A: Distribution approved for public release.

TF-A-3-7	0.6330	0.0878	-0.1292	**TF-A-6-6**	0.9597	0.1252	-0.1097
TF-A-3-8	0.6330	0.0891	-0.1417	**TF-A-6-7**	0.9597	0.1269	-0.1266
TF-A-3-9	0.6330	0.0917	-0.1625	**TF-A-6-8**	0.9597	0.1288	-0.1434
TF-A-4-1	0.8087	0.1022	-0.0265	**TF-A-6-9**	0.9597	0.1310	-0.1603
TF-A-4-2	0.8087	0.1028	-0.0442	**TF-A-6-10**	0.9597	0.1334	-0.1773
TF-A-4-3	0.8087	0.1036	-0.0618	**TF-A-6-11**	0.9597	0.1361	-0.1940

Table 7e Ahmic Skin Friction (SF) Gauges

Name	x (m)	y (m)	z (m)	Name	x (m)	y (m)	z (m)
SF-A-3-1	0.6838	0.0930	0.1207	**SF-A-5-1**	0.8715	0.1105	-0.04949
SF-A-3-2	0.6838	0.0906	0.0927	**SF-A-5-2**	0.8715	0.1120	-0.07744
SF-A-3-3	0.6838	0.0875	-0.0368	**SF-A-5-3**	0.8715	0.1142	-0.10539
SF-A-3-4	0.6838	0.0887	-0.0648	**SF-A-5-4**	0.8715	0.1170	-0.13335
SF-A-3-5	0.6838	0.0906	-0.0927	**SF-A-6-1**	0.9597	0.1271	0.12845
SF-A-3-6	0.6838	0.0930	-0.1207	**SF-A-6-2**	0.9597	0.1228	0.08028
SF-A-4-1	0.8214	0.11039	0.12845				
SF-A-4-2	0.8214	0.10619	0.08028				

Table 7f Ahmic Thermocouple Sensors

Name	x (m)	y (m)	z (m)	Name	x (m)	y (m)	z (m)
RTD-A-3-1	0.6838	0.0930	0.1207	**RTD-A-5-1**	0.8715	0.1105	-0.0495
RTD-A-3-2	0.6838	0.0906	0.0927	**RTD-A-5-2**	0.8715	0.1120	-0.0774
RTD-A-3-3	0.6838	0.0875	-0.0368	**RTD-A-5-3**	0.8715	0.1142	-0.1054
RTD-A-3-4	0.6838	0.0887	-0.0648	**RTD-A-5-4**	0.8715	0.1167	-0.1334
RTD-A-3-5	0.6838	0.0906	-0.0927	**RTD-A-6-1**	0.9597	0.1271	0.1285
RTD-A-3-6	0.6838	0.0930	-0.1207	**RTD-A-6-2**	0.9597	0.1228	0.0803

Table 7g PCB High Frequency Pressure Sensors

Name	x (m)	y (m)	z (m)	Name	x (m)	y (m)	z (m)
PCB-A-5-1	0.8842	0.1178	0.1264	**PCB-A-5-3**	0.8842	0.1111	0.0091
PCB-A-5-2	0.8842	0.1135	0.0773	**PCB-A-5-4**	0.8923	0.1151	0.0854

4.6 PDR AND CDR

The preliminary design review (PDR) was completed virtually on June 17 – 19, 2020 due to COVID. The review included nominally 100 participants from government, academia, and industry. The PDR was completed with the successful response to the request for actions as described in Appendix A.

The critical design review (CDR) was completed on Oct. 28, 2020. The review included nominally 100 participants from government, academia, and industry. The PDR was completed with the successful response to the request for actions as described in Appendix B. The 1.0-m configuration, flow field analyses, thermal analysis, materials selection, and instrumentation layouts described above was considered closed as the final design. Hence, Task 1 in Table 1 was considered completed.

DISTRIBUTION A: Distribution approved for public release.

4.7 *Risks and Risk Mitigation*

4.7.1 Flight System Risks

The NSROC and NASA Wallops team successfully completed the project Design Review for Flight: 46.027 Holden Flight. The details from that review are available in reports from NASA to AFOSR.

4.7.2 Research Geometry Risks

The risk introduced at the PDR and closed at the CDR are listed below, with the deemed acceptable mitigations.

- Instrumentation
  - Risk: Manufacturing delays (COVID and otherwise)
  - Impact: Flight Delay
  - Mitigation: Most orders were accomplished (MedTherms: Jan 2020, Endevcos: July 2020, Vatells: Sept 2020, Skin Friction Gauges: Sept 2020, and PCB: Oct 2020
  - Likelihood: Unlikely.
- Ground Test
  - Damage risk during ground test
  - Impact: Flight Delays and Cost
  - Mitigation: CUBRC research team and surplus of sensors
  - Likelihood: Unlikely
- Facility Delay
  - Impact: Flight Delay
  - Mitigation: Decision on go/no-go by AFOSR
  - Likelihood: Unlikely
- Side B oxidation of integrated trip (leading edge and top)
  - Impact: Compromise Side B experiment
  - Mitigation: Examining oxidation of 410 SS
  - Likelihood: Unlikely

4.7.3 Science Mission Risks

Transition not occurring on the test article during flight and meeting the aggressive timeline were considered the primary risks. The following risk reduction steps were taken:

1. A carefully selected research team was assembled specifically to address these risks. We believe this team had the experience to perform and interpret the appropriate ground test measurements and simulations to provide the best possible decisions with respect to developing the flight hardware.
2. A fully integrated research approach was developed that utilizes the latest tools in simulation and experimentation, with sufficient redundancy.

DISTRIBUTION A: Distribution approved for public release.

3. We employed highly trained students and research staff. The TAMU Students include post-docs (stability simulations) and graduate students (experiments).
4. We employed in-house capabilities at CUBRC and TAMU to manufacture all test articles. The manufacturing capabilities are listed in Section 4.
5. The primary experimental facilities were at TAMU and CUBRC for this effort.
6. We continued collaborations with JHUAPL BOLT team, who provided scientific support and lessons learned and advice.

DISTRIBUTION A: Distribution approved for public release.

5. Research Results – Task 2 Develop the Flight Research Hardware

After successful completion of the CDR, the began construction of the hardware. This task involved detailed collaborations between TAMU, CUBRC, and AFRL. This section outlines the manufacturing process, tolerances, and instrumentation of the flight geometry.

5.1 Manufacture the Flight Research Vehicle

The flight geometry was fabricated at CUBRC under the direction of A. Dufrene and T. Wadhams. The assembled test article is shown in Fig. 46. Material selection and thermal analysis indicated a flush nose to body joint was ideal, and, as during flight, would result in a small aft-facing step with minimal influence on boundary layer transition. Hence, the joint was machined smooth as shown in Fig. 47. Integral trips were machined into Side B (companion NASA study), as shown in Fig. 48. Mounting holes for 301 different instruments were machined into the body, as well as mounts for four embedded thermocouples into the nose. Mounting features for most of the instrumentation boards and PCB acquisition system were also included. Internal photos of Side A and B are shown below in Figs. 49 and 50, respectively. Fig. 51 shows the nose attachment joint, and Fig. 32 shows the aft attachment bulkhead. Lastly, the tungsten mass is shown in Fig.53. All external surfaces were polished to a 32-microinch finish or better and joints are blended to a smooth interface Nose to body joint was extremely smooth, less than 0.001”, and all gutter side interfaces have steps on the order of 0.001” or better. Gauge positions were machined to a tolerance of ±0.003”. There were couple of programming/setup errors which resulted in out of tolerance gauge positions. These positions were included in the master instrumentation spreadsheets.

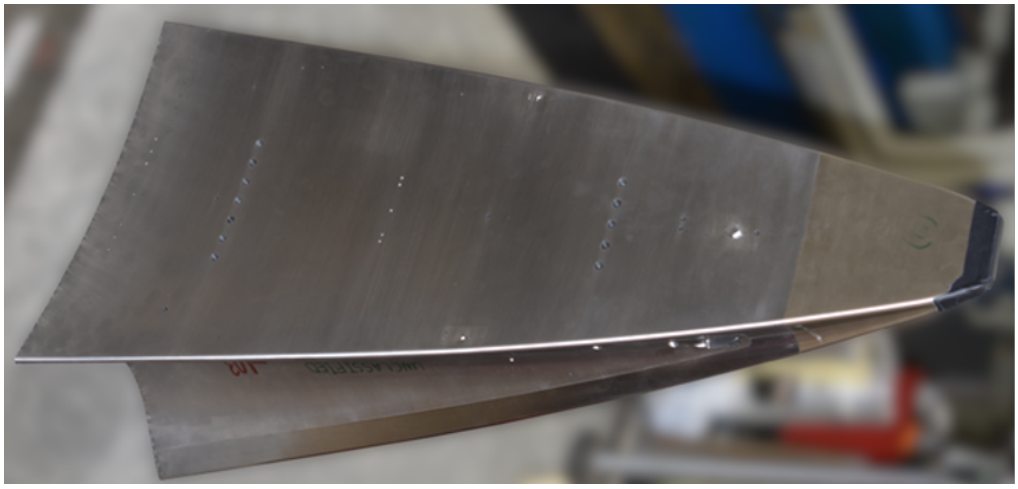

Fig. 46 Assembled Flight Vehicle

DISTRIBUTION A: Distribution approved for public release.

Fig. 47 Flight Vehicle Nose/Body Joint

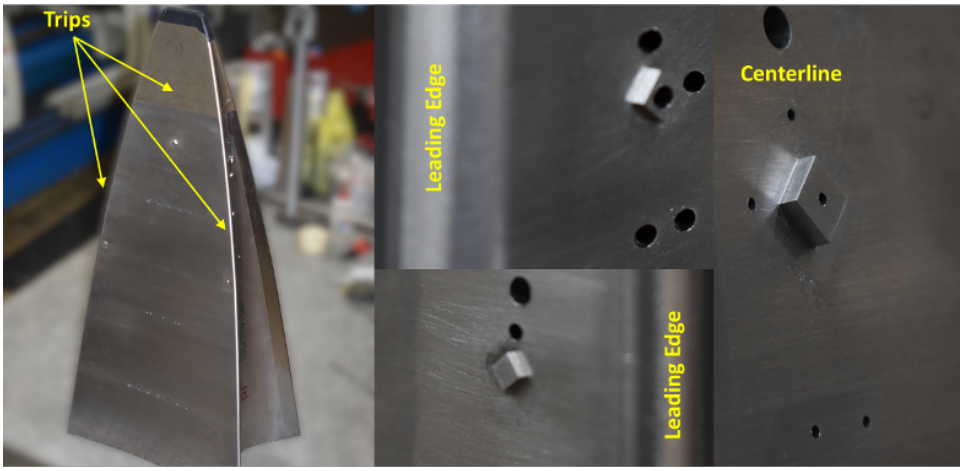

Fig. 48 Side B Trips

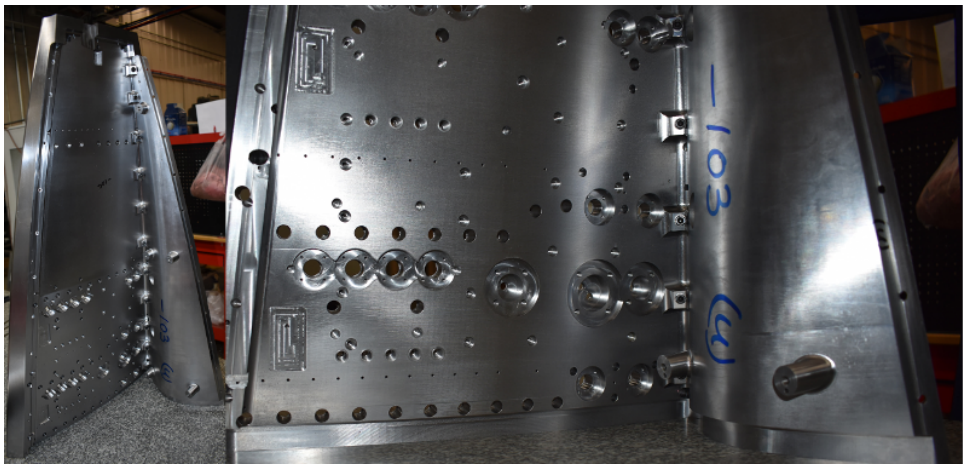

Fig. 49 Internal Side A Photographs

DISTRIBUTION A: Distribution approved for public release.

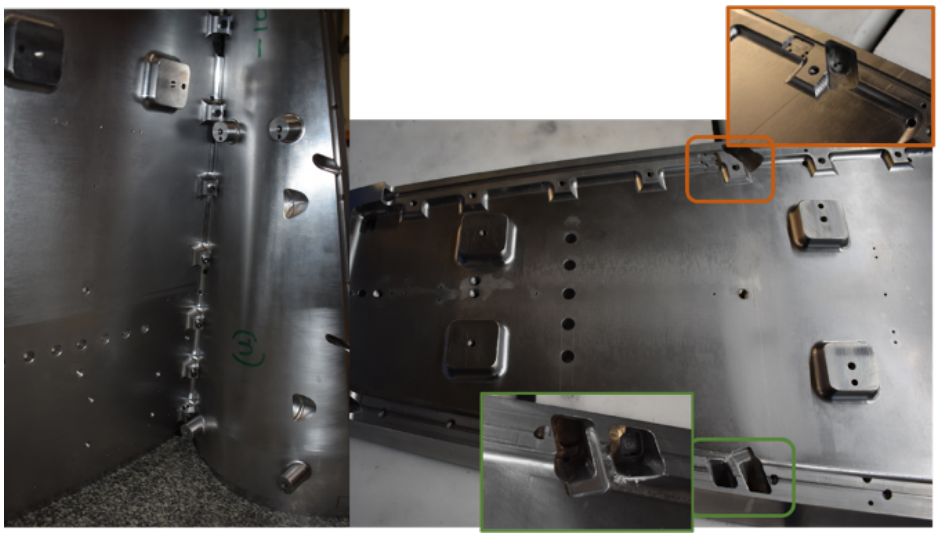

Fig. 50 Internal Side B Photographs

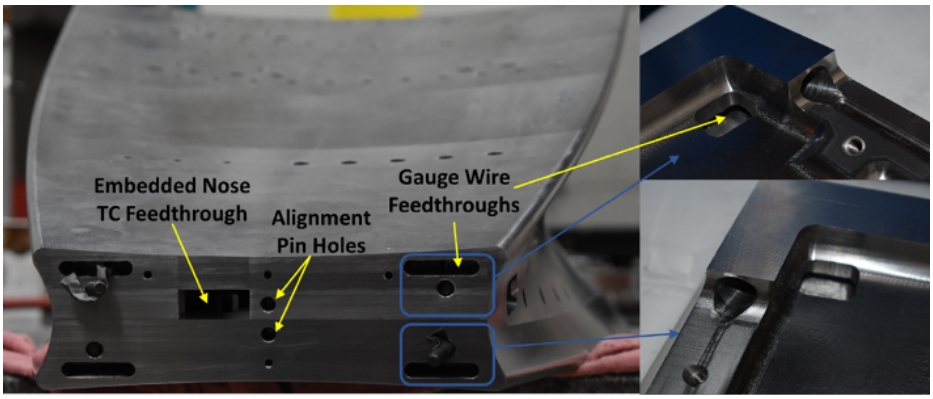

Fig. 51 Nose Attachment Photographs

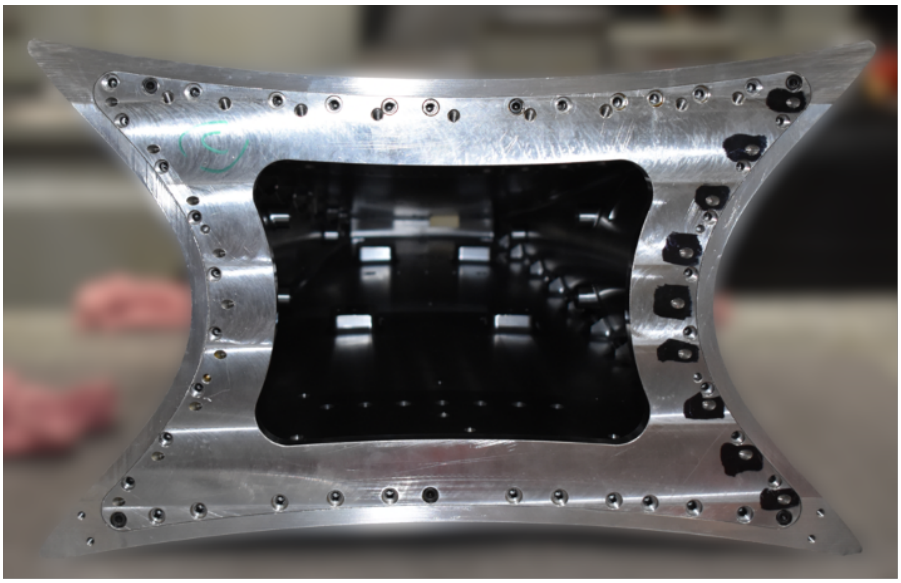

Fig. 52 Aft Bulkhead

DISTRIBUTION A: Distribution approved for public release.

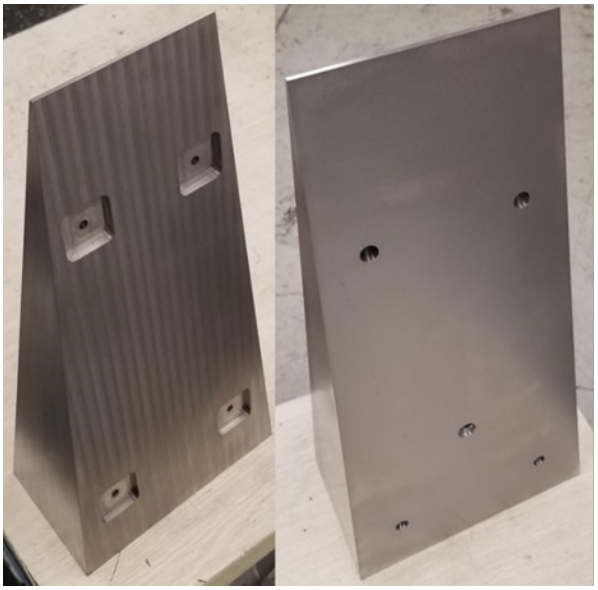

Fig. 53 Tungsten Ballast Mass (260 lb.)

5.2 INSTRUMENT THE FLIGHT RESEARCH VEHICLE

Installation of the flight instrumentation, flight computers, and data acquisition cards was completed by AFRL and CUBRC under the direction of D. Adamczak at AFRL and A. Dufrene. The instruments were listed earlier in Table 6. The final instrumentation suite with telemetry is listed in Table 8 (Adamczak). Sketches and photographs of the hardware are shown in Figs. 54 and 55, respectively. Three channels of 15 Mbs of telemetry were utilized. The high-speed data acquisition included 4 PCB boards to onboard process FFTs into serial data, which then transmitted the top 20 amplitude peaks every 9.2 msec, 13 digital signal processing (DSP) boards, and 26 sensor collection boards. At the time of this writing, dissemination of additional detail on the flight instrumentation was restricted.

Table 8 Instrumentation Telemetry

Instrument	DAQ Channels	Telemetry (bps)
Medtherm Thermocouple	192	1,843,200
Honeywell Mean Pressure	39	374,400
PCP RMS Pressure	24	21,888,000
Vatell Heat Transfer	60	2,764,800
CUBRC Thin Film	50	12,000,000
Ahmic Skin Friction	14	336,000
Ahmic Temperature	14	134,400
Acceleration	5	600,000
Payload Sensors	11	105,600
High-Speed PCB	0	705,810
Totals	**409**	**40,752,210**

DISTRIBUTION A: Distribution approved for public release.

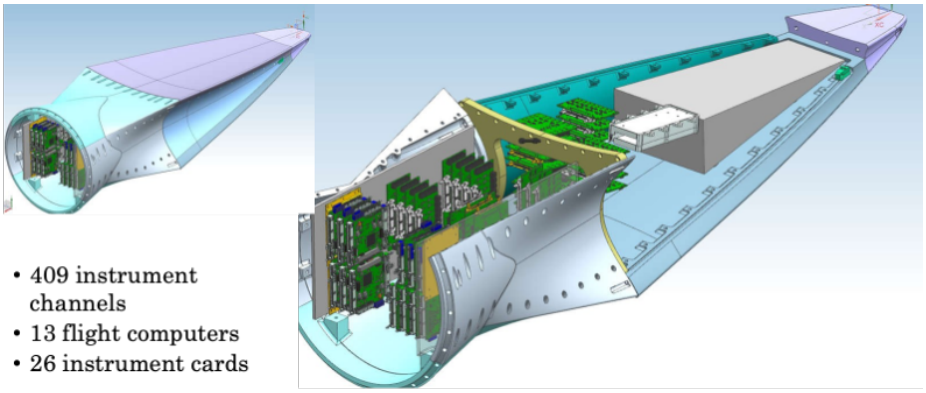

Fig. 54 Schematic of Flight Geometry with Instrumentation.

Fig. 55 Photographs of the flight hardware with instrumentation.

5.3 Ground Test of Flight Geometry in LENS II

The flight hardware was tested in LENSII with the flight instruments (Portoni and Dufrene 2023). The Mach number was set to 5.3, and three Reynolds numbers were tested. The flow conditions are summarized in Table 9. A photograph of the model in the tunnel is given in Fig. 56. Example results are plotted in Figs. 57 – 60. These data show good agreement with accompanying CFD for both laminar and turbulent flow. Comparison with flight data allows for verification of ground tests and simulations, as well tunnel effects on transition. For example, see the skin friction sensors across the ground and flight test in Fig. 61 (Meritt *et al.* 2024). These data also agreed with flight and subscale tests in the ACE tunnel.

DISTRIBUTION A: Distribution approved for public release.

Table 9 CUBRC Test Conditions

Run Condition	Run 01	Run 02	Run 03
Mach Number	5.33	5.29	5.30
Density (kg/m3)	0.152	0.059	0.032
Pressure (Pa)	9,816	3,529	1,945
Velocity (m/s)	1,604	1,536	1,545
Temperature (K)	225	209	211
Reynolds Number (×106/m)	15.5	6.07	3.32

Figure 56. Photograph of BOLT II Flight Geometry in CUBRC LENS II.

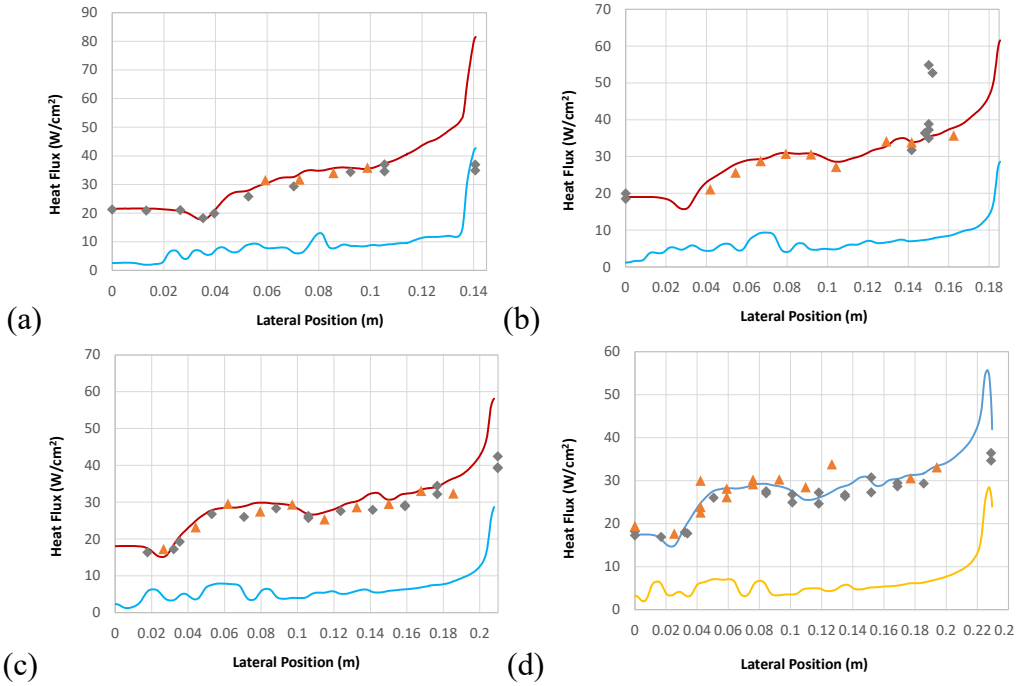

Figure 57. Example heat flux data for Run 01 (Re/m = 15.5x10^6, Table 8). (a) x/L = 0.36 (Red line: Turbulent CFD, Blue line: Laminar CFD). (b) x/L = 0.63 (Red line: Turbulent CFD, Blue line: Laminar CFD). (c) x/L = 0.80 (Red line: Turbulent CFD, Blue line: Laminar CFD). (d) x/L = 0.95 (Blue line: Turbulent CFD, Yellow line: Laminar CFD).

DISTRIBUTION A: Distribution approved for public release.

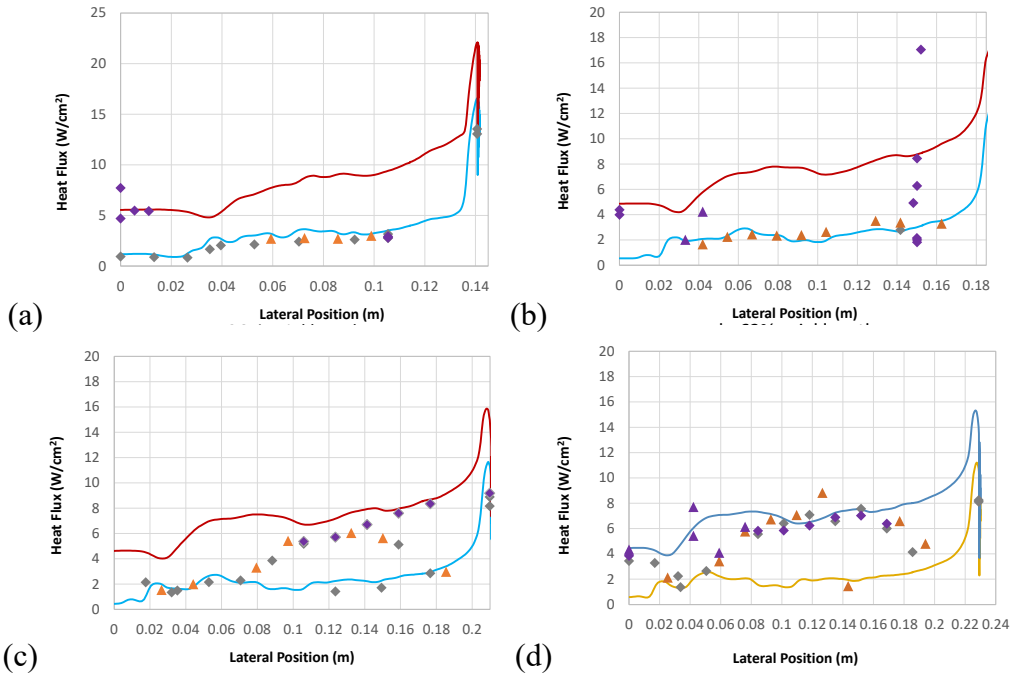

Figure 58. Example heat flux data for Run 03 (Re/m = 3.3x10^6, Table 8). (a) x/L = 0.36 (Red line: Turbulent CFD, Blue line: Laminar CFD). (b) x/L = 0.63. (c) x/L = 0.80. (d) x/L = 0.95 (Blue line: Turbulent CFD, Yellow line: Laminar CFD).

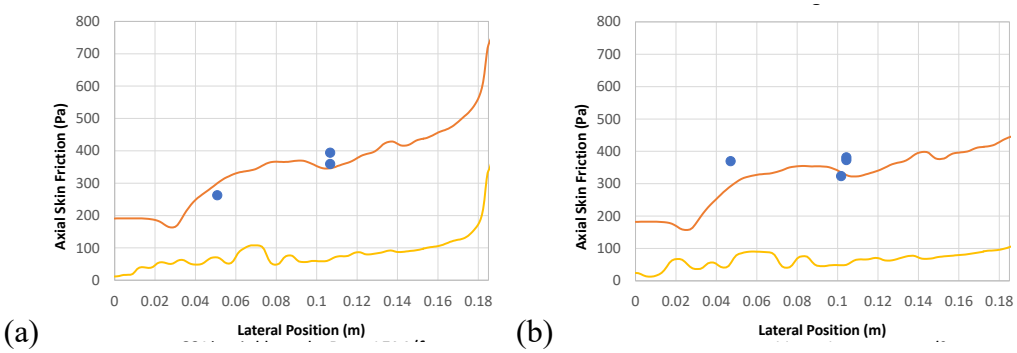

Figure 59. Example skin friction data for Run 01 (Re/m = 15.5x10^6, Table 8). (a) x/L = 0.63 (Orange line: Turbulent CFD, Yellow line: Laminar CFD). (b) x/L = 0.80.

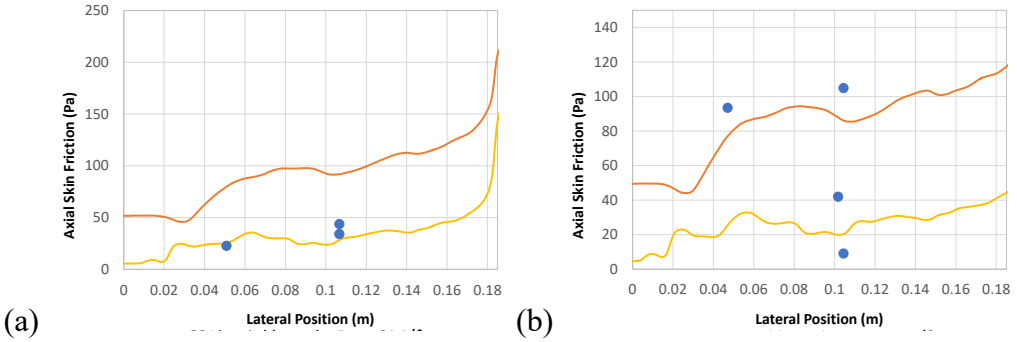

Figure 60. Example skin friction data for Run 03 (Re/m = 3.3x10^6, Table 8). (a) x/L = 0.63 (Orange line: Turbulent CFD, Yellow line: Laminar CFD). (b) x/L = 0.80.

DISTRIBUTION A: Distribution approved for public release.

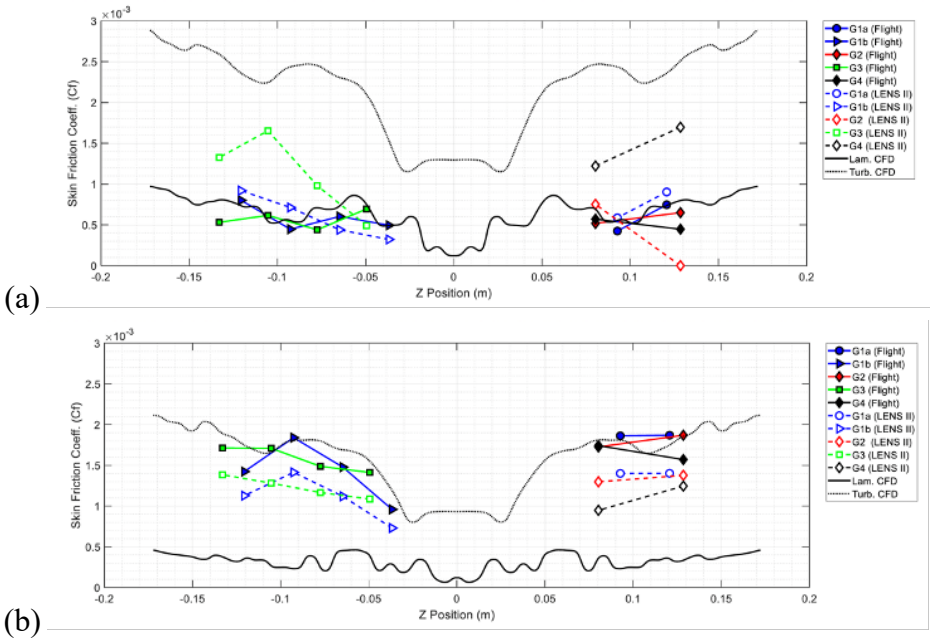

Figure 61. Example skin friction data for ground and flight test (Meritt *et al.* 2024). (a) Runs 01 (*Re*/m = 15.5x10^6, Table 7). (b) Runs 01 (*Re*/m = 3.3x10^6, Table 8).

5.4 Integration of the Flight Geometry with NASA Payload System

The payload integration system was constructed by NASA and NSROC. The integration of the flight test hardware was performed by NASA and the AFRL. The flight readiness tests were performed by NASA, NSROC, and AFRL, which include vibration, mass properties, spin balance, and sequence testing. A photograph of the hardware at NASA Wallops during this process is provided in Fig. 62.

Figure 62. Photographs of the BOLT II payload spin test.

DISTRIBUTION A: Distribution approved for public release.

6. Research Results – Task 3 Flight Experiment and Data Analysis

The flight experiment was successfully executed on March 21, 2022. A photograph of the flight experiment is provided in Fig. 63. This section describes the flight data, data reduction, and post flight results.

Figure 63. Photograph of the BOLT II flight.

6.1 Flight Experiment Summary

The AFOSR also enlisted the MURI HYFLITS Balloon atmospheric measurement team, as well as the ground-based NASA high altitude LiDAR atmospheric sensing (HALAS) team, to provide atmospheric measurements before and after the flight. These data were used by the AFRL to establish a best estimate of the atmosphere for data reduction, which are shown in Fig. 64. The incidence angles are defined in Fig. 65. Traces of the measured incidence angles are provided in Fig. 66. Note, that the full trajectory data are not presented to protect sensitivities with the rocket system. The Mach number was nominally 6.0 during the main portion of the test on descent. The mission success test windows were defined such that the Mach number was greater than 5.0. The test windows were:

- Ascent: M = 5.0 – 6.4 (±3.5%), *Re*/m = 0.2 – 17.0x10^6 (±6.0%), $|\alpha|<1.0$, $|\beta|<1.0$
- Descent: M = 5.1 – 6.1 (±3.5%), *Re*/m = 0.2 – 45.0x10^6 (±6.0%), $|\alpha|<1.0$, $|\beta|<1.0$

These test conditions met or exceeded the mission requirements in terms of both the hypersonic test window and the incidence angles. Even though the incidence angles were small, they were accounted for in the data reduction.

DISTRIBUTION A: Distribution approved for public release.

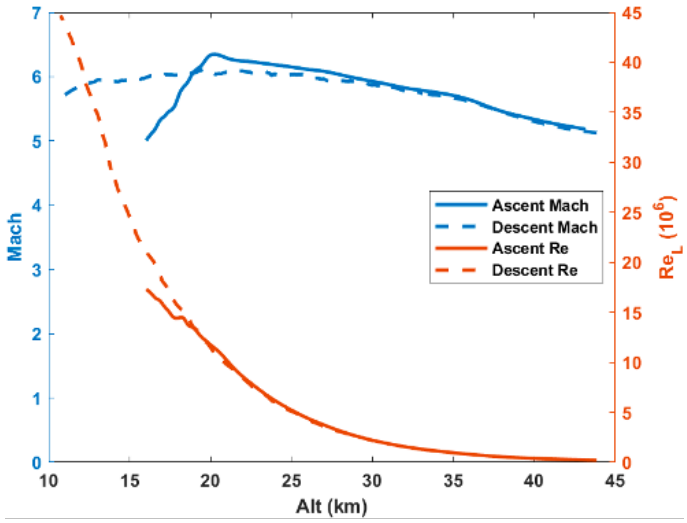

Figure 64. Flight trajectory test windows.

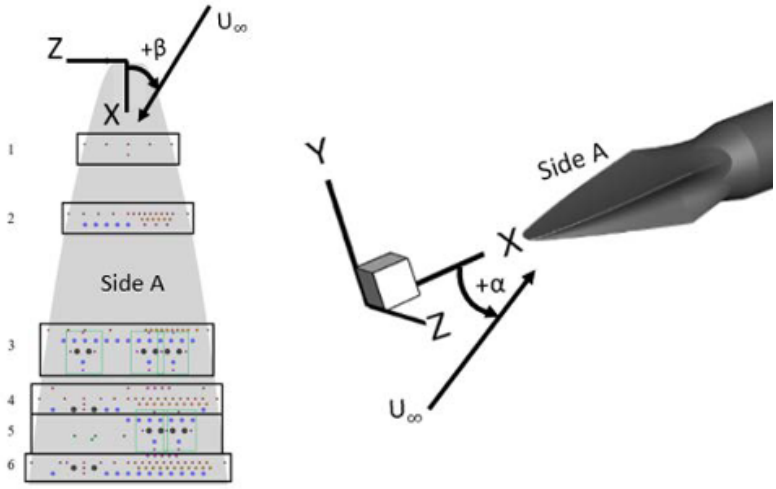

Figure 65. Vehicle attitude definitions.

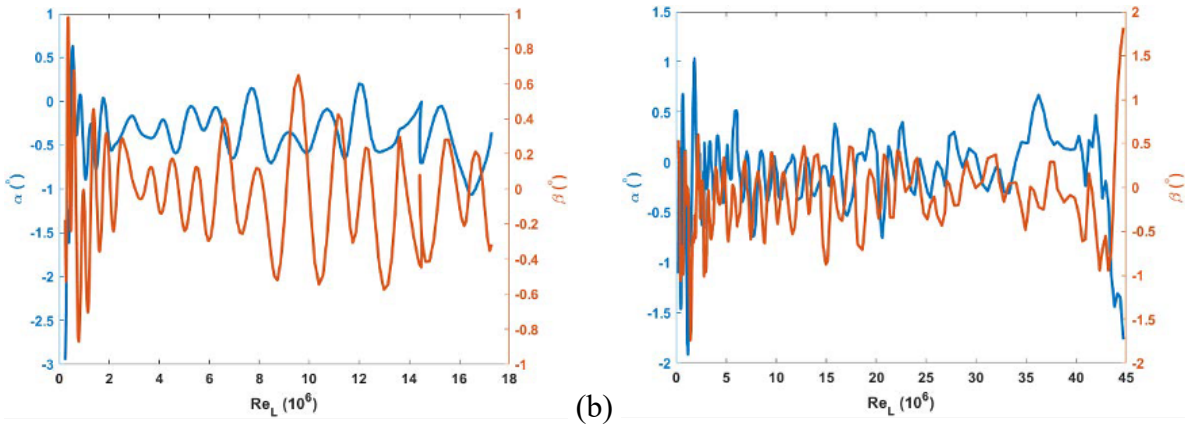

(a) (b)

Figure 66. Angle of attack and yaw angle variations during test windows. (a) Ascent. (b) Descent.

DISTRIBUTION A: Distribution approved for public release.

6.2 BOLT II FLIGHT DATA

The data presented in this Section were the primary focus of the TAMU PhD dissertation of 2LT John Wirth (Wirth 2023) under the direction of R. Bowersox. The results are also summarized in Wirth *et al.* (2023a, 2023b, 2024) and Wirth and Bowersox (2024).

6.2.1 DATABASE SUMMARY

The full data set (400MB in .csv format) was delivered to AFOSR. The full and active instrumentation suite on Side A are listed in Table 10. The instrumentation layout, shown earlier in Fig. 44a and Table 7 in Section 4.5, was organized into rows to track transition mechanisms, turbulence evolution, and the upstream initial conditions flowing into the downstream turbulent region. The sparse upstream sensor arrays were designed to track the sweeping motions of the heat streak due to potential variations in yaw and angle-of-attack, e.g., see Fig. 45c in Section 4.5. The flight experience minimal angle-of-attack and yaw during flight. Hence, these sensors were only used to provide additional heating. The dense sensor arrays in the aft four rows were used to collect detailed temperature, heat flux, skin friction, pressure, and pressure fluctuation data. The data analyses for the remainder of this report were limited to the aft sections, as shown in Fig. 67.

Table 10 Summary of Active Flight Sensors

Instrument	Purpose	Quantity	Flight Active
Medtherm TCS-061-EE (MT)	Temperature, Heat Transfer	116	99
Vatell TG-2000 (TG)	Heat Transfer	45	44
Honeywell 19CO15PA2K (HWP)	Static Pressure	29	28
PCB-112 (PCB)	Pressure Fluctuations (RMS)	12	0
CUBRC Thin Film Heat Flux (TF)	Turbulent Spots	38	-
Ahmic Skin Friction Sensors (SF)	Skin Friction	14	14
Ahmic RTD	Skin Friction Temperature	14	-
Endevco Accelerometers (ACC)	Acceleration	5	5
PCB-132B	Surface Pressure Spectra	4	4

DISTRIBUTION A: Distribution approved for public release.

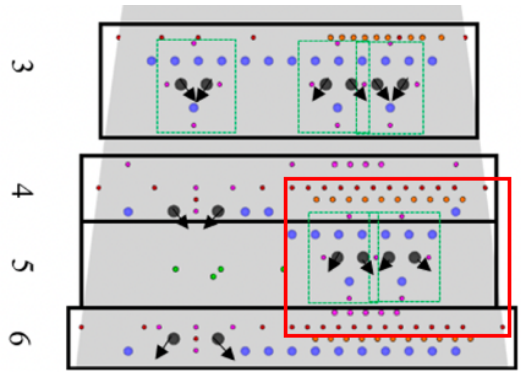

Figure 67. Dense instrumentation reduction. Arrows show skin friction gauge alignment and the red box outlines region for 3-D thermal reconstruction from the MT sensors (small red dots); the sensor key was shown earlier in Fig. 44a).

The Medtherm (MT) thermocouples were found to provide the reliable flux data. For most sensors, the results were independent of the data reduction method. The leading-edge region was the exception due to large spanwise temperature gradients. Key advantages were small diameter, good stability, and fast response, and no apparent drift. The MT temperature sensors ranged between 10°C and 600°C. A criterion was established such that if 50% of the data points measured temperatures were outside of the sensor limits, the data from that sensor was removed. Upon closer inspection, this revealed five sensors that did not respond at all and nine corrupt sensors that could not be corrected. The preliminary heat flux analysis identified an additional three sensors that, although they matched the temperatures of the surrounding sensors before launch and between test windows, did not measure a change in temperature during the test windows. These 17 sensors were removed from the 116 exterior (front-face) and interior (back- face) MT sensors on side A, leaving 99 that were considered for the 3D analysis. After the full, 3D analysis, it was found that sensor MT-A-4-11F failed when $Re_L = 25 \times 10^6$. The final analysis included this sensor up to that point but removed it to extend the heat flux results to the $Re_L = 45 \times 10^6$.

The Vatell thermogauge (TG) sensors directly measured heat fluxes between 0 and 1000 W. Unfortunately, these sensors experienced drift during the experiment. To help remove the drift, the sensors were zeroed prior to take-off and re-zeroed at apogee (out of the atmosphere) before the descent window when the heat flux was known to be zero as there was no freestream flow.

The Ahmic skin friction (SF) sensors measured skin friction values in the range of 0 to 700 Pa. The sensors experienced mild drift during the experiment. Temperature sensors RTD were embedded in the sensors but proved to be unnecessary. The sensors were zeroed before launch and before descent to remove drift. Additionally, the sensors were installed in pairs at a 45-degree angle with respect to the x-axis and 90 degrees to each other, to help detect crossflow.

The Honeywell pressure (HWP) and PCB-132B data were reported without alteration. The HWP data were converted into pressure through in-situ calibration. These results proved reliable and verified the small angle-of-attack observed by NASA sensors. Four PCB132B sensors were located on the positive z half of side A. One was planned to resolve the near-centerline vortex, and three were in the mixed-mode region. The PCB132B sensors were sampled at 2.5 MHz and converted to power spectral densities (PSDs) onboard. Due to bandwidth limitations, the top twenty frequencies and their relative amplitudes were telemetered off the vehicle at 213 Hz. These sensors

DISTRIBUTION A: Distribution approved for public release.

allowed the transition mechanisms to be tracked and characterized during the BOLT II flight. Unfortunately, the PCB112 sensors did not provide data and the CUBRC heat flux sensors were analyzed separately, as were the Ahmic RTD sensors.

6.2.2 Data Reduction Methods

Several methods were used to convert the MT data to heat flux. The Cook-Felderman (1966) (CF) technique was found to be preferred over most of the vehicle due to its simplicity and the minimal amount of required input data. The method, shown in Eq. (3), is a solution, not a numerical approximation, to the heat equation assuming a 1D, semi-infinite domain, and requires only the surface temperature at a point.

$$q(t_n) = 2\sqrt{\frac{k\rho c_p}{\pi}} \sum_{j=1}^{n} \frac{T_j - T_{j-1}}{\sqrt{t_n - t_j} + \sqrt{t_n - t_{j-1}}} \tag{3}$$

Multi-dimensional heat flux analyses were also developed and used to account for lateral heat conduction. The MT sensors provided temperature measurements on the exterior and interior surfaces of the frustum, which were used as boundary conditions to the heat conduction equation throughout the frustum during the flight. Hence, a 3-D subsection of the frustum, outlined in red in Fig. 67, was simulated across the trajectory, where the MT and TG sensors provided boundary conditions. The heat flux was then computed from the material temperature gradients at the surface. The 3-D solution (Q3D) employed a transient, finite element method on a tetrahedral mesh (Wirth and Bowersox 2022). The material properties as a function of temperature were considered. The number of sensors used are summarized in Table 11.

Table 11 Number of Sensors used in the 3-D Heat Flux Domain.

Sensor	Count
MT (Exterior)	17
MT (Interior)	19
TG	5
TF	6

Two-dimension (2-D) solutions were also computed. The comparison between methods favored the Cook-Felderman technique away from the leading-edge. In the 2-D method, mesh refinement was found to primarily affect the temporal response. The most refined mesh was set to a node spacing of 1.0 mm, which was below the MT sensor diameter. A typical comparison with grid convergence is shown in Fig. 68. The CF results are in excellent agreement with grid converged 2-D results and data from a nearby Vatell TG sensor, which provided a direct measurement of the heat flux. For all sensors, except the leading-edge-adjacent sensors, CF agreed with the 2-D method to within 3 W/cm^2. Under turbulent conditions, the CF results differed from the 2-D by 4%, with a standard deviation of 3%. The heat flux was also shown to be independent of the dimensionality of the data reduction method. However, the measured MT boundary conditions were also too sparce in the axial direction to adequately capture axial conduction, which was expected

DISTRIBUTION A: Distribution approved for public release.

to be relatively small. Hence. all presented heat flux data were grid converged and independent of the data reduction method0. The exception is the leading-edge sensors, where lateral conduction was important (discussed below), which resulted in error with the 1-D methods.

After conversion to heat flux, Stanton number was defined in Eq. (4) using the freestream total temperature since the adiabatic wall temperature was not measured in flight.

$$St = \frac{q}{\rho U c_p (T_0 - T_w)} \tag{4}$$

Also, $\rho = \rho_\infty$ (atmospheric condition) and $U = U_\infty$ (flight velocity).

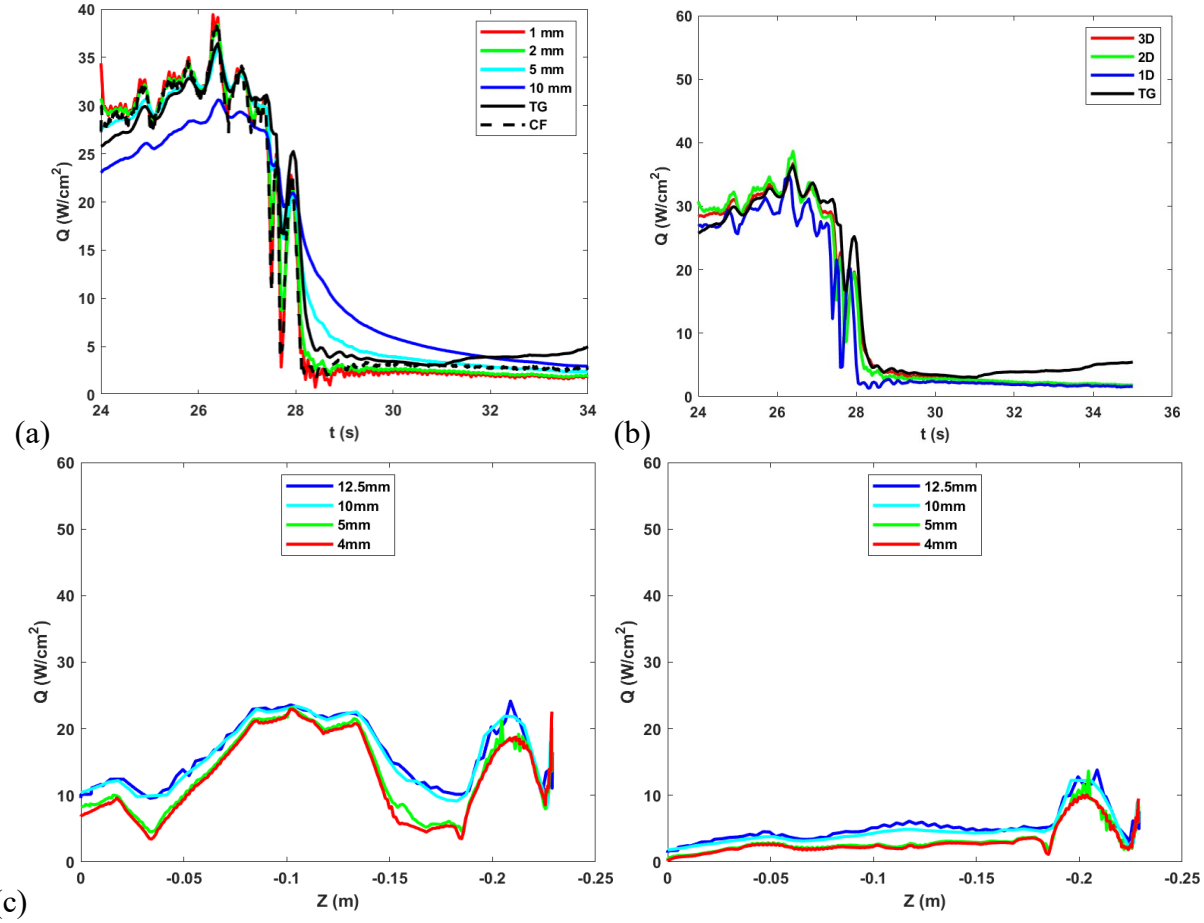

Figure 68. Representative heat flux data reduction comparisons (Wirth *et. al.* 2024). (a) CF and 2-D solutions for varying mesh sizes for the MT-A-6-14 sensor during descent; TG-A-6-10 sensor heat flux data are shown for comparison. (b) Dimensional effects on MT heat flux. (C) 3-D grid convergence study for the eat flux slices over the row 6 MT sensors during ascent.

A moving average applied over a 0.01 second window was applied to all MT, TG, and SF sensor data analyzed herein, which matched the 100 Hz low-pass filter applied to the MT sensors. An example snapshot of the available data is provided in Fig. 69. These figures show the high quality of the data. The uncertainties were listed earlier. The data in the top left (pink outlined

DISTRIBUTION A: Distribution approved for public release.

panel) compares the mean pressure (HWP sensor) on the front and back surfaces, confirming the small incidence angles mentioned earlier. The skin friction traces are plotted in the top right panel (black). These traces show the transition process starting with sensor 3 (third from the left) to sensor 4, then 2, and then 3 (which was near the centerline). These data suggested that transition occurred first in the mixed-mode region as indicated in the TAMU quiet tunnel ground test results. The heat flux data in the bottom left panel follow the same trend. The PCD data show the spectral modes leading to transition. Sensor 1, left most, shows a 700-800 frequency band consistent with second mode instabilities associated with the thin boundary layer in that region. At this instant, sensor 2, the next one in from the left, did not show signs of an instability. Note that sensor 4, behind and the left of sensor 2, did show an instability near 400 kHz, which may have been a secondary instability within the mixed-mode region. As described in Section 4.2, this instability would be highly localized within a vortex streak. Sensor 3, near the center- line, showed a 100-200 frequency, which likely indicates a 2-D second mode instability in a region with a thick boundary layer. In summary, this quick look suggests that the data are of high quality. A more detailed analysis is provided in later sections.

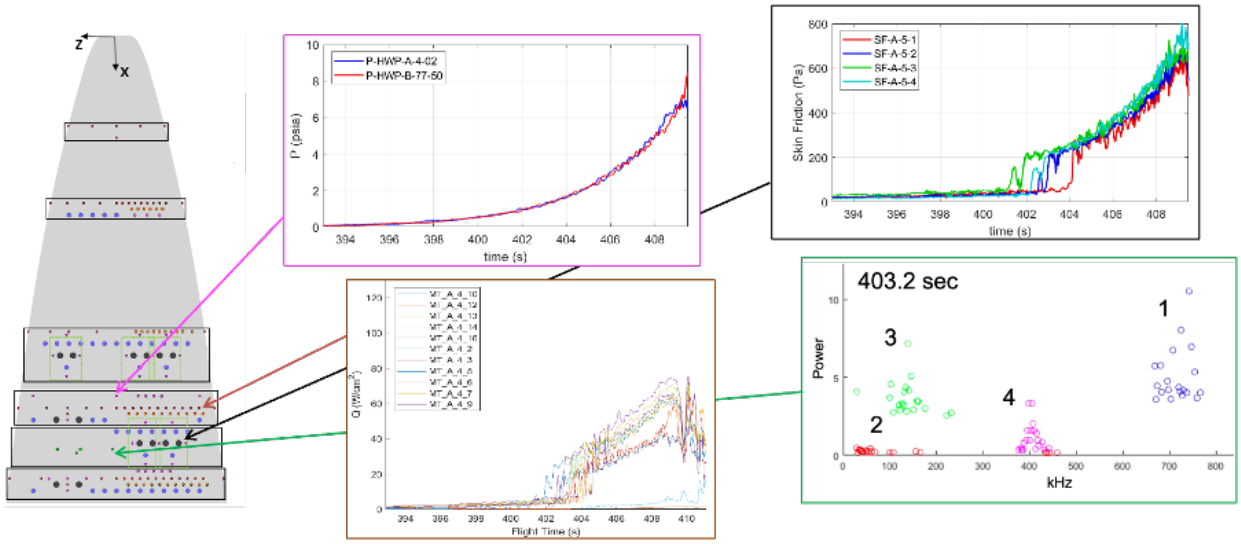

Figure 69. Sample data showing transition and turbulent flow on descent.

6.2.3 Numerical Simulations

The flight data were compared to experimental numerical simulations across the trajectory. A two-way conjugate heat transfer (CHT) simulations was performed at TAMU in collaboration with Sandia and Lawrence Livermore National Laboratories (Wirth *et al.* 2023a). The CHT simulations were accomplished by B. Morealle (TAMU graduate student under the direction of R. Bowersox).

The Sandia Parallel Aerodynamics and Reentry Code (SPARC) (Howard *et al.* 2017) was used to simulate the external flow and the Aria code (Notz *et al.* 2007) was used to compute thermal response within the frustum. The simulation proceeded as follows. First, the wall boundary temperature was initialized to the measured average temperature across rows 4 – 6, which was 333.5

DISTRIBUTION A: Distribution approved for public release.

K, while the BOLT II was exo-atmospheric. The time history of the flight Mach number and Reynolds number during descent is given in Fig. 70. Second, a laminar solution was computed from t = 390 s (M = 5.13, Re = 2.13 x 10^5, Alt. = 43.9 km) to t = 402 s (M = 6.03, Re = 6.22 x 10^6, Alt. = 23.7 km). Third, fully turbulent flow over the research geometry was then assumed and modeled with the Spalart & Allmaras (SA) (1992) turbulence model until t = 405 s (M = 6.07, Re = 1.86 x 10^7, Alt. = 18.6 km). In both the laminar and turbulent simulations, the SPARC was called every 0.75 seconds and Aria every 0.5 seconds, with a period of synchronization between. The compressible Navier-Stokes equations for a thermally and calorically perfect gas were solved to steady-state. Modified Steger Warming inviscid fluxes were used. The density residual was converged 8 orders of magnitude. The edge pressure, recovery enthalpy, and a convective heat transfer coefficient from SPARC were used as boundary conditions for the Aria code, which was converged 7 orders of magnitude.

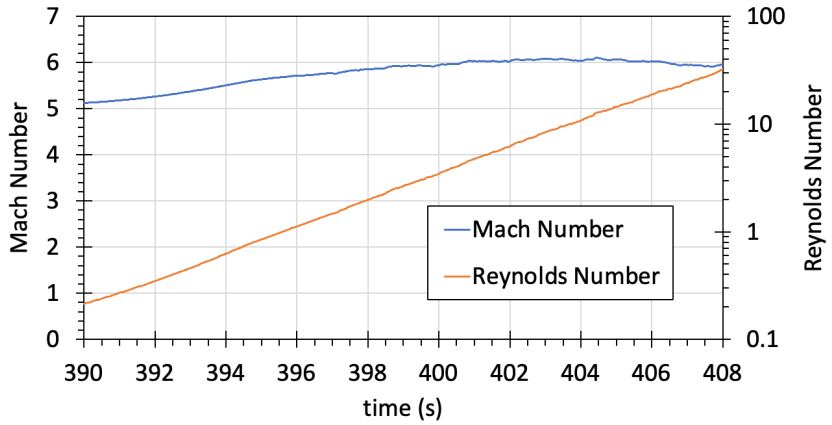

Figure 70. Time dependency of Mach and Reynolds numbers during descent.

The grids were generated in the Pointwise brand commercial meshing software Pointwise and were composed of structured body-fit hexahedra. The aero mesh had 35 million cells for a half symmetry. While 35 million cells were not expected to capture the fine laminar structures, the thermal response largely depended on the largest streaks, which were captured. The outer domain of the aero grid was approximately shock fit for a Mach 6 shock flight condition. Shown in Figure 71 are the flow and frustum grid domains. The aero domain can be seen in black outline and the thermal domain can be seen in the solid blue (Nickel) and red (SS) surfaces.

DISTRIBUTION A: Distribution approved for public release.

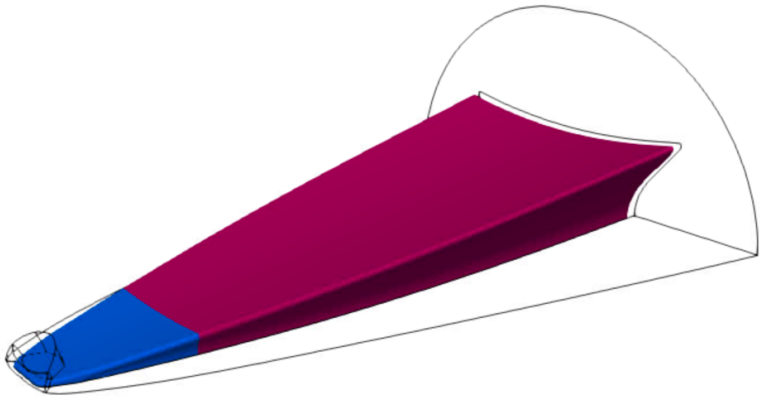

Figure 71 Domains for the coupled Conjugate Heat Transfer simulation (Wirth *et al.* 2023a).

In terms of data reduction, a comparison between the laminar CHT simulation and the heat flux for leading edge sensor MT-A6-17 reduced with both the CF and 2-D finite difference approach is shown in Fig. 72. The data reduced by the CF method were significantly higher than the simulation, where 2-D were in better agreement. This study suggested that lateral conduction effects were significant near the leading-edge of BOLT II, which was expected. Also, contributing the differences observed in Fig. 72 was a slight mismatch of the initial wall temperature for the CHT as compared to the mean of rows 4 – 6 MT sensors. Additional comparisons to the flight data across the frustum are shown in Fig. 73, where the inboard MT sensors matched the laminar temperature up to ~401 – 402 s. The rapid increases in temperature were the result of the transition fronts moving over specific sensors. The agreement of the Q3D and laminar CHT provided confidence in the application of the experimental techniques.

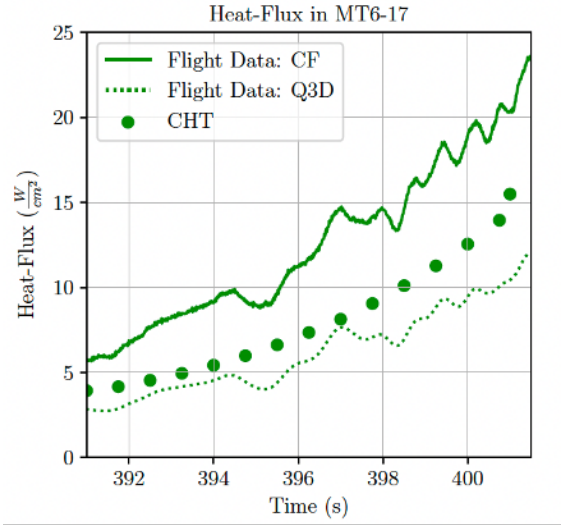

Figure 72. Leading-edge CHT comparison (Wirth *et. al.* 2023a). CF and 3-D solution (Q3D) with laminar CFD for the M-A-6-17 sensor near the leading edge.

DISTRIBUTION A: Distribution approved for public release.

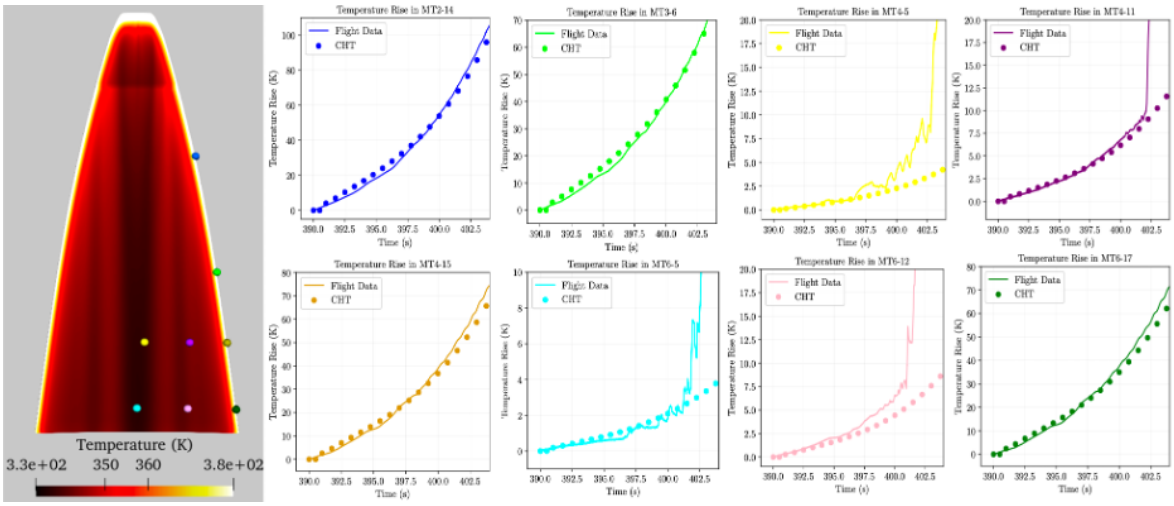

Figure 73. Temperature field from laminar CHT at 402 seconds and comparisons to flight data at from multiple MTs (Wirth *et al.* 2023a).

JHUAPL (B. Wheaton) also provided RANS simulations, which were accomplished with the commercial Metacomp brand CFD code CFD++ and employed the SA turbulence model. The wall temperature was fixed at 300 K. This method was less computationally intensive than the CHT approach, which led to a larger number of simulations across the trajectory.

6.2.4 Post Flight Results - Boundary Transition and Turbulence

To identify transition locations, global heat flux movie visualizations of the transition front were constructed using the 3-D heat flux data reduction method with the MT sensors (Wirth *et al.* 2023a); see Fig. 74 for an example contour at $Re_L \approx 8.5 \times 10^6$ for both ascent and descent. The heat flux from the 3-D solutions was considered qualitative due to the course spacing of the MT sensors, as mentioned in the previous section. Nonetheless, the analysis showed excellent agreement with the Vatell TG direct measurements in rows 4, 5, and 6; see Fig. 75 for line plot comparisons. From these visualizations, the data indicated that transition first occurred on $z < 0$ side in the mixed-mode region at $Re_x = 4 - 6 \times 10^6$ and progressed from row 6 to row 3 during descent, and vice-versa on ascent. The turbulent front seemed to have extended over a large portion of the model as a streak at lower Reynolds numbers formed into a wedge near the back of the model and moved forward on the model by higher Reynolds numbers. There was also a hot streak along the centerline, indicating transition at $Re_x = 5.5 - 7.5 \times 10^6$ associated with the near-centerline vortices. The centerline heating was less than that in the mixed-mode region. The boundary layer was thicker near the center, which resulted in lower heat transfer. The $z > 0$ mixed-mode region transitioned at $Re_x = 7.0 - 10.0 \times 10^6$. Additionally, the 3-D analysis indicated transition on the leading edge between $Re_x = 12.5 - 15.0 \times 10^6$.

DISTRIBUTION A: Distribution approved for public release.

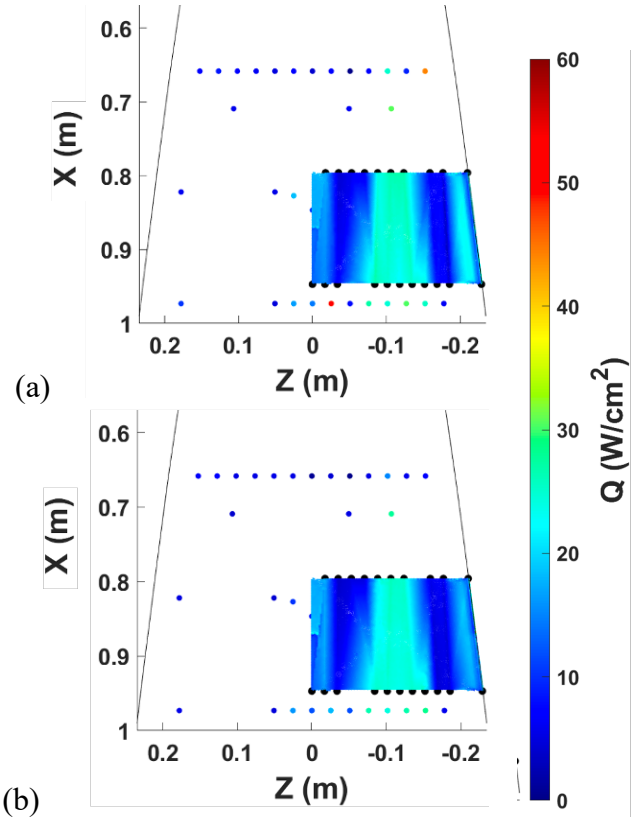

Figure 74. Global heat flux maps indicating the transition heating fronts on the aft highly instrumented section. (a) Ascent, $Re_L = 8.5 \times 10^6$. (b) Descent, $Re_L = 8.7 \times 10^6$.

Spanwise variation in the laminar and turbulent flow was observed in Fig. 75. The heating was highest outboard where the boundary layer was considerably thinner than in the centerline roll-up region, referring to Fig. 14a in Section 4.2.

The mixed-mode region was expected to experience competing transition mechanisms and could have been the first location to see transition, with the vortices being the primary competitor. As noted above, transition was tracked using 3-D heat flux for the $z < 0$ half of side A. However, it was also noted that transition seemed to occur in $z < 0$ mixed-mode region before $z > 0$. Additionally, when comparing data from side A to side B, all of which were in the $z < 0$ half of the model, a few sensors appeared to transition on side A before side B (Berry and Wheaton 2023). Two of these sensors, MT-A-4-10 and MT-A-6-10, were not the first on side A to transition. Thus, the transition asymmetry was significant.

The mixed-mode transition fronts were tracked by identifying the first sensor in each row in each region to transition. "Transition first" was defined for sensor when it reached and maintained a turbulent level. Conglomerated data in the mixed-mode region included heat flux from functional MT sensors (CF method), skin-friction data, TG heat flux, and PCB data are plotted in Fig. 76a. For the $z < 0$, the heat flux was directly measured by the TG sensors and extracted at the same coordinates as the MT sensors from the 3D solution. Skin friction data from the SF sensors were included. For $z < 0$, the SF-A-5-3 transitioned at $Re_x = 4.5 \times 10^6$. For $z > 0$, SF-A-6-1 transitioned

DISTRIBUTION A: Distribution approved for public release.

near Re_x = 7.0 x 10^6. Collectively, the data revealed that the -z, mixed-mode transition occurred between Re_x = 4.0 – 6.0 x 10^6, the range below which all sensors were laminar, and above which all were turbulent. At some sensors, intermittency was observed. Oscillations were also be observed in each of these traces, with these oscillations being more pronounced further forward on the model. The transition front was traced in Fig. 76c, where the circled sensors indicated the first locations to transition. For z > 0, in Fig. 76b, transition occurred between Re_x = 7.0 – 10.0 x 10^6, indicating transition asymmetry.

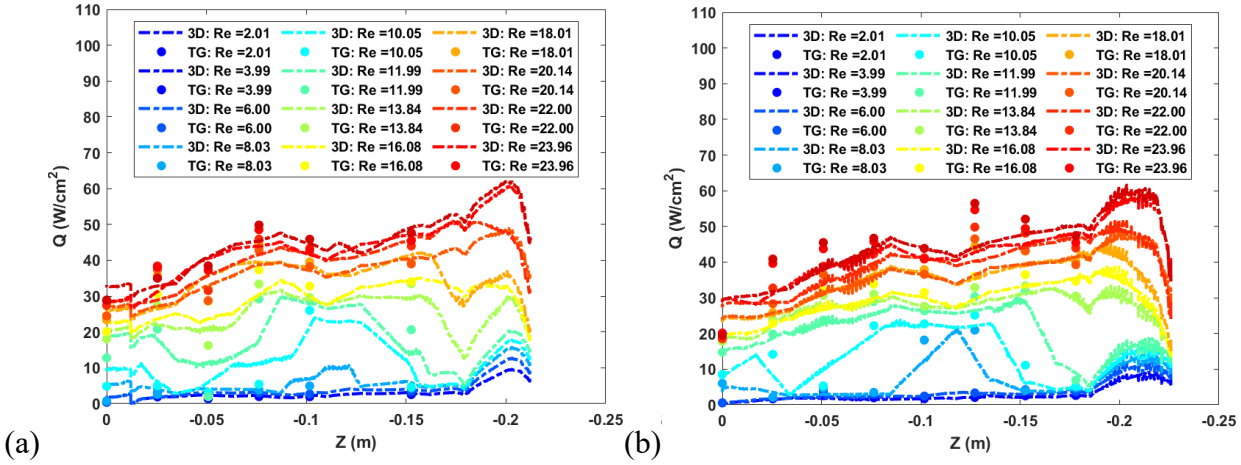

Figure 75. Comparison of 3-D heat flux data reduction of MT data (lines) to TG data (dots).

Several hypotheses were offered to explain the spanwise transition asymmetry. One hypothesis was that a slight, backward-facing step in the nose-frustum joint near the leading-edge tripped transition. Also, the dense sensors array on the z < 0 half may have introduced roughness. This seemed unlikely as the asymmetry extended to row 2. Detailed analysis of the joint between the nickel nose and stainless-steel frustum before flight revealed that a backward-facing step was present during flight near the leading edge (z = -0.102 m), which was estimated to be between 57.0-61.1 μm, with a step of 8-9 μm on the corresponding +z location (Leidy 2023). It is noted that the step was directly upstream of the transition streak, as indicated in Fig. 76. Thermal analysis indicated that expansion of the nickel during flight would have increased the backward facing steps by as much as 79 μm, making the step height even more effective in a location where the boundary layer was thin (Wheaten and Dufrene 2023). However, it was questionable how much thermal expansion affected transition, as it occurred over the same sensors at similar Reynolds numbers during both ascent and descent, even though the thermal soak would have been different. The effects of yaw were also considered as a potential cause for the asymmetry. However, the yaw angles were small, with $|\beta|$ (and $|\alpha|$) < 1.0° for both windows. The mean yaw angle was -0.24° across the descent window and -0.02° during the ascent window. Also, the first sensors to transition were largely the same and transitioned at similar Re_x during both windows. Transition first occurred in both mixed-mode regions for Re_L = 4.0 – 15.0 x 10^6.

DISTRIBUTION A: Distribution approved for public release.

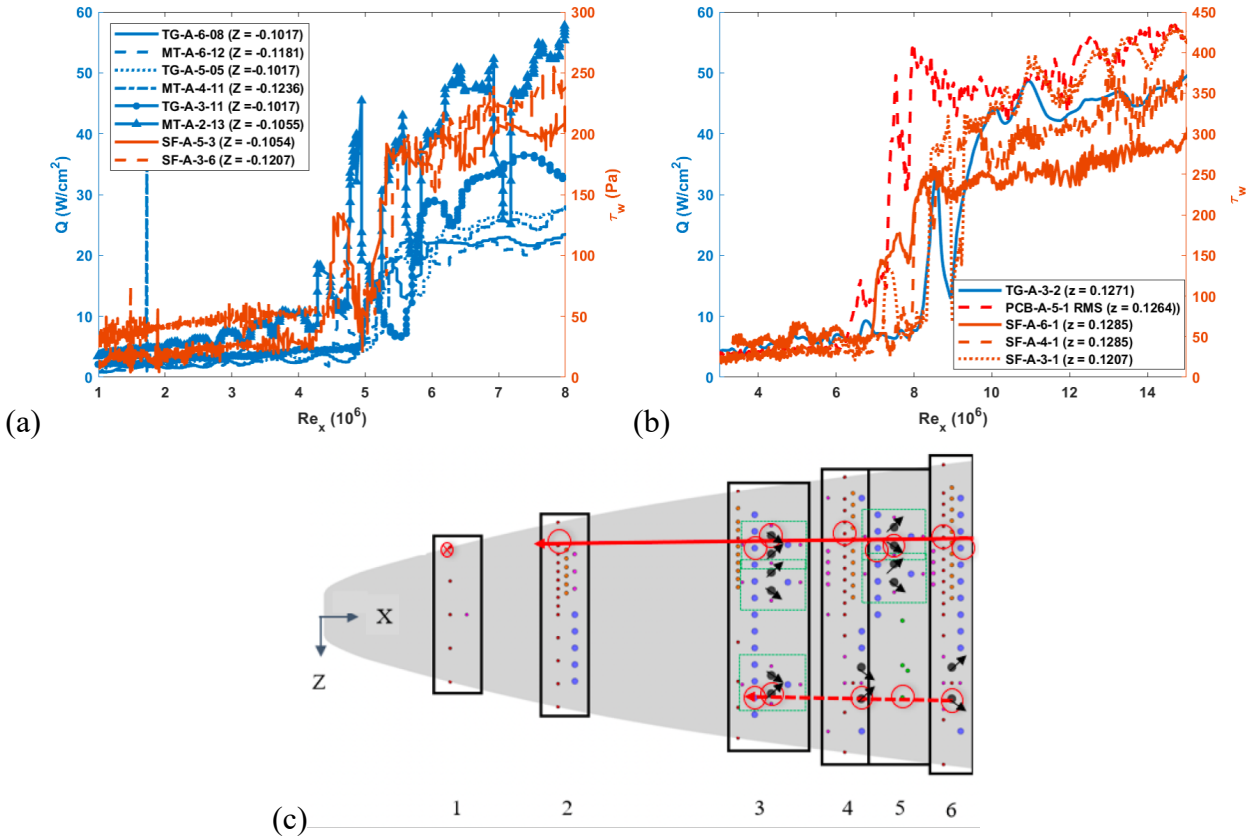

Figure 76. Mixed-mode transition. (a) Transition Reynolds number for first sensors to transition in the mixed-mode region for $z < 0$ (b) and $z >$. (c) Transition front identified as the first sensors to go turbulent, which are circled. The circled x shows location of tallest backward facing step.

Shown in Fig. 77 is the descent window, wind-corrected yaw angle overlaid with the Reynolds numbers during which each sensor transitioned. The plotted Reynolds numbers were selected to include the interval between the highest Reynolds number, where the flow was laminar, and the lowest, where the flow was turbulent. The averages over the entire window were $\alpha = -0.12°$ and $\beta = -0.13°$, with standard deviations $\sigma_\alpha = 0.24°$ and $\sigma_\beta = 0.32°$. The overlaid traces highlight the transition Reynolds number for each sensor. The transition interval for all sensors contained both positive and negative yaw angles. Hence, the yaw effect hypothesis was deemed unlikely. Stability analyses could provide insight into the causes for the transition asymmetry, e.g., the small nose-joint step or the small α and β angles.

The MT sensors were densely placed on the $z < 0$ half of side A to track spanwise variances. The first MT sensors to transition in rows 4 and 6 are plotted alongside their adjacent sensors in Fig. 78. Also plotted are CHT numerical simulation results computed at TAMU and turbulent RANS simulations from JHUAPL (Wirth *et al.* 2023a), where the surface temperature was fixed. The CHT simulations were intentionally stopped at 405 s. There appeared to be overlapping intermittency between these adjacent sensors, which was thought to correspond to the transitional streak oscillating in the spanwise direction. In row 4, intermittency was observed at MT-A-4-10

DISTRIBUTION A: Distribution approved for public release.

before MT-A-4-11, even though MT-A-4-11 achieved turbulent heating first. In all cases, the laminar results shown in Fig. 78 compared well with the flight heat flux. It was noted that the MT sensors that first transitioned showed large overshoots over the turbulent RANS heating, whereas the overshoots for MT-A-6-13 and MT-A-4-13 were noticeably smaller. The overshoot was also observed in SF-5-3, the first SF to transition, and in some sensors on the $z > 0$ half of side A. This was a characteristic of the mixed-mode transition mechanism. On the frustum, where the boundary layer was three dimensional, the sensors each experienced different elements of the transition process. For example, MT-A-4-11 was beneath a transitional streak and MT-A-4-13 was overtaken by a turbulent wedge that emanated outboard from the transitional streak. The sensor arrangement was selected based on the ground test to capture these differences.

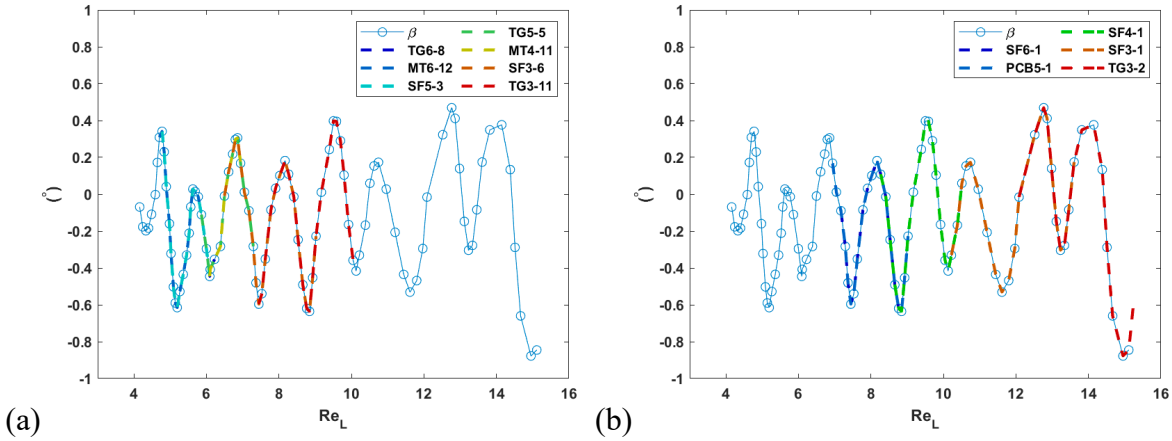

Fig. 77 β variation during each sensor transition.

In the downstream turbulent region, the agreement between the RANS and experiment was considered very good. The agreement with constant wall temperature simulations from JHUAPL was considered fortuitous as the wall temperature was held constant. The CHT results were, on average, about 20% lower than the fixed wall temperature results. Apparently due the higher predicted wall temperature.

The response of the transition streak to changing flight attitude on the $z < 0$ half of the model was captured with the MT sensors. To track the streak, data from the first two MT sensor to transition in rows 4 and 6 were compared with α and β variations. Transition was observed on the inboard sensors, MT-A-4-10 and MT-A-6-11, slightly after their outboard neighbors, MT-A-4-11 and MT-A-6-12. The data plotted in Fig. 79 were taken from these four sensors, accounting for intermittency. Each sensor has its own symbol. The laminar/intermittent Reynolds numbers were plotted in black and the turbulent in red. These points were scattered onto the wind-corrected β and α curves across those Reynolds numbers. The red and black points were generally clustered near the peaks and troughs of the β curves, which was expected as yaw should have dominated the streak spanwise location. The transition streak appeared first on MT-A-6-12 as β decreased from 0.2° to 0°, which then observed laminar heating. The inboard sensor (MT-A-6-11) observed turbulent heating when $\beta = -0.6°$ and laminar values as β approached 0°. Increasing the Reynolds

DISTRIBUTION A: Distribution approved for public release.

number resulted in full transition at the MT-A-6-12 sensor by Re_L = 5.5 x 10^6. The flow at the MT-A-6-11 sensor fully transitioned once β decreased below -0.2°. Similar trends were observed in row 4, with the inboard sensor measuring turbulence only at the lowest β. Comparisons with α are included for completeness. The trend was that each sensor saw turbulence or laminar heating on the slopes rather than the peaks or troughs, when α was either increasing or decreasing. One interesting feature was that the streaks appeared to move in the opposite direction than expected. Negative β meant that the +z side should have been windward, which should have driven the streaks outboard on the -z half, but at the smallest β, turbulent heating was observed at the inboard sensors. Similar analysis could have been accomplished at the edge of the turbulent wedge as it progressed up the model, but this analysis showed that the transitional streak oscillated between MT-A-4-10 and MT-A-4-11 in row 4 and MT-A-6-11 and MT-A-6-12 in row 6 due to flight attitude oscillations during the descent window.

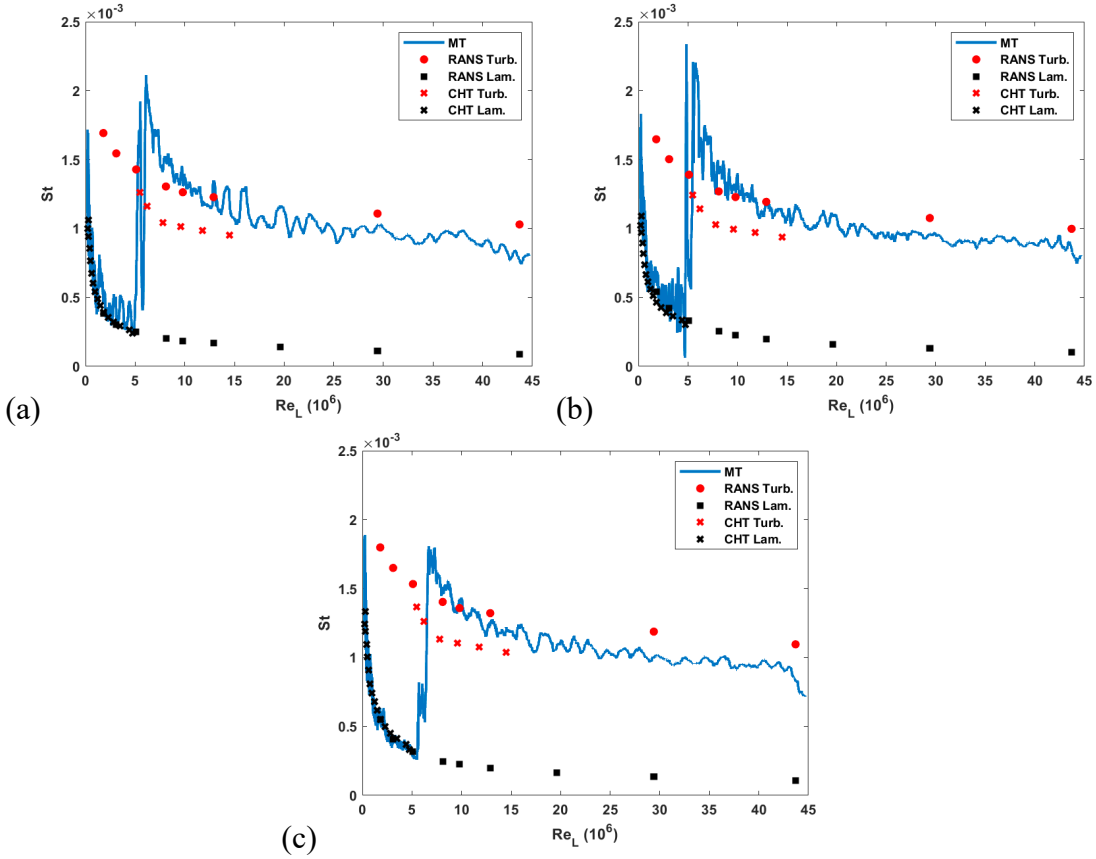

Fig. 78 Flight heat flux -z mixed-mode transition. (a) MT-A-6-11 (z = -0.101 m). (b) MT-A-6-12 (z = -0.118 m). (c) MT-A-6-13 (z = -0.135 m).

DISTRIBUTION A: Distribution approved for public release.

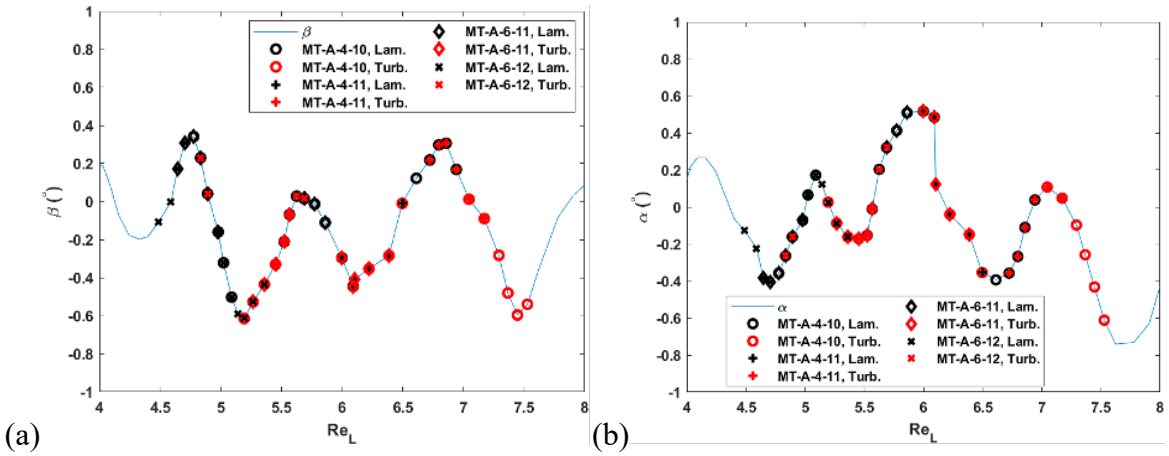

Figure 79 Mixed-mode transition streak oscillations in the MT data.

The four PCB-132 sensors provided spectral transition data for $z > 0$. The PCB data was converted into its power spectral density (PSD) and the top 20 frequencies and corresponding amplitudes (left in raw volts) were telemetered to the ground. A snapshot of the spectral peaks during transition was shown earlier in Fig. 69. A more complete description is provided in Figs. 80 and 81. To estimate the transition Reynolds number ranges, the data were converted into a pseudo-RMS by taking the square-root of the Riemann sum of the 20 data points. Then, spectrograms of the data were generated for Reynolds numbers close to transition. The symbol types in the spectrograms were used to indicate the quadrant of the windward meridian, where positive α meant that side A was leeward and positive β meant that the $+z$ half was leeward and the $-z$ half was windward. Using these methods, the first PCB in the mixed-mode region to transition was PCB-A-5-1, the data from which is displayed in Fig. 80. The pseudo-RMS was sampled at 217 Hz, with a moving average with a window of 10 Hz. The pseudo-RMS was low, indicating laminar flow, until $Re_L = 7.0 \times 10^6$, when a small increase was observed, corresponding to what was thought to be modal content between 300 and 500 kHz for $Re_L = 7.0 - 8.5 \times 10^6$, before turbulent flow was observed above $Re_L = 9 \times 10^6$, indicated by high-amplitude broadband content up to 800 kHz. It should also be noted that a few points at the lower frequency range (24 kHz) were observed during transition, which may give evidence of lower frequency instabilities in this region as well. The flight attitude was relatively stable, meaning that Reynolds number was dominant. Figure 81 was included for completeness, which shows the other two PCBs in the mixed-mode region. These data illuminated additional bands of frequencies at very low amplitude in the laminar phase of flight that were consistent across various flight attitudes. Both sensors captured a band of content near 400 kHz shortly before turbulence onset, although the spectrogram was markedly different from PCB-A-5-1; also, see Fig. 69. It appeared that the major modal frequencies were measured.

DISTRIBUTION A: Distribution approved for public release.

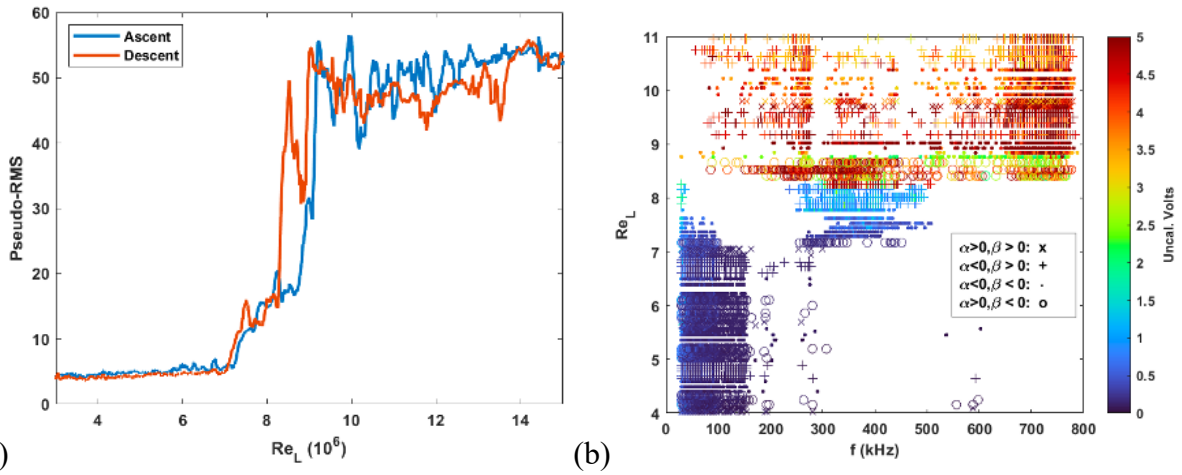

Figure 80. Mixed-mode transition measured by PCB-A-5-1. (a) Pseudo-RMS for transition. (b) Descent spectrogram around transition.

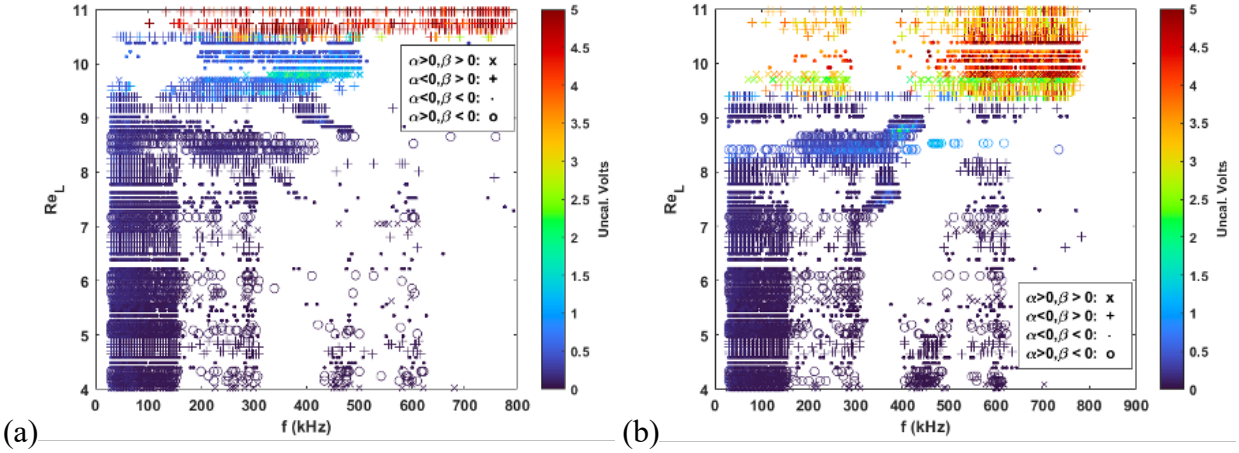

Figure 81. Spectrograms during transition. (a) PCB-A-5-2. (b) PCB-A-5-4

The centerline was the other region of interest for transition due to the large counter-rotating vortices. Pre-flight studies determined that these vortices were generated at the corner between the nose and the highly swept leading edges, moved inboard toward the centerline due to the general pressure gradients, and provided a bed for secondary instabilities. The vortical structure led to a much thicker boundary layer on the centerline, with a corresponding reduction of heat flux, skin friction, and maximum pressure fluctuation frequencies. In flight, a transition path was observed generally following the expected path of these vortices. In Fig. 82, the first sensors that transitioned are circled in red and their corresponding transition traces are plotted in Fig. 83. By row 6, the vortices had sufficiently converged on the centerline, where transition happened first or simultaneously with off-centerline sensors, as can be seen in Fig. 83. As the transition moved upstream, it split, with one path following each vortex. At row 3, the centerline TG was one of the last to transition, although the ones adjacent to it can be seen almost simultaneously transitioning in Fig. 83. This bifurcation extended as far forward as was measured. The row 2 data plotted in Fig. 84

DISTRIBUTION A: Distribution approved for public release.

show transitional oscillations at lower Reynolds number on either side of $z = 0$, with transition at much higher Reynolds number for the $z = 0$ sensor. The sensor between the vortices showed reduced oscillations with transition taking place later at $Re_L = 27x10^6$.

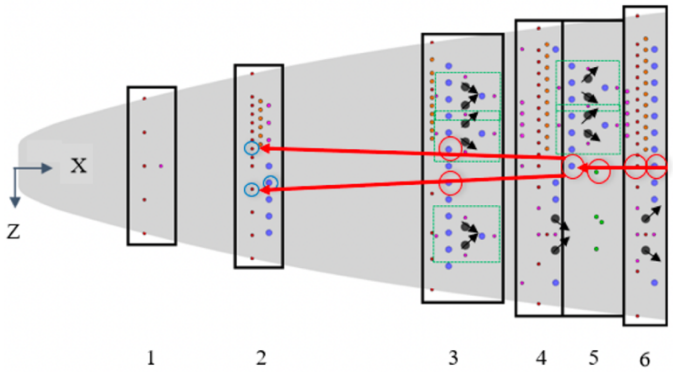

Figure 82. First turbulent sensors in centerline region, data from red sensors plotted in Fig. 83.

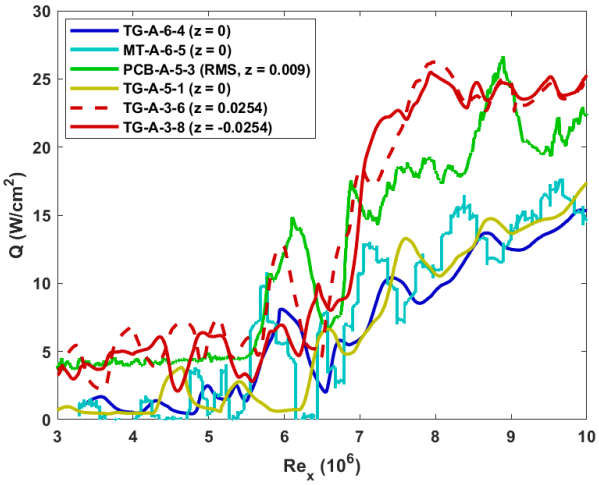

Figure 83. Transition for first sensors to transition in the centerline region.

The heat flux under vortices exhibited noticeably different behavior than the heating over the rest of the vehicle. Larger laminar oscillations were observed underneath the vortices. One interpretation of the descent window data in Fig. 84 was that boundary layer height changes due to flight path induced vortex path motions had the large observed impact on the heat flux when the flow was laminar. Interestingly, sensors slightly outboard of the vortex transition path exhibited larger oscillations after transition. Sensors SF-A-3-3, MT-A-4-6, and MT-A-6-7 were examples. Note that the sensors were spread further apart on the $z > 0$ half of side A, which hindered comparisons. Sensor MT-A-2-4 was located at $z = 0.035$ m, which appeared to be adjacent to the vortex, and thus experienced oscillations about the laminar heating up to $Re_L = 16.0 \times 10^6$, an intermittent period to $Re_L = 25.0 \times 10^6$, and turbulent values at higher Reynolds numbers. On the other side, MT-A-2-7 was closer to the centerline and measured laminar oscillations that grew in amplitude. It was difficult to distinguish between laminar, intermittent, and turbulent heating levels, but

DISTRIBUTION A: Distribution approved for public release.

it could be argued that oscillations about a turbulent value were achieved by Re_L = 22.0 x 10^6. Another indicator of the vortices may be the laminar simulation under MT-A-6-5 and MT-A-6-6, which indicated increasing Stanton numbers with increasing Reynolds numbers at Re_L < 5.0 x 10^6. Large laminar oscillations were observed at these sensors, and transition was more abrupt, with intermittency limited to a smaller range of Reynolds number.

Like with the mixed-mode region, JHUAPL and TAMU simulation results agreed well with laminar and turbulent regions. The CHT results again about 20% lower than the fixed temperature simulations. The oscillations in the experimental data appeared to be energetic along in the near centerline region, which were not captured in the fixed attitude simulations.

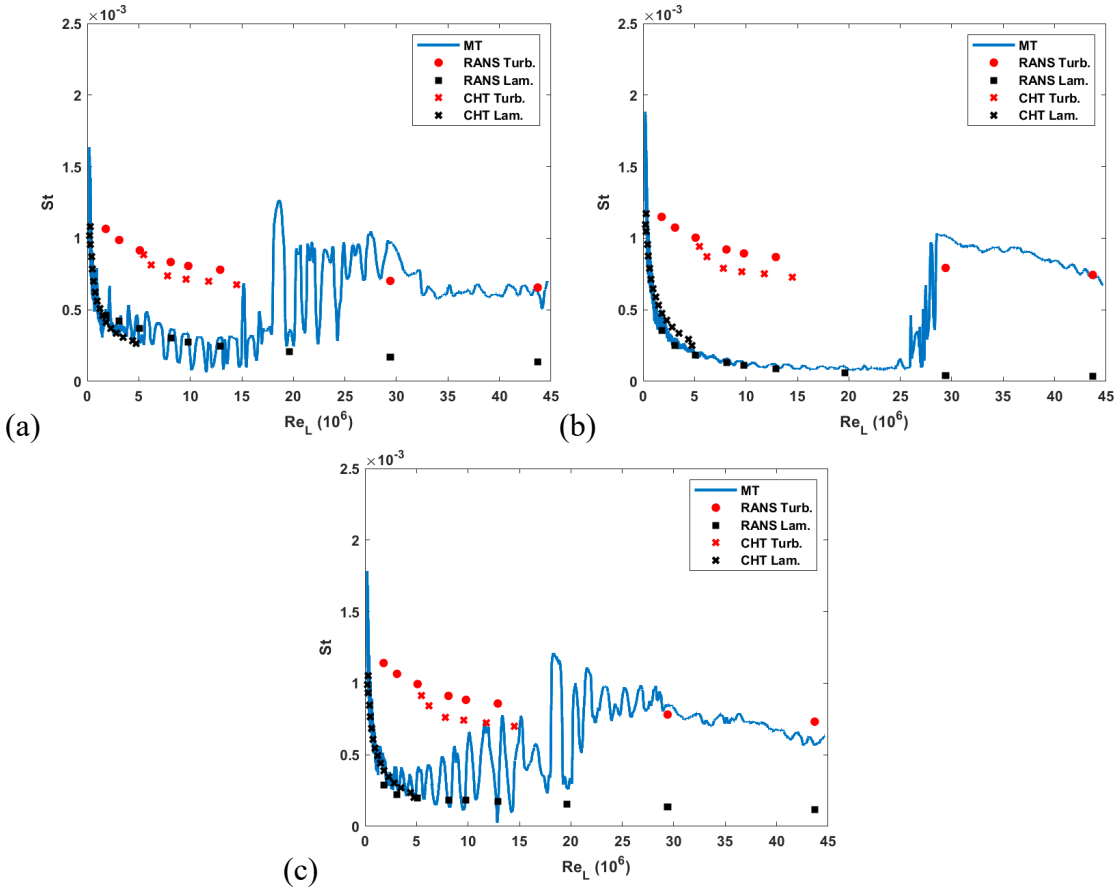

Figure 84. Near-centerline vortical transition bifurcation over row 2 MT sensors. (a) MT-A-2-4 (z = 0.035 m). (b) MT-A-2-6 (z = -0.013 m). (c) MT-A-2-7 (z = -0.026 m).

The effects of vehicle attitude on transition oscillations were tracked in the near-centerline region in a similar manner as they had been tracked in the -z, mixed-mode region. To account for the large oscillations, higher laminar heating levels were distinguished from the lower laminar heating levels, a process repeated for the turbulent heating. Data from sensors MT-A-6-5 and MT-A-6-6 are shown in Fig. 86. The turbulent data are shown in red, laminar data are shown in black, and high values were given bold symbols compared to the low. Trends were less discernible across

DISTRIBUTION A: Distribution approved for public release.

the whole Reynolds number range shown. It appeared that a laminar streak may have oscillated between the two sensors for $Re_L = 4.5 – 6.0 \times 10^6$, with the streak being over the centerline sensor at lower β and higher α. Turbulence was first observed on the centerline sensor for $Re_L = 6.0 \times 10^6$, then exclusively over MT-A-6-6 around $Re_L = 6.5 \times 10^6$. Fully turbulent flow was apparent for both sensors by $Re_L = 7.3 \times 10^6$. In the turbulent phase of flight, higher heating levels correlated to decreasing α, with lower levels when α was increased, which generally correlated to troughs and peaks respectively in the β traces. Drawing trends from the near-vortex heating and transition proved difficult as the vortices were relatively large Reynolds number and flight attitude dependent structures. While the BOLT-II flight experiment was successful in meeting its turbulence goals by achieving high Reynolds numbers with relatively low and stable α and β, improved perspectives on the role of flight attitude on the transition mechanisms may have been more apparent with larger α and β variations.

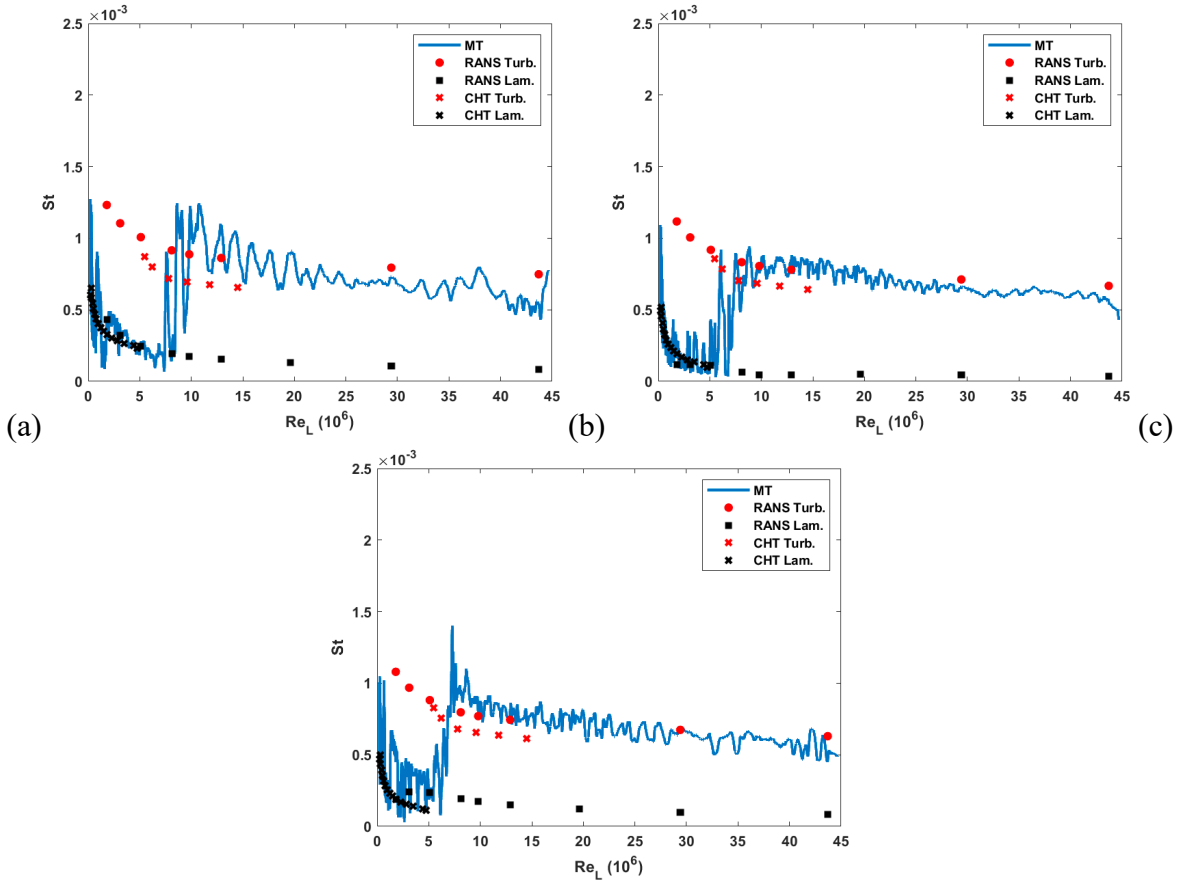

Figure 85. Near-centerline vortical transition over row 6 MT sensors. (a) MT-A-6-4 ($z = 0.032$ m). (b) MT-A-6-5 ($z = 0.000$ m). (c) MT-A-6-6 ($z = -0.017$ m).

As with the mixed-mode region, a PCB132B was used to captured high-frequency pressure data under the near centerline vortex. Specifically, PCB-A-5-3 was located at Z = 0.009 m between the row 4 and row 6 MT sensors. As shown in Fig. 87, transition occurred between $Re_L = 5.5 \times 10^6$ and $Re_L = 8.0 \times 10^6$. In general, the frequencies observed by the sensor were less than 300 kHz,

DISTRIBUTION A: Distribution approved for public release.

which were lower than the other sensors due to the thicker boundary layer near the centerline. The amplitudes were also lower. Unlike the mixed-mode PCBs, no separate modal signal could be identified during transition. However, it appeared that there may have been a brief instant with content near Re_L = 6.0 x 10^6. This was followed by a disappearance of content as the RMS trace dropped, before a higher amplitude, broader frequency spectrum was observed starting at Re_L = 7.0 x 10^6. Even though distinct modal frequencies were difficult to discern at this location, it was clear when transition began, and that the energy remained in frequencies below 300 kHz. The frequencies remained below 300 kHz while turbulent, which was due to the thicker boundary layer near the centerline.

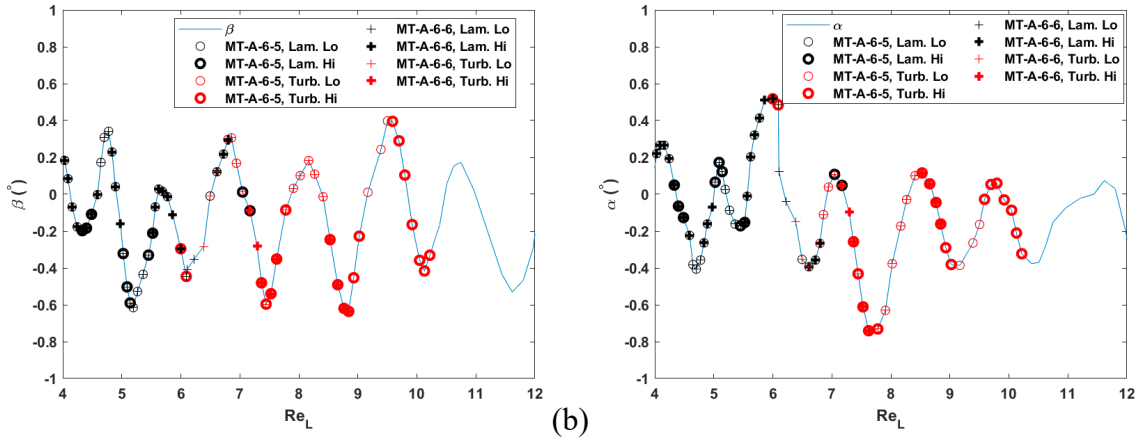

(a) (b)

Figure 86. Near-centerline heat flux oscillations in the MT data. (a) Yaw effects. (b) AoA effects.

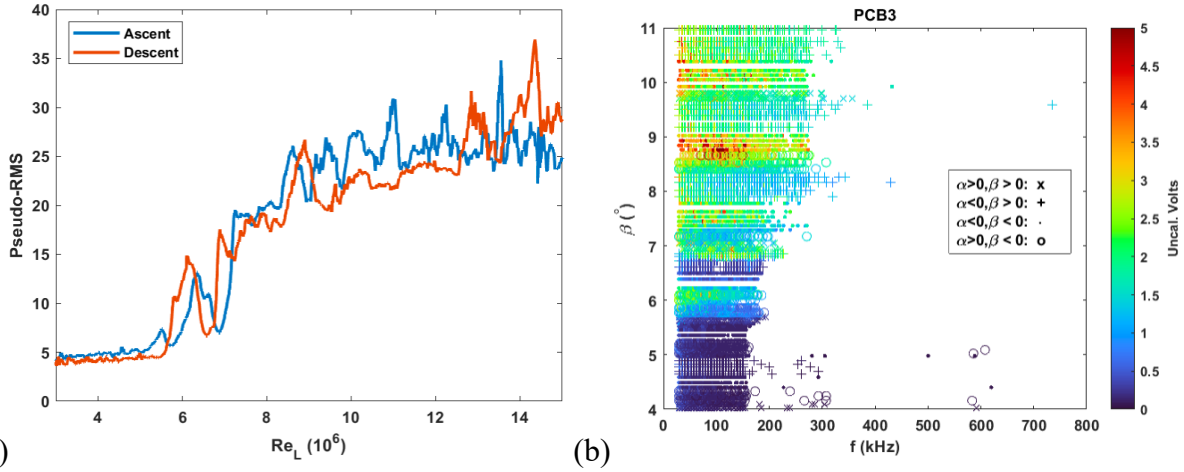

(a) (b)

Figure 87. Near-centerline vortex transition measured by PCB-A-5-3. (a) Pseudo-RMS. (b) Descent spectrogram around transition.

Shown in Fig. 88 are two traces of Stanton number taken from row 4 MT sensors for comparison to the RANS simulations. The MT-A-4-14 sensor in Fig. 88a was outboard of the mixed-mode transition. The St trace went through the RANS laminar and early turbulent data but was

DISTRIBUTION A: Distribution approved for public release.

close to 25% lower than the fixed wall RANS predictions for Re_L > 20.0 x10^6. The fixed wall temperature RANS were, in general, 20% greater than the more accurate CHT results. Hence, the CHT results would likely agree well with these data. The MT-A-4-15 sensor was close to the leading-edge and transitioned near Re_L > 15.0 – 20.0 x10^6. The fixed wall temperature RANS results significantly over predicted the leading-edge heat transfer as the fixed 300 K temperature was significantly below that expected for the hot leading edge.

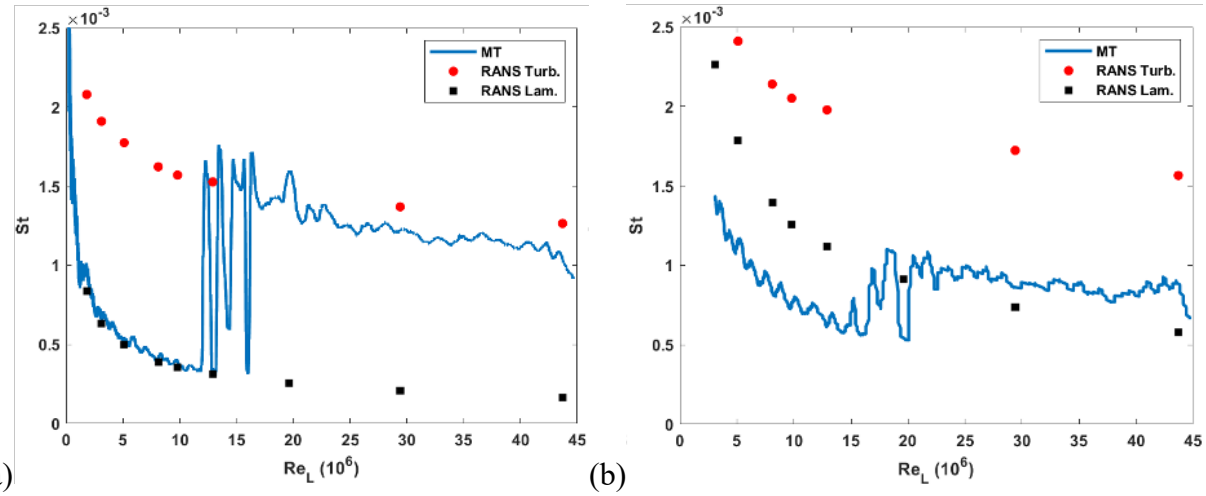

Figure 88. Row 4 outboard and leading-edge heat flux. (b) MT-A-4-14 (CF, outboard). (b) MT-A-4-15 (3-D, leading-edge).

6.2.5 Post Flight Results – Reynolds Analogy

The flight geometry was instrument with arrays of sensors designed to allow for approximate assessment of the Reynolds analogy:

$$\frac{C_f}{2St} = Const. \approx Pr^{\frac{2}{3}} \tag{5}$$

The sensor arrays were shown in Fig. 44 (outlined green boxes) in Section 4.5. The funding for the instrument array sensors was provided by AFOSR through a DURIP grant. The basic idea was to evaluate the Reynolds analogy by interpolating the heat flux from the MT and TG sensos. The 3-D method was planned for analysis reduction of the heat flux. The sensors are summarized in Table 12. As indicated in Fig. 67, the sensor arrays were confined toward the back of BOLT II.

The direct ratio of skin-friction and heat flux were inconclusive due primarily to interpolation across sensors. To help improve this, the data were fit with power law functions of Reynolds number. For laminar, incompressible, flat plat flows, both C_f and St are proportional to $Re_x^{-1/2}$. Extending to compressible turbulent flow, following fits were assumed:

$$C_f = A\frac{\rho_w \mu_w}{\rho_\infty \mu_\infty} Re_x^{-m} \tag{6}$$

$$St = B\frac{\rho_w T_\infty}{\rho_\infty (T_0 - T_w)} Re_x^{-m} \tag{7}$$

DISTRIBUTION A: Distribution approved for public release.

In these relations, compressibility was accounted for by compressibility factors, defined as $\rho_w \mu_w / \rho_\infty \mu_\infty$ and $\rho_w T_\infty / \rho_\infty (T_0 - T_w)$ for skin friction and Stanton number, respectively.

Least squares determination of the A and m was performed for each skin friction and heat flux trace. Each fit began at $Re_x = 12 \times 10^6$ to avoid the transitional overshoot for transducers beneath streaks and to allow for the adequate spread of the turbulence wedge over adjacent sensors, as discussed earlier. Shown in Figs. 89a and 89b are example fits. The SF-A-5-3 sensor (Fig. 89a) was apparently beneath as streak, with the previously mentioned overshoot. The SF-A-4-2 sensor (Fig. 89b) was not the first sensor to transition, and hence, the transition process was believed to be that of turbulent wedge front, which led to less of a transitional overshoot. An upper bound for the SF data was set at $Re_L = 30.2 \times 10^6$. At that Reynolds number (or time in the flight), 12 of 14 SF sensors measured anomalous dips in skin friction. The cause of the anomaly was not identified, but the synchronization across all sensors indicated it may have been a failure of the data card, telemetry, or the sensors. Similar profiles were observed for the Stanton number traces from MTs directly upstream and downstream of the skin friction sensor, particularly MT-A-6-11 and MT-A-6-12. No upper limit was set for the MT sensors, which apparently performed until the end of the flight.

Table 12 Reynolds Analogy Sensor Arrays

Array	SFs	TGs	HWPs
1	SF-A-3-1 SF-A-3-2	TG-A-3-02 TG-A-3-03 TG-A-3-04 TG-A-3-14	HWP-A-3-01 HWP-A-3-04 HWP-A-3-05 HWP-A-3-09
2	SF-A-3-3 SF-A-3-3	TG-A-3-08 TG-A-3-09 TG-A-3-10 TG-A-3-15	HWP-A-3-02 HWP-A-3-06 HWP-A-3-07 HWP-A-3-10
3	SF-A-3-5 SF-A-3-5	TG-A-3-10 TG-A-3-11 TG-A-3-12 TG-A-3-16	HWP-A-3-03 HWP-A-3-07 HWP-A-3-08 HWP-A-3-11
4	SF-A-5-1 SF-A-5-2	TG-A-5-02 TG-A-5-03 TG-A-5-04 TG-A-5-08	HWP-A-4-07 HWP-A-5-01 HWP-A-5-02 HWP-A-5-04
5	SF-A-5-3 SF-A-5-4	TG-A-5-05 TG-A-5-07 TG-A-5-09	HWP-A-4-08 HWP-A-5-02 HWP-A-5-03

DISTRIBUTION A: Distribution approved for public release.

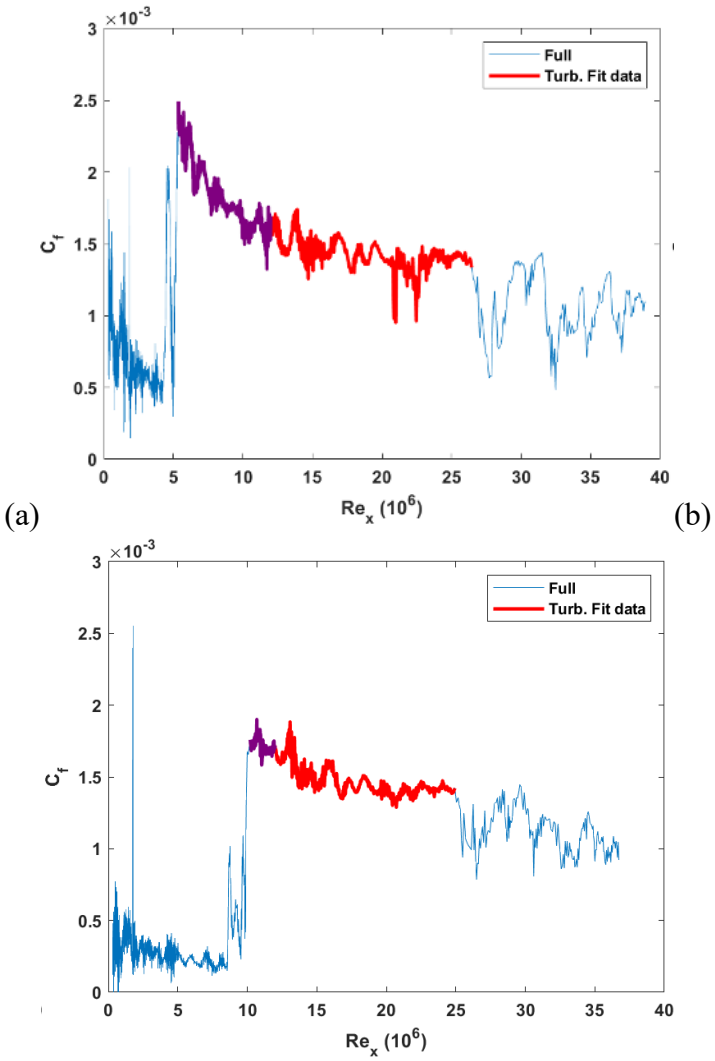

Figure 89. Example traces and fits. (a) SF-A-5-3, which was beneath a turbulent streak. (b) SF-A-4-2, which was adjacent to a streak.

To calculate the compressibility factors, both wall temperature and pressures were interpolated to the SF and MT sensors. Shown in Fig. 90 are the relative locations of the various sensors used to calculate the compressibility factors. The pressure at the nearest HWP sensor was assumed to be the pressure at the SF sensor. This accounted for oscillations in the C_f trace, albeit with some bias thought to be due to the spatial difference in measurements. The row 4 and row 6 SF sensors were on the $z > 0$ side. The MT-A-6-2 and MT-A-6-3 sensors were among the 17 that failed. Thus, the only nearby operating MT was MT-A-4-16. Hence, the row 4 MT sensors were assumed suitable for the SF sensors in row 6 as axial temperature variations were comparatively small. For the row 5 SF sensor, the temperature was estimated by interpolating the row 4 and 6 MT sensors data. The pressure from the nearest HWP was extrapolated to the MTs, with errors less than 10%, as the pressure was found to by < 10% from the mean value across the span model. Pressure and temperature interpolations were converted to density and viscosity via the ideal gas law and Sutherland's

DISTRIBUTION A: Distribution approved for public release.

law. For the 10 SF sensors considered in these fits, coefficients and exponents were listed in Table 12 with powers ranging from -0.17 to -0.26 and coefficients range from 0.014 to 0.078. For the MTs, curve-fit parameters were listed in Table 13 with powers ranging from -0.15 to -0.32 and coefficients ranging from 0.079 to 0.893.

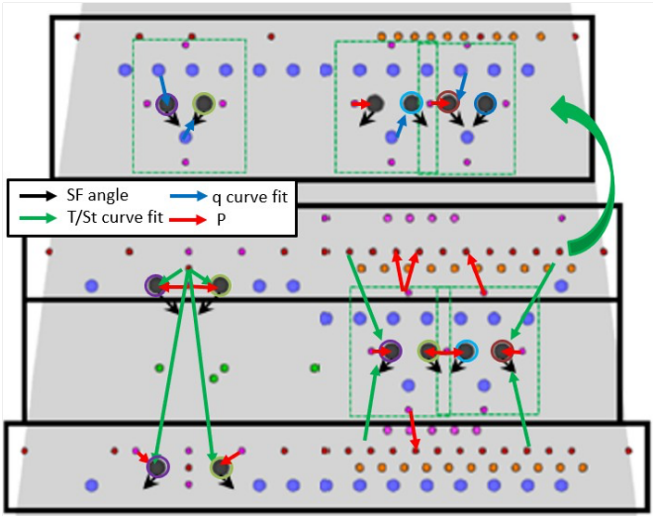

Figure 90. Sensor arrays and relative location of sensors used in compressibility factors and Reynolds Analogy analysis for rows 3 - 6.

Table 13: Rows 4 – 6 SF Curve Fits

	Separate Compressibility Factor			Compressibility Factor Subsumed		
Sensor	A	m	R^2	A'	m	R^2
SF-A-4-1	0.016	0.170	0.363	0.061	0.220	0.463
SF-A-4-2	0.030	0.210	0.528	0.133	0.270	0.568
SF-A-5-1	0.044	0.240	0.492	0.140	0.280	0.385
SF-A-5-2	0.014	0.170	0.766	0.045	0.210	0.577
SF-A-5-3	0.015	0.170	0.480	0.048	0.210	0.331
SF-A-5-4	0.026	0.200	0.679	0.085	0.240	0.550
SF-A-6-1	0.066	0.260	0.619	0.259	0.310	0.565
SF-A-6-2	0.078	0.260	0.729	0.333	0.320	0.723
mean	0.036	0.210	0.582	0.138	0.258	0.520
median	0.028	0.205	0.573	0.109	0.255	0.557

Curve fits were also generated across the descent window by subsuming the compressibility factor into the A and B coefficients, termed A' and B' in Tables 13 and 14. Note, in the subsumed case, the least-squares coefficient accounted for (i) the relationship between C_f and Re_x^{-m}, (ii) the installed sensor angle of the SFs, and (iii) the average pressure and temperature effects. Curve fit parameters for the rows 4 – 6 skin friction and MT sensors are listed in Tables 13 and 14, respectively. The powers ranged from -0.21 to -0.32 and coefficients range from 0.045 to 0.333. Sensor SF-A-3-3 was anomalous, with large oscillations, most likely due to its proximity to the near-centerline vortical structure, which made a curve fit difficult to discern and the exponent was at

DISTRIBUTION A: Distribution approved for public release.

the upper limit, indicating that it was not optimized. The corresponding MT parameters powers were between -0.22 and -0.36 and coefficients between 0.046 and 0.358.

Table 14: Rows 4 – 6 MT Curve Fits

	Separate Compressibility Factor			Compressibility Factor Subsumed		
Sensor	B	m	R^2	B'	m	R^2
MT-A-4-16	0.631	0.280	0.875	0.321	0.340	0.813
MT-A-4-5	0.777	0.320	0.625	0.244	0.350	0.574
MT-A-4-6	0.893	0.320	0.422	0.333	0.360	0.373
MT-A-4-7	0.594	0.280	0.560	0.358	0.350	0.407
MT-A-4-8	0.534	0.270	0.845	0.317	0.340	0.770
MT-A-4-9	0.285	0.230	0.672	0.140	0.290	0.626
MT-A-4-10	0.116	0.180	0.854	0.056	0.240	0.684
MT-A-4-13	0.221	0.220	0.920	0.151	0.290	0.819
MT-A-4-14	0.088	0.160	0.248	0.083	0.250	0.311
MT-A-6-5	0.255	0.250	0.147	0.131	0.310	0.145
MT-A-6-6	0.282	0.260	0.646	0.091	0.290	0.683
MT-A-6-7	0.275	0.250	0.419	0.104	0.290	0.331
MT-A-6-10	0.467	0.260	0.183	0.198	0.310	0.180
MT-A-6-11	0.230	0.220	0.651	0.097	0.270	0.586
MT-A-6-12	0.113	0.180	0.061	0.048	0.230	0.065
MT-A-6-13	0.191	0.210	0.906	0.072	0.250	0.847
MT-A-6-14	0.330	0.240	0.769	0.147	0.290	0.712
MT-A-6-15	0.413	0.250	0.406	0.184	0.300	0.389
MT-A-6-16	0.079	0.150	0.322	0.049	0.220	0.262
mean	0.357	0.238	0.554	0.164	0.293	0.504
median	0.282	0.250	0.625	0.140	0.290	0.574

In all cases, the exponents (m) were lower when the compressibility factor was considered separately from the coefficient. This was likely due to the wall temperature increasing as Re_x increased. Examples of the two fits are compared in Fig. 91. Towards the very end of the flight, the flight attitude oscillations increased, leading to a large pressure drop on side A at the very highest Re_x achieved.

A similar process was attempted to incorporate compressibility effects for the row 3 SF sensors. The failure of the row 3 MT sensors resulted in the wall temperature being unknown, which was a critical component of the compressibility factors. However, the heat flux was directly measured by the TG sensors that were densely places across row 3. The TG data was used to provide a Stanton number curve fit. The dimensional heat measurements from the TG sensor were fit as a function of Re_x. The coefficients B and m follow from Eq. (7). The wall temperatures were projected forward using data from the row 4 MT sensors, where it was assumed that T_w was a function of the normalized spanwise location (z/z_{LE}) to account for the leading-edge sweep. This necessarily introduced some error due to axial distances.

DISTRIBUTION A: Distribution approved for public release.

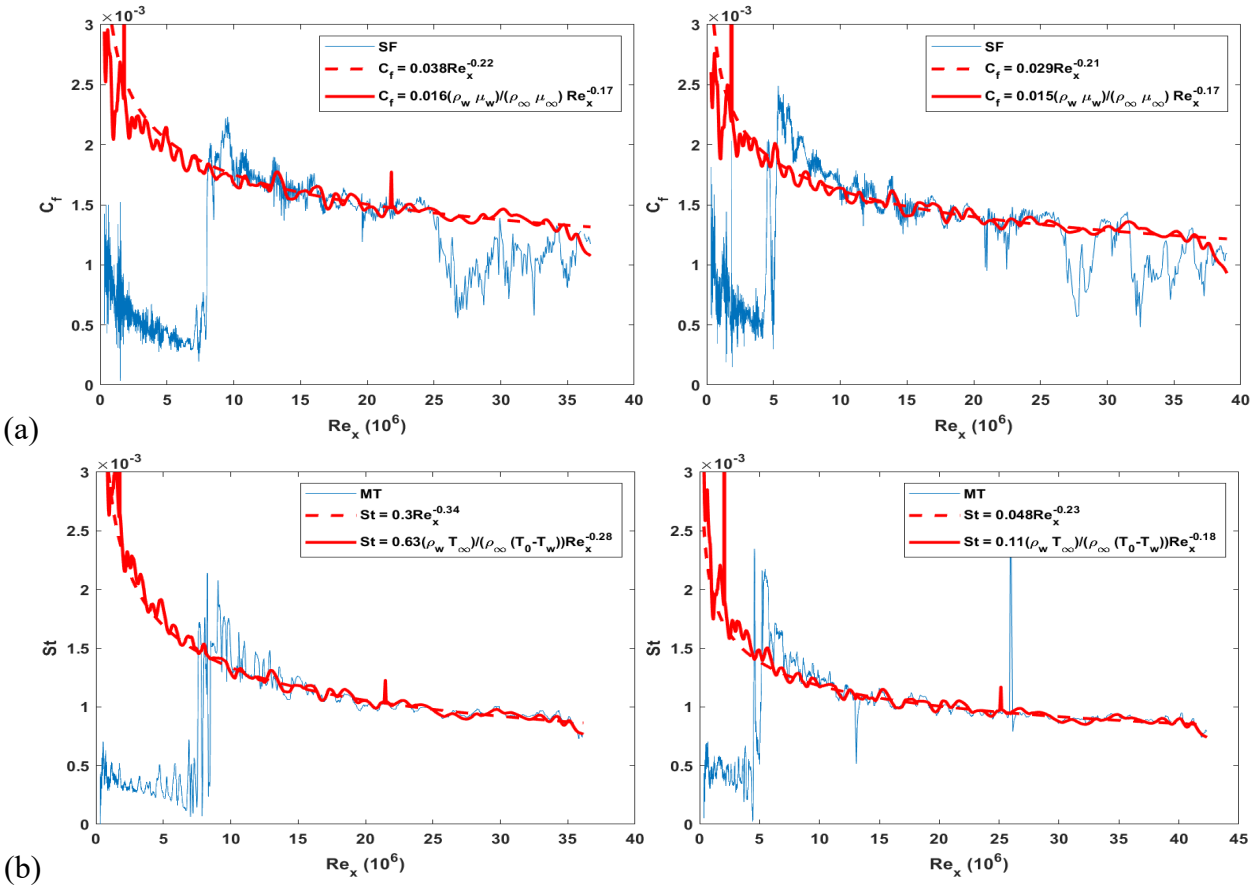

Figure 91. Curve fits with and without compressibility. (a) SF-A-4-1 (left), SF-A-5-3 (right). (b) MT-A-4-16 (left), MT-A-6-12 (right).

The data and curve fits over the row 3 sensors revealed detail on the transition asymmetry. Plotted in Fig. 92 are symmetrically placed TG and SF sensors in row 3. The TG-A-3-11 and SF-A-3- 6 sensors were the first to transition and had the most notable overshoots in the early-turbulent portion of flight. The compressible SF powers and coefficients are summarized in Table 15. The TG powers and coefficients are listed in Table 16. The TG-A-3-01 and 3-13 sensors were outliers, as the exponents were close or at the lower limit, indicating a possible processing error. The TG-A-3-08 sensor was near the centerline and transitioned after Rex = 12 x 10^6.

DISTRIBUTION A: Distribution approved for public release.

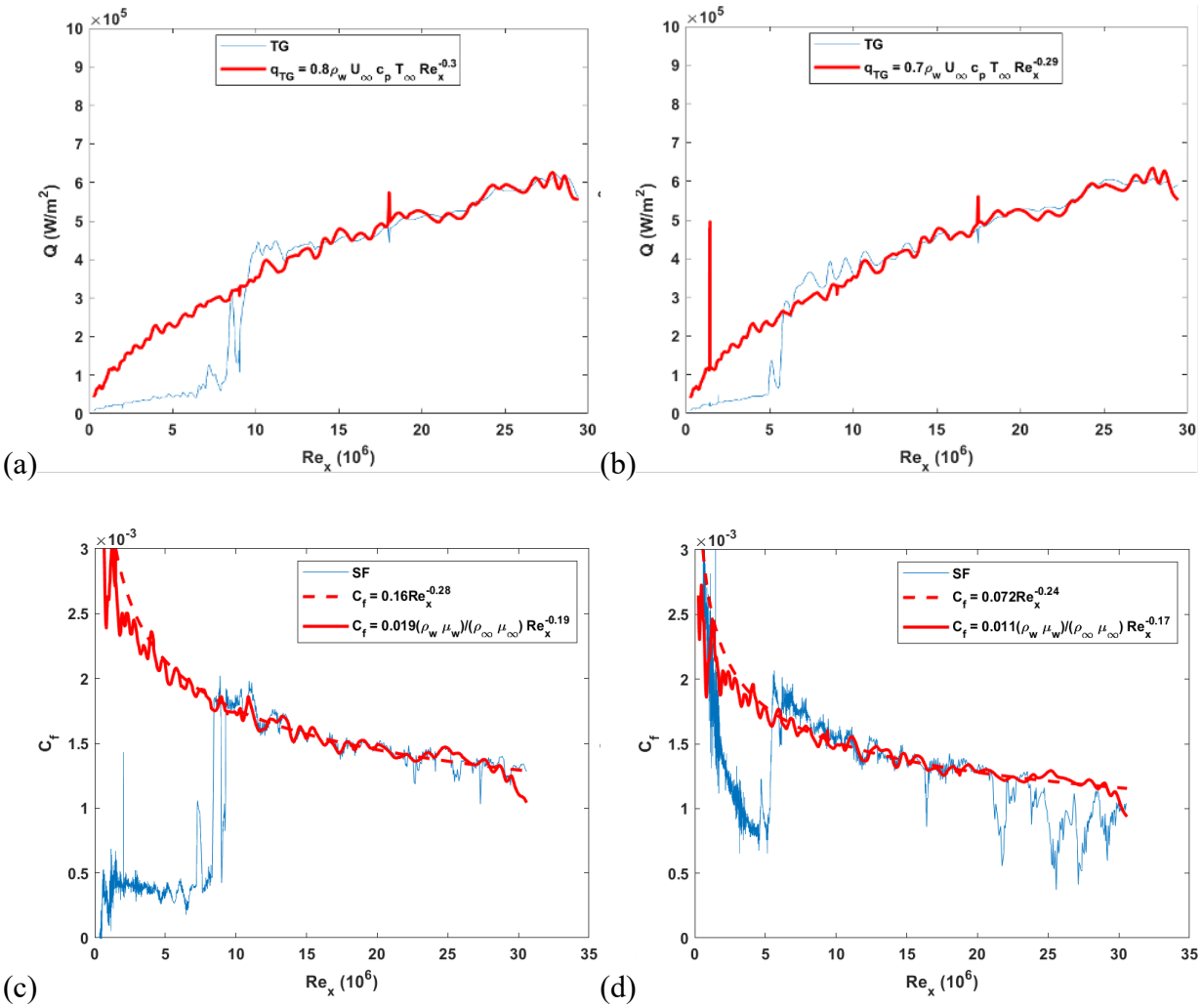

Figure 92. Curve fits of symmetrically placed row 3 TG & SF sensors. (a) TG-A-3-3. (b) TG-A-3-11. (c) SF-A-3-1. (d) SF-A-3-6.

Table 15 Row 3 SF Curve Fits

	Separate Compressibility Factor			Compressibility Factor Subsumed		
Sensor	*B*	*m*	R^2	*B'*	*m*	R^2
SF-A-3-1	0.631	0.019	0.190	0.161	0.280	0.641
SF-A-3-2	0.777	0.075	0.270	0.331	0.320	0.515
SF-A-3-3	0.893	1.926	0.500	3.669	0.500	0.409
SF-A-3-4	0.594	0.031	0.230	0.114	0.270	0.324
SF-A-3-5	0.534	0.032	0.220	0.120	0.260	0.614
SF-A-3-6	0.285	0.011	0.170	0.072	0.240	0.312
mean	0.116	0.033	0.216	0.159	0.274	0.481
median	0.221	0.031	0.225	0.120	0.270	0.515

DISTRIBUTION A: Distribution approved for public release.

Table 16 Row 3 TG Curve Fits

	Compressibility Factor Subsumed		
Sensor	B'	m	R^2
TG-A-3-01	0.038	0.100	0.947
TG-A-3-02	0.388	0.250	0.938
TG-A-3-03	0.800	0.300	0.935
TG-A-3-04	0.226	0.220	0.971
TG-A-3-05	0.355	0.260	0.939
TG-A-3-06	0.816	0.330	0.769
TG-A-3-07	0.173	0.230	0.972
TG-A-3-08	3.181	0.410	0.796
TG-A-3-09	0.147	0.210	0.918
TG-A-3-10	0.366	0.250	0.971
TG-A-3-11	0.699	0.290	0.956
TG-A-3-12	0.278	0.230	0.973
TG-A-3-13	0.049	0.110	0.955
TG-A-3-14	0.455	0.260	0.922
TG-A-3-15	0.254	0.230	0.926
TG-A-3-16	0.353	0.250	0.966
Mean	0.536	0.246	0.928
median	0.354	0.250	0.943

The curve fits described above were used to assess the Reynolds Analogy. The *St* number curve fits were projected to the SF locations, as indicated in Fig. 90. The skin friction values accounted for the alignment by adjusting by the cos(45°) and plotted in Fig. 93. Analysis of the SF pairs indicated that the turbulent skin friction was aligned closely with *x*-axis (private correspondence with R. Meritt, Ahmic CEO). This assumption was also verified by the present RANS simulations. Also plotted in black is the theoretical, incompressible, laminar value, $Pr^{2/3}$. For row 3, a similar process was completed, except that the curve fits for heat flux were interpolated from the TG sensors to the SF sensors. Recall, the wall temperature was projected forward from row 4, resulting in reduced confidence. For ease, a color-coordinated circle has been placed around each SF in Fig. 90 corresponding to the trace in Fig. 93. The results showed that the expected Reynolds Analogy under-predicted the flight data for rows 4 – 6 by 10%-25%. The row 3 data varied from 5% – 40%, but also had wall temperatures interpolated from downstream.

Several factors played a role in noted differences. An important factor was the relative spanwise location between MT sensors and SF sensors. In general, the heat flux was higher at outboard locations due to thinner boundary layers. This resulted in artificially inflated Reynolds analogy ratios when the *St* curves from inboard MT sensors were projected to the more outboard SF sensors. This primarily affected the row 4 SF sensors, with SF-A-4-2 showing a lower ratio than SF-A-4-1, which was almost entirely due to the MT-A-4-16, used in the denominator, being spatially located between them. Considering this error, the row 6 SF sensors were assessed

DISTRIBUTION A: Distribution approved for public release.

using the MT-A-4-16 curve, which was the surviving sensor with the smallest spanwise distance. By comparison, using MT-A-6- 4 almost doubled the ratio reported, since the heat flux near the centerline vortices was roughly half the outboard value. The angle of installation may have affected the results, as the average yaw during the test window was slightly negative, which would have aligned the freestream more with SF-A-4-1 and SF-A-6-2. The last potential factor was the change of variables to allow the flight heat flux data to be fitted. The flight Stanton number in Eq. (4) was defined with the following freestream-based denominator $\rho_\infty U_\infty c_p(T_0 - T_w)$. However, the theoretical definition, $\rho_e U_e c_p(T_{aw} - T_w)$, is based on boundary layer properties. The density was expected to be the largest source of error when the flight definition was compared to theory. The freestream stagnation temperature was nominally 10% higher than the adiabatic wall temperature, which may partially explain the observed differences with the theory. In summary, this analysis provided Reynolds analogy estimates accounting for compressibility, sensor placement, sensor failure, and a moving turbulent front in a 3-D boundary layer.

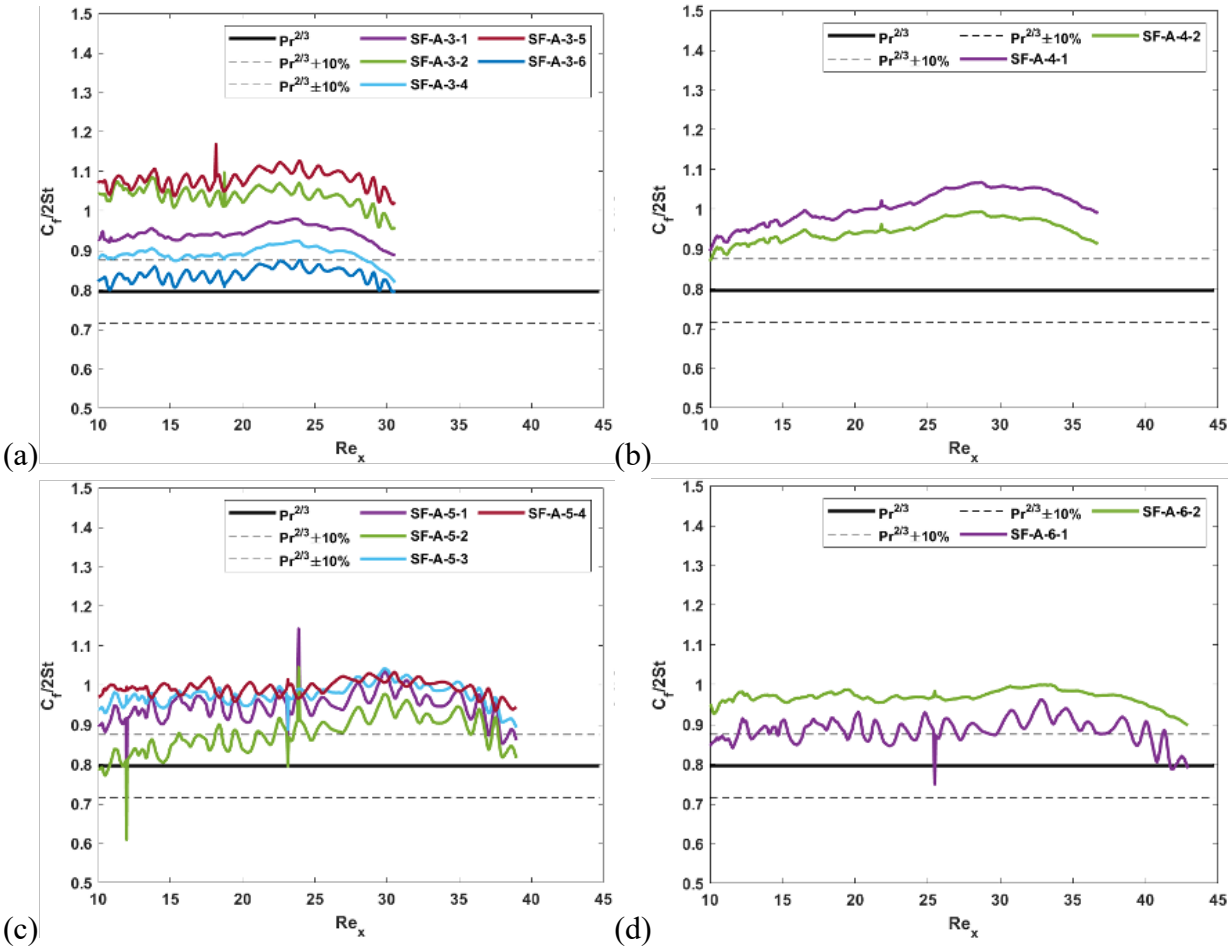

Figure 93. Reynolds Analogy using compressibility factor curve-fits. (a) Row 3. (b) Row 4. (c) Row 5. (d) Row 6.

DISTRIBUTION A: Distribution approved for public release.

7. CONCLUSIONS

7.1 SUMMARY

The basic research **bo**undary **l**ayer **t**urbulence (BOLT II) hypersonic flight experiment was executed. The research objective was to provide new data to close existing knowledge gaps to improve understanding and prediction of heat flux and skin friction associated with hypersonic flight. The flight geometry introduced a complex flow with pressure gradients, stationary vortex streaks, competing transition mechanisms, and a complex turbulent flow. The flight experiment was sponsored by the Air Force Office of Scientific Research (AFOSR). The name was changed by AFOSR to the "BOLT II Flight Experiment in Memory of Mike Holden." Experiments were performed on two sides of the flight hardware: Side A – natural transition and Side B – forced transition. The focus of the effort reported herein, and the delivered database, was Side A.

To meet the objective, the project had four goals, which were accomplished via four-year research program based on state-of-the-art numerical simulations, ground test, and flight test. The flight system design included determining the flight geometry, laminar and Reynolds averaged Navier-Stokes simulations, boundary layer stability analyses, subscale surface heating and off body measurements, flight system aerodynamic database generation, preliminary design review, flight vehicle design review, critical design review, thermal and structural loading analyses, instrumentation layout design, and design/procurement flight computers/data acquisition boards. The computations and stability analyses took place at Texas A&M University (TAMU), and the subscale tests took place in the TAMU Mach 6 Quiet tunnel (M6QT) and Actively Controlled Expansion tunnel. The fabrication included manufacture of the research geometry at CUBRC, installation of the instruments/flight computers/data acquisition boards, and ground tests on the instrumented flight hardware in the CUBRC LENSII tunnel. The flight experiment accomplishments included integration of the flight test article into the NASA flight payload, preflight tests, flight experiment (March 21, 2022), and postflight analyses. The full database was delivered to AFOSR. The key scientific contributions included:

1. Flight experiment design and execution. The Side A database for the BOLT II geometry was acquired to serve as a benchmark for laminar, transitional, and turbulent heating during flight. Two test windows were sampled, ascent and descent. On ascent, Mach numbers were hypersonic (> 5.0) for Re_L = 0.2 - 17.4 million. On descent, the hypersonic test window was extended to Reynolds up to 45.3 million and the Mach number was nominally constant at 6.0. During most of the test windows, $|\alpha|$ and $|\beta|$ remained less than 1.0 degrees. The acquired and analyzed data included heat flux, skin friction, surface and back face temperature, pressure, and pressure power spectra. These data were analyzed to provide new insights into the spatial and Reynolds number dependency on transition, early turbulence, equilibrium turbulence, and the Reynolds analogy.
2. Full-scale ground test database of the flight hardware and instruments in the CUBRC LENSII shock tunnel. The data were consistent across flight, full scale ground test, subscale ground test, and computation. These data provided confidence in current ground test and simulation methods.

DISTRIBUTION A: Distribution approved for public release.

3. Subscale ground test database for the 25% 1.35-m BOLT II geometry in the TAMU M6QT and ACE M = 5 – 8 Tunnel set to Mach 6. The ground test data included IR surface heat flux maps, surface pressure spectra focused on the mixed-mode transition region, and off-body field measurements of during breakdown of the mixed-mode transition mechanism. These data guided the flight instrumentation design.
4. Numerical simulation and boundary layer stability analyses for the BOLT II geometry at both wind tunnel and flight conditions. These data guided the flight instrumentation design.

The agreement across the methods demonstrated that the current research tools, if used collaboratively, have the potential to guide flight experiments and perhaps vehicle design. The non-technical contribution was the supported students and close engagement with the research community across academia, government, industry. A listing of key findings is provided in the next section.

7.2 KEY FINDINGS

The scientific flight objectives were met for the Side A. The low thermal conductivity of the stainless-steel frustum proved to mitigate spanwise conduction to justify use of the Cook-Felderman (CF) 1-D, semi-infinite data reduction technique. The CF method agreed with 3-D and 2-D finite difference methods for converting temperature to heat flux everywhere except near the leading edge, where spanwise conduction was found to be significant. The 2-D and 3-D data reduction methods agreed with conjugate heat transfer simulations across the flight trajectory. The Vatell heat flux sensors provided a direct measurement of the heat flux, but they experienced significant voltage drift that impacted interpretation of the results. The Ahmic brand skin friction, PCB surface pressure spectra, and mean pressure sensors all performed as planned.

Transition and turbulence were tracked across side A during ascent and descent. At least two mechanisms, a mixed-mode mechanism and a vortical instability, were responsible for transition in three separate regions of the vehicle. Transition was observed first the -z mixed-mode region, at Re_x = 4.0 – 6.0 x 10^6. This result is consistent with the TAMU M6QT ground tests, where transition was first observed at Re_x = ~3.5 x 10^6. In the +z mixed-mode region, transition took place later at Re_x = 7.0 – 10.0 x 10^6. Mixed-mode transition was characterized by a streak oscillating between 1 – 2 sensors that measured large transitional overshoots in both skin-friction and heat flux. Adjacent sensors experienced a muted overshoot and were likely overtaken by a turbulent wedge growing outward from the streak and moving upstream with increase Reynolds number. All functional high-frequency pressure sensors were located on the +z half, but the first to measure mixed-mode transition measured a broadband disturbance between 300-500 kHz just at the beginning of transition, although spectral content near the lower range of the sensor was also indicated. The other two sensors in the mixed-mode region also indicated a near 400 kHz disturbance just prior to turbulence onset, although they measured other frequencies as well. Stability calculations indicated that both second mode and crossflow were present. The subscale quiet tunnel off-body hot-film results indicated that the transition mechanism were likely Type-I and-II secondary instabilities associated with stationary mixed 2nd and crossflow mode vortex streak.

DISTRIBUTION A: Distribution approved for public release.

Near-centerline transition was characterized by large laminar oscillations and relatively stable turbulent values, although the sensors immediately outboard experience large oscillations during turbulence, suggesting growth of the vortical structure after transition. The near-centerline vortex path transition took place between $Re_x = 5.5 - 7.5 \times 10^6$. High-frequency pressure sensors indicated that all pressure fluctuations remained below 300 kHz. As far forward as row 2, it appeared that all sensors had transitioned by $Re_x = 12 \times 10^6$, although it may have been as high as 15×10^6 near the leading edge.

Leading-edge transition was observed at row 4 for $Re_x = 12.0 - 16.0 \times 10^6$.

The turbulent database from the BOLT II flight was also extensive. A subset of the temperature, heat flux, skin friction, pressure, and pressure fluctuations collected up to $Re_L = 45.3 \times 10^6$ were described herein. The data types were assimilated to create power-law curve fits Stanton number and skin friction coefficient verses Re_x, with and without including compressibility effects. Conjugate heat transfer simulations, both laminar and turbulent, agreed well with the experimental data, including the laminar leading edge. The Reynolds analogy ratios, based on the curve-fits to the data including compressibility, were generally between 0.9 and 1.0, which was slightly higher than the theoretical value of $Pr^{2/3}$. The observed differences were likely the result of spatial separation of the sensors and different definitions of Stanton number normalization between flight and theory.

Finally, in addition to these analyses, the flight data have been made available to researchers engaged in ground testing and simulations. *The full database was submitted to AFOSR in .csv format.*

7.2 Publications to Date

The initial public release of results was through the following papers (* indicates students supported by this project):

Meritt, R., Molinaro, N., Dufrene, A., MacLean, M., Bowersox, R. 2024. A Comparative Analysis of In-Flight and Full-Scale Ground Facility Wall Shear Measurements on the BOLT II Vehicle. *AIAA Pap. 2024-0308.*

Wirth,* J. 2023. *Characterizing 3D Hypersonic Boundary Layers with Transient Surface Heat Flux Measurements*. PhD Dissertation. Texas A&M University, College Station, TX.

Wirth,* J., Morreale,* B., Bowersox, R., Wheaton, B. 2023. Boundary Layer Turbulence Flight Experiment in Memory of Mike Holden: Side A Flight Data. *AIAA Pap. 2023-3440*.

Meritt, R., Molinaro, N., Dufrene, A., and Bowersox, R. 2023. A Summary of AFOSR BOLT II Direct Wall Shear Stress. *AIAA Pap. 2023-3452*.

Kostak-Teplicek,* H., Bowersox, R. 2023. Hypersonic Stability and Breakdown Measurements on the AFRL/AFOSR BOLT II Geometry," *AIAA Pap. 2023-0085*.

Wirth,* J., Morreale,* B, Kostak-Teplicek,* H., Bowersox, R., Dufrene, A., Portoni, P., Wadhams, T. 2023. Boundary Layer Turbulence Flight Experiment in Memory of Mike Holden: Side A Flight Data. *AIAA Pap. 2023-0862*.

DISTRIBUTION A: Distribution approved for public release.

Dufrene, A., Portoni, P., Wadhams, T., Kostak-Teplicek,* H., Bowersox, R. 2023. Boundary Layer Turbulence Flight Experiment in Memory of Mike Holden: Vehicle Design, Instrumentation, and Ground Test Results. *AIAA Pap. 2023-0478*.

Morreale,* B., Swinny,* E., Kostak-Teplicek,* H., Bowersox, R., White, E., Dufrene, A., Wadhams, T., Popkin, S., Adamczak, D., Tancred, T. 2023. Boundary Layer Turbulence Flight Experiment in Memory of Mike Holden: Pre-Flight Mission Design. *AIAA Pap. 2023-0477*.

Kostak-Teplicek,* H. 2022. *Stability and Breakdown Measurements on the AFRL/AFOSR Boundary Layer Turbulence (BOLT II) Flight Geometry.* PhD Dissertation. Texas A&M University, College Station, TX.

Berry, S., Semper, M., Riha,* A., Mullen,* C., Reed, H., Dufrene, A., Fasel, H. 2022. Development of the BOLT II Roughness Experiment for Flight. *AIAA Pap. 2022-0347.*

Swinny,* E. 2021. *Computational Heat Flux Predictions for the AFOSR BOLT-II Flight Test*. MS Thesis. Texas A&M University, College Station, TX.

Mullen,* C., Reed, H. 2021. Computational Modeling and Stability Analysis of BOLT Hypersonic Geometry Including Off-Nominal Conditions. *Theor. Comp. Fluid Dyn.*, Vol. 36, pp. 251 – 276.

Mullen,* C. 2021. *Investigations of Basic State Numerics Applied to Stability Problems on Complex Hypersonic Geometries*. PhD Dissertation. Texas A&M University, College Station, TX.

DISTRIBUTION A: Distribution approved for public release.

8. FACILITIES AND INSTRUMENTATION

8.1 TAMU NATIONAL AEROTHERMOCHEMISTRY AND HYPERSONIC FLIGHT LABORATORY

The mission of the Texas A&M University National Aerothermochemistry and Hypersonic Flight Laboratory (NAHL) is an experimental, numerical, and theory-based venue for students and research scientists to improve our knowledge and control of high-speed and hypersonic flows.

Wind Tunnel Facilities. The NAHL houses three facilities: (1) Actively Controlled Expansion Tunnel (ACE), (2) Mach 6 Quiet Tunnel (M6QT), and (3) Hypervelocity Expansion Tunnel (HXT); see Fig. 94 for photographs of the facilities.

HXT utilizes a 0.5-m diameter shock tube fitted with a 3-ft exit diameter nozzle and is tailored to provide true temperature "aerothermally clean" air for Mach numbers up to 15 (12 MJ/kg). Beyond this, the flow experiences real gas effects in the freestream. The facility can produce flight enthalpy test conditions to Mach 25. However, the facility can also be operated in a cold flow mode for high Reynolds numbers as shown in Fig. 95 and Table 16. The low Reynolds number operation is enabled by the use of an additional turbopump to reduce the pressure within the accelerator section to 10^{-4} Torr.

Figure 94. NAHL test capabilities with sponsors. (a) Hypervelocity Expansion Tunnel (HXT). (b) Mach 6 Quiet Tunnel (M6QT). (c) Actively Controlled Expansion (ACE) Tunnel. (d) Boundary Layer Turbulence (BOLT II) Hypersonic Flight Test.

DISTRIBUTION A: Distribution approved for public release.

The M6QT is a low-disturbance facility, where the tunnel wall boundary layers remain laminar to a unit *Re*/m of 10.5 x 10^6. The facility is described in detail by Hofferth *et al.* (2012). This facility is the original hypersonic quiet tunnel developed at NASA Langley. The flow disturbances are plotted in Fig. 78. The ACE tunnel is "conventional" noise tunnel, where the boundary layers on the tunnel walls transition to turbulence and radiate noise into the freestream, as shown as in Fig. 96. The ACE tunnel observes transition near *Re*/m = 3 x10^6. The tunnels share an air supply and vacuum system. The high-pressure air is filtered (99% efficient sub-micron), desiccant dried to 233K, and stored in a 23.5 m^3 tank at 170 atm. Air to the tunnels is heated by a 0.5 MW electric-resistance heater (up to 530K output) and filtered (99.9% at 1-micron) just before entering the tunnel. Additional direct electrical heating of the facilities is used to help ensure thermal stability. The vacuum is supplied by a two-stage venturi air-ejector system capable of generating a vacuum of 4.0 torr. The maximum tunnel run time is 40 s, which is limited by the high mass-flow requirements for the ejector. The ACE tunnel can pitch and roll models during tunnel runs.

M6QT and ACE tunnel facility freestream conditions are computed using the settling chamber total conditions and nozzle static pressure. The settling chamber pressure for the M6QT pressure is measured using a temperature compensated MKS Baratron 615A High-Accuracy Capacitance Manometer (±0.12% of reading) with an MKS 670B Signal Conditioner. The ACE tunnel settling chamber pressure is measured with an Endevco 8540-200 high temperature transducer (±0.75%). The settling chamber temperature for both tunnels is measured with a Type K thermocouple probe (±1.0%). The ACE tunnel static pressure is measured with an MKS Baratron 631C capacitance manometer that is internally heated to 473K (±0.5% of the reading). The quiet tunnel static pressure is measured by an MKS 902 vacuum transducer (±1.0% of reading). The available flow conditions are summarized in Fig. 95 and Table 16.

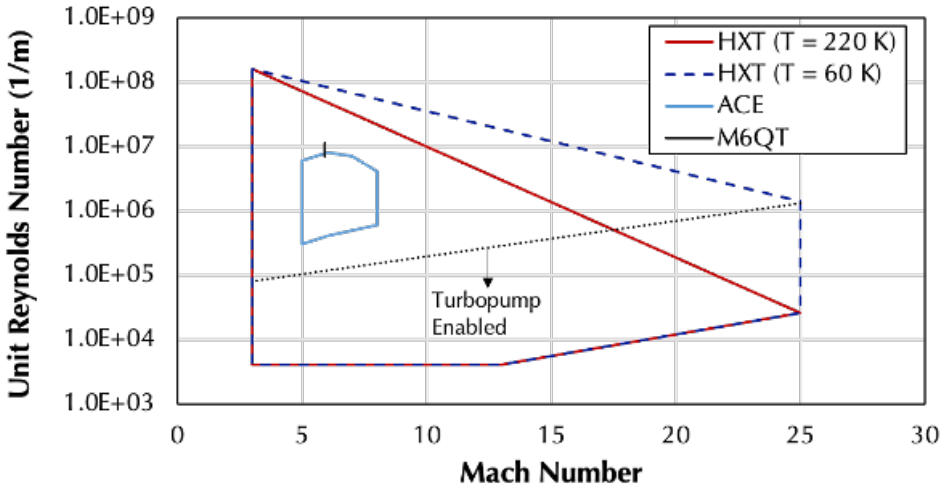

Figure 95. Available flow conditions for NAHL facilities.

DISTRIBUTION A: Distribution approved for public release.

Table 16: NAHL Facilities

Facility	Mach No.	Enthalpy (MJ/kg)	Test Section	Run Time
Hypervelocity Expansion (HXT)	3 – 25	0.4–30	0.92 m	0.2–3.0 ms
Mach 6 Quiet Tunnel (M6QT)	5.9	Cold	0.19 m	40 s
Actively Controlled Exp. (ACE) Tunnel	5 – 8	Cold	0.23x0.36 m	40 s

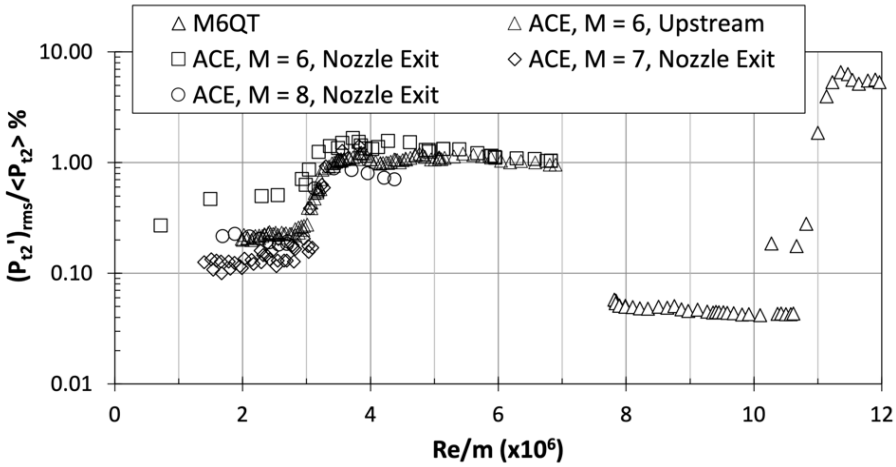

Figure 96. Available flow conditions for NAHL facilities.

Instrumentation. The conventional instrumentation housed within the NAHL includes planar laser induced fluorescence (PLIF), molecular tagging velocimetry (MTV), vibrationally excited NO monitoring (VENOM), particle image velocimetry (PIV), hot-wire anemometry, pressure sensitive paint, temperature sensitive paints, conventional schlieren, focusing schlieren w/deflectometry, FLIR infrared thermography (8-9 μmand 3-5 μm), high-speed (1 MHz) photography/focused schlieren, floating element skin friction sensors, and a Keyence LK-H022 laser profilometer with 0.02-micron resolution to quantify the surface finish. A key advantage of the NAL is the proximity to the Aerospace Laboratory for Lasers, Electromagnetics, and Optics (ALLEMO, Director R. Miles). This laboratory provides access to an extensive suite of advanced laser diagnostics including MHz pulse burst lasers, FLEET, two-photon PLIF, fs/ps hybrid CARS, filtered Rayleigh scattering, and Thomson scattering. The lab also contains many photonic devices and cameras, including a variety of single and multimode optical fibers, etalons, high-speed photodetectors and electro-optic devices including several visible and NIR acousto-optic modulators with RF amplifiers, electro-optic modulator, high-speed Shimadzu framing cameras (HPV-2 and HPV-X2), for 1+ MHz imaging, Photron SA-Z high speed camera for FLEET and high speed OES, LaVision High-Speed IRO intensifiers capable of operating at MHz rates with different photocathodes optimized for UV and NIR detection, Princeton Instruments Isoplane-160, and two Isoplane-320 imaging spectrometers with triple gratings for low and high resolution spectroscopy over UV-VIS-NIR,

DISTRIBUTION A: Distribution approved for public release.

Light Machinery high-resolution NIR VIPA spectrometer, and PIMAX 1024i intensified cameras with dual gating capability.

Computational Methods. The TAMU researchers have developed a suite of research codes to examine theoretical model performance; these codes include computational fluid dynamics codes, method of characteristics, and boundary layer solvers. The available government/commercial codes include DPLR CFD (NASA), US3D CFD (UMN, VirtusAero), Pointwise grid generation (Pointwise), and NEQAir (NASA) for non-equilibrium radiative transport and spectra. The team also utilizes the TAMU High Performance Research Computing and UT Texas Advanced Computing centers.

8.2 CUBRC LENS SHOCK TUNNEL FACILITIES

During the past 20 years, three large new ground test facilities, LENS I, LENS II, and LENS XX, have been constructed for the US Government and its contractors by CUBRC and successfully employed to directly replicate flight conditions on flight vehicles flying at velocities from 900 m/s to 9,000 m/s at altitudes from sea level to 60 km. The construction of these wind tunnels was driven by the need to design and evaluate hypersonic vehicles whose performance were controlled by complex flow phenomena, such as boundary layer transition and turbulence, compressible turbulent shear layer mixing, shock/turbulence interaction, and "real gas" or combustion chemistry, which are poorly understood and cannot currently be predicted with a confidence level necessary for design of flight vehicles. Additionally, such flows cannot be easily scaled. The nonequilibrium fluid dynamic and chemical processes which occur in regions of boundary layer transition and turbulence can only be replicated with any accuracy on full-scale test articles with flight matching free-stream conditions.

The LENS I facility has been employed to successfully evaluate the performance of seekerhead, guidance, and control systems for hypersonic interceptors traveling at velocities from 900 m/s to 4,500 m/s. These studies were performed on full-scale vehicle configurations with operating components (such as rocket motors) to directly replicate transitional, unsteady, burning and radiating flowfields which control the aerothermal, aero-optic, aero-acoustic and propulsion characteristics of the interceptor systems. The LENS I tunnel has been used successfully in direct simulation studies to evaluate the propulsion characteristics of the X-43, the Hy-Tech/ARRMD, HYCAUSE, and ASET class of inward turning hydrogen- and hydrocarbon-fueled scramjet engines. Here the transitional and tripped flows over the inlet and shock interaction that dominated flows in the isolator, combustor and nozzle were replicated with full-scale hardware in combusting flows at duplicated flight conditions (Holden *et al.* 2008, 2008a, 2008b). In addition, LENS I has become a key facility for the testing of reentry vehicle configurations such as the X-38, Mars Science Laboratory, Space Shuttle Orbiter, and ORION CEV/CRV configurations (Wadhams *et al.* 2009 & 2010). These studies were conducted with the goal of studying laminar, transitional, and turbulent heating, gap and cavity heating, and studies of Mach number, Reynolds number, and model attitude trends. Finally LENS I was employed in the original pre-flight evaluations of HIFiRE-1 and HIFiRE-5.

DISTRIBUTION A: Distribution approved for public release.

The LENS IIS tunnel was constructed specifically to conduct full-scale testing of interceptor systems designed to operate at velocities from 900 m/s to 2,700 m/s at altitudes from 3 to 36 km. The tunnel has been used in aerothermal studies for the Standard Missile, THAAD, HyFly, and IH-108 OTS Return to Flight Shuttle programs and has provided heating data which directly duplicates those generated under actual flight conditions. In ground tests of the SM BLK IVA, heat transfer measurements were made over the full-scale flight hardware to directly determine the aerothermal loads and levels of coolant required to control the seekerhead dome temperature. Here the complex coolant and shock interactions over the dome made it impossible to compute the aerothermal and aero-optic loads with accuracy or replicate with sub-scale tests at simulated flight conditions. More recently, the LENS IIS facility has been employed in post-flight evaluations of boundary layer transition on HIFiRE-1 and HIFiRE-5 to close the loop between ground, computation, and flight environment. LENS I and LENS IIS now have overlapping capabilities in the Mach 6-8 range with the addition of a large, higher Mach number nozzle for LENS IIS in 2010. LENS IIS is ideally suited for BOLT flight duplicated ground testing with significantly longer test times than LENS I and a nozzle exit plane diameter of 180 cm compared to the 110 cm. A photograph of both facilities is shown below in Fig. 97 with LENS I on the left-hand side and LENS IIS on the right-hand-side.

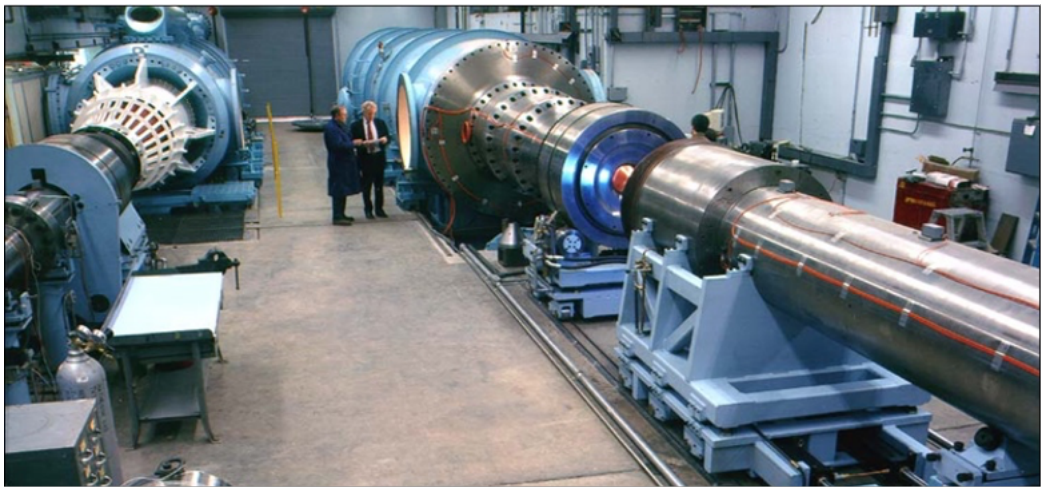

Figure 97. Photograph of LENS Shock Tunnels

8.3 COMPUTATIONAL RESOURCES

The 3-D Nonlinear Parabolized Stability Equation toolkit EPIC was developed in house (Oliviero *et al.* 2015) and offers true 3-D LPSE and NPSE predictions. NASA DPLR, University of Minnesota US3D and Pointwise are all available in-house for the basic states. The EPIC code is formulated in primitive variables for compressible 3-D flow and uses an orthogonal curvilinear coordinate system with grid clustering. The code presently assumes an ideal gas but, because of its modular architecture, it can be expanded in a straight-forward fashion to include the effects of thermo-chemical nonequilibrium (Stuckert & Reed 1994). Models for a predefined marching path and the spanwise wavenumber variation in the marching direction have been formulated. A global

DISTRIBUTION A: Distribution approved for public release.

stability module (the 2-D analog of the classic linear stability theory) to predict secondary instabilities and thus insipient breakdown for nonlinearly distorted basic state profiles, has been formulated and seamlessly integrated (Moyes *et al.* 2016). EPIC and its features have all been verified and validated for the range of instabilities and interactions (crossflow [stationary, travelling], second mode, Görtler, oblique modes, interactions, etc.) with various 2-D and 3-D hypersonic experiments at TAMU– see, for example, Reed *at al.* (2015), Moyes *et al.* (2016), Kocian *et al.* (2016, 2017).

The Texas Advanced Computing Center (TACC) is a high-performance, computing resource center at The University of Texas at Austin. TACC maintains the Lonestar cluster for export-controlled software; all Lonestar administrators are US Citizens.

8.4 Design and Analysis Software at TAMU and CUBRC

The design staffs at TAMU and CUBRC have full complements of design and analysis tools at their disposal to ensure the highest degree of accuracy and quality for hardware and model design work. Computer-Aided Design (CAD) work is primarily performed with NX (Unigraphics), but other design tools including SolidWorks, AutoCAD, Mechanical Desktop, and Inventor are available as needed. NX is a powerful design tool using the parasolid format as its geometric modeling kernel for parametric and direct solid/surface modelling. All components of the Flight Geometry assembly will be modeled, including fasteners, instrumentation, and government provided sensor data collection boards to ensure geometric and weight constraints are met, ensure proper fit of all components, provide estimates of mass, center-of-gravity and moments of inertia, and aid in finite element structural analyses of both the main structure and internal components.

Complementing the design capabilities, ANSYS Mechanical Enterprise is utilized by our professional engineers and design team to complete robust structural analyses to guarantee quality and safety prior to fabrication of hardware. Mechanical Enterprise is the most comprehensive license option available and provides stress, thermal, and vibrational simulations on simple parts or complex assemblies for engineering assessments. In-depth analysis of coupled thermal and mechanical loading can be completed with both steady-state and transient analyses, and non-linear deformations and stresses will be evaluated, where applicable. The thermal analysis is fully 3-D and supports conduction, convection and radiation effects with temperature-dependent material properties.

8.5 Machining Capabilities

8.5.1 CUBRC

CUBRC uses a variety of CNC lathes and mills to machine complex model parts and assemblies every day. Parts as long as 2 m and as wide as 1 m are regularly machined, as well as parts with small specialized inserts or protuberances on the millimeter scale. CUBRC has skilled machining and fabrication personnel to construct complex parts and assemblies with high precision. When testing demand is high, local machine shops are sourced to help with the demand, but the CUBRC machine shop machines a large majority of the models tested in the LENS facilities and

DISTRIBUTION A: Distribution approved for public release.

has machined models for other tunnels as well, including the Purdue University Quiet Tunnel. In addition to the machining capabilities, CUBRC has a fabrication shop and has procedures for welding stainless, mild, and alloy steels, as well as aluminum, Inconel, titanium, magnesium, and copper. It is unlikely that the Flight Geometry will require welded components, but the capability exists in-house if required.

8.5.2 TAMU

The TAMU Aerospace Machine Shop will be employed to construct the sub-scale model. This resource is listed as back-up to help alleviate any unforeseen manufacturing delays. The Aerospace Engineering Low-Speed Wind Tunnel machine shop houses numerous CNC and manual milling machines operated by an excellent machinist with extensive experience meeting wind-tunnel model fabrication requirements. The major CNC equipment includes a Fadal CNC milling machine with a 60-in range and a 4^{th} axis, a Romi M20 CNC lathe, a Romi D1250 CNC milling machine, and an Agie Charmilles Wire EDM machine.

DISTRIBUTION A: Distribution approved for public release.

9. Acknowledgement and Disclaimer

The authors gratefully acknowledge the AFOSR (Drs. Popkin, Leyva, Pokines) for supporting this project and a companion DURIP award. Their leadership was essential to the success of the program. Additional support was provided for the flight systems by OUSD(R&E) (Dr. Nair) and AFRL (Dr. Bisek). The authors also gratefully acknowledge Lockheed Martin Company for additional financial support of post flight data. The authors acknowledge the technical support and advice from the government, industry, and academic reviewers and collaborators.

The contents herein are solely the responsibility of the author and do not necessarily represent the official views of Department of Defense Office or other sponsors.

DISTRIBUTION A: Distribution approved for public release.

10. REFERENCES

Adrian, R., Meinhart, C., and Tomkins, C. 2000. Vortex Organization in the Outer Region of the Turbulent Boundary Layer. *J. Fluid Mech.*, Vol. 422, pp. 1-54.

Aftosmis, M., Berger, M., Adomavicius, G. 2010. A Parallel Multilevel Method for Adaptively Refined Cartesian Grids with Embedded Boundaries. AIAA Pap 2010-0808.

Balakumar, P., Owens, L. 2010. Stability of hypersonic boundary layers on a cone at angle of attack. *AIAA Pap. 2010-4718.*

Balakumar, P., Reed, H. 1991. Stability of 3-D supersonic boundary layers. *Phys. Fluids A*. Vol. 3, No. 4, pp. 617-32.

Beresh, S., Henfling, J., Spillers, R., Pruett, B. 2011. Fluctuating wall pressures measured beneath a supersonic turbulent boundary layer. *Physics of Fluids*, Vol. 23, No. 7, pp. 075110.

Berridge, D., Kostak, H., Mckiernan, G., Wheaton, B., Wolf, T. D., Schneider, S. P. 2019. Hypersonic Ground Tests with High-Frequency Instrumentation in Support of the Boundary Layer Transition (BOLT) Flight Experiment. *AIAA Pap. 2019-0090.*

Berry, S., and Wheaton, B. 2023. BOLT II Roughness Side Flight Results. *AIAA Pap*. 2023-0684.

Berry S., Auslender A., Dilley A., and Calleja J. 2001. Hypersonic Boundary Layer Trip Development for Hyper-X. *Journal of Spacecraft and Rockets*. Vol. 38, No. 6, pp. 853–864.

Blanchard, A., Lachowicz, J., Wilkinson, S. 1997. NASA Langley Mach 6 quiet-tunnel performance. *AIAA J*. Vol. 35, No. 1, pp. 23-8.

Borg, M., Kimmel R. 2016. Simultaneous infrared and pressure measurements of crossflow instability modes for HIFiRE-5. *AIAA Pap. 2016-0354*.

Borg, M, Kimmel R, Hofferth J, Mai C, Bowersox R. 2015. Freestream effects on boundary layer disturbances for HIFiRE-5. *AIAA Pap. 2015-0278* (AFRL-RQ-WP-TP-2015-0148).

Borg, M., Kimmel R, Stanfield S. 2011. Attachment-line and crossflow instability in a quiet hypersonic wind tunnel. *AIAA Pap. 2011-3247*.

Borg, M., Kimmel R, Stanfield S. 2012. Stationary crossflow instability and co-located traveling disturbances on an elliptic cone in quiet hypersonic flow, Paper 34, ATV-200 Specialist Meeting on Hypersonic Transition, San Diego, CA.

Borg, M., Kimmel R. 2017. Measurements of crossflow instability modes for HIFiRE-5 at angle of attack. *AIAA Pap. 2017-1681.*

Borg, M., Schneider S., and Juliano T. 2008. Effect of Freestream Noise on Roughness-Induced Transition for the X-51A Forebody. *AIAA Paper 2008-0592*.

Bowersox, R. 1996. Combined Laser Doppler Velocimetry and Cross-Wire Anemometry Analysis for Supersonic Turbulent Flow. *AIAA Journal,* Vol. 34, No. 11, pp. 2269-2275.

Bowersox, R. 2009. Extension of Equilibrium Turbulent Heat Flux models to High-Speed Shear Flows. *J. Fluid Mech.* Vol. 633, pp. 61-70.

Butler, C., McKiernan, G., Wheaton, B. 2023. Initial BiGlobal Stability Analysis of the BOLT II Flight Experiment. *AIAA Pap.* 2023-0291.

Cebeci, T., Smith, O. 1974. *Analysis of Turbulent Boundary Layers*, Academic Press.

DISTRIBUTION A: Distribution approved for public release.

Chen, F., Wilkinson, S., Beckwith, I. 1991. Görtler instability and hypersonic quiet nozzle design. *AIAA Pap. 1991-1648.*

Choudhari M., Chang, C., Jentink, T., Li, F., Berger, K., Candler, G., Kimmel, R. 2009. Transition analysis for the HIFiRE-5 vehicle. *AIAA Pap. 2009-4056.*

Cook, W., Felderman, E. 1966. Reduction of Data from Thin-Film Heat- Transfer Gages: A Concise Numerical Technique. *AIAA Journal*, Vol. 4, No.3, pp.561-562.

Corke, T., Arndt, A., Matlis, E., Neel, I., Bowersox, RDW. 2018. Hypersonic Boundary Layer Crossflow Transition Characteristics and Control," *AIAA pap. 2018-0352*.

Craig, S., Saric, W. 2016. Crossflow instability in a hypersonic boundary layer. *J. Fluid Mech.* Vol. 808, pp. 224-244.

Daly, B. and Harlow, H., "Transport Equations in Turbulence," *Physics of Fluids*, Vol. 13, No. 11, 1970, pp. 2634-2649.

Dinzl, D., Candler, G. 2016. Direct numerical simulation of crossflow instability excited by microscale roughness on HIFiRE-5. *AIAA Pap. 2016-0353*.

Duan, L., Beekman, I., and Martin, M. 2010., Direct Numerical Simulation of Hypersonic Turbulent Boundary Layers: Part. 2 Effect of Wall Temperature. *J. Fluid Mech*. Vol. 655.

Dufrene, A., Portoni, P., Wadhams, T., Kostak-Teplicek, H., Bowersox, R. 2023. Boundary Layer Turbulence Flight Experiment in Memory of Mike Holden: Vehicle Design, Instrumentation, and Ground Test Results. *AIAA Pap. 2023-0478*.

Ekoto, I., Bowersox, RDW, Goss, L., and Beutner, T. 2009. Response of Supersonic Turbulent Boundary Layers to Local and Global Mechanical Distortions. *J. Fluid Mech.*, Vol. 630, pp. 225-265.

Favre, A. 1969. Statistical Equation of Turbulent Gases, in *Problems of Hydrodynamics and Continuum Mechanics*, SIAM, Philadelphia, PA.

Fedorov, A. 2011. Transition and stability of high-speed boundary layers. *Annu. Rev. Fluid Mech.* 43:79-95

Gatski, T. and Bonnet, J.-P. 2013. *Compressibility, Turbulence, and High-Speed Flow*, 2nd Ed., Elsevier.

Gnoffo, P., Berry, S., and Van Norman, J. 2013. Uncertainty Assessments of Hypersonic Shock Wave–Turbulent Boundary-Layer Interactions at Compression Corners. *J. Spacecraft and Rockets*, Vol. 50, No. 1, pp. 69-95.

Gronvall, J., Johnson, H., Candler, G. 2012. Hypersonic three-dimensional boundary layer transition on a cone at angle of attack. *AIAA Pap. 2012-2822*.

Hofferth, J., Bowersox, R., Saric, W. 2010. The Mach 6 Quiet Tunnel at Texas A&M: quiet flow performance. *AIAA Pap. 2010-4794*

Holden, M., Wadhams, T., MacLean, M., Mundy, E. 2008. Review of studies of boundary layer transition in hypersonic flows over axisymmetric and elliptic cones conducted in the CUBRC shock tunnels. *AIAA Pap. 2009-0782.*

Holden, M., Wadhams, T., and MacLean, M. 2008a. A Review of Full-Scale Ramjet and Scramjet Engine Studies conducted at Duplicated Flight Conditions in the LENS I and II Hypersonic

DISTRIBUTION A: Distribution approved for public release.

Tunnels," JANNAF-1006, 30th JANNAF Airbreathing Propulsion Meeting, Boston, MA.
Holden, M., Wadhams, T., MacLean, M. 2008b. Ground Tests at Duplicated Flight Conditions of Boundary Layer Transition and Shock Interaction Phenomena on the HTV-2, X-51 and HIFiRE 1. *AIAA Pap.*
Horvath, T. et al. 2010. The HYTHIRM Project: Flight Thermography of the Space Shuttle During Hypersonic Re-Entry, *AIAA Pa. 2010-0241.*
Horvath, T., Berry, S., Hollis, B., Chang, C., Singer, B. 2002. Boundary layer transition on slender cones in conventional and low disturbance Mach 6 wind tunnels. *AIAA Pap. 2002-2743.*
Howard, M., Bradley, A., Bova, S., Overfelt, J., Wagnild, R., Dinzl, D., Hoemmen, M., Klinvex, A. 2017. Towards Performance Portability in a Compressible CFD Code. *AIAA Pap. 2017-4407.*
Johnston, Z., Candler, G. 2021. Hypersonic simulations of the BoLT-II subscale geometry. *AIAA Pap. 2021-0366.*
Johnston, Z., Hemati, M., Candler, G.. 2022. Modal analysis of instabilities in the BOLT-2 flow-field. *AIAA Pap.* 2022-0348.
Johnston, Z., Candler, G., "Hypersonic Boundary Layer Transition of the BoLT-2 Flowfield at Flight Conditions," *AIAA Pap.* 2023-0084.
Kays, W. and Crawford, M. 1993. *Convective Heat and Mass Transfer, 3rd Ed.*, McGraw-Hill, New York.
Kilcoyne, D. 2020. BOLT II CDR Presentation: BOLT 2 46.027 DR/Holden DR.
Kimmel, R., Poggie, J., Schwoerke, S. 1999. Laminar-turbulent transition in a Mach 8 elliptic cone flow. *AIAA J.* 37(9):1080-87.
Knutson, A., Thome, J., Candler, G. 2021. Numerical Simulation of Instabilities in the Boundary-Layer Transition Experiment Flowfield. *Journal of Spacecraft and Rockets*. Vol. 58, No. 1, pp. 90-99.
Kocian, T., Moyes, A., Mullen, D., Reed, H. 2016. PSE and spatial biglobal instability analysis of HIFiRE-5 geometry. *AIAA Pap. 2016-3346.*
Kocian, T., Moyes, A., Mullen, D., Reed, H. 2017. PSE and spatial biglobal instability analysis of reduced scale and flight HIFiRE-5 geometry. *AIAA Pap. 2017-0768.*
Kostak, H., Bowersox, R., McKiernan, G., Thome, J., Candler, G., King, R. 2019. Freestream Disturbance Effects on Boundary Layer Instability and Transition on the AFOSR BOLT Geometry. *AIAA Pap. 2019-0088*.
Kostak, H., Bowersox, R., 2021. Preflight Ground Test Analyses of the Boundary Layer Transition (BOLT) Flight Geometry. *J. Spacecraft and Rockets*, Vol.58, No. 1, pp. 67-77.
Kostak-Teplicek, H. 2022. Stability and Breakdown Measurements on the AFRL/AFOSR Boundary Layer Turbulence (BOLT II) Flight Geometry. *PhD dissertation*. Texas A&M University, College Station, TX.
Kostak-Teplicek, H., Bowersox, R. 2023. Hypersonic Stability and Breakdown Measurements on the AFRL/AFOSR BOLT II Geometry," *AIAA Pap. 2023-0085*.
Kuehl J, Perez E, Reed H. 2012. JoKHeR: NPSE simulations of hypersonic crossflow instability.

DISTRIBUTION A: Distribution approved for public release.

AIAA Pap. 2012-0921.

Landsberg, W. Sandral, J., Mee, D., Veeraragavan, A., Dufrene, A. 2023. Heat Transfer Measurements of the BoLT II Flight Experiment Model in the T4 Reflected Shock Tunnel," *AIAA Pap.* 2023-0087.

Lau, K. 2008. Hypersonic boundary-layer transition: Application to high-speed vehicle design. *J. Spacecr. Rockets* Vol 45, No. 2, pp. 176-83.

Launder, B., Reece, G., and Rodi, W. 1975. Progress in the Development of a Reynolds-Stress Turbulence Closure," *J. Fluid Mech.*, Vol. 68, pp. 537-566.

Leidy, A. N. 2023. BOLT II Forebody Surface Measurement Analysis. NASA/TM-20230000169, 2023.

Leidy, A., Neel, I., Tichenor, N., Bowersox, R., Schmisseur, J. 2021. Tunnel Noise Effects on Hypersonic Cylinder-Induced Transitional Shock Wave Boundary Layer Interactions. *AIAA Journal,* Vol. 59, No. 7, pp. 2357-2367.

Leidy, A., Neel, I., Tichenor, N., Bowersox, R. 2020. High-Speed Schlieren Imaging of Cylinder-Induced Hypersonic-Shock-Wave–Boundary-Layer Interactions. *AIAA Journal*, Vol. 58, No. 7, pp. 3090-3099.

Lesieur, M., Metais, O., and Comte, P. 2005. Large-Eddy Simulations of Turbulence. Cambridge University Press.

Li, F., Choudhari, M., Chang, C-L., Kimmel, R., Adamczak, D., Smith, M. 2011. Transition analysis for HIRiRE experiments. *AIAA Pap. 2011-3414.*

Li. F., Choudhari, M., Chang, C-L,, White, J., Kimmel, R., Adamczak, D., Borg, M., Stanfield, S., Smith, M. 2012. Stability Analysis for. HIFiRE Experiments. *AIAA Pap. 2012-2961*.

Li. F., Choudhari, M., Chang, C-L,, White, J. 2010. Analysis of instabilities in non-axisymmetric hypersonic boundary layers over cones. *AIAA Pap. 2010-4643.*

Lin, T. 2008. Influence of laminar boundary-layer transition on entry vehicle designs. *J. Spacecr. Rockets* 45(2):165-75.

Mack, L. 1984. Boundary Layer Stability Theory. AGARD Report No. 709: *Special Course on Stability and Transition of Laminar Flow*. 3.1-81.

Mckiernan, G. R., Chynoweth, B. C., Schneider, S. P., Berridge, D. C., Wheaton, B. M. 2021. Boundary Layer Transition Preflight Experiments in a Mach-6 Quiet Tunnel. *Journal of Spacecraft and Rockets*. Vol. 58, No. 1, pp. 54-66.

Menter, F. August 1994. Two-Equation Eddy-Viscosity Turbulence Models for Engineering Applications. *AIAA Journal*, Vol. 32, No. 8, pp. 1598–1605.

Merritt, R., Molinaro, N., Dufrene, A., and Bowersox, R. 2023. A Summary of AFOSR BOLT II Direct Wall Shear Stress. *AIAA Pap. 2023-3452*.

Merit, R., Molinaro, N., Dufrene, A., MacLean, M., Bowersox, R. 2024. A Comparative Analysis of In-Flight and Full-Scale Ground Facility Wall Shear Measurements on the BOLT II Vehicle. *AIAA Pa. 2024-0308*.

Morkovin, M. 1961. Effects of Compressibility on Turbulent Flows," in Mechanique de la Turbulence, CNRS, Paris.

DISTRIBUTION A: Distribution approved for public release.

Morkovin, M., Reshotko, E. 1990. Dialogue on progress and issues in stability and transition research. In *Laminar-Turbul. Transit.*, ed. Arnal and Michel, New York: Springer-Verlag. pp. 3–29.

Morreale, B., Swinny, E., Kostak-Teplicek, H., Bowersox, R., White, E., Dufrene, A., Wadhams, T., Popkin, S., Adamczak, D., Tancred, T. 2023. Boundary Layer Turbulence Flight Experiment in Memory of Mike Holden: Pre-Flight Mission Design. *AIAA Pap. 2023-0477*.

Moyes, A., Paredes, P., Kocian, T., Reed, H. 2016. Secondary instability analysis of crossflow on a hypersonic yawed straight circular cone *J. Fluid Mech.* 812:370-97

Mullen, C., Reed, H. 2021. Computational Modeling and Stability Analysis of BOLT Hypersonic Geometry Including Off-Nominal Conditions. *Theor. Comp. Fluid Dyn.*, Vol. 36, pp. 251–276.

Neel, I., Leidy, A., Bowersox, R. 2017. Preliminary study of the effect of environmental disturbances on hypersonic crossflow instability on the HIFiRE 5 elliptic cone. *AIAA Pap. 2017-0767.*

Neel, I., Leidy, A., Bowersox, R. 2018. Characterization of Environmental Disturbances on Hypersonic Crossflow Instability on the HIFiRE-5 Elliptic Cone. *AIAA Pap. 2018-5375.*

Notz, P., Subia, S., Hopkins, M., Moffat, H., and Noble, D. 2007. Aria 1.5: User Manual. *Sandia Report.*

Oliviero, N., Kocian, T., Moyes, A., Reed, H. 2015. EPIC: NPSE analysis of hypersonic crossflow instability on yawed straight circular cone. *AIAA Pap. 2015-2772.*

Paredes, P., Theofilis, V. 2014. Traveling global instabilities on the HIFiRE-5 elliptic cone model flow. *AIAA Pap. 2014-0075*.

Paredes, P., Theofilis, V. 2014. Centerline instabilities on the hypersonic international flight research experimentation HIFiRE-5 elliptic cone model. *J. Fluids and Structures* 53:36-49.

Paredes, P., Perez, E., Reed, H., Theofilis, V. 2014. High frequency instabilities along the windward face of a hypersonic yawed circular cone. *AIAA Pap. 2014-2774*.

Peltier, S., Humble, R., and Bowersox, RDW. 2014. The Influence of Favorable Pressure Gradients upon the Coherent Motions in a Mach 5 Turbulent Boundary Layer. *AIAA Pap. 2014-3060.*

Peltier, S., Humble, R., and Bowersox, RDW. 2016. Crosshatch Roughness Distortions on a Mach 5 Turbulent Boundary Layer," *Physics of Fluids*, Vol. 28, 045105.

Poggie, J. 2015. Compressible Turbulent Boundary Layer Simulations: Resolution Effects and Turbulence Modeling. *AIAA Pap*. 2015-0983.

Portoni, P., Dufrene, A. 2023. Boundary Layer Turbulence Flight Experiment in Memory of Mike Holden: Ground-to-Flight. *AIAA Pap.* 2023-0683.

Pope, S, 2005. *Turbulent Flows*. Cambridge University Press.

Reed, H., Perez, J,. Kuehl, J., Kocian, T., Oliviero, N. 2015. Verification and validation issues in hypersonic stability and transition prediction. *J. Spacecr. Rockets.* Vol. 52, No. 1, pp. 29-37.

Reed, H., Saric, W. 1989. Stability of 3-D boundary layers. *Annu. Rev. Fluid Mech.* Vol. 21,, pp. 235-84.

Reed, H., Saric, W., Arnal, D. 1996. Linear stability theory applied to boundary layers. *Annu. Rev. Fluid Mech.* Vol. 28, pp. 389-428.

DISTRIBUTION A: Distribution approved for public release.

Reed, H., Kimmel, R., Schneider, S., Arnal, D. 1997. Drag prediction and transition in hypersonic flow. *AIAA Pap. 97-1818.*

Reshotko, E. 1976. Boundary-layer stability and transition. *Annu. Rev. Fluid Mech.* Vol. 8, pp. 311–49.

Reshotko, E. 1991. Hypersonic stability and transition. In *Hypersonic Flows for Reentry Problems*. ed. JA Desideri, R Glowinski, J Periaux, Springer: Berlin. Vol. 1, pp. 18–34.

Reshotko, E. 2007. Is Re_θ/Me a meaningful transition criterion? *AIAA J.* Vol. 45, No. 7, pp. 1441-1443.

Reshotko, E. 2008. Transition issues for atmospheric entry. *J. Spacecr. Rockets*. Vol. 5, No. 2, pp. 161–4.

Roy, C. and Blottner, F. 2006. Review and Assessment of Turbulence Models for Hypersonic Flows. *Progress in Aerospace Sciences*, Vol. 42, No. 7-8, p. 469-530

Saric, W., Reed, H., White, E. 2003. Stability and transition of three-dimensional boundary layers *Annu. Rev. Fluid Mech.* Vol. 35, pp. 412-40.

Schetz, J. and Bowersox, R. 2011. *Boundary Layer Analysis*, *2nd Ed.*, AIAA Ed. Series.

Schneider, S. 1999. Flight data for boundary-layer transition at hypersonic and supersonic speeds. *J. Spacecr. Rockets.* Vol. 36, No. 1, pp. 8-20.

Schneider, S. 2001. Effects of high-speed tunnel noise on laminar-turbulent transition. *J. Spacecr. Rockets.* Vol. 38, No. 3, pp. 323-333.

Schneider, S. 2004. Hypersonic laminar-turbulent transition on circular cones and scramjet fore-bodies. *Progress in Aerospace Sciences.* Vol. 40, No. 1–2, pp. 1-50.

Schneider, S. 2006. Laminar-Turbulent Transition on Reentry Capsules and Planetary Probes. *J. Spacecr. Rockets.* Vol. 43, No. 6, pp. 1153-1173.

Schneider, S. 2008. Effects of roughness on hypersonic boundary-layer transition. *J. Spacecr. Rockets.* Vol. 45, No. 2, pp. 193-209.

Schneider, S. 2010. Hypersonic boundary-layer transition with ablation and blowing. *J. Spacecr. Rockets.* Vol. 47, No. 2, pp. 225-237.

Schuele, C., Corke, T., Matlis, E. 2013. Control of stationary cross-flow modes in a Mach 3.5 boundary layer using patterned passive and active roughness. *J. Fluid Mech.* Vol. 718, pp. 5-38.

Semper, M., Bowersox, R. 2017. Tripping a Hypersonic Low Reynolds Number Boundary Layer. *AIAA Journal*, Vol. 55, No. 3, pp. 808-817.

Smits, A. and Dussuage, J. 1996. *Turbulent Shear Layers in Supersonic Flow*, American Institute of Physics, Woodbury, New York.

Spalart, P. and Allmaras, S. 1992. A One-Equation Turbulence Model for Aerodynamic Flows. *AIAA Pap. 1992-0439*.

Speziale, C. 1996. Modeling of Turbulent Transport Equations, in *Simulation and Modeling of Turbulent Flows*. Ed. Gatski, T., Hussaini, M. and Lumley, J., Oxford University Press, New York, 1996.

DISTRIBUTION A: Distribution approved for public release.

Stetson, K. 1987. On predicting hypersonic boundary layer transition. AFWAL-TM-87-160-FIMG.

Stetson, K. and Kimmel, R. 1992. On hypersonic boundary-layer stability. *AIAA Pap. 1992-0737*.

Stuckert, G., Reed, H. 1994. Linear disturbances in hypersonic, chemically reacting shock layers. *AIAA J.* Vol. 32, No. 7, pp. 1384-1393.

Sweeney, C., Chynoweth, B., Edelman, J., Schneider, S. 2016. Instability and transition experiments in the Boeing/AFOSR Mach 6 quiet tunnel. *AIAA Pap. 2016-0355.*

Thome, J., Dwivedi, A., Nichols, J., Candler, G. 2018. Direct Numerical Simulation of BOLT Hypersonic Flight Vehicle. *AIAA Pap. 2018-2894.*

Tichenor, N., Humble, R., and Bowersox, RDW. 2013. Response of Hypersonic Turbulent Boundary Layer to Favorable Pressure Gradients," *J. Fluid Mech.,* Vol. 722, pp. 187-213.

Tichenor, N., Neel, I., Leidy, A., and Bowersox, RDW. 2017. Influence of Streamline Adverse Pressure Gradients on the Structure of a Mach 5 Turbulent Boundary Layer. *AIAA Pap. 2017-1697.*

Wadhams, T., Mundy, E., MacLean, M., Holden, M. 2008. Ground test studies of the HIFiRE-1 transition experiment Part 1: experimental results. *J. Spacecr. Rockets*. Vol. 45, No. 6, pp. 1134-1148.

Wheaton, B., Berridge, D., Wolf, T., Araya, D., Stevens,R., McGrath, B., Kemp, B., Adamczak, D. 2021. Final Design of the Boundary Layer Transition (BOLT) Flight Experiment. *J. Spacecraft and Rockets*, Vol. 58, No. 1., pp. 6 – 17.

Wheaton, B. M., and Dufrene, A. T. 2023. Thermal and Structural Analysis of BOLT-2: The Holden Mission. *AIAA Pap.* 2023-0685.

Wilcox, D. 2003. *Turbulence Modeling for CFD, 2nd Ed.,* DCW Inc., La Canada, CA.

Wikstrom, P., Wallin, S. and Johansson, A. 2000. Derivation and Investigation of a New Explicit Algebraic Model for the Passive Scalar Flux. *Physics of Fluids*, Vol. 12, No. 3 pp. 688-702.

Wirth, J. 2023. Characterizing 3D Hypersonic Boundary Layers with Transient Surface Heat Flux Measurements. *PhD Dissertation*. Texas A&M University, College Station, TX.

Wirth, J., and Bowersox, R. D. W. 2022. Tunnel Environment Effects on the Single Fin-Cone at Mach 6. *AIAA Pap. 2022-4137*.

Wirth, J., Bowersox, R. 2024. Measurements of Natural Turbulence during the BOLT II Flight Experiment, in-review, *Journal Spacecraft and Rockets.*

Wirth, J., Morreale, B., Bowersox, R. 2024. Measurements of Natural Transition during the BOLT II Flight Experiment, in-review, *Journal Spacecraft and Rockets.*

Wirth, J., Morreale, B., Bowersox, R., Wheaton, B. 2023. Boundary Layer Turbulence Flight Experiment in Memory of Mike Holden: Side A Flight Data. *AIAA Pap. 2023-3440*.

Wirth, J., Morreale, B, Kostak-Teplicek, H., Bowersox, R., Dufrene, A., Portoni, P., Wadhams, T. 2023. Boundary Layer Turbulence Flight Experiment in Memory of Mike Holden: Side A Flight Data. *AIAA Pap. 2023-0862*.

Zhong, X., Wang, X. 2012. Direct numerical simulation on the receptivity, instability, and transition of hypersonic boundary layers, *Annu. Rev. Fluid Mech*. Vol. 44, pp. 527-561.

DISTRIBUTION A: Distribution approved for public release.

APPENDIX A – PDR REQUEST FOR ACTION (RFA) RESPONSES

The responses reported here are taken from those submitted to the RFA authors and the AFOSR. The formatting and element numbering have been adjusted to match this document.

A.1 RFA #1: FLIGHT OBJECTIVE

I. Leyva,[1] S. Popkin,[1] R. Bowersox,[2] and A. Dufrene[3]
[1]AFOSR, Air Force Research Laboratory
[2]Aerospace Engineering Department, Texas A&M University
[3]Aeronautics Division, CUBRC

Concern or Issue. *Flight tests are expensive and usually provide poorer-quality data than a wind tunnel test. You should not perform a flight test unless there is critical information that you can get only in flight (AIAA 2011-3415). A flight test is high-profile and makes you a target for criticism from other parties who will paint it as a waste of money. You need to develop a short, succinct statement about why a flight test is necessary.*

One rationale for doing this flight test is that when we predict turbulent heating for flight vehicles, we apply a generous uncertainty margin. These margins are often over-conservative. Some of this margin is to take into account issues that are peculiar to flight – time-dependent wall temperature, non-uniform wall temperature, day-of-flight density, vehicle attitude oscillations, etc. We can't measure these in detail in production flight tests, but with BOLT II we can do this. BOLT II can allow us to put some reasonable uncertainty bounds on these uncertainties.

The corollary to this statement is that the flight measurements have to accurate enough to resolve these uncertainties. If the flight data have error bars that are comparable to or larger than our current uncertainties, why bother doing the flight?

Response. Drs. Kimmel, Leyva, and Bowersox discussed the objectives thoroughly. We have subsequently discussed this RFA with Dr. Popkin. The attached point paper by Dr. Kimmel articulates the need for the BOLT II flight test, which aligns closely with the original project objective and goals (also attached). Based on these discussions, we believe this RFA has been closed with the objective and impact statements as summarized below:

- **Objective.** The basic science objective is to advance our understanding and modeling of hypersonic boundary layer turbulence, natural (Side A) and forced (Side B), on a concave surface with highly swept leading edges. We do this by bringing together results of high-fidelity numerical simulations, ground test data from several facilities and flight test data.
- **Impact.** BOLT II will serve as a scientific benchmark for hypersonic heating. The data and analyses can provide a scientific basis from which to initiate applied research programs to reduce uncertainties and design margins for flight vehicles in a critical flow regime, where the thermal and mechanical loading are controlled by turbulent flow processes that cannot be reproduced in ground test. Specifically, the BOLT II will experience a complex thermal

DISTRIBUTION A: Distribution approved for public release.

history coupled to an equally complex flow structure. The flow structure is shown in Fig. 1a for laminar and turbulent flow. A key flow feature is the streak structure which may be a key factor in the transition to turbulence process. Comparing the Quiet Tunnel and ACE tunnel results shown in Fig. 1b indicates that quantification of the evolution from transition, through early turbulence, and ultimately to equilibrium turbulence is not possible in current ground test due to limited Reynolds numbers in quiet tunnels and contamination by free stream disturbances in conventional tunnels. Therefore, flight experiments are essential to improve our understanding of hypersonic boundary layer turbulence.

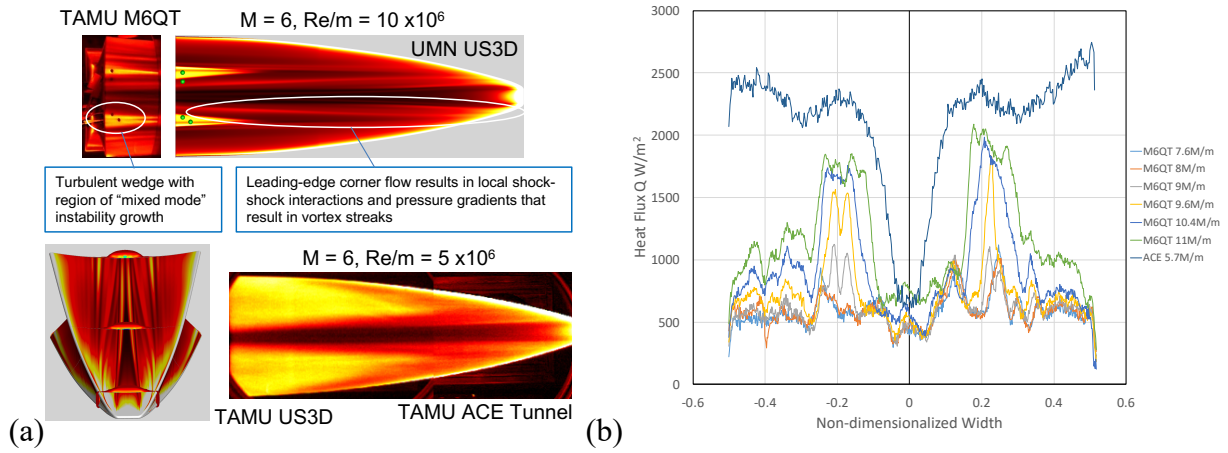

Figure A.1.1. TAMU/UMN Ground Test and CFD Results. (a) Planar results (1.0 m and 1.5 m BOLT II). (b) Spanwise traces at x = ~95% from tests in the TAMU M6QT and ACE Tunnel.

DISTRIBUTION A: Distribution approved for public release.

Attachment 1. Position paper by R. Kimmel.

Point Paper on Rationale for BOLT II Flight Test

- Why a flight test on hypersonic turbulence is required:
  - Transitional effects on turbulent heating – The path by which a boundary layer transitions from laminar to turbulent impacts initial turbulent heating, and effects may persist far downstream. This process cannot be simulated in noisy wind tunnels, and quiet wind tunnels cannot attain high enough quiet Reynolds number to assess it.
  - Turbulent heating uncertainty – Turbulent heating predictions are subject to large uncertainties. Some uncertainty sources cannot be simulated well in ground test. These include wall temperature distribution, transition process and location, air transport properties, surface roughness, and geometry deviations.
  - Complex thermal history – Turbulent heating to hypersonic vehicles varies both temporally and spatially. This cannot be simulated in wind tunnels.
- How BOLT II will address these issues:
  - BOLT II will fly at Reynolds numbers unattainable in quiet wind tunnels, with sufficient instrumentation to document the transition path and its effects on turbulence.
  - BOLT II will be non-ablating and have non-reacting flow, eliminating these uncertainty sources. Unlike demonstrator flight tests, the vehicle possesses dense internal and external instrumentation to fully document boundary conditions. The aeroshell will be precisely measured prior to flight and its thermal properties are well-characterized.
  - BOLT II will provide a well-characterized flight data set to validate coupled aerodynamic / heating codes. The complex geometry, trajectory and transition process on BOLT II provide realistic stressors for predictions. BOLT II's dense instrumentation and well-defined material properties eliminate boundary condition and material property uncertainty as error sources.
- One-sentence summary: BOLT II will serve as a benchmark for hypersonic heating predictions.

10 July 2020 / Roger Kimmel / roger.kimmel@us.af.mil

DISTRIBUTION A: Distribution approved for public release.

Attachment 2: Project Goals (Dr. I. Leyva)

Air Force Research Laboratory

Science Flight Experiments in Hypersonics

September 5, 2019

Ivett Leyva, Ph.D., P.E.
High Speed Aerodynamics Program Officer
AFRL/AFOSR

Integrity ★ Service ★ Excellence

DISTRIBUTION C: Distribution to U.S. Government agencies and their contractor's. To protect draft, planning, or other preliminary information from premature dissemination. Other requests for this document shall be referred to AFOSR/RT

Background

BOLT II VISION:

1. Challenge the academic community to predict flight hypersonic boundary layer ***turbulence*** on the BOLT geometry
2. Educate Ph.D., M.S. and undergrad students on what it really takes to go from a concept in the lab or at a computer to flight
3. Give more universities the opportunity to work with Government, UARCs and Industry

TIMELINE: April 2019 – Dec 2021 – Flight event is in July 2021

SUCCESSES FROM THE START

- AEDC Tunnel 9 chose BOLT II the geometry for their next data truck – reach more academicians and bring in T&E community to the project!
- Domestic launch from NASA Wallops – US facilities ready to support hypersonic science experiments
- NASA Langley leading roughness side including completely new strategy to build trips
- Testing new instrumentation in flight from Ahmic Aerospace
- Giving more industrial partners an opportunity to be part of the team

BOLT II Shape

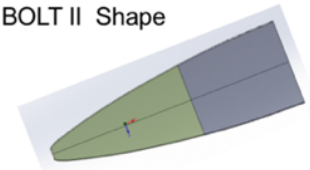

TEAM

PI: Prof. Rodney Bowersox, TAMU

DISTRIBUTION C: Distribution to U.S. Government agencies and their contractor's. To protect draft, planning, or other preliminary information from premature dissemination. Other requests for this document shall be referred to AFOSR/RT

DISTRIBUTION A: Distribution approved for public release.

OBJECTIVES

TURBULENT FLOW: Not such an active area of research until now

- ***A lot of empirical "models" to numerically simulate turbulent flows***

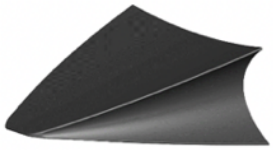

Concave surfaces & swept leading edge

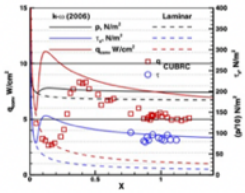

Gnoffo et al 2013 - 40% error in heat flux

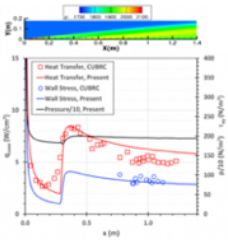

Bowersox (2009) 25% error

Objectives:

- ***At what point does the turbulent boundary layer become independent of initial conditions (tunnel noise)***
- ***Check our simplifying assumptions on our correlations to relate skin friction to heat transfer in flight***
- ***Test new instrumentation in flight for turbulent hypersonic boundary layers***
- ***Compare flight data with tunnel data at same Mach and Reynolds number – check effect of wall temperature, and initial conditions***
- ***Create benchmark flight data against which to compare academia and industry codes***

DISTRIBUTION C: Distribution to U.S. Government agencies and their contractor's. To protect draft, planning, or other preliminary information from premature dissemination. Other requests for this document shall be referred to AFOSR/RT

DISTRIBUTION A: Distribution approved for public release.

A.2. RFA GROUP #2: BOLT II INSTRUMENTATION DESIGN

R. Bowersox,[1] A. Dufrene,[2] D. Adamczak,[3] S. Popkin,[3] I. Leyva,[3] H. Kostak,[2] and E. Swinny[2]
[1]Aerospace Engineering Department, Texas A&M University
[2]Aeronautics Division, CUBRC
[3]Air Force Research Laboratory (AFOSR and RQHV)

This section is in response to a series of RFAs, which are grouped under the common theme of data analysis for planned instruments. The relevant PDR RFAs include:

B. Wheaton #2 - Data analysis plan to ensure layout addresses scientific objectives
J. Lafferty #1 - Interpretation of Medtherm gage data during flight test
J. Lafferty #2 - Interaction/Proximity of heat flux gage to Medtherm coax gages
R. Kimmel #2 - TC backface placement uncertainty
R. Kimmel #3 - Measurements on dynamic vehicle
K. Rock #1 – Convective heat transfer margin verification
R. King #1 – Sensor diameter effects

Preflight data analyses were performed to estimate sensor performance and uncertainties. The analyses were guided, in part, by the PDR RFA questions. The analyses are in the order of the instruments in Table A.2.1.

Table A.2.1 Sensor Suite

Sensor	Brand	Model	Sensitivity	Unc[a]	Freq Resp (kHz)	Amount (Side A/B)	Samp Freq (kHz)
Heat Flux	Medtherm	TCS-061-EE	68 μV/(deg C)	3-5%	1000	62/38	0.4
Heat Flux	Vatell	TG-2000	33 μV/(W/cm^2)	3%	1	40/12	2
RMS Press.	Endevco	8540-15a	20 mV/psia	5-18%	140	9/8	20
Attitude	Endevco	8540-15a	20 mV/psia	0.3-0.8° [b]	140	8/4	0.2
Press. Grad.	Endevco	8540-15a	20 mV/psia	7-25%	140	23/0	0.2
Skin Fric.	Ahmic	Custom	Custom	10%	0.5	12/0	0.4
Spectra	PCB	132B38	140 mV/psi	***	1000	4/0	2500
Thin Film	CUBRC	Custom	Custom	***	1000	36/12	10
Accel.	Endevco	7270AM4	100 μV/g	3%	150	4	20

[a] Manufacturer provided values, team experience, and the analyses that follow below. [b] Resolvable angle.

A.2.1 Instrumentation Design Objective

DISTRIBUTION A: Distribution approved for public release.

The objective for the instrumentation suite for BOLT II is to experimentally quantify in flight turbulent thermal and mechanical loading in flight on a concave surface with highly swept leading edges. The instruments will also provide data during the CUBRC preflight ground tests. The BOLT II flow structure is shown in the experiments and simulations in Figs. A.2.1a,b for laminar and turbulent flow. A key flow feature is the streak structure which may be a key factor in the transition to turbulence process. One of the main goals for the Holden Flight is to map the early turbulence (e.g., overshoot) and determine how long into the turbulence the streak and transitional effects last before equilibrium is achieved. Comparing the Quiet Tunnel and ACE (conventional) tunnel results shown in Fig. 1c indicate that quantification of these effects is not possible in current ground test due to limited Reynolds numbers in quiet tunnels and contamination by free stream disturbances in conventional tunnels. The acoustic disturbances that result from the turbulent boundary layers on the wind tunnel wall trigger early transition and instabilities not active in flight.

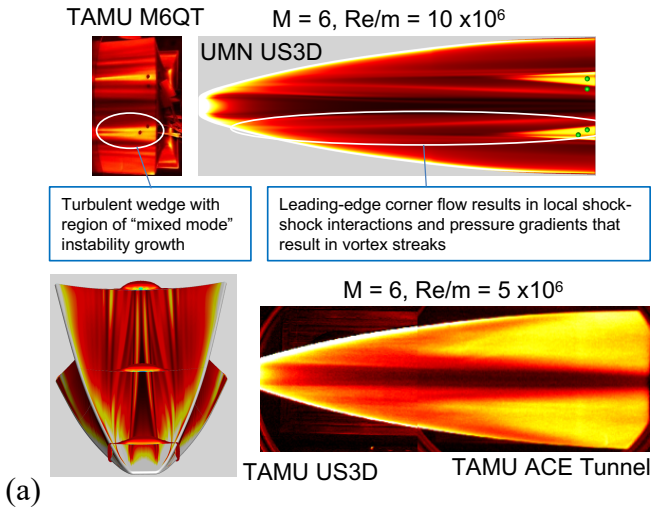

(a)

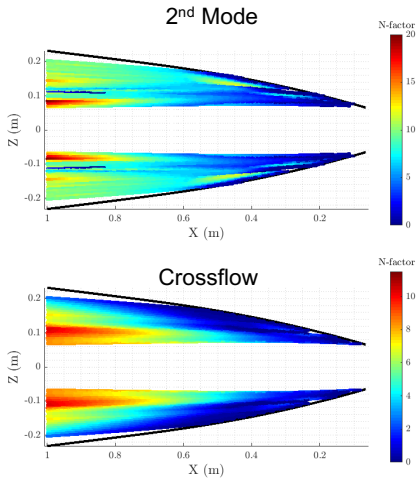

(b)

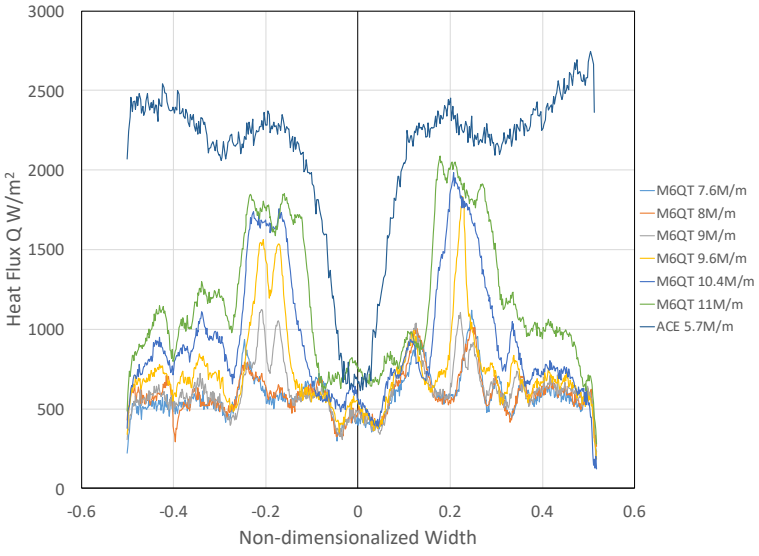

(c)

DISTRIBUTION A: Distribution approved for public release.

Figure A.2.1. TAMU/UMN Ground Test and CFD Results. (a) Planar results (1.0 m and 1.5 m BOLT II). (b) Boundary layer stability results; left: 2nd mode; right: stationary crossflow (TAMU, Reed and Mullen). (c) Spanwise traces at x = ~95% from tests in the TAMU M6QT and ACE Tunnel.

A.2.2 Instrumentation Design

The instrumentation suite for BOLT II is summarized in Table A.2.1 and the resulting layout is shown in Fig. A.2. The instrumentation selection and position were developed to quantify the turbulence evolution in Fig. A.2.1a. The final instrumentation design presented here was the result of (1) the computational and subscale wind tunnel results generated for both BOLT II and BOLT I, (2) the Preliminary Design Review (PDR) Request for Action (RFA) questions, and (3) consultations with APL, AFRL (including AFOSR), AEDC, and NASA. The onboard DAQ systems operate at 24-bit with customized gains. Hence, the digitization errors were neglected in the present analysis. More complete explanations of the uncertainties are provided in Section A.2.3.

As indicated in Fig. A.2.2, five primary rows of data are planned. The goal for each row is summarized in Fig. A.2.2a. The goals for each row are: **Row 1:** Quantify temperature near Ni-SS interface; **Row 2:** Quantify thermal loading and streak structure locations as inflow conditions for turbulent flow during flight. Also provides turbulent burst if the front moves this far forward; **Row 3:** Quantify turbulent fronts, bursts, and thermal loading (CUBRC Thin Film sensors and Pressure fluctuations); **Row 4:** Quantify turbulent front, bursts, thermal loading, skin friction, & pressure gradients (full suite of instruments), and **Row 5:** Quantify turbulent front, bursts, thermal loading, skin friction, & pressure gradients (full suite of instruments). In addition, PCB sensors are included for spectral content, and their locations were chosen to correspond to 2nd mode and cross-flow secondary instabilities. Also, the circled Endevco sensors are planned for attitude determination. Similar sensors are located on side B, with two sensors each gutter.

DISTRIBUTION A: Distribution approved for public release.

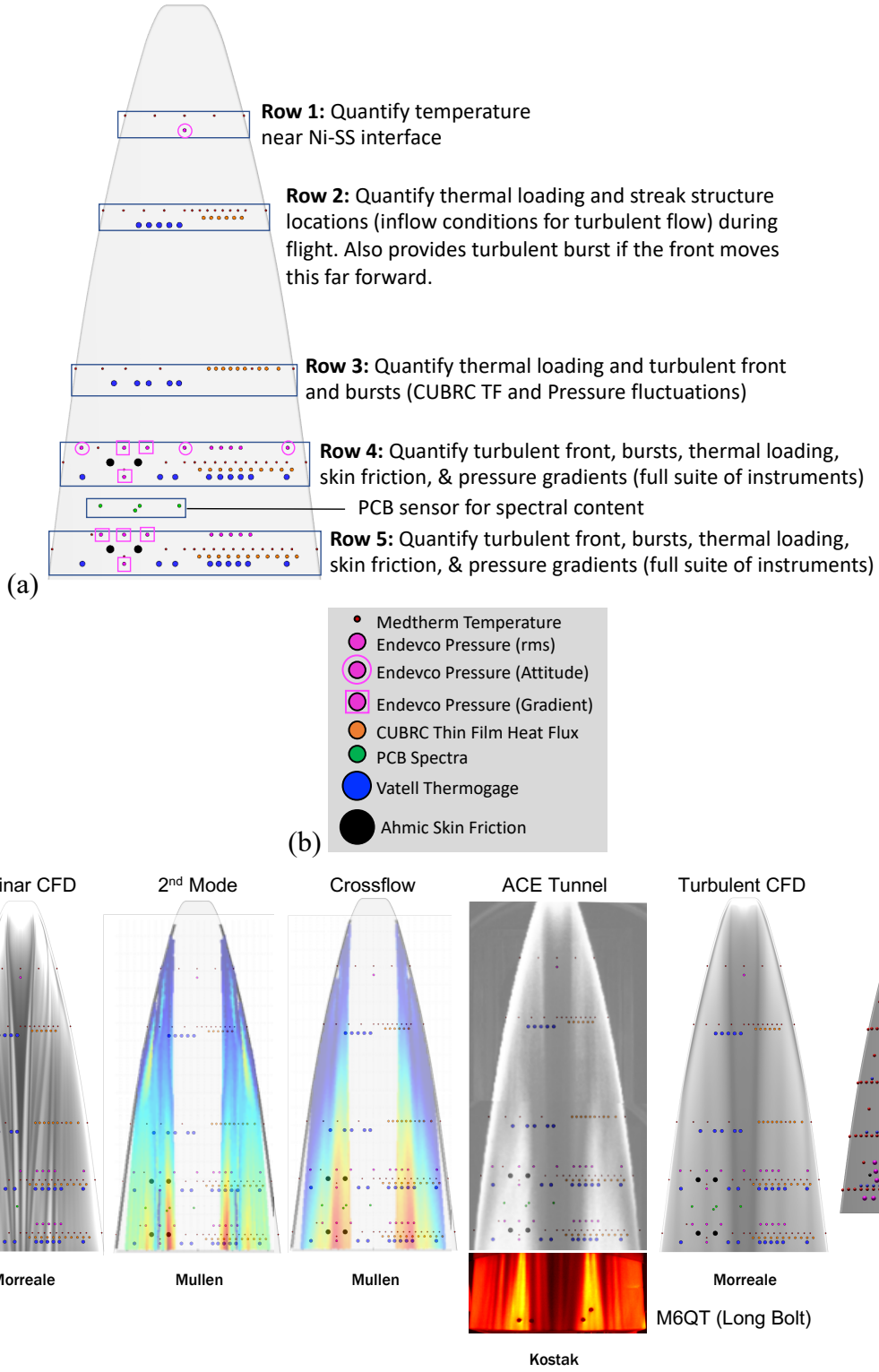

Figure A.2.2. Sensor Layouts. (a) BOLT II Side A. (b) Key (scale is arbitrary). (c) Instrumentation overlain over the flow structure for laminar CFD (TAMU with US3D), boundary layer instability mechanisms (TAMU EPIC), turbulent flows wind tunnel (TAMU ACE and M6QT), and fully turbulent CFD (TAMU with US3D).

DISTRIBUTION A: Distribution approved for public release.

A.2.3 RFA #2: Preflight Data Analyses

Heat flux measurements are planned with Medtherm TCS-061-EE thermocouples and Vatell TG-2000 direct heat flux sensors. The manufacturer uncertainties are included in Table A.2.1. The following sections quantify additional uncertainties in post flight data reduction.

J. Lafferty RFA #1 Interpretation of Medtherm Gage Data During Flight Test

Concern or Issue. *My suggestion is to dry-run what you think might get from the coax gages for a handful of locations on the body. Define front- and back-face temperatures based on the nominal trajectory, position on the model and the relative BL state as a function of time for the entire flight time. Take these as measurements and exercise you planned flight data reduction. Then one at a time add noise and some cyclic variation base on the rotational rate of the SR to determine how to deal with these non-ideal factors. I think this will be different (better and or worse) then the aluminum body used previously. I think doing this for the entire time series could be instructive. This may be similar to the ROA that Kimmel submitted.* - J. Lafferty

Response. Kostak and Swinny analyzed the Medtherm sensor response for the reentry trajectory for fourteen spanwise locations at an axial location near x = 0.95m (see Fig. A.2.3). The CFD and material response data were provided by B. Wheaton (APL). The coordinates for the "sensor locations" are given in Table A.2.2. The TAMU heat flux data reduction code was used to analyze the data. Plotted in Fig. A.2.4 is a representative result midway between the leading-edge and the centerline. The difference between the input heat flux and the simulated sensor response with the 1-D data reduction code was well within the expected measurement uncertainty. For example, the difference at location 3 was the largest at 2.7%, at location 9, the difference was 0.6%, and at location 7, 0.8%. The expected uncertainty was estimated to be between 2-5%, which includes a ±1 mm uncertainty in the back-face sensor location.

The results for all of the locations are given in Fig. A.2.5. The plots show that the simulated sensor response using the 1-D code agrees well with the data for all but two locations. The two exceptions are as follows: one near the centerline (loc. 1) and the other near the leading-edge (loc. 14). The differences at these locations are not unexpected. At both locations, we expect lateral conduction to be important. The higher-heating at the leading-edge results in significant dT/dz (spanwise gradient) and the cool centerline also results in a more significant dT/dz. However, over the majority of sensor locations, the differences between the sensor reading and CFD heat flux was within 4% (sensor 3), with the vast majority within 1%. The TAMU team has developed a 3-D conjugate heat transfer code which is being evaluated as part of other projects within the PI's lab.

The analysis was taken further by varying the boundary conditions by ±5% within the TAMU 1-D heat conduction code where the heat flux was compared to the CFD calculations. These results are given in Fig. 6 for a few locations. These data show that the expected heat flux uncertainties are within ~5% over the flight test window (~390 – 400 sec).

The team, based on this analysis, is better prepared to reduce the flight test data, including the 3-D data reduction code.

DISTRIBUTION A: Distribution approved for public release.

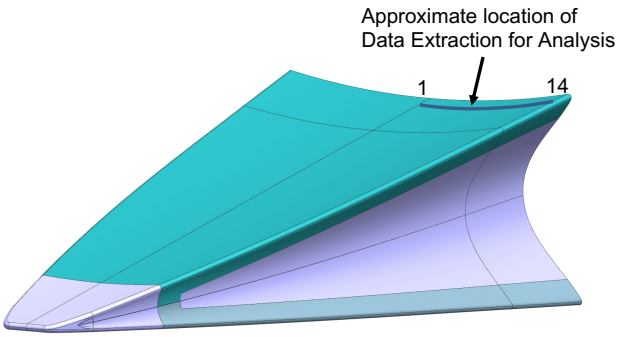

Figure A.2.3. Sketch showing location of the line where the measurements were extracted.

Table A.2.2 Summary of Medtherm Analysis Locations (left: surface, right: backface)

Outer Surface Medtherm Location			Inner Surface Medtherm Location		
X (m)	Y (m)	Z (m)	X (m)	Y (m)	Z (m)
0.947	0.119	0.001	0.950	0.100	0.001
0.947	0.119	0.016	0.950	0.100	0.018
0.947	0.119	0.031	0.950	0.100	0.033
0.947	0.119	0.033	0.950	0.100	0.034
0.947	0.120	0.050	0.950	0.101	0.052
0.948	0.121	0.068	0.950	0.102	0.069
0.948	0.122	0.085	0.950	0.103	0.086
0.948	0.123	0.102	0.950	0.104	0.103
0.948	0.125	0.118	0.950	0.106	0.120
0.948	0.126	0.135	0.950	0.108	0.138
0.948	0.128	0.152	0.950	0.110	0.155
0.947	0.131	0.169	0.950	0.112	0.171
0.947	0.133	0.185	0.949	0.114	0.188
0.947	0.139	0.228	0.955	0.115	0.189

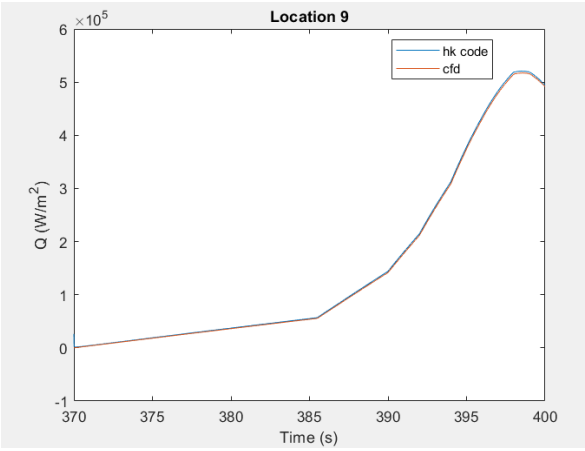

Figure A.2.4. Representative case near 25% span (z = 0.12 m).

DISTRIBUTION A: Distribution approved for public release.

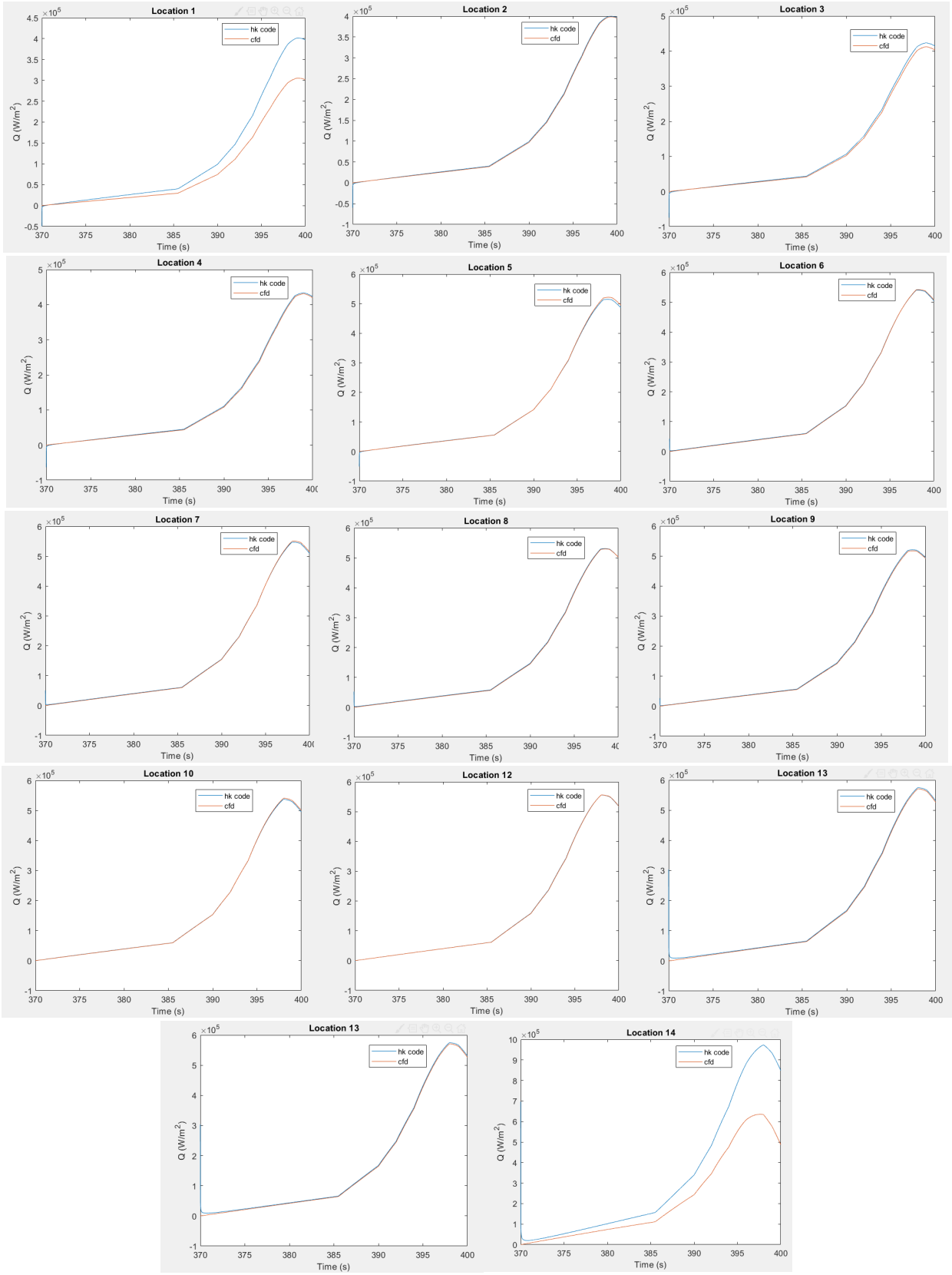

Figure A.2.5. Summary of all 14 locations across the 50% span at x = 0.95 m.

DISTRIBUTION A: Distribution approved for public release.

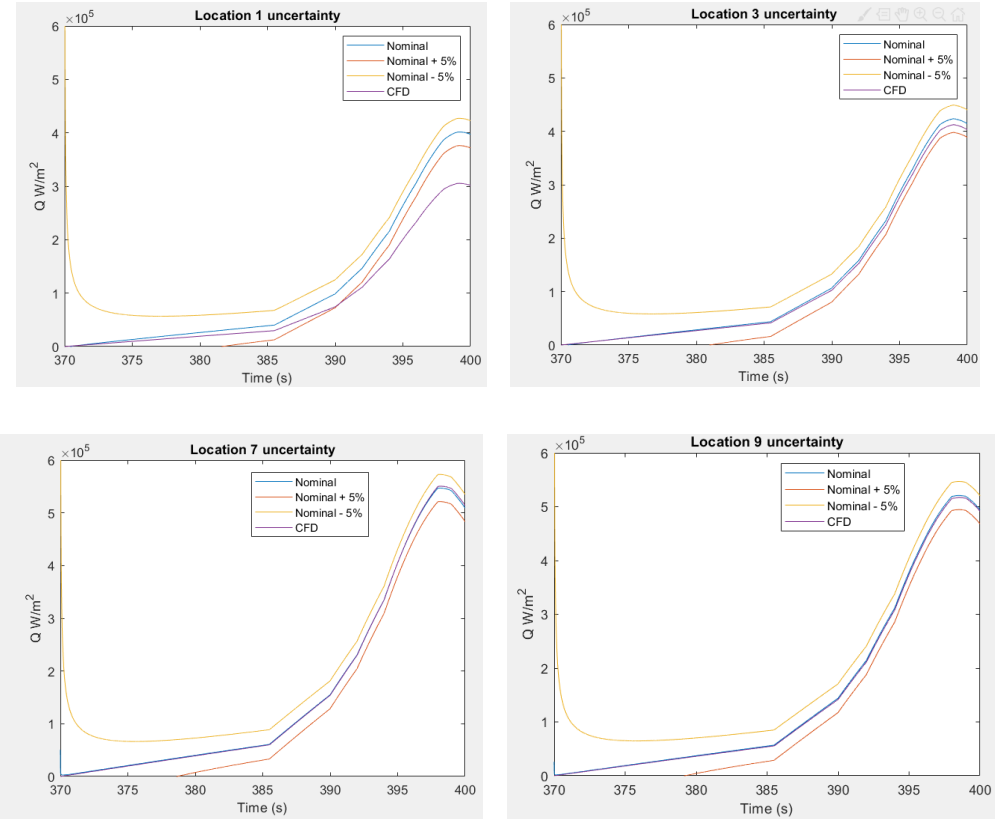

Figure A.2.6. Example uncertainty calculations for four Medtherm locations.

Lafferty RFA #2 Interaction/Proximity of Heat Flux Gages to Medtherms

Concern or Issue. *Perform a FEA to investigate the effect of the instrumentation hole for the direct read HT gages to the Medtherm coaxial thermocouples. The Medtherm gages assume thermally homogeneous material. If the hole is too close it will violate this assumption. This may be exacerbated by the long-time record that is being recorded that might set up lateral gradients. BTW the selection of 15-5 or 17-4 best matches the lump thermal properties of a Type E gages for uses in cold wind tunnel. However, we do not heat the wall up for this long or these temperatures typically. This could be looked at as well I think doing this for the entire time series could be instructive.* - J. Lafferty.

Response. Finite element simulations were performed for all of the thermal sensors (Medtherms, Vatell Gardon Gauges, and CUBRC thin films). Vatell Gardon gauges (TG-2000) have a 9.5 mm (0.375 inch) OD copper tube construction. They were modeled here as a solid copper rod for conservatism, since copper is significantly more conductive & alters local temperature profile. Transient convective heating FEA was completed to determine proximity of Vatell gauges and the Medtherm TCs (1/16th OD). The basic finding was that the sensor centerlines should be greater than 1.3 cm (0.5 inch) away from each other, where a 1.9 cm (0.75 inch) center-

DISTRIBUTION A: Distribution approved for public release.

line spacing between Vatells and Medtherms results in no disturbance to the temperature or temperature gradients through the frustrum. The results are shown in Fig. A.2.7a. The Medtherms were seen to be an excellent thermal match to the stainless frustrum. The thermal properties of the type E sensors are similar to 410 SS. The results are shown in Fig. A.2.7b. The thin film results are shown in Fig. A.2.7c, with a 4 mm (~0.15 inch) required separation.

The spacing requirements identified through this analysis were used to determine the final instrumentation locations in Fig. A.2.2.

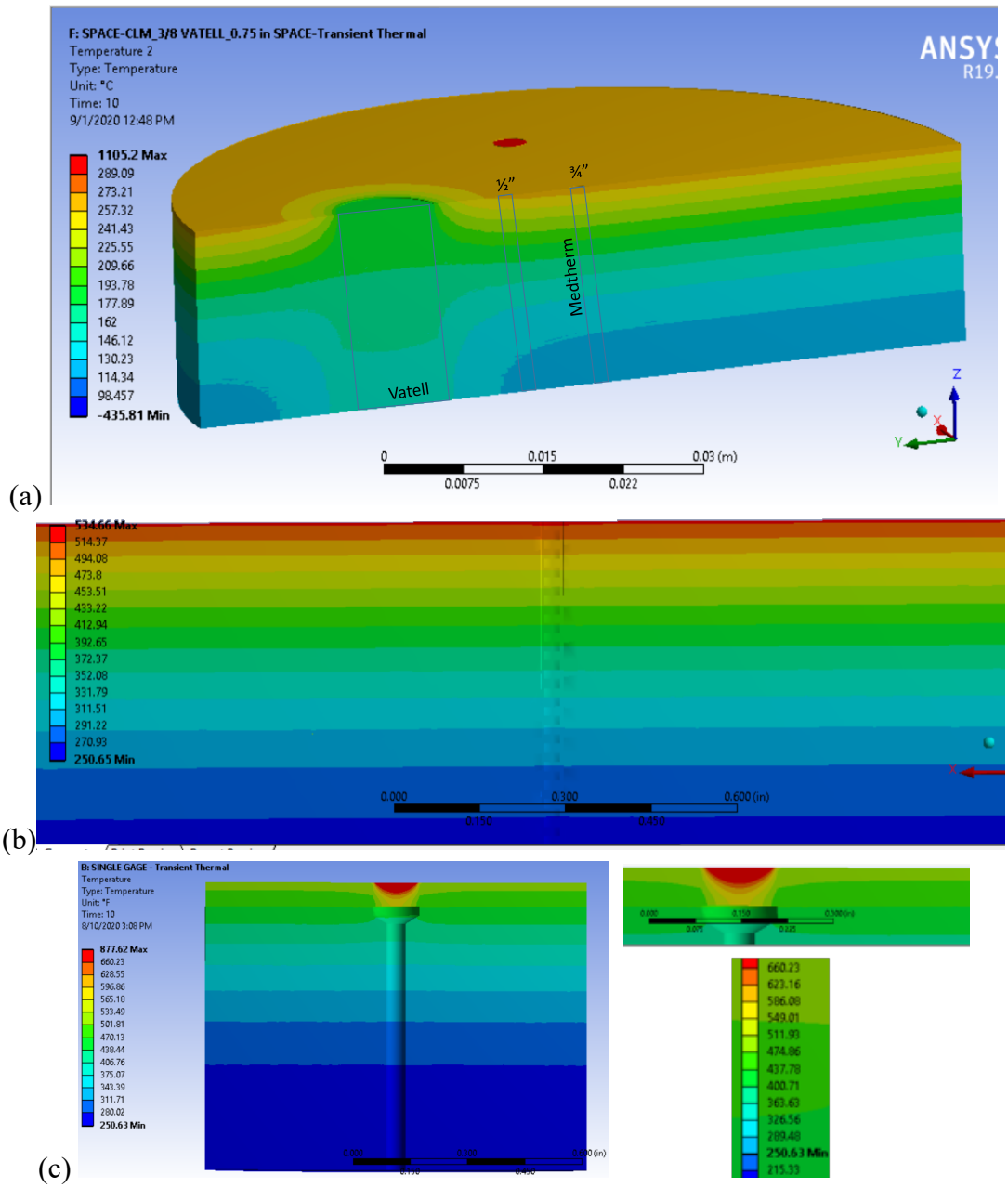

Figure A.2.7. Finite element thermal results for the heat flux sensors. (a) VaTell Gardon Gauges. (b) Medtherm sensors, and (c) CUBRC thin film sensors.

DISTRIBUTION A: Distribution approved for public release.

R. Kimmel RFA #2 TC Backface Placement Uncertainty

Concern or Issue. *You should probably do a thermal analysis to look at the sensitivity of backface thermocouple placement. This could be as simple as taking a FE heating solution and picking off front face, backface, and backface +/- 1mm, and using these as BCs for an inverse solver. You could even grid a thermocouple, if you want to get detailed, but I don't think you will be highly sensitive to the backface TC placement, and this is a fairly simple analysis to prove this.* - R. Kimmel.

Response. We performed two analyses. (1) A semi-infinite solid analysis (hand calculation), where the back-face temperature was held fixed by adjusting the initial temperature distribution for L = 19 mm ±1 mm. The estimated uncertainty for this case was < 2%. (2) Assuming a linear temperature distribution, the uncertainty was 5%. Additional uncertainties are being considered as part of other RFA responses. (2) Finite element heat flux simulations from CUBRC (Fig. A.2.8), which showed that the backface temperature error would be ~1K. Hence, the uncertainty in the heat flux due to a ±1 mm uncertainty in the placement of the back-face thermocouple is estimated to be less than 2 - 5%.

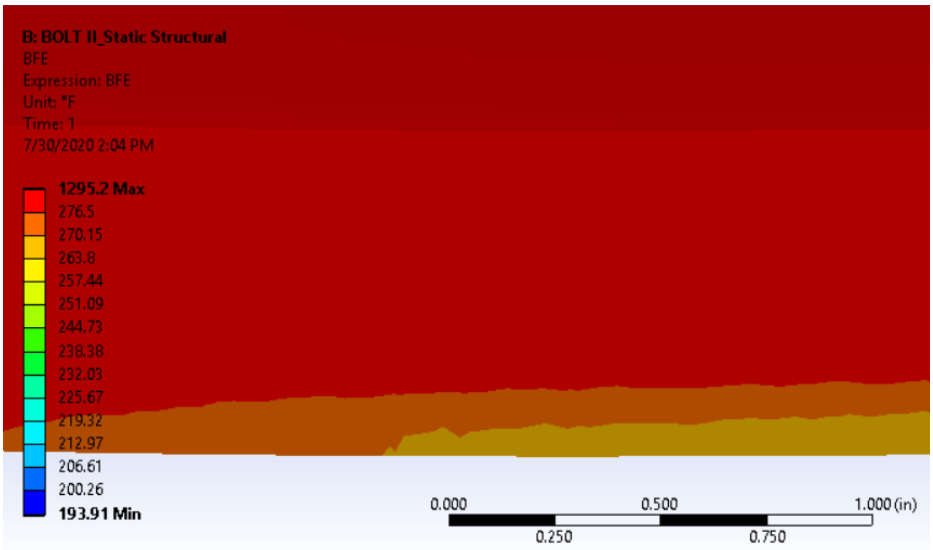

Figure A.2.8. Finite element simulation of thermal transport within the stainless steel frustrum. The Back-face thermocouple placement uncertainty should not be a large source of heat transfer uncertainty where the temperature differences over 0.025" are within 1-2 degrees Fahrenheit (or 1K).

R. Kimmel RFA #3 Measurements on Dynamic Vehicle

Concern or Issue. *My concern is whether the instrumentation can resolve the differences in transitional heating between the quiet and noisy heating fields that were observed in wind tunnels, especially when the vehicle is spinning, and these features are meandering over the transducers.*

DISTRIBUTION A: Distribution approved for public release.

I would suggest that you try to simulate the expected flight signals with an unsteady heating simulation. In its simplest form, you could take a flat plate, impose the quiet and noisy wind tunnel heating fields (or CFD heating fields), oscillate them periodically, and record temperature signals from the analysis (with some simulated noise added). You could add layers of modeling sophistication to this, but it should be a fairly straightforward means of assessment. I think Wheaton did something like this for BOLT I. - R. Kimmel.

Response. We analyzed the expected signal for Medtherm and thermogauge sensors accounting for a 4 Hz spin rate. The TAMU subscale wind tunnel data for the Long Bolt (25% of 1.5 m) configuration acquired within the Mach 6 QT and ACE tunnel were examined (Figs. A.2.9a,b). The streak sweep extent during a cycle was estimated from TAMU laminar CFD simulations (Fig. 1c). The streaks swept back and forth over a distance of roughly 0.25W (W = width of BOLTII). The resulting time traces for a sensor located at the centerline are given in Fig. A.2.10. The data are area averaged over the diameter of the sensors and sampled at the planned sampling rates during flight. Three traces are presented: laminar streak (M6QT), turbulent streak (M6QT), and fully turbulent (ACE). These data indicate that the laminar streaks are 75 – 125% below turbulent streak and fully turbulent flow. Hence, resolving these differences is well within the capabilities of the planned sensors.

Performing this analysis helped prepare the team to interpret the time traces expected in the flight test.

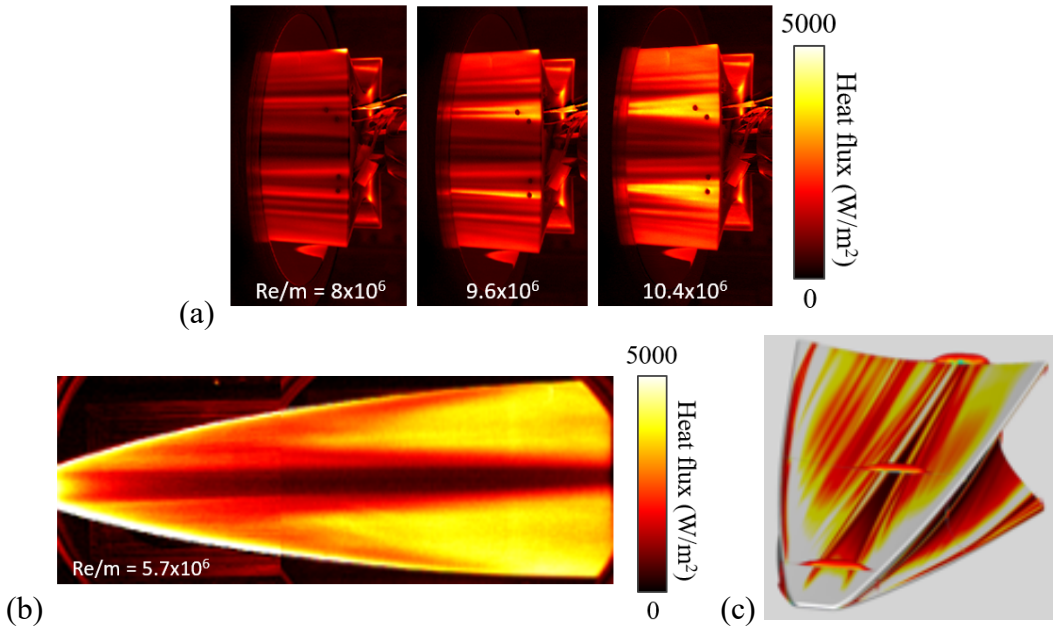

Figure A.2.9. BOLT II heat flux results. (a) M6QT, (b) ACE (c) CFD at flight conditions (4-deg Yaw).

DISTRIBUTION A: Distribution approved for public release.

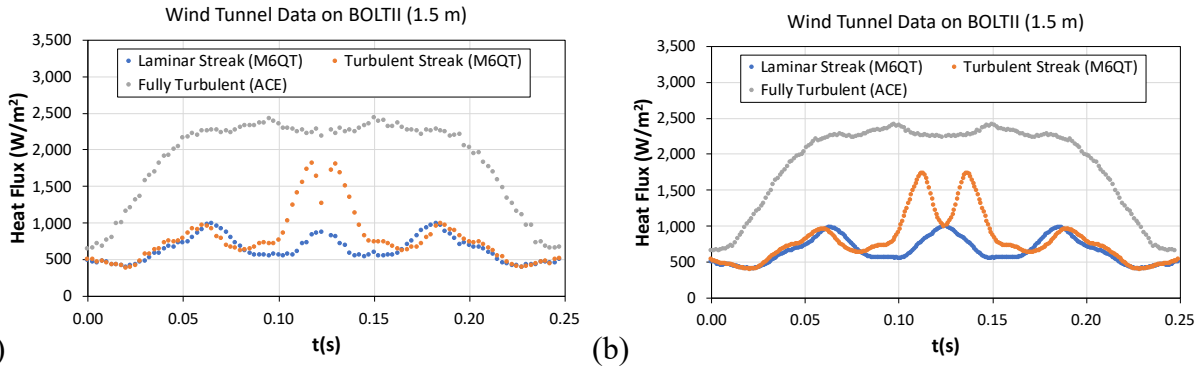

Figure A.2.10. Estimated heat flux signals for senors located at the centerline at x/L = 0.95. (a) Medtherm sensor (SR = 400 Hz, Diameter = 0.061 inch), (b) Thermogauge (SR = 2000 Hz, Diameter = 0.25 inch). Data were scaled to the flight geometry. Laminar streak (M6QT, *Re*/m = 8M), Turbulent streak (M6QT, *Re*/m = 9.6M), and Fully Turbulent (ACE, *Re*/m = 5.7M).

K. Rock RFA #1 Convective Heat Flux Margin

Concern or Issue. *Thermal load case analyzed based on Nominal Trajectory with 20% added to heat load (referred to as Margin). How does this load case compare to the 2-sigma high heat load trajectory? What is the appropriate thermal Margin on the 2-sigma high heat load trajectory?* – K. Rock.

Response. We utilized the NSROC and Chandler fin thermal analysis to answer this question. The focus was on 3-sigma and 30% margins. The results are listed in Table A.2.3. These data show that the margins adequately capture the flight trajectory variances. These data are taken as preliminary as the Chandler final report was not available at the time of this writing. This analysis increases the confidence in conservatism of the preflight analyses.

Table A.2.3 Fin Heating Analysis Temperatures (deg F) (NSROC and Chandler)

	Final Altitude				Survival Altitude			
Locations	Nom	3sH	3sL	+30%	Nom	3sH	3sL	+30%
Bolt Location	407	410	415	451	375	369	372	414
Panel - Foreword	321	337	339	398	275	277	276	300
Honeycomb Center - Foreword	242	246	245	252	221	246	245	235
Panel - Aft	303	318	327	339	257	255	260	273
Honeycomb Center - Aft	217	220	219	219	205	220	219	214

R. King RFA #1 Convective Heat Flux Margin

Concern or Issue. *On the layout, Vatell gauges (~0.25" dia) were shown at upstream locations. Are you able to contour these sensors to the OML of the model? If not, is there any concern about tripping the downstream BL?* – R. King.

DISTRIBUTION A: Distribution approved for public release.

Response. The skin friction sensors will be contoured. However, the pressure and heat flux sensors are not. In the planned locations, the maximum step for the 0.375-inch Vatell sensors is 0.0003-inch. This was a valuable assessment, as the steps produced by the sensors are not considered a concern.

Pressure Measurements

Surface pressures will be measured with Endevco model 8540-15a sensors to (1) determine research vehicle attitude, (2) provide root-mean-square (rms) fluctuation levels, and (3) quantify the pressure gradients near the skin friction sensors. Performing an L2-norm of the manufacturer provided uncertainties yields the following expression: 290 Pa + 5% (for thermal induced zero and sensitivity shifts). The resulting estimates are summarized in Table 4 over the test window altitudes (the Mach number was set to 6.0) for a range of angles-of-attack (α). The percent pressure uncertainty estimates (ε_P) are summarized in the last row of Table A.2.4. The resolvable attitude angles (α_{min}) were estimated to range from 0.3 – 0.8 as the vehicle altitude increases over a test window from 10 – 30 km. To estimate this range, we assumed a wedge flow. For the rms uncertainty estimates, the thermal zero shift uncertainty is removed and the uncertainty expression is: 290 Pa + 3%. Hence, the rms uncertainty varies from 5% - 18% of the mean pressure as the altitude increases from 10 – 30 km. The primary goal of the rms measurements is to help identify when the flow is turbulent. Finally, the pressure gradient uncertainty estimate is taken as $2^{1/2}\varepsilon_P$ (L2-norm).

The estimated uncertainties indicate that the pressure sensors will meet the flight test goals of attitude determination, pressure gradient determination near the skin friction sensors (if needed as described in the next Section), and determination of the transition location and turbulence rms content.

Table A.2.4 Endevco Pressure Measurement Uncertainties

	H = 30 km		H = 20 km		H = 10 km	
α	Δp (Pa)	Unc. (Pa)	Δp (Pa)	Unc. (Pa)	Δp (Pa)	Unc. (Pa)
0	0	632	0	1423	0	5192
0.5	360	628	1650	1405	7800	5107
1	720	633	3300	1428	15600	5221
2	1560	639	7150	1464	33800	5417
4	3120	658	14300	1583	67600	6051
	ε_P = 20%, α_{min} = 0.8°, ε_{rms} = 18%		ε_P = 10%, α_{min} = 0.4°, ε_{rms} = 7%		ε_P = 8%, α_{min} = 0.3°, ε_{rms} = 5%	

Skin Friction

Ahmic brand custom-built skin friction sensors for single-component measurement are to be employed. The wall shear range is ±500 Pa, with a resolution <1.0 Pa. The frequency response is 500 Hz. The sensors have been designed to be independent of vehicle vibration, acceleration, and orientation. The diameter is 1.47 cm (0.58 inch), hence the sensor will be contoured to match the surface of the flight vehicle, and the materials are selected to match the surrounding wall to reduce hot/cold spots. The uncertainty listed in Table 1 is based on the team's experience with this type

DISTRIBUTION A: Distribution approved for public release.

of sensor. Moreover, pressure gradients have also impacted accuracy for earlier models. Additional studies will be performed to quantify the uncertainty for the BOLT II geometry. This includes pressure and temperature sensors in the vicinity of the skin friction gauges to allow for including pressure gradient and temperature effects in the post processing. Also, accelerometers are included to facilitate quantification of acceleration effects during post processing.

PCB Spectra

Four PCB sensors with the GoHypersonics gauge inserts and DAQ will be used to quantify surface spectral content during transition and turbulence. The system components include: sensors installed in custom conduction cooled housing with Peek electrical insulation inserts, high-speed signal conditioner and data system 2.5MHz, and on-board FFT processing. System frequency range is 29.3-898.4kHz and FFT size is 1024 over 0.4096 ms. FFTs are sorted to output 20 highest frequency components. This processing and sorting routine allow processing and transmission time to be reduced to 5 ms, so approximately 8% of the temporal data will be processed and frequency domain peak signals telemetered. The heritage RS-232 interface will be use like other sounding rocket programs and the bitrate has been increased to a 921, 600 bit/s. Data will be continuously telemetered throughout flight, and the new sorting prioritization procedure and increase bitrate improve temporal coverage by an order of magnitude compared to the heritage system which covered less than 1% of the time domain. Conduction cooled housings have been designed and tested to keep PCB pressure transducers well within operational temperature limits through ascent, but heat soak prior to descent could put PCB sensors out of operational range.

CUBRC Thin Films

The CUBRC thin film gages will be used to identify turbulent spots. Hence, an uncertainty is not reported. Platinum thin film gauges have been developed and tested in sustained high temperature environments at or exceeding flight heat fluxes and temperatures. Frequency response of gauges is greater than 1MHz, but gauges will be sampled at lower frequencies to preserve telemetry bandwidth and focus on turbulent spots and fluctuating features. Surface temperature of Pyrex substrate, thin film gauges will be higher than surrounding material, but thermal mass is extremely small and FEA shows influence on neighboring gauges is negligible. In addition to tracking turbulent spots and fluctuating features, the frequency content of these gauges can often be used qualitatively to determine boundary layer state. This assessment may be more qualitative than tracking spots versus time but should still yield valuable information in the post-flight analysis. Additionally, thin film gauges will be used for heat flux measurements in the full-scale, short-duration wind tunnel tests at CUBRC.

Accelerometers

The accelerometer specifications listed in Table A.2.1 are the assumed uncertainties. Additional analyses were not performed.

DISTRIBUTION A: Distribution approved for public release.

APPENDIX B – CDR RFA RESPONSES

B.1 CONFIGURATION CONTROL

Name:___Ken Rock_____
Subject:___Configuration Control_____
Presenter_____N/A_____ Slide Page Number__N/A__

Concern or Issue: Lack of clear Configuration Control process
Assign Action To: Rodney Bowersox
Specific Actions Assigned: Suggest implementing a Configuration Control Process including a Configuration Control Board that meets regularly or as needed to review and accept/reject post-CDR changes to the system.
Response: by R. Bowersox, A. Dufrene, S. Berry

- The BOLT II team created a configuration team consisting of: S. Popkin, I. Leyva, D. Adamczak, R. Bowersox, A. Dufrene, S. Berry, and B. Wheaton.
- Side A and Side B each have layout plans that will be integrated into the AFRL (DAQ) and CUBRC (manufacturing) plans. Each side has a configuration numbering scheme.
- The instrumentation numbering scheme is archived and available for review to the BOLT II team and stakeholders at https://teesportal.engr.tamu.edu/sites/bolt/_layouts/15/start.aspx#/ *(Comment in Final Report: Link no longer maintained. Data and configuration data were submitted to AFOSR).*

  - An example for side A: (MT-A-1-1 is Medtherm Sensor (1,1) on Side A located at position x, y, z. The coordinate system sensor layout (v. 12) is shown in Fig. B.1.1a.

Prefix	Row	Column	x (m)	y (m)	z(m)
MT-A-	1	1	0.19300	0.02881	0.10261

  - An example for side B: (Sensor B-19-28 is Medtherm Sensor (19,28) on Side B located at position x, y, z. The sensor layout v. 12162020_sab is shown in Fig. B.1.1b.

Unique ID	Side B Row	Side B Column	x (m)	y (m)	z(m)
B-19-28	19	28	0.19300	0.02881	0.10261

Close Action By (check one) ___ CDR ___ Post-CDR

DISTRIBUTION A: Distribution approved for public release.

Side A Instrumentation Layout + DURIP Sensor Array V. 12 (CDR+DURIP)

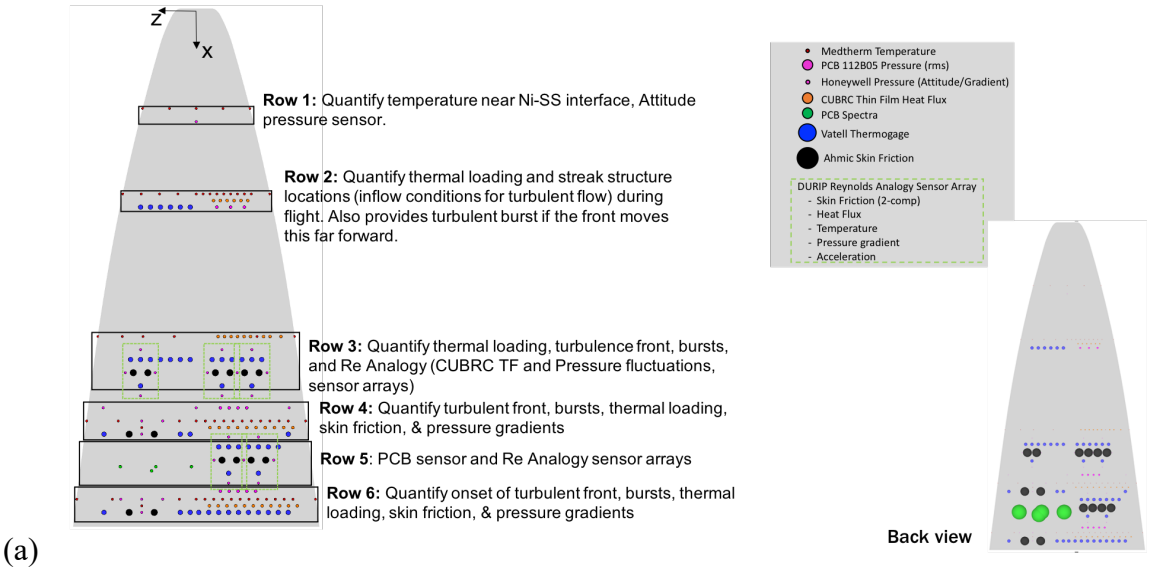

(a)

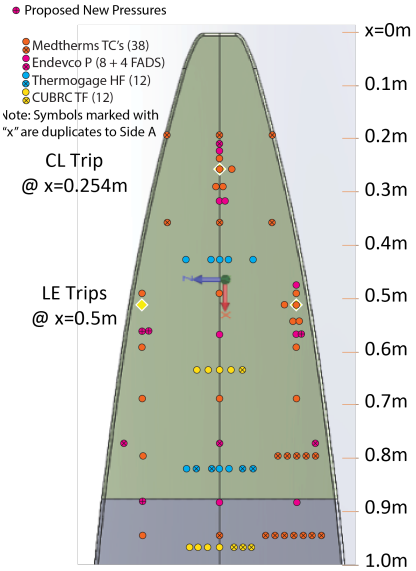

(b)

Figure B.1.1. Sensor layouts. (a) Side A. (b) Side B.

DISTRIBUTION A: Distribution approved for public release.

B.2 PCB DATA

Name:____Rudolph King/Roger Kimmel_____
Subject:___PCB data_____
Presenter_David Adamczak_____ Slide Page Number_____

Concern or Issue: Usefulness of PCB data in current configuration. PCB 132s are known to be acceleration and vibration sensitive as well as dependent on sensor installation. The extraction of the max 20 FFT modes to be telemetered could misrepresent the fluid mechanics. Team may need to look at ways to mitigate this by potentially using a blind sensor that's shielded from the flow or updating the GHI software to download average FFT (full spectral set) over selected time windows. Determine that the planned PCB data acquisition range is suitable for the flight test.

Assign Action To: Bowersox

Response: by R. Bowersox, A. Dufrene, D. Adamczak

- The team (Dufrene, Adamczak, and Bowersox) considered a number of options to mitigate vibration effects. It was determined that limiting the FFT response to block transmitting within the resonance frequencies of the sensor was a logical approach. Accelerometers will be included in the instrumentation package. Because of the limited number of returned FFT peaks, a dummy probe was deemed to be marginally effective.
- The sensor range was examined in three ways. First, the team reviewed the expected boundary layer instabilities (2^{nd} mode and similarly secondary) from TAMU calculations indicated that frequencies are expected to ~400 kHz near the rear of the test article where the instruments are situated. Second, the turbulent boundary layer thickness was estimated to be order 1 cm, which indicates ~150-200 kHz. Third, the team consulted with AFRL (Dr. Borg), and it was determined that the planned range of 30-900 kHz is appropriate and is consistent with upcoming AFRL test flight plans with PCB sensors. For the BOLT II flight, the sensors will be sample at 2.5 MHz and filtered to 900 kHz.

Close Action By (check one) ___ CDR _x__ Post-CDR

DISTRIBUTION A: Distribution approved for public release.

B.3 SIDE B EXPERIMENT

Name:____Dr. R. Cummings_____
Subject:___Side B Experiment_____
Presenter_Scott Berry_____ Slide Page Number_____

R. Cummings RFA: Completion of Side B Experiment

Concern or Issue: Scott Berry mentioned that there were still some decisions to make concerning the placement and size of the trips, which may be based on some additional wind tunnel testing or simulations. He also mentioned that the final location/type of the sensors will be completed within about one week.

Assign Action To: Scott Berry

Specific Actions Assigned: Complete design of Side B trip size/location and location/type of sensors.

Response: by S. Berry, NASA Langley Research Center

The following RFA response describes the final trip and sensor locations, and the supporting analysis, for the Side B Experiment of BOLT II. Most of the information to finalize plans for the roughness experiment was already available prior to the Critical Design Review (CDR), such as the 3 locations where the trips are to be located. No new wind tunnel tests were planned; however, V&V of the computational results used to size the trips for flight were completed by the TAMU group to finalize the trip dimensions. To ensure trip survival during flight, structural-thermal analysis of the trips via a FEA was completed by Aaron Dufrene of CUBRC. These results also supported the decision to move a few sensors from the notional plan presented at CDR to locations on and around two of the trips to capture any local heating as post flight verification of the FEA analysis. The specific locations for the near-trip sensors were selected based on an examination of computational results of the flow around the trips and the resulting horseshoe vortex heating pattern that would be expected in flight.

The remainder of this document provides details of the additional analysis completed after CDR and captures the final trip locations, dimensions, and sensor map.

Final trip locations (selected prior to CDR)

One trip on centerline @ X=0.254m & Z=0.0m

Two symmetric trips near the leading edge @ X=0.5m & ±Z=0.15m

These locations identify the center of each trip.

Also decided prior to CDR was to utilize a trip height to boundary layer thickness (k/d) of 0.7 for transition onset based on a review of the wind tunnel (WT) results obtained from the USAFA. The computational solutions used to derive this scaling parameter approach were obtained from the Texas A&M group based on the range of WT flow conditions. Utilization of k/d = 0.7 is consistent with the approach that was successfully used for the Hyper-X program (see Ref. [i]).

DISTRIBUTION A: Distribution approved for public release.

Final trip dimensions (finalized post CDR)

The trip dimensions were finalized based on three important results that were closed out post CDR. The first was the calculation of a new flight trajectory point (TP) at a different freestream Reynolds number (Re = 2.5 million) than was previously available. This new TP, at a slightly earlier time during descent than before, became the design point for the trips allowing for the dimensions to be slightly bigger. Part of the rationale for choosing a lower Re for design based on transition onset is to reduce likelihood of natural transition obscuring and confusing the observations obtained from the sensor array. The calculated boundary layer parameters for the range of trajectory points are captured in Table B.3.1 for the centerline trip and Table B.3.2 for the leading-edge trips. Originally, there were four points during ascent (labeled as a1 through a4) and four points during descent (labeled as d1 through d4). The new trajectory point used for the final design is shown below (in bold) and listed as d1.5. The second result obtained post-CDR was to complete a grid-sensitivity study to ensure calculated BL parameters at the trip locations were fully converged. Across four different grids, the error relative to the most converged case decreased monotonically with increasing resolution, and the BL-thickness calculations presented at CDR were found to vary by less than ±0.5% when the grid cell count was increased by a factor of 8. The final input was to select an aspect ratio for the trip width to trip height (b/k) of 3. Based on the analysis detailed in Ref. [ii] where it was suggested that the aspect ratio of the trips could influence the resulting onset data, the decision here was to be consistent with the same aspect ratio for all three trips. Based on these three new inputs and the scaling approach identified from the WT data, the final trip dimensions have been determined to be:

Centerline trip: k = 2.625 mm & b = 7.87 5mm
Leading edge trips: k = 0.903 mm & b = 2.709 mm

Table B.3.1: Calculated BL parameters for range of trajectory points for the centerline trip

Case	a1	a2	a3	a4	d1	d1.5	d2	d3	d4
M_∞	5.3	6.1	5.8	5.5	5.3	5.4	5.5	5.6	5.6
Re_L (x10^6)	18.2	11.9	4.1	1.5	1.5	2.5	5.1	8.8	15.3
δ [m]	0.00147	0.00192	0.00304	0.00464	0.00459	**0.00375**	0.00271	0.00211	0.00164
δ* [m]	0.00054	0.00063	0.00100	0.00156	0.00156	**0.00128**	0.00093	0.00072	0.00057
θ [m]	0.00020	0.00026	0.00041	0.00062	0.00060	**0.00049**	0.00036	0.00028	0.00022
M	2.56	2.68	2.65	2.63	2.60	**2.61**	2.60	2.61	2.61
Re_θ	910.38	645.46	391.17	248.54	252.65	**315.85**	453.68	592.30	787.52

Table B.3.2: Calculated BL parameters for range of trajectory points for the leading-edge trips

Case	a1	a2	a3	a4	d1	d1.5	d2	d3	d4
M_∞	5.3	6.1	5.8	5.5	5.3	5.4	5.5	5.6	5.6
Re_L (x10^6)	18.2	11.9	4.1	1.5	1.5	2.5	5.1	8.8	15.3
δ [m]	0.00049	0.00064	0.00103	0.00161	0.00161	**0.00129**	0.00092	0.00071	0.00055
δ* [m]	0.00027	0.00035	0.00057	0.00086	0.00086	**0.00070**	0.00050	0.00039	0.00030

DISTRIBUTION A: Distribution approved for public release.

θ [m]	0.00004	0.00005	0.00009	0.00015	0.00015	**0.00012**	0.00008	0.00006	0.00005
M	4.13	4.60	4.45	4.28	4.16	**4.23**	4.27	4.32	4.32
Re_θ	877.61	737.44	427.11	259.25	255.13	**323.97**	467.58	618.54	816.30

A final comment on the trip dimensions: it is expected that during fabrication of the trips on the flight article, some reduction in the number of significant digits is likely to occur and that a small radius will be included both at the base of the trip and at the top edge (to reduce both heating and any safety hazards due to sharp corners). The as-built dimensions can vary by a small amount from the design-point requirements (above), as long as any deviations are fully documented prior to flight.

Thermal-Structural Assessment (conducted post CDR)

A preliminary assessment was conducted of the robustness of the trips to the flight environment using a finite element analysis (FEA) model with conservative assumptions. A fully turbulent boundary layer was assumed throughout the BOLT2 flight trajectory with an additional 20% margin added to the baseline surface heating, as a first cut analysis. Augmentation factors to account for the trips above the baseline surface were derived from calculations, provided by Hermann Fasel (University of AZ), of heat flux based on a "pizza box" trip that was 75% of the boundary layer thickness. The trip augmentation factors were applied on top of the baseline heating based on an "ultra conservative" 10x assumption. The worst case predicted temperature on either trip for this extreme case was under 1600°F. Stainless steel 410 has a melting point of nearly 2800°F and only begins to see oxidation effects (where a protective chromium-oxide film forms on the surface) at temperatures between 1300-1500°F. Knowing that the trip surface might at best see "oxidation" temperatures for only a few seconds during flight, no thermal or structural concerns seem warranted. Additional analysis and refinements of assumptions may continue to ensure the results thus far are truly conservative, however we believe that there should be no concern with the structural integrity of the trips during the flight of BOLT2.

Final Sensor Layout (finalized post CDR)

Most of the Side B sensor layout plan presented at CDR is still considered final. There are a handful of thermocouples that have been moved specifically for obtaining temperature measurements in the near vicinity to the trips. Figure 1 provides a notional sketch of the near-trip thermocouples, including an approach to scaling the locations around the trips. The heating patterns shown are from preliminary mean flow calculations around a trip and are only intended to provide context as to the placement of the sensors around the trip. The spacing of one trip diagonal (D) away from the center of the trip was deemed a minimum to ensure the temperature measurements were not obscured by internal surface conduction from the trip.

DISTRIBUTION A: Distribution approved for public release.

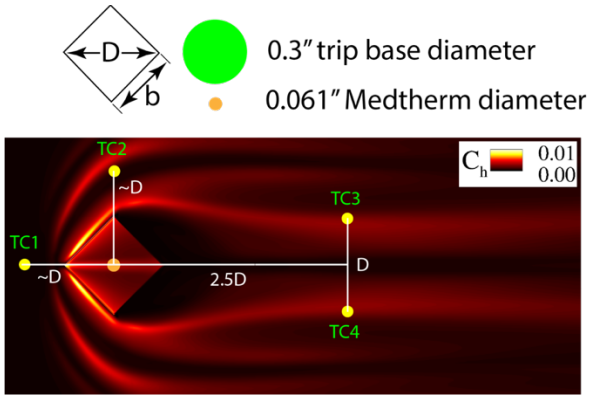

Figure B.3.1. Near trip thermocouple locations.

Based on the notional drawing of Fig. B.3.1 for the surface thermocouples, near trip pressure sensors have also been rearranged to be two diagonals in front and five diagonals behind each trip. Behind the centerline trip, a pair of pressure sensors will be placed to see if the frequency content changes within the near field wake. The remaining three pressure sensors will be placed in the far field wake of two of the trips (on centerline and behind one of the two leading edge ones). With this finalization of the near-trip sensor plan, the entire sensor map has now been updated and is shown in Fig. B.3.2. Note that the sensors marked with an "x" are ones that are duplicates (type and location) of those found on the other side, for side-to-side comparisons and the ones marked with a "+" are newly added (total four) pressure sensors.

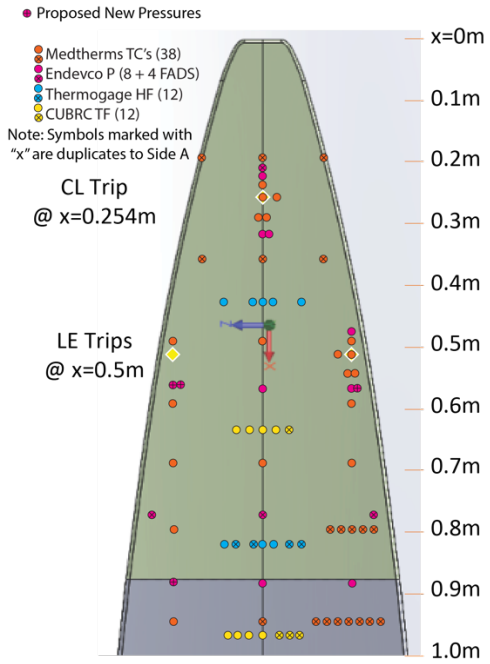

Figure 2. Side B sensor map (post CDR).

References

DISTRIBUTION A: Distribution approved for public release.

[1] Berry, S., Daryabeigi, K., Wurster, K., and Bittner, R., "Boundary Layer Transition on X-43A," Journal of Spacecraft and Rockets, Vol. 47, No. 6, pp.922-934, 2010. (DOI: 10.2514/1.45889)
[1] Choudhari, M., Li, F., Wu, M., Chang, C., Edwards, J., Kegerise, M., and King, R., "Laminar-Turbulent Transition behind Discrete Roughness Elements in a High-Speed Boundary Layer," AIAA Paper 2010-1575, Presented at the 48th Aerospace Sciences Meeting in Orlando, FL, 2010.

DISTRIBUTION A: Distribution approved for public release.

B.4 FLIGHT SYSTEM RFA GROUP

J. Lanzi,[1] A. Dufrene,[2] D. Adamczak,[3] S. Popkin,[3] I. Leyva,[3] R. Bowersox[4]
[1]NASA, Wallops
[2]Aeronautics Division, CUBRC
[3]Air Force Research Laboratory (RQHV and AFOSR)
[4]Aerospace Engineering Department, Texas A&M University

B.4.1. K Rock RFA #2: Nutation

Concern or Issue. *Has a thorough analysis of the tendency for this configuration and flight conditions to result in excessive nutation? I didn't fully capture the attitude control system, how it functions, how it is modeled and analyzed, and how it is tested. A concern is the potential for the attitude control system to excite nutation.*

Response. (Jim Lanzi, NASA Wallops). A concern has been expressed over the potential for the ACS to interact with vehicle aerodynamics and gyrodynamics during the descent of the finned reentry body (producing unwanted nutation motion). The currently proposed concept for operating the ACS involves a low-impulse bang-coast-bang acquisition of the estimated velocity vector target (a fixed earth-relative velocity propagated from an onboard navigation solution to a desired altitude). This is followed by a period of proportional-derivative control about the target. At a pre-programmed condition, the ACS will transition to a rate-damping only mode for a brief period of time, after which it will be placed into a quiescent mode. When the ACS is in a target hold mode, it will be necessarily attempting to hold the vehicle at a non-zero angle of attack (due to the velocity point-solution nature of the target along with other error sources). This will produce an aerodynamic disturbance moment which increases as the vehicle descends. The disturbance moment will cause the angular momentum vector of the vehicle to precess in a way that could produce undesirable nutation dynamics for a spinning vehicle. Figure B.4.1 gives a chart showing the disturbance moment resulting from a 3-deg angle of attack in relation to the moment producing capacity of the ACS.

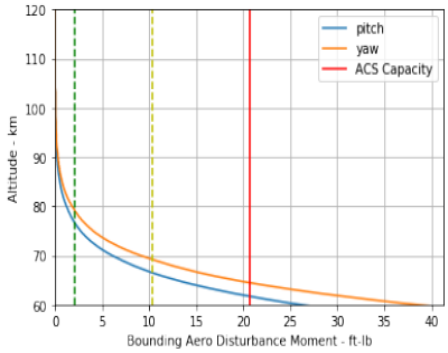

Fig. B.4.1 Disturbance moment resulting from a 3-deg angle of attack in relation to the moment producing capacity of the ACS.

The BOLT2 design team has adopted a criterion which ensures that the ACS will not attempt to null target angle error (proportional control) as long as the bounding aerodynamic torque exceeds 10% of the ACS moment capacity. The team is holding open the option for placing the ACS in a rate-damping mode (to augment the damping produced by the fins) until such a point where the bounding aerodynamic disturbance exceeds 50% of the ACS capacity. In our current design, the Improved Malemute fins are set at a low fin cant (1') to prevent roll-pitch resonance during

DISTRIBUTION A: Distribution approved for public release.

the ascent. Because of this, we do not expect the body to exhibit substantial roll rates during periods of ACS control; therefore, we do not expect the ACS to drive nutation dynamics.

B.4.2. R. King RFA #2: Electrical

Concern or Issue. *One concern on the BOLT1 launch was that the Dave is basically one deep. Is this something that needs to be addressed for BOLT2?*

Response. CUBRC and TAMU are working directly with Dave to try to provide some redundancy. However, there is not a plan to duplicate his capability in terms of constructing the flight computers and DAQ systems. There may be an opportunity at NASA Wallops/NSROC, but this had not been explored.

B.4.3. B. Wheaton RFA #1: Bolts (fasteners)

Concern or Issue. *We never got to this, but in BOLT1 the loads at each of the bolts were comprised approximately at 50% thermal loads and 50% aerodynamic loads. This was at the 16.5km end of flight altitude. I'd expect much higher aero loads at the higher Q at 9km. This might drive you to the MP35N material, or more importantly to a large diameter bolt with might require changing the interfaces.*

Response. Aaron and Brad are working together on this for both BOLT and BOLT II.

---

[i] Berry, S., Daryabeigi, K., Wurster, K., and Bittner, R., "Boundary Layer Transition on X-43A," Journal of Spacecraft and Rockets, Vol. 47, No. 6, pp.922-934, 2010. (DOI: 10.2514/1.45889)

[ii] Choudhari, M., Li, F., Wu, M., Chang, C., Edwards, J., Kegerise, M., and King, R., "Laminar-Turbulent Transition behind Discrete Roughness Elements in a High-Speed Boundary Layer," AIAA Paper 2010-1575, Presented at the 48th Aerospace Sciences Meeting in Orlando, FL, 2010.

DISTRIBUTION A: Distribution approved for public release.